



HAL
open science

Ultra-low temperatures microwave optomechanics for quantum sensing

Dylan Cattiaux

► **To cite this version:**

Dylan Cattiaux. Ultra-low temperatures microwave optomechanics for quantum sensing. Condensed Matter [cond-mat]. Université Grenoble Alpes, 2021. English. NNT: 2021GRALY003. tel-03396741

HAL Id: tel-03396741

<https://hal.science/tel-03396741>

Submitted on 22 Oct 2021

HAL is a multi-disciplinary open access archive for the deposit and dissemination of scientific research documents, whether they are published or not. The documents may come from teaching and research institutions in France or abroad, or from public or private research centers.

L'archive ouverte pluridisciplinaire **HAL**, est destinée au dépôt et à la diffusion de documents scientifiques de niveau recherche, publiés ou non, émanant des établissements d'enseignement et de recherche français ou étrangers, des laboratoires publics ou privés.

THÈSE

Pour obtenir le grade de

DOCTEUR DE L'UNIVERSITE GRENOBLE ALPES

Spécialité : **Physique de la Matière Condensée et du Rayonnement**

Arrêté ministériel : 25 mai 2016

Présentée par

Dylan CATTIAUX

Thèse dirigée par **Eddy COLLIN**, Chercheur, Institut Néel CNRS et Université Grenoble Alpes, et codirigée par **Xin ZHOU**, Chercheuse, IEMN CNRS et Université Lille 1

préparée au sein du **Laboratoire Institut Néel**
dans **l'École Doctorale de Physique de Grenoble**

Optomécanique micro-onde à ultra-basses températures pour la détection quantique

Thèse soutenue publiquement le **03/03/2021**,
devant le jury composé de :

Monsieur Florian MARQUARDT

Professeur, Max Planck Institut, Rapporteur

Monsieur Antoine HEIDMANN

Professeur, LKB, Rapporteur

Madame Natalia ARES

Professeure associée, Université d'Oxford, Examinatrice

Monsieur Olivier Bourgeois

Directeur de recherche, Institut Néel, Examineur

Monsieur Jean-Philippe POIZAT

Directeur de recherche, Institut Néel, Président

Monsieur Tobias KIPPENBERG

Professeur, EPFL, Invité



UNIVERSITÉ GRENOBLE ALPES



PHD IN PHYSICS

PHD THESIS

Ultra-low temperatures microwave optomechanics for quantum sensing

Candidate
Dylan Cattiaux
INSTITUT NÉEL

Advisor
Dr. Eddy Collin
INSTITUT NÉEL - UNIV. GRENOBLE
ALPES

Advisor
Dr. Xin Zhou
IEMN - CNRS UNIV. LILLE 1

ACADEMIC YEAR 2020/2021

To my family

CONTENTS

ACKNOWLEDGMENTS	xv
I INTRODUCTION: A MECHANICAL QUANTUM OBJECT FOR QUANTUM DETECTION	
1 BUILDING AN ULTRA-LOW TEMPERATURE QUANTUM DETECTOR	3
1.1 What is optomechanics ?	4
1.1.1 Historical context	4
1.1.2 Quantum limited detection	4
1.1.3 Beyond standard optomechanics	7
1.2 Microwave optomechanics for quantum electronics	9
1.2.1 What is microwave optomechanics ?	9
1.2.2 A new resource for quantum processes	10
1.3 Microwave optomechanical quantum sensor	12
1.3.1 The Copenhagen interpretation	12
1.3.2 The wave-packet reduction postulate	14
1.3.3 Stochastic collapse theories	15
1.3.4 Gravity induced collapse	16
1.3.5 Probing the quantum stochastic background	17
1.4 Résumé en français	20
II INPUT-OUTPUT FORMALISM IN ELECTRIC CIRCUITS	
2 MEASUREMENT THEORY AND QUANTUM NOISE	25
2.1 The harmonic oscillator heat bath	26
2.2 Hamiltonian formulation	27
2.2.1 Closed optomechanical system Hamiltonian	28
2.2.2 Optical bath interaction Hamiltonian	29
2.2.3 Mechanical bath interaction Hamiltonian	29
2.2.4 Drive Hamiltonian	30
2.2.5 Rotating wave transformation	31
2.3 Markovian quantum stochastic differential equation (QSDE)	32
2.3.1 System dynamics	32
2.3.2 Bath dynamics	32
2.3.3 Quantum Langevin equations (QLE)	36
2.4 Semi-classical limits of Langevin equations	37
2.4.1 Linearized equations of motion	37
2.4.2 Fourier domain solving	38
2.4.3 Spectral densities of mechanics and optics	39
2.4.4 Dynamical back-action	43
2.4.5 Output optical power spectral density	46
2.4.6 Quanta flux and measured quantities	48
2.5 Classical limits	49
2.5.1 Zero coupling limit	49
2.5.2 Coupled system	51
2.6 Quantum limits	55
2.6.1 Cavity back-action	55

2.6.2	Mechanical field	55
2.6.3	Optical field	58
2.7	Beyond linear coupling interaction	62
2.7.1	Nonlinear optomechanical coupling dynamics	63
2.7.2	Limit cycle solving	64
2.8	Conclusion	70
2.9	Résumé en français	71
3	CLASSICAL ELECTRIC CIRCUIT ANALOGUE	73
3.1	Modeling of the classical electric analogue	73
3.1.1	Generic microwave optomechanical circuit	73
3.1.2	Electrical dynamics equation	76
3.1.3	Solving the dynamics equation	78
3.1.4	Classical back-action of cavity onto mechanics	80
3.1.5	Spectral properties and input-output relationships	82
3.2	Classical versus Quantum	86
3.2.1	Planck's postulate	86
3.2.2	Sideband Assymetry	88
3.2.3	Heisenberg limit	90
3.3	Conclusion	94
3.4	Résumé en français	94
III MEASURING BENCHMARK DEVICES: BEAMS AND DRUMS		
4	MECHANICAL STRUCTURES	99
4.1	1D beam structure	99
4.1.1	Beam modal decomposition	99
4.1.2	Beam nonlinear behaviour	102
4.2	2D drumhead structure	104
4.2.1	Drum modal decomposition	104
4.2.2	Drum nonlinear behaviour	107
4.3	Conclusion	108
4.4	Résumé en français	109
5	MICROWAVE CIRCUIT PROPERTIES	111
5.1	Superconducting microwave resonators	111
5.1.1	Idealized resonator	111
5.1.2	Microwave cavity characterization	114
5.2	Modeling optomechanical coupling	117
5.3	Conclusion	118
5.4	Résumé en français	118
6	CRYOGENIC TECHNIQUES: SIDEBAND MEASUREMENTS DOWN TO BELOW 1mK	119
6.1	On-chip design	120
6.1.1	Multiplexed readout design	120
6.1.2	Measured NEMS	121
6.2	The BlueFors [®] machine: base temperature 7.5 mK	122
6.2.1	Working principle of dilution refrigerator	122
6.2.2	Thermometry	123
6.3	The nuclear adiabatic demagnetization cryostat: down to 400 μ K	124
6.3.1	Nuclear Entropy and heat capacity	124
6.3.2	High temperature approximation	125
6.3.3	Electronic heat capacity	125

6.3.4	Phonon heat capacity	126
6.3.5	The case of copper	126
6.3.6	Adiabaticity of the demagnetization process	126
6.3.7	Thermodynamic cycle of the demagnetization process	127
6.3.8	Nuclei-Phonons coupling	128
6.3.9	The home-made refrigerator	129
6.4	^3He thermometry	131
6.5	Microwave experimental platform	132
6.6	Conclusion	134
6.7	Résumé en français	134
7	STOKES SIDEBAND: AMPLIFICATION FOR THERMOMETRY	137
7.1	In built parametric amplifier	137
7.1.1	Optomechanical interaction calibration	137
7.1.2	Blue-detuned pumping method	138
7.2	Optomechanical thermometry	140
7.2.1	Phononic and Two-Level Systems (TLS) thermometry	140
7.2.2	In-equilibrium results	142
7.3	Unstable Stochastic driving force	146
7.4	Ground state cooling	150
7.4.1	Sideband asymmetry thermometry	151
7.4.2	Thermodynamic equilibrium below 1 mK	154
7.5	Conclusion	160
7.6	Résumé en français	161
8	STOKES SIDEBAND: SELF-OSCILLATION BEYOND LINEAR OPTOMECHANICS	163
8.1	Experimental measurement of attractor diagrams	163
8.1.1	Comb structure generation	164
8.1.2	Heating and material dependent effects	164
8.1.3	Microwave measurement technique	167
8.2	Quantifying geometric nonlinearities	167
8.2.1	Optical and mechanical induced frequency shifts	167
8.2.2	3D Fitting procedure	168
8.2.3	Basic estimate of nonlinear coupling strengths	171
8.3	Comparing Beams and Drums behaviour	174
8.3.1	Beams and Drums attractor diagrams	174
8.3.2	Frequency and amplitude fluctuations	176
8.4	Conclusion	178
8.5	Résumé en français	178
	CONCLUSION: MICROWAVE OPTOMECHANICS NEAR ZERO TEMPERATURE	181
	BIBLIOGRAPHY	185

LIST OF FIGURES

FIGURE 1.1	Optical scheme of an advanced gravitational wave detector and typical measured spectral strain sensitivity	5
FIGURE 1.2	Different types of NEMS used for nano-optomechanics in the optical domain	6
FIGURE 1.3	Principle of microwave optomechanics based on beam and drum-head types NEMS	9
FIGURE 1.4	Typical microwave optomechanical design used for quantum electronic experiments	11
FIGURE 1.5	Example of exclusion diagram in the CSL parameters space	17
FIGURE 2.1	Scheme of a completely generic optomechanical system coupled to its mechanical and optical environment	36
FIGURE 2.2	Experimental data of the optical spring effect measured with a beam and a drum device	44
FIGURE 2.3	Experimental data of the optomechanical damping effect measured with a beam and a drum device	45
FIGURE 2.4	Principle of cavity optomechanics presented in the scattering picture with a corresponding transition diagram	46
FIGURE 2.5	Computed output optical power spectral density (PSD) as a function of the input pump power in both cases of Stokes and anti-Stokes pumping	48
FIGURE 2.6	Computed mechanical quantum spectra within the "green" pumping scheme as a function of the injected power	56
FIGURE 2.7	Computed stability curves describing the stability in the self-induced oscillation regime	67
FIGURE 2.8	Measured power spectral density (PSD) of the full generated comb with a zoom-in on the Stokes peak in the self-induced oscillation regime	67
FIGURE 2.9	Calculated colormaps of the output photon flux of the self-oscillating Stokes peak	68
FIGURE 2.10	Theoretical colormaps of the mechanical frequency shift of the self-oscillating Stokes peak	69
FIGURE 3.1	Comparing optical and microwave optomechanical setups	74
FIGURE 3.2	Three equivalent electric circuits for microwave optomechanics with different input and output designs	75
FIGURE 3.3	Norton-Thevenin equivalence for microwave optomechanical circuits	77
FIGURE 3.4	Schematic frequency dependence of both Stokes and anti-Stokes peaks under "blue" sideband pumping	79
FIGURE 3.5	Experimental data of the output photon flux obtained for the "green" pumping scheme displaying noise squashing	90

FIGURE 3.6	Calculated inverse signal-to-noise ratio in the "green" pumping scheme illustrating the "standard classical limit" (SCL)	92
FIGURE 3.7	Computed inverse signal-to-noise ratio in the "blue" pumping scheme	93
FIGURE 4.1	Schematic of a doubly-clamped beam device in its fundamental flexure	100
FIGURE 4.2	Numerical eigenmode simulations of a doubly-clamped beam . . .	101
FIGURE 4.3	Power spectral densities of thermomechanical noise measured with a beam and a drum device	104
FIGURE 4.4	Schematic of a drum device in its fundamental flexure	105
FIGURE 4.5	Numerical eigenmode simulations of a drumhead device	106
FIGURE 5.1	T equivalent circuit for a reciprocal two-port network	111
FIGURE 5.2	Numerical simulation and SEM picture of the lumped element type microwave resonator designed for the beam device motion detection	113
FIGURE 5.3	Comparing transmission and reflection measurements for the two-port bidirectional beam-based design	114
FIGURE 5.4	Cavity reflection measurement of the one-port drum-based design	115
FIGURE 5.5	Phase-resolved measurements of a niobium microwave lumped element cavity and its frequency temperature dependence	115
FIGURE 5.6	Temperature dependence of both the linewidth and the resonance frequency of an aluminum transmission line microwave cavity . .	116
FIGURE 5.7	Measured photon flux due to excess occupation of the cavity mode	116
FIGURE 5.8	Electromechanical simulation of a capacitively coupled beam device	117
FIGURE 6.1	Chip arrangement with picture of the PCB and the microwave optomechanical device based on the beam NEMS	120
FIGURE 6.2	SEM picture and scheme of the NEMS beam structure	121
FIGURE 6.3	SEM picture and scheme of a typical drumhead NEMS structure .	121
FIGURE 6.4	Principles of dilution refrigerators	123
FIGURE 6.5	Heat capacity as a function of temperature for copper	126
FIGURE 6.6	Adiabatic nuclear demagnetization process represented in a T-S thermodynamic diagram	127
FIGURE 6.7	Schematic of the nuclear demagnetization cryostat	129
FIGURE 6.8	Properties of the nuclear demagnetization cryostat	130
FIGURE 6.9	Calibration measurements of the ^3He thermometer	131
FIGURE 6.10	Experimental measurements giving the frequency shift of the tuning fork resonance as a function of its linewidth	132
FIGURE 6.11	Comparative pictures of the mixing chamber stage of both cryostats	133
FIGURE 6.12	Simplified common wiring of the experimental platforms	134
FIGURE 7.1	Experimental optomechanical measurements performed with the beam device	139
FIGURE 7.2	Measured temperature dependence of the mechanical resonance frequency shift and the mechanical damping for the three devices .	140
FIGURE 7.3	Microwave heating characterization	141

FIGURE 7.4	Temperature dependence of the heating effect measured with a drum device	142
FIGURE 7.5	Data of optomechanical thermometry for beam and drum devices	143
FIGURE 7.6	T_{NEMS} and T_{mode} as a function of T_{cryo} for the three devices	145
FIGURE 7.7	Spectrogram of the stokes resonance peak of the beam mode at about 1 mK	146
FIGURE 7.8	Spectrogram of the Stokes resonance peak of the beam mode at 5 mK	147
FIGURE 7.9	Comparing beam measurements with and without applied DC voltage	148
FIGURE 7.10	Comparing beam and drum spike statistics	149
FIGURE 7.11	Sliding average as a function of time measured with the beam device	150
FIGURE 7.12	Characterization of the temperature-independent out-of-equilibrium pump photon contribution	151
FIGURE 7.13	Observation and characterization of motional sideband asymmetry	152
FIGURE 7.14	Sideband asymmetry thermometry	153
FIGURE 7.15	Self-sustained oscillation and optical spring measurement performed with the highly-coupled drumhead device	154
FIGURE 7.16	Monitoring of drum and fork temperatures as a function of time during a demagnetization procedure	155
FIGURE 7.17	Phonon fluctuations properties	156
FIGURE 7.18	Phonon fluctuations as a function of the average phonon occupation	157
FIGURE 7.19	Properties of the statistical analysis	158
FIGURE 7.20	Characteristics of frequency and damping fluctuations of the highly-coupled drum device	159
FIGURE 8.1	Measured heating effect of a drum device due to the applied microwave power	165
FIGURE 8.2	Measured colormap of the output photon flux in the self-induced oscillation regime compared to the linear optomechanical theory .	166
FIGURE 8.3	Measured output photon flux of the self-oscillating Stokes peak compared to the nonlinear optomechanical theory	168
FIGURE 8.4	Measured mechanical frequency shift of the self-oscillating Stokes peak compared to the nonlinear optomechanical theory	169
FIGURE 8.5	Impact of the variation of g_1 and g_2 on the theoretical map	170
FIGURE 8.6	Fitting procedure for both nonlinear coupling terms	171
FIGURE 8.7	Attractors diagram measured with the beam device compared to the nonlinear theory	173
FIGURE 8.8	Comparing the beam and the drumhead self-induced oscillation behaviours	174
FIGURE 8.9	The hysteretic unexplained behaviour of the beam device	174
FIGURE 8.10	Frequency and amplitude fluctuation spectra measured on the broad state of both devices	175
FIGURE 8.11	Frequency and amplitude fluctuation spectra measured on the observed narrow state of the beam device	176
FIGURE 8.12	Frequency and damping fluctuations properties of the badly-coupled drum device	177

LIST OF TABLES

TABLE 3.1	Comparing quantum and classical limits	93
TABLE 6.1	Summary of the experimental parameters for the three devices measured in this thesis	122
TABLE 7.1	Typical highly-coupled drumhead NEMS parameters	154
TABLE 8.1	Fitted nonlinear parameters at different temperatures	171
TABLE 8.2	Typical drumhead NEMS parameters	172

ACKNOWLEDGMENTS

Avant toutes choses, je tiens à exprimer toute ma gratitude à mon directeur de thèse, Dr Eddy Collin, chargé de recherche à l'institut Néel/CNRS pour m'avoir guidé et accompagné durant ces années de travail. Je souhaite en particulier lui exprimer mes chaleureux remerciements pour m'avoir patiemment transmis ses précieuses connaissances en physique, ainsi que pour m'avoir formé aux techniques des ultra-basses températures. Cette thèse n'aurais en aucun cas vu le jour sans son incroyable expertise scientifique. Merci pour ton soutien et ta bonne humeur en chaque moment de réussite comme d'incertitude. Tu as su me transmettre d'incalculables compétences et méthodes scientifiques qui j'en suis sûr s'avéreront indispensables pour la suite de ma vie professionnelle, je t'en serais toujours profondément reconnaissant.

Mes vifs remerciements s'adressent également à ma co-directrice de thèse, Dr Xin Zhou, chargée de recherche à l'institut IEMN/CNRS. Rien de tout cela n'aurait été réalisable sans ses exceptionnelles connaissances en ingénierie micro-onde ainsi que sans ses talents en nanofabrication. J'ai tout particulièrement apprécié ta sympathie ainsi que nos discussions enrichissantes.

D'autre part, je témoigne toute ma reconnaissance aux membres de mon jury. Notamment au Dr Jean-philippe Poizat, directeur de recherche à l'institut Néel/CNRS pour avoir accepté de présider le jury de cette thèse ainsi que pour avoir suivi mon travail durant ces quelques années. Je remercie vivement Dr Antoine Heidmann, directeur de recherche au LKB ainsi que Pr Florian Marquardt, tout deux rapporteurs de cette thèse de doctorat, pour leur présence parmi les membres du jury afin de juger et questionner le contenu de ce travail. Enfin, je remercie les examinateurs et invités, Dr Natalia Ares, Dr Olivier Bourgeois ainsi que Pr. Tobias Kippenberg pour le temps qu'ils consacreront à la relecture de ce manuscrit.

Ce travail de recherche ne se serait pas concrétisé sans tous les membres de l'institut Néel ainsi que les collègues de l'équipe UBT, je pense tout particulièrement au Dr Rasul Gazizulin, expert en réfrigération par désaimantation nucléaire.

Merci au Pr Andrew Armour, professeur à l'université de Nottingham, pour son apport théorique non négligeable dans ce travail de thèse ainsi qu'à l'équipe de recherche du Dr Mika Sillanpää de l'université de Aalto qui a joyeusement accepté de collaborer avec nous, notamment en nous apportant leur savoir-faire de salle blanche.

Enfin, je remercie du fond du coeur toute ma famille et tout particulièrement la femme de ma vie, ma chère épouse, Tania, sans qui rien ne serait possible.

Grenoble, janvier 2020

D. C.

Part I

INTRODUCTION: A MECHANICAL QUANTUM OBJECT FOR QUANTUM DETECTION

"The Copenhagen interpretation of quantum theory starts from a paradox. Any experiment in physics, whether it refers to the phenomena of daily life or to atomic events, is to be described in the terms of classical physics. The concepts of classical physics form the language by which we describe the arrangements of our experiments and state the results. We cannot and should not replace these concepts by any others. Still the application of these concepts is limited by the relations of uncertainty. We must keep in mind this limited range of applicability of the classical concepts while using them, but we cannot and should not try to improve them."

— from Werner Heisenberg about the "Heisenberg cut",
"Physics and Philosophy" [250], page 46

1

BUILDING AN ULTRA-LOW TEMPERATURE QUANTUM DETECTOR

In this chapter, we give a general introduction to this thesis by first explaining what is the field of optomechanics and for what use one can apply its related technologies. We present the amazing force/position sensitivity of optomechanical systems, and discuss some of their tremendous capabilities such as gravitational wave detection. Besides, the recent interest in observing and exploiting macroscopic mechanical motion at the quantum limit brought the experiments down to always lower temperatures (and also smaller sizes), which boosted a new area of research where (more compatible) low energy photons are employed: microwave optomechanics. Superconducting microwave circuits are thus in use and bridge optomechanics with quantum electronics, which positions the former as a new resource for quantum information processing. Microwave optomechanical platforms provide also unique capabilities for testing quantum mechanics at the most basic level. Obviously, there is no doubt that quantum mechanics applies to the harmonic oscillator that represents the mechanical motion. However, almost all experiments focus on the two modes (bosons) involved in the optomechanical coupling, namely the mechanical one and the optical one; and people rely on an active cooling scheme to bring the single motional degree of freedom on which their interest is focused as close as possible to the quantum ground state. These mechanical objects are thus operated out-of-equilibrium, their direct environment being kept essentially uncontrolled. But if one thinks about these devices in terms of quantum-limited detectors, where shall then be the focus? It is obviously the bath that continuously interacts with the mechanical degree of freedom. To date, this is not the route followed by the main stream research, and only few experiments are tackling this issue. In this case the subject of the study is no more the device but its surrounding baths. What is thus looked for is deviations to the expected signature of the environment's impact on the mechanical dynamics. These signatures could be due to any type of stochastic collapse, especially what is believed to stem from quantum gravity. We finally come to the point that for this purpose one obviously needs to understand perfectly the classical and quantum behaviors of these microwave optomechanical devices and that one absolutely needs to control their surrounding baths. This extremely challenging project thus requires expertise in quantum theory, ultimate cryogenics (nuclear demagnetization), and microwave technology (quantum-limited detection).

CONTENTS

1.1	What is optomechanics ?	4
1.1.1	Historical context	4
1.1.2	Quantum limited detection	4
1.1.3	Beyond standard optomechanics	7
	QND and BAE measurements	7
	Self-induced oscillation regime	8
1.2	Microwave optomechanics for quantum electronics	9
1.2.1	What is microwave optomechanics ?	9
1.2.2	A new resource for quantum processes	10
1.3	Microwave optomechanical quantum sensor	12
1.3.1	The Copenhagen interpretation	12
1.3.2	The wave-packet reduction postulate	14
1.3.3	Stochastic collapse theories	15
1.3.4	Gravity induced collapse	16
1.3.5	Probing the quantum stochastic background	17
	Mesoscopic quantum object	18

	Brute force cooling versus active cooling	18
	The system Hamiltonian	19
1.4	Résumé en français	20

1.1 WHAT IS OPTOMECHANICS ?

1.1.1 Historical context

The optomechanical interaction arises from the force exerted by light onto movable objects [136]. It corresponds to the transfer of momentum carried by light (i.e. photon particles) to the surfaces on which it reflects: namely the radiation pressure effect. This dynamical effect of light was first described by J. Kepler in 1619 [235] explaining the direction of comet tails deflected by the solar radiation flux. Much later, in the 19th century J.C. Maxwell formalized the idea of radiation pressure force: "A flat body exposed to sunlight would experience this pressure on its illuminated side only, and would therefore be repelled from the side on which the light falls." [236] and proposed explanations to the first experimental apparatus based on radiation pressure effect, the so-called Crookes's radiometer or light mill [93, 78, 173]. It is only some decades later that A. Einstein made us understand the nature of light fluctuations and in particular the duality wave-particle within blackbody radiation [8, 7], opening the modern field of optomechanics.

With the arrival of optical lasers following the work of A.L. Schawlow [38], pioneering modern experiments begun. In particular, A. Ashkin demonstrated the ability of trapping and feedback-cooling small particles [1, 243]. Laser cooling techniques [189, 80] thus quickly became a new resource for precision experiments such as ultracold atoms, Bose-Einstein condensates, leading to atomic clocks.

V.B. Braginsky was the first to propose theoretically to observe radiation pressure forces on a macroscopic mechanical object [248]. In particular, he investigated the ability of optomechanical techniques to provide cooling of mesoscopic objects placed into an interferometric configuration. Indeed, considering a Fabry-Pérot cavity design with one movable mirror, he demonstrated that the retarded nature of this so-called radiation pressure force, due to the finite lifetime of light inside the cavity, leads to damping or anti-damping of the mirror motion [207]. In practice, depending on the frequency detuning of the input light with respect to the cavity resonance, one can cool or amplify the mechanical motion. Following V.B. Braginsky's work, optical bistability due to radiation pressure in a Fabry-Pérot cavity with a macroscopic movable end mirror was observed experimentally [6]. However, at this time, the optical lasers in use were still dominated by thermal noise preventing observations of genuine quantum effects.

1.1.2 Quantum limited detection

Considering a cavity interferometer used as a position detector for a free test mass, V.B. Braginsky together with C.M. Caves [249, 58] demonstrated that quantum fluctuations of light inside the cavity impose a limit on the position measurement accuracy. Indeed, on the detector side, the photon statistic results in the well-known quantum shot noise whereas on the mirror side, it defines the quantum back-action noise. These Authors were the first to define the ultimate limit imposed by quantum mechanics on "weak and continuous phase-resolved" position measurements, and to speak about the so-called standard

quantum limit (SQL). Their work was essential to the emerging field of gravitational wave detection with the rise of different types of experiments, getting always more and more sensitive.

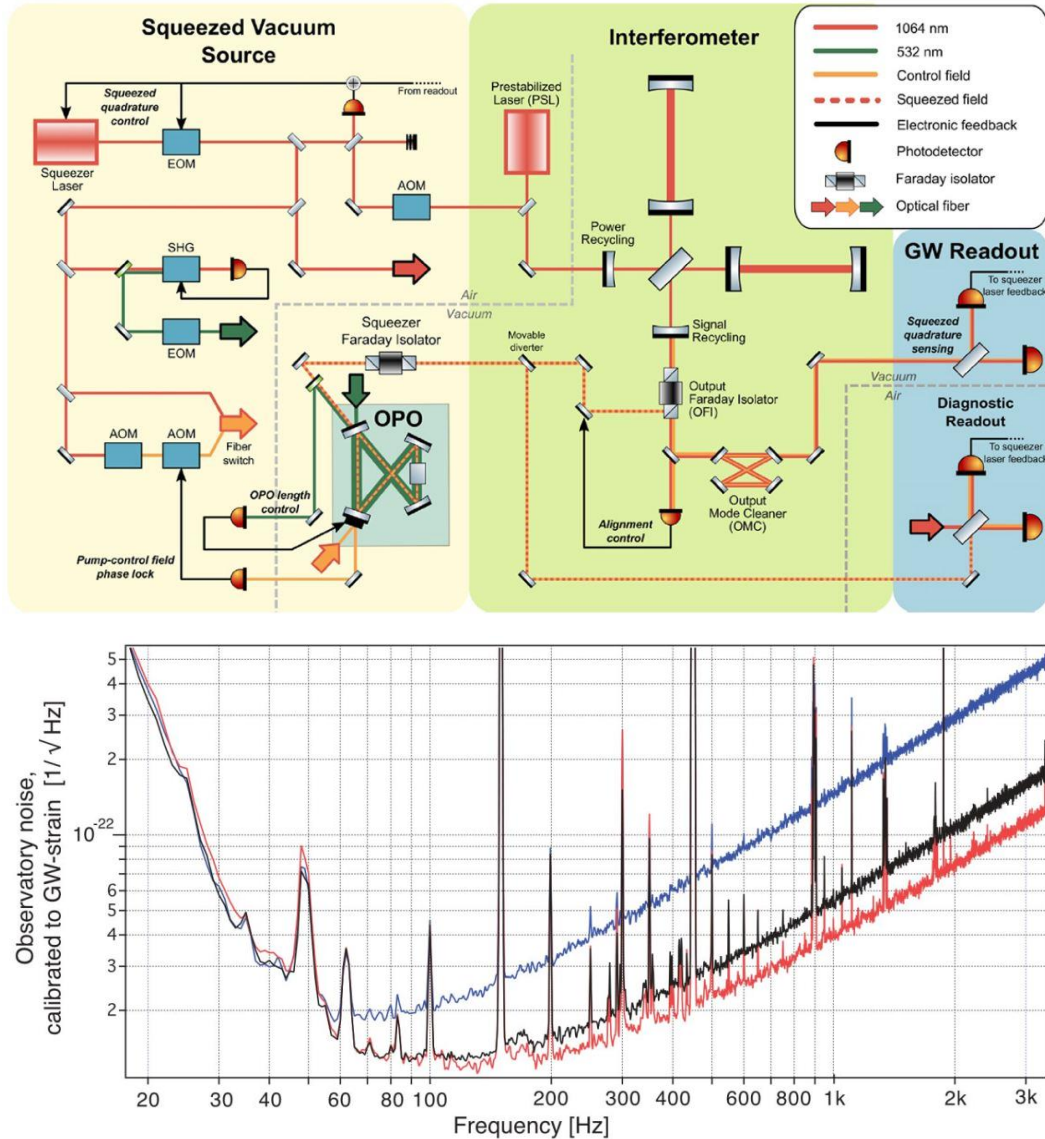


FIGURE 1.1 – Top: Scheme of the squeezed vacuum subsystem and interferometer of Advanced LIGO (adapted from Ref. [148]). A continuous 1 W Nd:YAG laser at 1064 nm, phase-locked to the prestabilized laser (PSL), is used to derive three fields that are launched into fibers: (i) a pump field (green arrow) produced by a second harmonic generator (SHG) and imprinted with 80 MHz sidebands, by an electro-optic modulator (EOM), for feedback control of the optical parametric oscillator (OPO) length via Pound-Drever-Hall sensing; (ii) a control field (orange arrow), produced by two acousto-optical modulators (AOMs), used for sensing the phase of the squeezed vacuum field; and (iii) a local oscillator (red arrow) used for diagnostic homodyne measurements. Bottom: Measured spectral strain sensitivity of the Advanced VIRGO detector in different conditions of squeezed light injection. The black trace corresponds to the reference sensitivity in the absence of squeezed light. The measured sensitivities with squeezing or antisqueezing are shown as the red and blue traces, respectively (adapted from Ref. [79]).

Nowadays kilometer-size Michelson interferometers work, and in particular LIGO and VIRGO, the most sensitive instruments ever built, are able to detect gravitational waves [179, 178, 177], proving the truthfulness of A. Einstein’s theory of general relativity [224]. These kinds of interferometers can now reach sensitivities lower than 10^{-18} in relative

mechanical displacement by optically cooling the vibrational modes of their huge 3 kilogram mirrors down to 200 thermal phonons, bringing them rather close to the quantum regime, but not down to the quantum ground state yet (see Fig. 1.1 bottom). In such apparatuses, feedback cooling [188] of mirror vibration modes using radiation pressure is an essential technique, which has been developed experimentally by the group of P.F. Cohadon [180].

Moreover, the arrival of squeezed light technologies allowed almost 50% increased detection rate. Quantum squeezing is essentially based on nonlinear optics. In practice, the uncertainty due to the Heisenberg principle associated with the measurement of a quadrature of the light can be beaten by transferring all the noise onto the other quadrature [59]. The resolution of conventional interferometers being bound by the Gaussian spread of the vacuum state of light, the use of squeezed signals allows thus to reduce the uncertainty of the detectors [79, 148] (see Fig. 1.1 top). Nevertheless, utilization of strong squeezing tends to increase low-frequency radiation pressure noise on the mirror. To deal with this phenomenon, Advanced LIGO has just been upgraded with frequency-dependent squeezing [215], decreasing phase uncertainty due to shot noise at high frequencies and reducing amplitude uncertainty related to radiation pressure at low frequencies.

Since the early 90s several optomechanical experiments appeared with successful results and in particular some approaches aiming at miniaturizing the studied mechanical objects. Indeed, as optomechanics is an amazing tool for ultra-small displacement/force sensing, it was a perfectly logic development to use it with extremely small objects, thus micro- and nano-mechanical devices. Examples of experiments at micrometer scale include demonstration of feedback damping [106] as well as standard optomechanical effects [149].

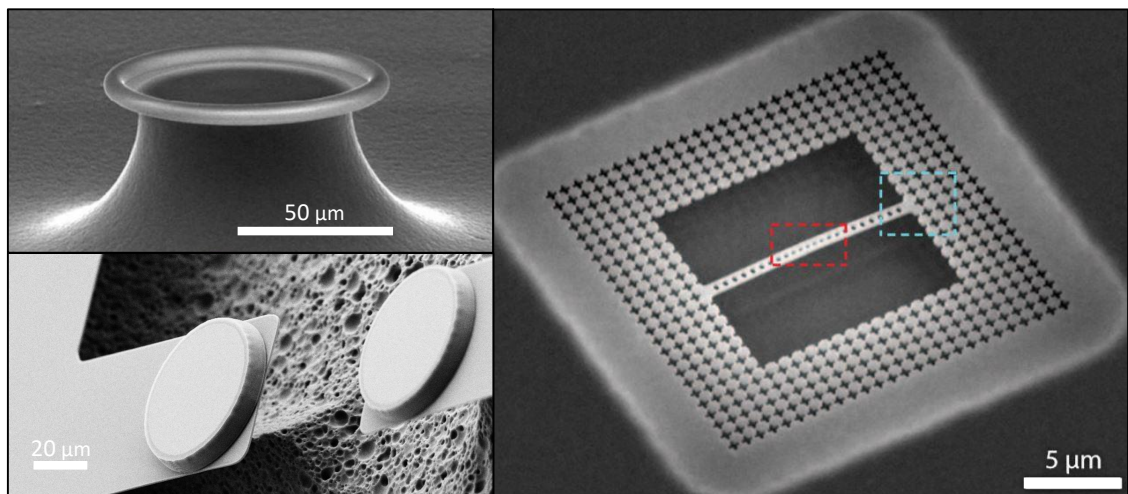


FIGURE 1.2 – Top left: SEM image of a typical toroid microcavity used in Ref. [16]. Bottom left: SEM picture of the mechanical system used in Ref. [187] composed of high-reflectivity Bragg mirrors forming the end part of a Fabry-Pérot cavity. Right: SEM picture of the patterned Si nanobeam with its external phononic bandgap shield used in Ref. [103]; the center red square localizes the cavity region of the nanobeam whereas the blue square shows the interface between the nanobeam and the phononic bandgap shield. Images adapted from Refs. [16, 187, 103].

15 years ago, based on V.B. Braginsky’s developed concepts, a new experimental type of platform for optomechanical interaction study appeared, the so-called microtoroid. These types of micromechanical elements present optical whispering gallery mode (WGM) resonances and acoustic breathing modes (see Fig. 1.2 top left). Both acoustic and optical

modes are (at least partially) co-localized, and coupled through radiation pressure. It was shown that these particular resonators can be excited through evanescent coupling and can display ultra-high quality factors [71], making them a useful platform for observation of dynamical backaction due to radiation pressure effects [194, 203]. In particular, optomechanically induced transparency as well as radiation pressure cooling of such WGM resonators [16] was demonstrated; as well, the same route has been followed with suspended micromirrors [166], with in both cases the ultimate goal of ground state cooling of macroscopic mechanical objects, similarly to what had been performed before on trapped ions by resolved sideband Raman cooling [51].

Besides, due to Stokes scattering processes, quantum mechanics imposes a limit to sideband cooling techniques. The lowest achievable mode phonon number is shown to be reached in the sideband resolved regime where the cavity linewidth is much bigger than the mechanical resonance frequency. To date, reaching the motional quantum ground state of a single mode with a mechanical resonator using lasers at room temperature has only been achieved for a confined levitated nanoparticle [205].

Clean-room technologies thus made it possible over the last decades to create mechanical elements with one (or more) dimensions smaller than a micron [41], and to embed them in optical cavities. Within the field of micro/nano optomechanical systems, adapting the cavity size to the movable element has the clear advantage of allowing higher optomechanical couplings [89] (see Fig. 1.2). Cavity nano-optomechanics thus recently reached the peculiar regime of ultra-strong coupling [132], enabling e.g. photon counting [81]. Small moving objects also have much higher mode resonance frequencies, compared to their macroscopic counterparts. This makes them more suitable for quantum mechanical studies, since the condition $k_B T \ll \hbar\omega$ can be fulfilled with higher (and thus more practical) temperatures. However, relying only on optical active cooling schemes for the mechanical mode when starting from room temperature is very challenging, and it appears that pre-cooling it down to cryogenic temperatures is a real advantage, if not a necessity [187]. Indeed, quantum ground state cooling of a patterned Si nanobeam has been demonstrated experimentally using sideband cooling starting from about 6 K, with in this case a device built from a phononic/photonic crystal co-localized within a 1D object, itself embedded in a phononic crystal shield [103] (see Fig. 1.2 right). Such optomechanical crystals are cavity nano-optomechanical systems in which co-confinement of photons and phonons is realized by nanopatterning periodic structures in thin films (creating so to speak a meta-material for both optics and mechanics) [239, 141]. Unfortunately, all optical laser based nano-optomechanical devices suffer from endemic heating problems due to high energy-photons.

1.1.3 Beyond standard optomechanics

QND AND BAE MEASUREMENTS Today's definition of a Quantum non-demolition (QND) detection is that repeated measurements of an observable \hat{O} of a given system will not increase the uncertainty in the obtained outcomes: so to speak, the measurements will always give the same outcome [209]. Obviously in quantum mechanics, this means that some other observables will be essentially completely unknown. Because of these observables, and the way they couple to \hat{O} through the system Hamiltonian \hat{H} , it is obvious that not all observables \hat{O} of the system can be, even just in principle, monitored by a detection apparatus in a QND fashion. Actually, only a rather specific class of observables can fulfill this property [209, 26]. As well, a specific measurement protocol has to be set up

to be QND; when measuring e.g. with a linear (quantum) amplifier in a "phase-resolved weak-and-continuous" manner the two quadratures of motion \hat{x} and \hat{p} (which do not commute), the output of any measurement is bound by Heisenberg's uncertainty, the so-called standard quantum limit (SQL) [24, 136]. QND measurements in optomechanics have been well explored theoretically and first proposed by V.B. Braginsky [208, 214, 116, 121]. First successful experimental implementations of such a measurement was performed with an optical cavity made of mirrors coated on a piezoelectric crystal [144]. In this case QND measurements of the optical laser beam intensity was performed. Beyond the standard optical frequency pulling proportional to mechanical position x , higher-order couplings appear to be also desirable for specific QND realizations: from an x^2 coupling, one can measure the energy of the mechanics and build QND measurements of mechanical quanta occupancy [126, 45]. Experimental realization of such nonlinear couplings have been realized using optics, with membrane in-the-middle configurations [40]. Recent experiments even proposed a new kind of systems based on superfluid optomechanics; for instance by coupling surface vibrations of a levitated helium droplet to its own optical whispering gallery modes: in this case the droplet plays two roles, the optical cavity and the mechanical resonator [125]. It has been shown that this particular optomechanical configuration could allow QND measurements of angular momentum. QND measurements are nowadays of fundamental interest since they are central to the concept of decoherence measurements of mechanical states, providing essential information concerning quantum collapse theories [45]. For position measurements, the standard quantum limit (SQL) reached for "weak-and-continuous phase-resolved" measurements can be specifically beaten by so-called back-action evading (BAE) techniques [209, 121]. In optomechanics, using two pump tones one can devise a BAE measurement that feeds all measurement noise on one quadrature, while leaving the other one completely free [209, 25]. Nowadays, these measurements represent an amazing tool for nano-optomechanics since experiments are reaching a level of sensitivity where the quantum noise of the cavity does impact the dynamics of the mechanics [98, 107].

SELF-INDUCED OSCILLATION REGIME Driving an optomechanical cavity with a strong Stokes (i.e. blue-detuned) sideband pumping power can trigger self-sustained oscillations of the mechanical degree of freedom [136]. This particular regime is characterized by a rich attractor diagram which has been described theoretically [85], with specific phase-noise and amplitude-noise properties [28, 65, 122]. The mechanical amplitude of motion becoming very large, this coherent state dynamics is extremely sensitive to all nonlinearities present in the system, as already discussed in the early Ref. [153]. Experiments in this regime have been performed in the optical domain [197, 198, 50]; but the strong optical laser pump power always produces dominant thermo-optical nonlinearities (and even instabilities) that require specific modeling, and limit the dynamic range accessible to these systems [32]. While this regime possesses very interesting (and certainly useful) capabilities, only few experimental realizations can be found in the literature. It certainly deserves to be studied more profoundly in the future.

1.2 MICROWAVE OPTOMECHANICS FOR QUANTUM ELECTRONICS

1.2.1 What is microwave optomechanics ?

Experiments performed at low temperatures allow both to reduce the impact of the noisy environment, and also to get closer to the quantum regime $k_B T < \hbar \omega$. In order to reduce the impact of heating on the optomechanical systems due to photon absorption, low-energy photons are more adapted to this regime; this is what we gain in the first place using microwave fields. In addition, microwaves have already been used experimentally exploiting superconducting circuits, within the field of quantum electronics where they are routinely used e.g. to control and measure quantum bits (qubits). In particular, coherent coupling between a single microwave photon and an "artificial atom" (the two lowest energy levels forming the superconducting qubit mimicking an atomic transition) demonstrated that microwave fields can be manipulated at the quantum level [23]. Therefore, this is what we gain in the second place: microwaves make optomechanics compatible with superconducting quantum electronics. Indeed, few years later the quantum ground state of a vibrational mode was reached by cooling to milli-Kelvin temperature a nano-mechanical device, and demonstration of single phonon control was performed by coupling the device to a qubit [30]. The very same tools (cryostats, generators, microfabrication...) as the ones used for quantum electronics can then be applied to perform microwave optomechanics [54]. Such experiments are strictly analogous to their optical counterpart (based on laser control), but shifted down in the microwave domain. These systems are described by the same standard optomechanical Hamiltonian formalism used to characterize a Fabry-Pérot cavity with an oscillating end mirror. In microwave optomechanics however, the radiation mode (the cavity) is an electromagnetic degree of freedom confined in a LC circuit, usually a superconducting resonator made out of lumped elements or a given length of transmission line (Fig. 1.3). The nano- or micro-mechanical object (NEMS) corresponding to the movable mirror degree of freedom is capacitively coupled to the microwave cavity, modulating the capacitance $C(x)$ of this electrical circuit [239, 136] (see Fig. 1.3 bottom right).

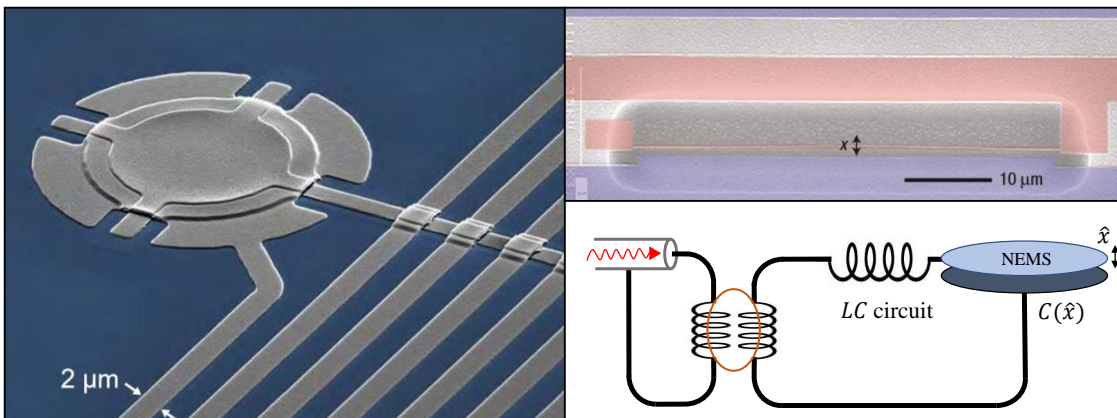


FIGURE 1.3 – Left: SEM image of a drumhead NEMS device embedded in a lumped element type microwave cavity resonator [112]. Top right: False color SEM picture of the doubly-clamped nano-beam capacitively coupled to a transmission line microwave resonator used in Ref. [54]. Bottom right: Scheme of a typical microwave optomechanical system; a microwave drive tone is fed into a transmission line inductively (and/or capacitively) coupled to the microwave resonator represented by a LC circuit. The mechanical displacement of the NEMS device induces a change in the total capacitance of the electrical circuit, altering the microwave resonance frequency. Images adapted from Refs. [112, 54].

The first cryogenic experiment involving nano-mechanical objects embedded in microwave cavities has successfully led to Brownian motion measurements of a nano-beam down to dilution temperatures [54] (see Fig. 1.3 right panel). Demonstration of dynamical backaction in microwave optomechanics due to microwave radiation pressure [110] then quickly allowed to implement active cooling of a mechanical resonator down to its motional quantum ground state [200, 112, 150].

Compared to optics, using superconducting resonant circuits has the advantage of providing a highly versatile platform. Indeed, since quantum limited microwave optomechanical technologies are entirely compatible with quantum electronics, the devices can be efficiently coupled to various types of qubits, or integrated in quantum information processes. Microwave optomechanics thus provides a new resource for quantum engineering [30, 112, 202, 113].

1.2.2 A new resource for quantum processes

Reaching the quantum ground state of a mechanical resonator by radiation pressure cooling has now become routinely accessible with microwave optomechanical systems [112]. Since microwave optomechanics is a highly flexible technology directly compatible with quantum electronics components, these new platforms can be thought of as a new resource for the development of specific quantum electronics components.

Indeed, in order to couple quantum processors and memories through optical photons for quantum communication, photon converters are being built around quantum-mechanical degrees of freedom [43, 14, 101]. Quantum limited optical-photon/microwave-photon converters would allow hybrid quantum network communications, which require interfaces able to preserve quantum coherence during transmissions [114, 184]. Moreover, by engineering the coupling between photons and phonons (what is called bath reservoir engineering), non-reciprocal microwave quantum limited on-chip components could be built [11, 164]. These devices have the peculiarity to present different transmission coefficients from ports say $1 \rightarrow 2$, as compared to transmitting from port $2 \rightarrow 1$. In this context, frequency-converting microwave isolators [90] as well as on-chip microwave circulators [185] have demonstrated their efficiency, both based on optomechanical techniques instead of standard magnetic material properties. Quantum memories [76] as well as hybrid quantum circuits [113] constitute also another amazing (and growing) field of application for microwave optomechanical circuits. Indeed, quantum state transfert between a microwave field and a mechanical resonator has already been demonstrated experimentally [202, 154] (see Fig. 1.4 right); along these lines, in Ref. [190] different state transfer and storage protocols are proposed.

On the other hand, quantum microwave optomechanics is also a new support to generate non-classical states of light and mechanics in order to explore profound quantum concepts. For instance, QND measurements using microwave optomechanical systems have been demonstrated with the creation of quantum squeezed mechanical states [77]. Moreover, BAE schemes become of fundamental interest, as they allow to beat the standard Quantum Limit (SQL) by evading the quantum backaction noise intrinsically produced by microwave detectors [109, 56, 107]. While of great importance, it appears that the fine tuning of system parameters is extremely challenging experimentally; a specific two-tone instability limits strongly the dynamic range of BAE measurements [99]. Optomechanical experiments are also used to find signatures of quantumness, resolving phonon Fock states [134] or quantum motional sideband asymmetry [37]. Besides, creat-

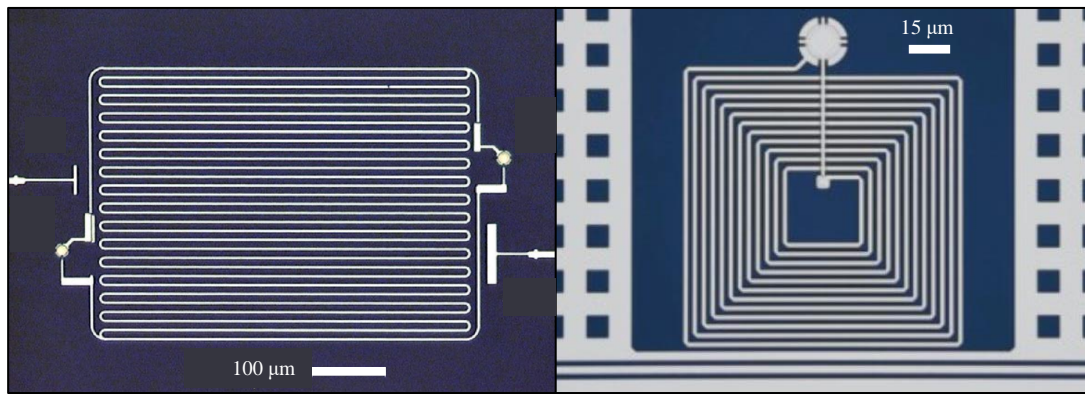


FIGURE 1.4 – Left: SEM image of a microwave cavity resonator coupled to two distinct drumhead NEMS at its both ends. This particular optomechanical device was used to demonstrate quantum entanglement of two mechanical modes in Ref. [57]. Right: SEM picture of the optomechanical setup based on a lumped element cavity coupled to a drumhead mechanical resonator used for coherent state transfert demonstration between photons and phonons in Ref. [202]. Images adapted from Refs. [57, 202].

ing quantum mechanical entangled states is today an intense subject of study. A. Einstein had outlined in a famous paradox (EPR, initials of the Authors, see next Section) how this concept leads to great intellectual difficulties: two separated systems cannot be described independently, which seems to violate relativity as "information" seems to be non-local [9]. Although quantum entanglement has already been demonstrated experimentally using optical photons [10, 213], and macroscopic scale objects as superconducting qubits [146, 127], we have to remind that they correspond to electromagnetic degrees of freedom which are substantially different from mechanical ones [35]. Building on optomechanical systems with more than one mechanical element [88], quantum entanglement of macroscopic mechanical objects has recently become possible [57, 201] (see Fig. 1.4 left), opening emerging information processing capabilities as optomechanical quantum teleportation [105].

All these beautiful experiments demonstrate that mechanical resonators could perform useful functions in the framework of quantum electronics. Besides, in order to operate at the quantum limit, the mechanical modes in use have to be initially in their quantum ground states; for experiments on microwave optomechanics based on Megahertz motion, even within a milli-Kelvin facility this shall rely on a strong red-detuned pump signal that actively cools the mode, with an environment remaining hot. Furthermore, these recent results demonstrate that microwave optomechanics can be applied to the study of the grounds of quantum mechanics; but obviously as expected, quantum mechanics *works*. The subject of the study is here the *mechanical device* itself, and measurements simply confirm what can be calculated within quantum theory.

This is obviously an extremely important step forward. But optomechanical devices are far more than that: they are sensors of their environment, and here they are even quantum sensors. In this case, the subject of study is the *environment* itself, and active pumping is not desired, as shall be discussed in the next Section: experiments should be performed in-equilibrium with all the baths surrounding the device, and the parameter T (*environment* temperature) is one of the most relevant ones, as in most condensed-matter research.

1.3 MICROWAVE OPTOMECHANICAL QUANTUM SENSOR

Quantum mechanics is an extremely well established theory, with tests demonstrating its veracity performed with an amazing precision; even now in metrology, the definitions of fundamental units are based on quantum effects (with e.g. the second from the hyperfine transition of Caesium 133). But quantum mechanics is not complete, as we shall discuss below; for instance, Gravity is not yet incorporated in its formalism in an accepted way. Probing the quantum background of Nature therefore means: performing experiments at this limit of our present-day knowledge of physics. But the question that immediately arises is then: what resources are necessary to perform such quantum sensing of the environment ?

The simplest approach is to (try to) measure steady-state properties which are a direct consequence of quantum mechanics, like e.g. the zero-point-motion [21, 22], or the "static" entanglement created between two objects [57, 183]. An extremely careful quantitative measurement could then be related to the basics of quantum theory, and potentially to *deviations* therein. While being conceptually the simplest approach, it is nonetheless already very challenging and relies on extremely precise calibrations; but the precision that may be required for detecting deviations to quantum mechanics could be just completely out of reach. Clearly, today's experiments are not there yet.

The second, and even more demanding approach is to study both the spatial, but also the *time-dependence* of fundamentally quantum properties. What is there meant by "fundamentally quantum" is states of the mechanical system that cannot be described within classical physics, so-called "non-classical" states: these shall be Fock states (eigenstates of the phonon number), or states involving entanglement to some degree [30, 57, 201, 134]. One should then study how "quantumness" decays over time, as a function of motion amplitude (or phonon number), and compare it to theoretical predictions [155, 29, 62, 4]. This is obviously extremely challenging: the environment should be under control (both the genuine baths and drive/measurement scheme), and the mechanical object cooled to the ground state. But it should also be sufficiently massive to be called "macroscopic", and should be able to sustain large motion as well. At least in principle, comparison between experiments and emerging theories is possible [4, 233]. All these capabilities have not been met *together* yet, and we shall discuss our strategy at the end of this Section. But to contextualize the aims of this research field, we shall first discuss grounds of Quantum Mechanics, and its potential (speculative yet) extensions.

1.3.1 The Copenhagen interpretation

The modern approach to quantum mechanics is essentially the pragmatic one provided by N. Bohr and W. Heisenberg, and named the "Copenhagen Interpretation". This view essentially postulates that the microscopic world follows the Quantum Mechanics description, with in strong contrast with the classical one the *superposition rule*: any linear combination of states (from the Hilbert space describing the system) is allowed. They will evolve following the Schrödinger equation, given the Hamiltonian \hat{H} of the system. This evolution is unitary, and reversible in time under $t \rightarrow -t$. On the other hand, our comprehension of the world is classical, and any measurement shall be understood in classical terms (were only single states are observed). Therefore the Copenhagen interpretation postulates an *artificial boundary* between these two worlds, the so-called "Heisenberg cut" [157, 108]. At some point, the superposition has to reduce to a single state: this is the

projection postulate [3]. This action is strongly non-unitary, and realized in a probabilistic way: from the amplitudes weighting the states in the superposition, one can calculate the probability to obtain it in a measurement. This is known as the *Born rule*. The actual position of the Heisenberg cut is rather ill-defined, but mandatory; understanding what it actually means is outside the scope of this interpretation, and somehow meaningless. The axiomatic construction presented is all that theory has to provide to make proper predictions on measurement outcomes.

However, it is clear that this view of Quantum Mechanics leaves a lot of room for misinterpretations, paradoxes, and... the frustration of *not* understanding what it actually means. There is, essentially, an internal inconsistency since one postulates *at the same time* unitary (Schrödinger) and non-unitary (projection) evolution. Since years, theoreticians try to explain the quantum/classical duality of Nature. One key step in understanding this lies in how a pure quantum state transforms into a classical statistical mixture: this is the so-called "program of decoherence", named so by W.H. Zurek [212, 34, 233]. In order to illustrate this mechanism, let us recall the von Neumann approach to an ideal measurement [233, 4]. Consider a pure state $|\psi\rangle = \sum_i c_i |i\rangle$ which is a superposition of eigenstates $|i\rangle$ of an observable \hat{O} of the system under study. Von Neumann assumes an interaction Hamiltonian with the measuring apparatus of the form:

$$\hat{H}_{int} = \sum_i |i\rangle \langle i| \otimes \hat{A}_i, \quad (1.3.1)$$

where \hat{A}_i is an operator acting only on the Hilbert space of the measuring system, but which does depend on the state i of the measured system (like e.g. measuring a "click" on the left or the right of a Stern & Gerlach experiment, depending on the spin value $\pm 1/2$ of a particle crossing it). The detection apparatus is itself coupled to an environment, that in principle is macroscopic; we shall call $|\Phi_{ME}\rangle$ the quantum state corresponding to them. When a measurement is performed, the total state representing the system plus the measuring device (and its environment) evolves as [233, 4]:

$$\left(\sum_i c_i(0) |i\rangle \right) |\Phi_{ME}(0)\rangle \xrightarrow{t} \sum_i c_i(t) |i\rangle |\Phi_{ME,i}(t)\rangle, \quad (1.3.2)$$

where starting from a factorized state at $t = 0$, the combined system evolves towards an *entangled state* between the system and the detection apparatus. The $|\Phi_{ME,i}(t)\rangle$ (evolution of $|\Phi_{ME}(0)\rangle$ under the action of \hat{H}_{int} and the detection Hamiltonian) is called a "pointer state", since it can discriminate the $|i\rangle$'s within the superposition. The $c_i(t)$ follow the Hamiltonian evolution of the (uncoupled) system.

Writing the density matrix ρ_S of the system alone, its evolution is then:

$$\rho_S = \sum_{i,j} c_i(0) c_j^*(0) |i\rangle \langle j| \langle \Phi_{ME}(0) | \Phi_{ME}(0) \rangle \xrightarrow{t} \sum_{i,j} c_i(t) c_j^*(t) |i\rangle \langle j| \langle \Phi_{ME,j}(t) | \Phi_{ME,i}(t) \rangle. \quad (1.3.3)$$

By definition $\langle \Phi_{ME}(0) | \Phi_{ME}(0) \rangle = 1$, and non-diagonal elements $i \neq j$ [the coherences $c_i(t) c_j^*(t)$] are multiplied by the overlap of the pointer states $\langle \Phi_{ME,j}(t) | \Phi_{ME,i}(t) \rangle$. What is demonstrated by the "Program of decoherence" is that:

$$\langle \Phi_{ME,j}(t) | \Phi_{ME,i}(t) \rangle_{i \neq j} \xrightarrow{t} 0, \quad (1.3.4)$$

therefore the density matrix ends up being diagonal (in the basis defined by the measurement), with $\langle \Phi_{ME,i}(t) | \Phi_{ME,i}(t) \rangle = 1$:

$$\rho_S \xrightarrow{t} \sum_i |c_i(t)|^2 |i\rangle \langle i|. \quad (1.3.5)$$

This means that *interferences* between states cannot be observed anymore for the system; they have been somehow "diluted" into the detection apparatus and its environment.

Note that the evolution of the system plus measuring device is unitary; it is just the fact of looking at the system alone that makes its evolution look like non-unitary. The entanglement with the detection system, which is the source of many paradoxes, is here the mechanism that generates the diagonal form of ρ_S . But the density matrix is still describing a superposition of states, and no "collapse" (or reduction of wave packet in a spatial description) has occurred yet. The weights $|c_i|^2$ are interpreted in the Copenhagen view as the probabilities of finding out one of the states, defining thus the Born rule. But one has then to *postulate* a projection mechanism occurring after the decoherence process, ensuring the classicality. This probabilistic process remains outside of the "Program of decoherence", and has to be added *in addition* to the unitary evolution.

1.3.2 The wave-packet reduction postulate

The heart of paradoxes and misunderstandings is then the projection postulate. This is what makes Quantum Mechanics probabilistic, and avoids quantum superpositions at the macroscopic level. In order to bypass the problem, various theoretical approaches/interpretations have been proposed since the genesis of Quantum theory.

The famous EPR paradox proposed by Einstein, Podolsky and Rosen [9], builds on the idea of "hidden variables" to reconcile entanglement (e.g. created from superposition in quantum mechanics) with locality (e.g. special relativity which forbids transfer of information faster than light). Indeed, Einstein did not accept in the first place the probabilistic nature of quantum theory ("God does not play dice" [158]). Such theories are among so-called *macrorealistic theories*, which circumvent the projection postulate by simply not accepting the superposition rule. Macrorealistic approaches lead to inequalities, Bell's inequality and Leggett-Garg's inequality [36], which are *violated* by quantum mechanics: this clearly disproves pure classical approaches of Nature's law, and proves the validity of the concept of entanglement. Another early approach questioning the basic superposition concept is "superselection rules". In this case, the inexistence of some quantum states at the macroscopic level is explained by postulating some extra selection mechanism. Even if there has been attempts to derive some of these from symmetry arguments postulated in quantum field theories, this approach merely shifts the problem from one axiomatic view to another [233].

Subtle arguments have been put forward for the interpretation of quantum mechanics. In the view of D. Bohm, quantum mechanics is completely deterministic, and the wave function corresponds to a "pilot wave" that drives elementary particles [60, 61]. In this de Broglie-Bohm formalism (or Bohmian mechanics), a state is perfectly well defined, even when not observed. But the theory is by construction non-local (i.e. from the wave function), and the stochastic aspect of the projection postulate is shifted into a different postulate of "quantum equilibrium", where the probabilistic nature of a measurement is understood as a sort of fundamental thermodynamic underlying property. All predictions are equivalent to the standard Copenhagen description, just the projection postulate

has been replaced by another one (the quantum equilibrium). Preferring one or the other becomes then a matter of taste, only.

H. Everett proposed a rather counter-intuitive explanation to the apparent paradox of the inexistence of macroscopic superposed states [95]. In his view, the entire Universe follows the rules of quantum mechanics (as it should), but the probabilistic collapse is just apparent: in reality, the superposition still exists, each part living in a different "branch" of our Universe. Despite extensive works, the main difficulty in this interpretation is the justification of the Born rule [4]. A new recent ontological approach is based on the notion of "context", which justifies the appearance of random results in measurement from the quantization itself [2]. But like for the Bohm mechanics, this shifts one axiomatic view to another, with no new predictive outcome. These approaches are to be contrasted with Stochastic collapse theories, which *do introduce* a new ingredient with potentially measurable consequences [4].

1.3.3 Stochastic collapse theories

In order to explain the origin of probabilities in measurement theory, an underlying (and fundamental) stochastic (and nonlinear) process has been postulated as a new ingredient in quantum mechanics [96, 160, 161, 130, 129]. Following the first modification of the Schrödinger equation by adding such a nonlinear term [176], a plethora of stochastic collapse theories appeared. Some of them induce a wavefunction collapse in momentum space, spin space or energy space. It appears that this is not appropriate to explain measurement outcomes: as an example, two entangled systems far apart sharing (almost) the same energy would essentially not collapse on the position measurement eigenbasis within an energy-dependent collapse model. It is therefore required that the stochastic components acts on *position operators*; besides, the mechanism should be nonlinear in order to create a non-unitary evolution. The first consistent model proposed was the Ghirardi-Rimini-Weber (GRW) one [91]. In this simple space-collapse model, the collapse noise is considered as white and the resulting dynamics is Markovian. Also known as QMSL model (quantum mechanics with spontaneous localization), the reduction of the wave packet in position space introduces two new fundamental constants of Nature: the rate of the spontaneous collapse λ_{GRW} and the characteristic lengthscale over which it operates r_C .

The continuous spontaneous localization model (CSL) then appears as an upgraded version of the GRW theory [92]. CSL theory artificially generates the phenomenon of collapse onto localized states by coupling a *stochastic classical field* to the density operator $\hat{\rho}$ of a particular quantum system. The power of the CSL model is to describe the collapse of the wave function as well as the Schrödinger dynamics by means of a single stochastic differential equation. Compared to other collapse theories, the CSL model remains the most realistic and advanced theory proposed so far. In Fock space, the CSL model is governed by the following mass-proportional nonlinear integro-differential stochastic Schrödinger equation depending on both λ_{CSL} and r_C parameters [175, 4]:

$$\begin{aligned} \frac{d}{dt} |\Psi_t\rangle = & \left[-\frac{i}{\hbar} \hat{H} + \frac{\sqrt{\gamma}}{m_0} \int [\hat{M}(x) - \langle \Psi_t | \hat{M}(x) | \Psi_t \rangle] \frac{dW_t(x)}{dt} dx \right. \\ & \left. - \frac{\gamma}{2m_0^2} \int [\hat{M}(x) - \langle \Psi_t | \hat{M}(x) | \Psi_t \rangle]^2 dx \right] |\Psi_t\rangle, \end{aligned} \quad (1.3.6)$$

where \hat{H} is the Hamiltonian of the quantum system under consideration, m_0 the reference nucleon mass, and γ represents a constant characterizing the strength of collapse. γ is linked to the collapse rate λ_{CSL} as follows:

$$\lambda_{CSL} = \frac{\gamma}{(4\pi r_C^2)^{3/2}}. \quad (1.3.7)$$

$W_t(x)$ is an ensemble of independent Wiener processes, and $\hat{M}(x)$ is a smeared mass density operator:

$$\hat{M}(x) = \sum_j m_j \int \frac{1}{(\sqrt{2\pi}r_C)^3} e^{-\frac{(y-x)^2}{2r_C^2}} \hat{\Psi}_j^\dagger(y) \hat{\Psi}_j(y) dy. \quad (1.3.8)$$

Here, the operator $\hat{\Psi}_j^\dagger(y) \hat{\Psi}_j(y)$ represents the particle density, with m_j the mass of each particle.

Since years, theoretical approaches tend to set bounds on λ_{CSL} and r_C parameters by analyzing existing experiments, and preserving the quantum and classical behaviors on the two sides of the "Heisenberg cut". But within essentially a decade, it has even become possible to realize experiments aiming directly at probing the new physics postulated by CSL models, within various types of systems [115, 186, 199, 21]. This is the field of research the present PhD thesis is aiming at, but obviously from a purely experimental point of view: we propose a specific platform for experiments, with no intention to privilege one model or another. The idea is really to be able to set up measurements in the future which could provide experimental input, and report on the mechanical decoherence of macroscopic moving objects. By no means do we postulate any specific source of stochastic collapse; only measured data shall be able to quantify the deviations to standard Quantum Mechanics, if any.

1.3.4 Gravity induced collapse

However from a pure conceptual point of view, the source of the stochastic noise is indeed the key; otherwise, one would have just replaced one obscure axiom by another. But this replacement is not bland, since it enables to make all the theory fully-consistent: there is no more ill-defined separation between the macro and the micro. But it comes at a cost: the new fundamental noise field introduced in the theory. Even if this construction happens to be a too simple description of Nature, the stochastic underlying process introduced here has to have a fundamental meaningful origin. It is then natural to imagine that it should be related to cosmological properties. Specifically, Gravity is not yet unified with quantum physics, and this issue remains one of the most important challenges of modern Science.

Since the position of massive objects affects the curvature of space-time, it is logical to imagine that with a delocalized object (by the zero point motion), space-time acquires itself a degree of fluctuations. This could be interpreted e.g. as the vacuum fluctuations of gravitons, the gauge bosons mediating the gravitational interaction.

Such a models have been proposed by Karolyhazy (and named the K model) [83], by Diosi [128] and Penrose [182]. These theories propose different approaches which would generate a gravitationally induced spontaneous quantum state reduction. Gravity induced collapse is a promising suggestion which potentially could, if validated by

extremely challenging experiments, allow to reconcile quantum mechanics with general relativity [42].

1.3.5 Probing the quantum stochastic background

Compared to standard Quantum Mechanics, collapse models have a *predictive* outcome: the stochastic background responsible for the wave-function collapse creates also an additional decoherence channel which, at least in principle, is measurable. Therefore, similarly to Bell's or Leggett-Garg's inequalities, well-designed experiments could disprove/prove the extension of quantum theory, and in the latter case could even measure the new constants of Nature λ_C and r_C (whatever their cosmological nature).

A discussion on feasibility is first in order. What one has usually in mind is numbers obtained from dimensional analysis, linking quantum mechanics (\hbar), gravitational interaction (G) and special relativity (c). The resulting parameters are called *Planck's scales*, with a mass $m_P = \sqrt{\hbar c/G} = 2.17 \times 10^{-8}$ kg, a lengthscale $l_P = \sqrt{\hbar G/c^3} = 1.62 \times 10^{-35}$ m, and a timescale $t_P = \sqrt{\hbar G/c^5} = 5.39 \times 10^{-44}$ s. They relate a rather large mass with amazingly small space-time dimensions; this seems to be rather far out of reach of any experiment to date, and only few experimental proposals discuss them specifically [97, 62, 195].

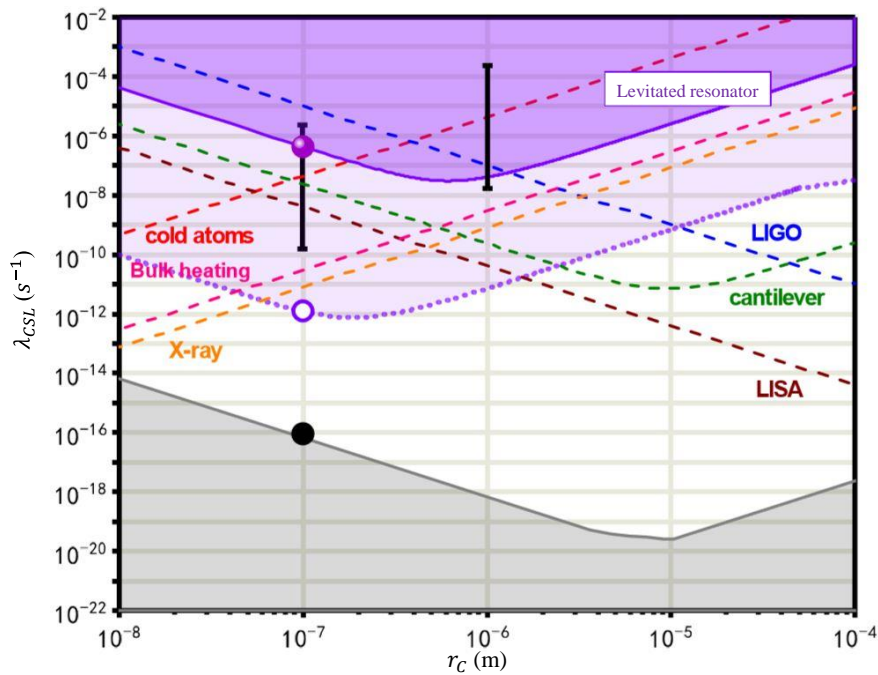


FIGURE 1.5 – Typical exclusion diagram obtained for the CSL parameters: Bounds are given in the $\lambda_{\text{CSL}} - r_C$ space for the levitated microresonator experiment exposed in Ref. [64], and compared with the best experimental results from other sources [purple dot (purple solid line and shaded region for the experiment) and purple circle (purple dashed line and light shaded region for theoretical estimation)]; LIGO (blue dashed line), cantilever (green dashed line) [20], LISA (claret dashed line) [138], cold atoms (red dashed line) [137], X-ray emissions (orange dashed line) [117] and bulk heating in solid matter (pink dashed line) [193]. The suggested theoretical value given by S.L. Adler [192] are represented by the dark bars. The black dot is the value from the GRW model [91] and the grey shaded region is the theoretical lower bound [147]. Adapted from Ref. [64].

But CSL is *not* a relativistic theory, and does not contain c in principle; so maybe Planck's scale relates to an even deeper superior theory, a relativistic extension of collapse

theories which to date even does not exist [4]. As a matter of fact, the constants λ_c and r_c are believed to be much larger than the Planck scale, which puts them within reach of modern physics.

A number of recent articles discuss these parameters within experimental results. What is created is usually exclusion plots in the $\lambda_c - r_c$ space, as shown in Fig. 1.5 (reproduced from Ref. [64]). Pioneering experiments include matter-wave interferometry [115], clouds of cold atoms [199] and bulk phonon modes in diamond [186]. Particular interest has been focused on optomechanics experiments using levitated (macroscopic) particles [22, 64, 13], or in general using micro/nano mechanical elements [21, 4, 131, 62, 210]. The field of ultra-cold microwave optomechanics based on micro/nano mechanical devices seems to offer unique capabilities for experiments probing this new frontier of fundamental physics. This is the technology we have been setting up during this PhD. The key ingredients which justify our route can be summarized as follows:

MESOSCOPIC QUANTUM OBJECT Typical scales probed by collapse theories are given in Ref. [4], especially the lengthscale $r_c \approx 10$ to 100 nm, perfectly within the mesoscopic range. In the case of a cantilever MEMS with mass about 2×10^{-12} kg, which would be in a superposition of states 10^{-15} m apart (about the zero point motion), the collapse time quoted by these Authors is of order a μs , which is very convenient for modern electronics measuring apparatuses. Besides, the collapse rate should scale with the mass of the object, and also increase rapidly with the amplitude of the motion [4]. It is therefore not appropriate to use mechanical modes with very light effective masses and/or extremely small motional amplitudes; this somehow excludes the use of piezoelectric breathing modes [30], surface acoustic waves (SAW) [171], and phononic crystals [94, 103]. This is rather unfortunate, since these modes resonate easily at frequencies in the GHz range, which is typically the frequencies of qubits (with which they can be resonantly interfaced) and makes them ground-state cooled at milli-Kelvin temperatures in conventional dilution cryostats.

On the other hand, MHz beam and drumhead NEMS devices have masses in the right range. They can also sustain rather large motion amplitudes without degrading or even breaking (see Chapter 8, in which our devices are excited up to about 15 nm motion amplitude in the self-sustained oscillation regime).

However, a 15 MHz mode requires a temperature below 1 mK in order to have a thermal population < 1 quantum, which is the definition of ground state cooling. This is particularly difficult, and about an order of magnitude lower than the base temperature of commercial dilution units.

BRUTE FORCE COOLING VERSUS ACTIVE COOLING In order to cool to the ground state MHz devices, people in the literature rely on milli-Kelvin (dilution) commercial cryostats and (active) sideband cooling [112]. This technique requires to have an extra and strong red-detuned pumping tone always on, which can induce heating of the system (physical, or just out-of-equilibrium noise from imperfect generators), and unwanted mixing with other signals in use. The heating is usually the limiting effect for the cooling efficiency, and spurious effects from this extra signal are simply discarded; results are usually compared to a theory with *no* red pumping tone. Full control over the optomechanical Hamiltonian, as discussed in the following argument, obviously cannot be satisfied by such an approach: all terms shall be included in the modeling, with all their implications. This can be rather demanding (and sometimes people rely on numerical simulations), and technically challenging (because of the number of nonlinear components that can create

spurious tones). Moreover, the technique guarantees the cooling *only* of a single mode: all the rest of the structure remains hot.

In a complex structure like a beam or a drum, this is a real problem because all the modes do couple due to nonlinear effects that cannot be avoided [120]. Therefore "hot" modes (that is, thermally populated) can impact the dynamics of other ones, which is precisely why in gravitational wave detection feedback cooling is performed on many of them [188]. Besides, Brownian motion of a mode generates frequency noise onto the other ones to which it is coupled [169]. This looks precisely like decoherence [168], and shall thus be avoided if fundamental sources of it are to be sought. If one cools down to the quantum ground state the *fundamental* mode of a structure by brute-force cooling, this obviously means that all the higher modes will be also in their ground state. In this case, the whole object can indeed be called "quantum" (and not only a single mode of it); the zero point fluctuations of all the modes will thus simply renormalize the resonance of the fundamental one, similarly to a vacuum Lamb shift. When the bath is the subject of the study, environmental decoherence from known sources has to be mastered. The simplest situation assumes that the measurement is *at the quantum limit* (meaning: does not bring any extra uncertainty apart from what is in built in quantum mechanics), and other degrees of freedom interacting with the system are all thermalized at the same temperature T . This can then be modeled, and taken into account [62, 212]. Fitting this dependence to experimental data is then an important first step, which demonstrates that standard quantum mechanics (and the "program of decoherence") does work. However, this source of decoherence can be extremely large, for instance with (actively) cooled microspheres or mass interferometry [115], where internal degrees of freedom can reach temperatures of about a thousand degrees Celsius. It is obviously not desirable, and shall be avoided by cooling *the whole system, i.e. mechanical mode plus environment* as low as possible.

The first Author who proposed to use ultimate cryogenics, namely nuclear demagnetization cryostats, is D. Bouwmeester [72]. Building on the technology of Leiden Cryogenics, the aim was to cool down to microkelvin temperatures macroscopic optomechanical mirrors. This project was extremely ambitious, and never succeeded to our knowledge. On the other hand, cooling to the ground state MHz microwave-optomechanical devices is much less demanding: temperatures around 1 milli-Kelvin are enough, while heat loads are much smaller (less material releasing heat, lower energy photons). In Chapter 6 we describe the technology used during this thesis: a 4 – 8 GHz microwave platform capable of reaching a temperature of order 500 μK . The experimental results acquired with both beam-based and drumhead devices are presented in Chapter 7.

THE SYSTEM HAMILTONIAN If one is concerned with a quantitative understanding of the physics involved here, it is obviously mandatory to control and model perfectly the Hamiltonian describing the optomechanical system at stake. For instance, if one is seeking for deviations to quantum mechanics at the Planck scale, the nonlinear features of the optomechanical coupling, which are usually simply discarded, become relevant [195, 195]. The experimental measurement of these nonlinearities is precisely the subject of Chapter 8.

Furthermore, microwave optomechanics has the ability to interface moving objects with quantum electronics. This capability enables to use e.g. qubits, which make it possible to create non-classical states like Fock states [30, 134, 57]. With MHz devices, the coupling is dispersive since qubits resonances are in the GHz range. But one can built on this capability specific schemes aiming directly at the measurement of quantum decoherence of

delocalized states: this is precisely the subject of the "echo scheme" proposal of Blencowe and Armour [155, 29]. Besides, specific schemes can be engineered like phonon counting from an x^2 coupling [126]. But these new interaction terms shall be well characterized and understood, beyond the standard optomechanical Hamiltonian.

In principle, with a microkelvin/microwave facility such experiments become feasible.

In order to present the experimental/theoretical results achieved during this PhD, the manuscript is divided as follows:

THE PRESENT CHAPTER introduces the motivations and the context of this thesis. In particular, we present the state of the art and discuss the reasons that lead to this work.

THE SECOND CHAPTER is dedicated to the complete derivation of the quantum theory of standard optomechanical systems. Based on the quantum optics formalism and input-output theory, we give a detailed description of the optomechanical coupling mechanism.

THE THIRD CHAPTER presents optomechanics from a completely classical point of view. We derive the classical electric circuit analog of microwave optomechanics, and discuss the bridges between both quantum and classical dynamics, explaining which features are really quantum and which are not.

THE FOURTH CHAPTER exposes a brief characterization of the mechanical devices used in this thesis in the framework of classical continuum mechanics.

THE FIFTH CHAPTER is concerned with microwave circuits characterization. In particular, we present electro-mechanical and electromagnetic finite element simulations allowing us to design the optomechanical coupling.

THE SIXTH CHAPTER exposes the technical aspects of the experiments. The key elements needed in order to build such a microwave optomechanical platform on a nuclear adiabatic demagnetization cryostat are described.

THE SEVENTH CHAPTER is the heart of the experimental work realized in this thesis. It provides experimental measurements of microwave optomechanics at nuclear demagnetization temperatures. Motional ground state cooling of a complete macroscopic device is for the first time demonstrated experimentally.

THE LAST CHAPTER finally presents measurements of microwave optomechanics in the self-induced oscillation regime. We describe a new method to characterize experimentally all relevant types of nonlinearities present in the optomechanical system.

THE SUMMARY concludes the work achieved in this thesis and presents the possible future developments. Particularly, we detail future steps towards characterization of quantum mechanical decoherence, a necessity for testing grounds of quantum mechanics.

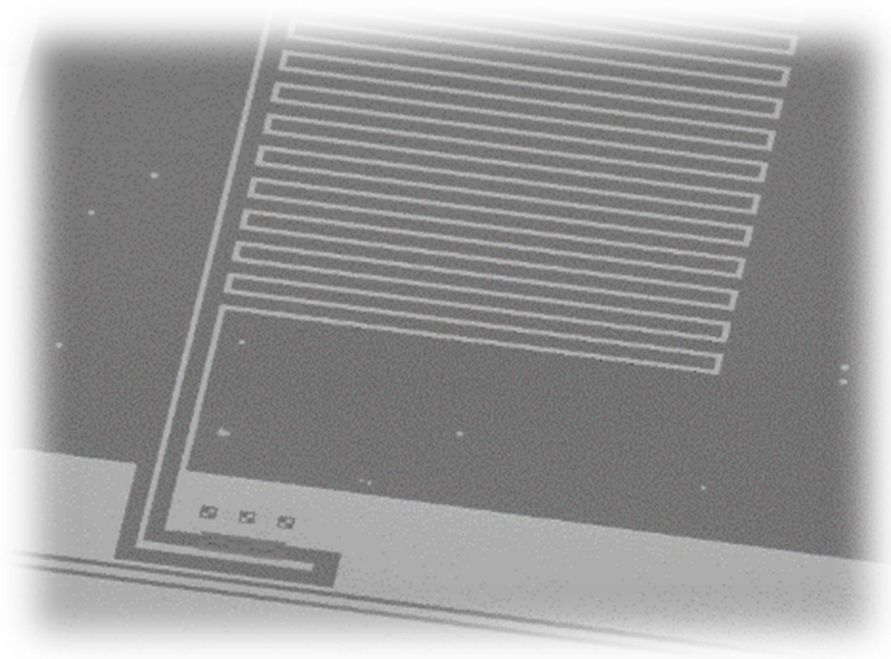
1.4 RÉSUMÉ EN FRANÇAIS

Dans ce chapitre, nous introduisons cette thèse en définissant premièrement ce qu'est l'optomécanique ainsi qu'en expliquant ce pourquoi les technologies basées sur cette

physique peuvent-être utilisées. Nous présentons les systèmes optomécaniques comme étant d'une incroyable sensibilité en force/position et discutons de leurs extraordinaires capacités tel que la détection d'ondes gravitationnelles. De plus, les récents intérêts portant sur l'observation et l'exploitation des mouvements mécaniques macroscopiques à la limite quantique nous ont amené à mesurer toujours plus bas en températures (ainsi qu'à réduire la taille des objets utilisés), ce qui a stimulé le développement d'un nouveau domaine de recherche dans lequel des photons de plus basse énergie (bien plus compatibles avec les basses températures) sont utilisés : l'optomécanique micro-onde. Des circuits micro-ondes supraconducteurs sont donc utilisés et font ainsi passerelle entre l'optomécanique et l'électronique quantique, ce qui positionne l'optomécanique micro-onde comme une nouvelle ressource pour le traitement quantique de l'information. Les plateformes optomécaniques micro-onde fournissent aussi des capacités uniques pour ce qui est de tester la mécanique quantique au niveau le plus basique. En effet, il ne fait aucun doute que la mécanique quantique s'applique à l'oscillateur harmonique qui représente le mouvement mécanique. Cependant, presque toutes les expérimentations se concentrent sur les deux modes (bosoniques) impliqués dans le couplage optomécanique, à savoir, le mode mécanique ainsi que le mode optique. La plupart des expérimentateurs s'appuient aujourd'hui sur le refroidissement optique actif pour amener l'unique degré de liberté mécanique sur lequel l'intérêt est porté au plus proche de l'état quantique fondamental. Ces objets mécaniques sont donc utilisés hors-équilibre, leur environnement directe étant essentiellement incontrôlé. Cependant, considérant ces systèmes en termes de détecteur opérant à la limite quantique, où devons nous concentrer notre attention ? Sur le bain bien sûr, celui-ci interagissant continûment avec le degré de liberté mécanique. A ce jour, ce n'est pas l'objectif suivi par la plupart des groupes de recherche, et seulement très peu d'expérimentateurs font face à ces questions. Dans ce cas, le sujet d'étude n'est plus le système lui-même, mais son bain environnant. L'objectif est donc de rechercher des déviations aux signatures attendues de l'impact de l'environnement sur la dynamique de la mécanique. Ces signatures pourraient être due à un certain type d'effondrement stochastique lié par exemple à la gravité quantique. Pour étudier ce sujet, nous avons donc besoin de comprendre parfaitement les comportements des systèmes optomécaniques micro-onde en régime classique ainsi qu'en régime quantique. De plus, contrôler à la perfection leurs bains environnants est une nécessité. Ce projet extrêmement ambitieux requiert donc une expertise certaine en théorie quantique, en cryogénie (démagnétisation nucléaire), ainsi qu'en technologie micro-onde (détection à la limite quantique).

Part II

INPUT-OUTPUT FORMALISM IN ELECTRIC CIRCUITS



Theoretical description of optomechanics.

2

MEASUREMENT THEORY AND QUANTUM NOISE

In this chapter we introduce the basic quantum theory of common optomechanical systems coupled to an environment. We employ standard Input-Output theory and the Heisenberg-Langevin equations in order to describe optomechanical coupling interactions in a completely generic way. Semi-classical limits of the problem as well as the influence of nonlinear position coupling on the optomechanical dynamics are also discussed.

CONTENTS

2.1	The harmonic oscillator heat bath	26
2.2	Hamiltonian formulation	27
2.2.1	Closed optomechanical system Hamiltonian	28
	Quantum harmonic oscillators	28
	Nonlinear coupling interaction Hamiltonian	28
	Mechanical Duffing Hamiltonian	28
	Optical Kerr nonlinearity	29
2.2.2	Optical bath interaction Hamiltonian	29
2.2.3	Mechanical bath interaction Hamiltonian	29
2.2.4	Drive Hamiltonian	30
2.2.5	Rotating wave transformation	31
2.3	Markovian quantum stochastic differential equation (QSDE)	32
2.3.1	System dynamics	32
2.3.2	Bath dynamics	32
	Markov's first approximation	33
	Input-Output bosons	34
	Input-Output relations	35
2.3.3	Quantum Langevin equations (QLE)	36
2.4	Semi-classical limits of Langevin equations	37
2.4.1	Linearized equations of motion	37
2.4.2	Fourier domain solving	38
2.4.3	Spectral densities of mechanics and optics	39
2.4.4	Dynamical back-action	43
	Optical spring	44
	Optomechanical damping	44
	Scattering picture and optically induced transitions	45
2.4.5	Output optical power spectral density	46
2.4.6	Quanta flux and measured quantities	48
2.5	Classical limits	49
2.5.1	Zero coupling limit	49
	Average intracavity occupation	49
	The damped harmonic oscillator	50
2.5.2	Coupled system	51
	Red detuned pumping	52
	Blue detuned pumping	53
	Quanta flux	54
2.6	Quantum limits	55
2.6.1	Cavity back-action	55
2.6.2	Mechanical field	55
	"Green" pumping	55
	"Red" pumping	57

	"Blue" pumping	58
2.6.3	Optical field	58
	"Green" pumping	59
	"Red" pumping	60
	"Blue" pumping	61
2.7	Beyond linear coupling interaction	62
2.7.1	Nonlinear optomechanical coupling dynamics	63
2.7.2	Limit cycle solving	64
	Ansatz and static deflection	64
	Optical dynamics	64
	Mechanical dynamics	66
	Stable state computation	66
	Output amplitude of the comb structure	69
	Mechanical Duffing nonlinearity	70
2.8	Conclusion	70
2.9	Résumé en français	71

2.1 THE HARMONIC OSCILLATOR HEAT BATH

The classical treatment of a system coupled to a heat bath composed of many degrees of freedom was first proposed by Langevin [172]. He conceptually introduced the equation for a Brownian particle of mass m moving in a viscous fluid under the influence of a potential $V(x)$:

$$\ddot{x} = -\frac{1}{m}V'(x) - \Gamma\dot{x} + \frac{1}{m}\xi(t). \quad (2.1.1)$$

Here we will derive the analog equation in the case of an open quantum optomechanical system. This derivation is at the core of the Fluctuation-Dissipation theorem, which means that the system and the heat bath can exchange energy, leading to both fluctuations $\xi(t)$ and dissipation Γ . Classically, the thermal motion of the bath degrees of freedom creates a stochastic driving force acting on the oscillator, linked to the damping coefficient through: $\langle \xi(t)\xi(t') \rangle = 2mk_B T \Gamma \delta_0(t-t')$. Quantum-mechanically, it can be understood as follows: the effect of the vacuum noise of the bath on the system produces a random driving term which adds up in the Langevin equations, which in turn creates the zero point fluctuations of the system when the commutation rules are imposed [229, 26].

In the case of an optomechanical system, the intracavity field loses energy radiating into the electromagnetic heat bath, and thus the cavity feels the stochastic fluctuations provided by the electromagnetic field. The mechanical mode radiates in the mechanical environment and feels the random fluctuations that this other bath provides. Heat baths, for both the mechanics and light, are assumed to be ensemble of harmonic oscillators (phonons and photons) and the Hamiltonian of such a system can be written as:

$$\hat{H}_B = \sum_n \left[\frac{\hat{p}_n^2}{2m_n} + \frac{1}{2}m_n\omega_n^2\hat{q}_n^2 \right], \quad (2.1.2)$$

where p_n and q_n are canonical operators of the system and follow: $[\hat{q}_n, \hat{p}_m] = i\hbar\delta_{nm}$. \hat{q}_n refers to a position (or an electromagnetic phase), and \hat{p}_m to a momentum (a charge) [26].

We now let the bath interact with a system of corresponding Hamiltonian $\hat{H}_{sys}(\hat{Z}_i)$, \hat{Z}_i representing all the system operators (with $i = 1 \cdots N$). Let \hat{X} be a particular operator

of the system which interacts with the heat bath. Let us also assume that \hat{X} represents a position. The total disturbed Hamiltonian is expressed as:

$$\hat{H} = \hat{H}_{sys}(\hat{Z}_i) + \sum_n \left[\frac{\hat{p}_n^2}{2m_n} + \frac{1}{2}m_n\omega_n^2(\hat{q}_n - \hat{X})^2 \right], \quad (2.1.3)$$

which corresponds to a standard first order linear coupling. By expanding the expression above, one finds a first term $\frac{1}{2}m_n\omega_n^2\hat{q}_n^2$ which represents the bath isolated from the system, a second term $m_n\omega_n^2\hat{q}_n\hat{X}$ which is the linear interaction, and a third term $\frac{1}{2}m_n\omega_n^2\hat{X}^2$ which does not depend on the bath operators and is just a renormalization of the system energy.

Written in this way it is a restoring force shifting \hat{q}_n towards a new rest position which depends on \hat{X} . The \hat{X} operator is assumed to couple the same way to all \hat{q}_n degrees of freedom, without losses of generality; the coupling strength can indeed be incorporated in the definition of the effective mass m_n , at fixed ω_n .

The Hamiltonian can be rewritten by applying the following canonical transformation [229] :

$$\begin{cases} \hat{p}_n \rightarrow -\hat{q}_n\sqrt{k_n}, \\ \hat{q}_n \rightarrow \hat{p}_n/\sqrt{k_n}. \end{cases} \quad (2.1.4)$$

It leads to the following form with $k_n = m_n\omega_n^2$:

$$\hat{H} = \hat{H}_{sys}(\hat{Z}_i) + \frac{1}{2} \sum_n \left[\omega_n^2\hat{q}_n^2 + \left(\hat{p}_n - \sqrt{k_n}\hat{X} \right)^2 \right]. \quad (2.1.5)$$

The new \hat{p}_n, \hat{q}_n are still Bosonic operators, with the same frequency ω_n ; but their masses m_n have been normalized out, and the role of position/momentum has been exchanged. \hat{q}_n and \hat{p}_n are bath operators only, and \hat{X} a system operator, which means that the interaction part of the Hamiltonian is given by:

$$\hat{H}_{int} = - \sum_n \sqrt{k_n}\hat{p}_n\hat{X}. \quad (2.1.6)$$

With this formulation, the interaction takes the canonical form of a linear coupling between a position operator (\hat{X}) and a momentum operator (\hat{p}_n). A completely similar treatment can be performed where the rest position of the system is shifted by the bath bosons, i.e. replacing Eq. (2.1.3). The expansion of the quadratic term leads to the same linear coupling, the only difference being that the renormalization (the last term of the quadratic expansion) is on the bath modes, and not on the system mode. This is actually the physical situation corresponding to the optomechanical modeling, explicitly discussed in the following Sections.

2.2 HAMILTONIAN FORMULATION

The aim of this part is to provide a detailed derivation of the Hamiltonian of the optomechanical system coupled to the environment. The total Hamiltonian of the open system can be expressed with the different terms defined below by:

$$\hat{H} = \hat{H}_0 + \hat{H}_{0,int} + \hat{H}_{M,Duffing} + \hat{H}_{O,Kerr} + \hat{H}_{OB} + \hat{H}_{OB,int} + \hat{H}_{MB} + \hat{H}_{MB,int}. \quad (2.2.1)$$

Note that we define here a single bath per sub-systems (optical or mechanical). This formalism will then be generalized easily to the case of several baths by sub-systems (Section 2.3.3).

2.2.1 Closed optomechanical system Hamiltonian

QUANTUM HARMONIC OSCILLATORS This part of the Hamiltonian (our system \hat{H}_0) is composed of two separate bosonic fields, and is written under the following form with the mechanical mode resonating at the pulsation Ω_m and the radiation mode at ω_{cav} respectively:

$$\hat{H}_0 = \hbar\omega_{cav}\hat{a}^\dagger\hat{a} + \hbar\Omega_m\hat{b}^\dagger\hat{b}. \quad (2.2.2)$$

Here, \hat{a} and \hat{b} are the usual photon and phonon annihilation operators respectively. In this writing, we omitted the zero point energies $\hbar\omega_{cav}/2$ and $\hbar\Omega_m/2$ which do not play any role in the dynamics.

NONLINEAR COUPLING INTERACTION HAMILTONIAN The optomechanical interaction originates in the fact that the optical mode frequency depends on the mechanical displacement. Expanding the interaction to the N^{th} order we can write the nonlinear optomechanical interaction hamiltonian as:

$$\hat{H}_{0,int} = -\hbar g_0 \hat{a}^\dagger \hat{a} (\hat{b}^\dagger + \hat{b}) - \frac{1}{2} \sum_{k=1}^N \hbar g_k \hat{a}^\dagger \hat{a} (\hat{b}^\dagger + \hat{b})^{k+1}, \quad (2.2.3)$$

where g_0 represents the usual single photon-phonon coupling strength and the $g_{k \in \mathbb{N}^*}$ correspond to the higher order coupling terms. These higher terms are responsible for multi-phonon processes, and become relevant when the photon/phonon amplitudes are very large; this is discussed in Section 2.7. Note that we choose to perform such a nonlinear expansion for experimental reasons described in Chapter 8.

A direct link to the radiation pressure force $\hat{F} = -\partial_{\hat{x}} \hat{H}_{0,int}$ can be made, where $\hat{x} = x_{zpf}(\hat{b}^\dagger + \hat{b})$ is the mechanical displacement operator in quantum mechanics:

$$\hat{F} = \hbar \frac{g_0}{x_{zpf}} \hat{a}^\dagger \hat{a} + \frac{1}{2} \sum_{k \in \mathbb{N}^*} (k+1) \hbar \frac{g_k}{x_{zpf}} \hat{a}^\dagger \hat{a} (\hat{b}^\dagger + \hat{b})^k. \quad (2.2.4)$$

This force corresponds to the back-action of the optical field on the mechanics. With the non-linear terms, it also explicitly depends on the displacement of the mechanical element.

MECHANICAL DUFFING HAMILTONIAN At very large amplitude of motion the mechanics can become nonlinear (see Chapter 4). This effect is modeled writing a Duffing-type nonlinear Hamiltonian of the form:

$$\hat{H}_{M,Duffing} = \hbar \frac{\beta_m}{4} (\hat{b}^\dagger + \hat{b})^4, \quad (2.2.5)$$

where we introduce the mechanical duffing parameter β_m (see Chapter 8).

OPTICAL KERR NONLINEARITY The optical analog of the mechanical Duffing effect is called the Kerr nonlinearity. Similarly to the mechanics we write the Kerr-type nonlinear Hamiltonian as:

$$\hat{H}_{O,Kerr} = \hbar \frac{\beta_{cav}}{4} (\hat{a}^\dagger + \hat{a})^4, \quad (2.2.6)$$

where we define the Kerr parameter β_{cav} [162]. This term will be discussed in Chapter 8.

2.2.2 Optical bath interaction Hamiltonian

The environment of the optical mode is represented by a bath of photons constituted of an infinity of harmonic oscillators of frequencies ω_l and annihilation operators \hat{A}_l :

$$\hat{H}_{OB} = \hbar \sum_l \omega_l \hat{A}_l^\dagger \hat{A}_l. \quad (2.2.7)$$

We do not write the zero point energies, which again do not play any role in the dynamics; we just assume that, even when we take the continuum limit for the index l , the sum remains finite (which is nothing but the well known problem of the divergence of the vacuum energy).

The optical bath interacts only with the intracavity field and each of its bosons is coupled to the optical mode by a coupling coefficient K_l . In the following we will discuss the consistency of this term applying the first Markov approximation. Analogously to Eq. (2.1.6), the interaction Hamiltonian between bath and environment is given by:

$$\hat{H}_{OB,int} = -i\hbar \sum_l K_l [\hat{A}_l^\dagger + \hat{A}_l] [\hat{a}^\dagger - \hat{a}], \quad (2.2.8)$$

with $(\hat{A}_l^\dagger + \hat{A}_l) \propto \hat{q}_l$ operator of the bath, and $(\hat{a}^\dagger - \hat{a})/i \propto \hat{P}_a$ operator of the cavity field. K_l is defined in Rad/s.

In the following we will apply a rotating wave approximation (see Section 2.2.5) to this kind of Hamiltonian, which means that the counter-rotating and/or rapidly oscillating terms are dropped out. We follow only the slow dynamics of the system, slow compared to the optical drive field frequency. We will neglect multi-bosons processes, the only kept processes are single-boson ones:

$$\hat{H}_{OB,int} = -i\hbar \sum_l K_l [\hat{a}^\dagger \hat{A}_l - \hat{A}_l^\dagger \hat{a}]. \quad (2.2.9)$$

Multi-photon/phonons interactions will be discussed in Section 2.7.

2.2.3 Mechanical bath interaction Hamiltonian

The mechanical mode is surrounded by a phononic bath. Similarly to the optical bath, the mechanical bath is treated as an infinite number of harmonic oscillators of frequencies Ω_k and annihilation operators \hat{B}_k . Each mode of the bath is coupled to the mechanical mode by a coupling coefficient F_k :

$$\hat{H}_{MB} = \hbar \sum_k \Omega_k \hat{B}_k^\dagger \hat{B}_k, \quad (2.2.10)$$

$$\begin{aligned}
\hat{H}_{MB,int} &= -i\hbar \sum_k F_k \left[\hat{B}_k^\dagger + \hat{B}_k \right] \left[\hat{b}^\dagger - \hat{b} \right], \\
&= -i\hbar \sum_k F_k \left[\hat{b}^\dagger \hat{B}_k - \hat{B}_k^\dagger \hat{b} \right],
\end{aligned} \tag{2.2.11}$$

with $(\hat{B}_k^\dagger + \hat{B}_k) \propto \hat{q}_k$ for the bath and $(\hat{b}^\dagger - \hat{b})/i \propto \hat{p}_b$ operator of the mechanics, having used the same rotating wave approximation as for the optical field. Again, zero point energies have been omitted.

Note that the bosonic operators \hat{A}_l, \hat{B}_k correspond to traveling waves (incoming, outgoing from the optical cavity and the mechanical mode, respectively). This is usually referred to by defining the mode operators as $\sqrt{\omega_l} \hat{A}_l$ and $\sqrt{\Omega_k} \hat{B}_k$, having thus units of $\sqrt{\text{Rad}/\text{s}}$ [229]. We come back to this point in Section 2.3 when defining explicitly incoming and outgoing bosons. Besides, all operators $\hat{A}_l, \hat{a}, \hat{B}_k$ and \hat{b} commute since they represent distinct modes of the complete system.

2.2.4 Drive Hamiltonian

A standard scheme considers excitation drives which are coherent states, essentially semi-classical fields [231]. This excitation corresponds to the mode at frequency $\omega_{l=p}$ included in the interaction Hamiltonian of the optical bath $\hat{H}_{optic} = \hat{H}_{OB} + \hat{H}_{OB,int}$, populated by our classical generator. This state is represented by $|\alpha_p(t)\rangle$ and the eigenvalue equation:

$$\hat{A}_p |\alpha_p(t)\rangle = \alpha_p(t) |\alpha_p(t)\rangle. \tag{2.2.12}$$

In order to take into account the phase noise of the incoming excitation drive, we now consider the driving term as a combination of coherent drives. The source excitation is thus intrinsically a superposition of very close modes of density ρ_c resonating around ω_p , over a narrow bandwidth $\Delta\omega_p$. The standard procedure is to apply two types of unitary transformations on the Hamiltonian \hat{H}_{optic} : One transformation is our rotating wave transform (which leads to the rotating wave approximation, Section 2.2.5) which re-centers the dynamics of our degree of freedom of interest in the vicinity of the excitation frequency ω_p . The other transformation is a displacement in phase-space that re-centers the operator \hat{A}_p around its classical amplitude $\alpha_p(t)$. Note that these two transformations can be applied in any order since they commute.

We thus introduce a superposed displacement operator applied on the superposition of coherent drives $A_{in}(t) = \sum_{q \approx p} \alpha_q(t)$:

$$\hat{D} [A_{in}(t)] = \prod_{q \approx p} \exp \left[\alpha_q(t) \hat{A}_q^\dagger - \alpha_q^*(t) \hat{A}_q \right]. \tag{2.2.13}$$

Each of the displacement terms shifts an optical field operator [227]; we then end up with the Hamiltonian corresponding to this shifted dynamics. The operators having an explicit time dependence, and the only term in \hat{H} which does not commute with \hat{D} being \hat{H}_{optic} the transformation to the new Hamiltonian $\hat{H}_{D,optic}$ takes the form:

$$\hat{H}_{D,optic} = \hat{D}^\dagger [A_{in}(t)] \hat{H}_{optic} \hat{D} [A_{in}(t)] + i\hbar \frac{\partial \hat{D}^\dagger [A_{in}(t)]}{\partial t} \hat{D} [A_{in}(t)], \tag{2.2.14}$$

which re-writes into:

$$\begin{aligned}
\hat{H}_{D,optic} &= \hbar \sum_l \left[\omega_l \hat{A}_l^\dagger \hat{A}_l - iK_l \left(\hat{a}^\dagger \hat{A}_l - \hat{A}_l^\dagger \hat{a} \right) \right] - i\hbar \sum_{q \approx p} K_q \left[\hat{a}^\dagger \alpha_q - \alpha_q^* \hat{a} \right] \\
&+ \hbar \sum_{q \approx p} \omega_q \left[\hat{A}_q^\dagger \alpha_q + \alpha_q^* \hat{A}_q \right] + i\hbar \sum_{q \approx p} \left[\hat{A}_q \dot{\alpha}_q^* - \hat{A}_q^\dagger \dot{\alpha}_q \right] \\
&+ i\frac{\hbar}{2} \sum_{q \approx p} \left[\alpha_q \dot{\alpha}_q^* - \dot{\alpha}_q \alpha_q^* \right] \hat{\mathbb{1}} + \hbar \sum_{q \approx p} \omega_q \alpha_q^* \alpha_q \hat{\mathbb{1}}. \tag{2.2.15}
\end{aligned}$$

$\hat{\mathbb{1}}$ represents the Unity operator.

The optical drive temporal dependence following $\alpha_q(t) = \tilde{\alpha}_q e^{-i\omega_q t}$, the transformed optical bath interaction of the Hamiltonian finally becomes:

$$\hat{H}_{D,optic} = \hbar \sum_l \left[\omega_l \hat{A}_l^\dagger \hat{A}_l - iK_l \left(\hat{a}^\dagger \hat{A}_l - \hat{A}_l^\dagger \hat{a} \right) \right] - i\hbar \sum_{q \approx p} K_q \left[\hat{a}^\dagger \tilde{\alpha}_q e^{-i\omega_q t} - \tilde{\alpha}_q^* e^{i\omega_q t} \hat{a} \right]. \tag{2.2.16}$$

The same procedure could be applied to the Hamiltonian of the mechanical bath $\hat{H}_{meca} = \hat{H}_{MB} + \hat{H}_{MB,int}$ in order to explicit a mechanical drive Hamiltonian representing an external coherent drive acting on the mechanics. We shall not perform this here. The full Hamiltonian, following the displacement transformation, is written \hat{H}_D .

2.2.5 Rotating wave transformation

The full (phase-space shifted) Hamiltonian \hat{H}_D can now be simplified by translating the cavity dynamics in frequency-space to a frame rotating at the incoming microwave frequency ω_p . This transformation called the rotating wave transformation is very useful in order to study slow evolution regarding the excitation frequency taken as being the reference. By doing so, we will neglect all fast oscillating terms, a procedure called rotating wave approximation. Following the same philosophy as for the displacement operator above, we apply a unitary transformation defined by the operator $\hat{U}[\omega_p] = \exp[-i\omega_p \hat{a}^\dagger \hat{a} t]$ to our Hamiltonian in order to generate a new one:

$$\hat{H}_{RWT} = \hat{U}^\dagger \hat{H}_D \hat{U} + i\hbar \frac{\partial \hat{U}^\dagger}{\partial t} \hat{U}. \tag{2.2.17}$$

The total Hamiltonian in this new frame is thus expressed by (neglecting the nonlinear coupling, Duffing and Kerr effects):

$$\begin{aligned}
\hat{H}_{RWT} &= -\hbar \Delta \hat{a}^\dagger \hat{a} + \hbar \Omega_m \hat{b}^\dagger \hat{b} - \hbar g_0 \hat{a}^\dagger \hat{a} \left(\hat{b}^\dagger + \hat{b} \right) \\
&- i\hbar \sum_{q \approx p} K_q \left[\hat{a}^\dagger \tilde{\alpha}_q e^{i(\omega_q - \omega_p)t} - \tilde{\alpha}_q^* e^{-i(\omega_q - \omega_p)t} \hat{a} \right] \\
&+ \hbar \sum_l \left[\omega_l \hat{A}_l^\dagger \hat{A}_l - iK_l \left(\hat{a}^\dagger \hat{A}_l e^{i\omega_p t} - \hat{A}_l^\dagger e^{-i\omega_p t} \hat{a} \right) \right] \\
&+ \hbar \sum_k \left[\Omega_k \hat{B}_k^\dagger \hat{B}_k - iF_k \left(\hat{b}^\dagger \hat{B}_k - \hat{B}_k^\dagger \hat{b} \right) \right], \tag{2.2.18}
\end{aligned}$$

where $\Delta = \omega_p - \omega_{cav}$ corresponds to the detuning of the pump frequency with respect to the microwave cavity frequency.

Our final Hamiltonian thus describes the dynamics of the coupled optical and mechanical fields with the optics shifted in frequency-space around ω_p , and in phase-space

around A_{in} . We essentially re-centered the full problem around the properties of the incoming excitation field.

Besides, we treat here only the linear problem; nonlinearities are discussed in Section 2.7 and Chapter 8 explicitly.

2.3 MARKOVIAN QUANTUM STOCHASTIC DIFFERENTIAL EQUATION (QSDE)

2.3.1 System dynamics

We now derive the quantum Langevin equations for both operators \hat{a} and \hat{b} by writing the equations of motion in the Heisenberg picture [231]:

$$\begin{cases} \dot{\hat{a}} = -\frac{i}{\hbar} [\hat{a}, \hat{H}_{RWT}], \\ \dot{\hat{b}} = -\frac{i}{\hbar} [\hat{b}, \hat{H}_{RWT}]. \end{cases} \quad (2.3.1)$$

Using the Hamiltonian formulation obtained in Eq. (2.2.18) the equations of motion become:

$$\begin{cases} \dot{\hat{a}} = i\Delta\hat{a} + ig_0\hat{a}(\hat{b} + \hat{b}^\dagger) - \sum_{q \approx p} K_q \tilde{\alpha}_q e^{i(\omega_p - \omega_q)t} - \sum_l K_l \hat{A}_l e^{i\omega_p t}, \\ \dot{\hat{b}} = -i\Omega_m \hat{b} + ig_0 \hat{a}^\dagger \hat{a} - \sum_k F_k \hat{B}_k. \end{cases} \quad (2.3.2)$$

These equations thus describe the coupled dynamics of the mechanics and the optical field, the latter being described in the rotating frame, with shifted input fields in phase-space. They depend on the baths dynamics (the two last sums over l and k); to remove these terms we should explicitly compute their dynamics, which is the point of the following Section.

2.3.2 Bath dynamics

We now simplify the equations of motion by studying the external terms (last one in above eqs.) which have the same form in both equations. The method is thus the same for both optical and mechanical baths. We shall then make the demonstration with the Heisenberg equations of motion for the optical bath variables (the equations for the mechanical bath being of the same form):

$$\dot{\hat{A}}_l = -\frac{i}{\hbar} [\hat{A}_l, \hat{H}_{optic}], \quad (2.3.3)$$

$$\Rightarrow \dot{\hat{A}}_l = -i\omega_l \hat{A}_l + K_l \hat{a}, \quad (2.3.4)$$

calculated directly in the laboratory frame, without any transformations applied. This first order differential equation has the standard form of a driven harmonic oscillator where the cavity field \hat{a} plays the role of the drive. This equation has a known exact solution of the following form:

$$\hat{A}_l(t) = e^{-i\omega_l(t-t_0)} \hat{A}_l(t_0) + \int_{t_0}^t e^{i\omega_l(t'-t)} K_l \hat{a}(t') dt'. \quad (2.3.5)$$

We defined the time $t' = t_0$ as being the initial time when the cavity and the bath are totally decoupled, which means that the system and bath density operators both factorize for $t < t_0$. The first term in the solution represents the evolution of the bath isolated from its environment, while the second term is the counterpart of the optical mode that leaks into the bath by means of the coupling mechanism. In this case $\hat{A}_l(t_0)$ corresponds to the bath operators before interaction, they are identified as being input modes. A similar solution to this differential equation can be written such that:

$$\hat{A}_l(t) = e^{+i\omega_l(t_1-t)} \hat{A}_l(t_1) - \int_t^{t_1} e^{i\omega_l(t'-t)} K_l \hat{a}(t') dt', \quad (2.3.6)$$

where in this case $\hat{A}_l(t_1)$ characterizes the bath operators after the interaction (i.e the output modes) and $t' = t_1$ represents the time until the interaction persists. We can now write:

$$\sum_l K_l \hat{A}_l(t) = \sum_l K_l \hat{A}_l(t_0) e^{-i\omega_l(t-t_0)} + \int_{t_0}^t \sum_l K_l^2 e^{-i\omega_l(t-t')} \hat{a}(t') dt', \quad (2.3.7)$$

and:

$$\sum_l K_l \hat{A}_l(t) = \sum_l K_l \hat{A}_l(t_1) e^{i\omega_l(t_1-t)} - \int_t^{t_1} \sum_l K_l^2 e^{-i\omega_l(t-t')} \hat{a}(t') dt', \quad (2.3.8)$$

which should now be simplified.

MARKOV'S FIRST APPROXIMATION We now apply the first Markov approximation that specifies that the spectrum of the coupling K_l for the photonic bath (or respectively F_k for the phononic bath) is white, or in other terms that the coupling is constant over the full range of frequencies (we thus write $K_l \approx K_p$). This assumption made here is relevant within the hypothesis of a high quality factor for both optics and mechanics (which is already the assumption underlying the rotating wave approximation). Since the optical modes of the bath are infinitely close, we can transform the discrete sum into an integral over a continuum:

$$\begin{aligned} \sum_l K_l^2 e^{-i\omega_l(t-t')} &\approx \frac{1}{\Delta k} \int_{k_{min}}^{k_{max}} K_k^2 e^{-i\omega_k(t-t')} dk, \\ &\approx \frac{K_p^2}{v_p \Delta k} \int_{\omega_{min}}^{\omega_{max}} e^{-i\omega(t-t')} d\omega, \end{aligned} \quad (2.3.9)$$

where we introduced the phase velocity $v_p = d\omega/dk$ of the incoming/outgoing optical modes (with k_l the wavenumber of mode l). Physically the continuum assumption means that we consider an infinitely long transmission line/optical fiber ($\Delta k/k_p \ll 1$).

Markov's first approximation states in this case that the quantity K_p is constant over the full frequency bandwidth $\Delta\omega = \omega_{max} - \omega_{min}$ (which is not yet specified). We end up with:

$$\sum_l K_l^2 e^{-i\omega_l(t-t')} \approx \frac{K_p^2}{v_p \Delta k} \Delta\omega \exp \left[-i \frac{\omega_{max} + \omega_{min}}{2} (t-t') \right] \text{sinc} \left[\frac{\Delta\omega}{2} (t-t') \right]. \quad (2.3.10)$$

The interaction time $\Delta t = t_1 - t_0$ between bosons being infinitely small we can assume $\Delta\omega \gg 1/|(t-t')|$ meaning that:

$$\Delta\omega \text{sinc} \left[\frac{\Delta\omega}{2} (t-t') \right] \rightarrow 2\pi\delta(t-t'). \quad (2.3.11)$$

The bandwidth $\Delta\omega$ thus dropped out of the calculation. The external bath term of the differential equation can therefore be written as:

$$\begin{aligned} \sum_l K_l \hat{A}_l(t) &= \sum_l K_l \hat{A}_l(t_0) e^{-i\omega_l(t-t_0)} \\ &\quad + 2\pi \frac{K_p^2}{v_p \Delta k} \int_{t_0}^t \exp \left[-i \frac{\omega_{max} + \omega_{min}}{2} (t-t') \right] \delta(t-t') \hat{a}(t') dt', \\ &= \sum_l K_l \hat{A}_l(t_1) e^{i\omega_l(t_1-t)} \\ &\quad - 2\pi \frac{K_p^2}{v_p \Delta k} \int_t^{t_1} \exp \left[i \frac{\omega_{max} + \omega_{min}}{2} (t'-t) \right] \delta(t-t') \hat{a}(t') dt', \end{aligned} \quad (2.3.12)$$

where the last terms are directly linked to $\hat{a}(t)$.

INPUT-OUTPUT BOSONS In analogy to the transmission lines theory, we define an input mode $\hat{\xi}(t)$ for the optical bath term as well as an output boson $\hat{a}_{out}(t)$, both expressed as a superposition of bosons $\hat{A}_l(t)$ resonating around the excitation wave frequency ω_p within the interval $[\omega_{min}; \omega_{max}]$.

Let us take the two first terms of the right-hand-side of Eqs. (2.3.12). They write:

$$\begin{cases} \sum_l K_l \hat{A}_l(t_0) e^{-i\omega_l(t-t_0)} \approx \frac{K_p \sqrt{2\pi}}{\sqrt{v_p \Delta k}} \hat{\xi}(t), \\ \sum_l K_l \hat{A}_l(t_1) e^{i\omega_l(t_1-t)} \approx \frac{K_p \sqrt{2\pi}}{\sqrt{v_p \Delta k}} \hat{a}_{out}(t), \end{cases} \quad (2.3.13)$$

having defined:

$$\begin{aligned} \hat{\xi}(t) &= \sqrt{\frac{v_p \Delta k}{2\pi}} \sum_l \hat{A}_l(t_0) e^{-i\omega_l(t-t_0)}, \\ &\approx \sqrt{\frac{\rho_c}{2\pi}} \int_{\omega_{min}}^{\omega_{max}} \hat{A}_l(t_0) e^{-i\omega(t-t_0)} d\omega, \\ \hat{a}_{out}(t) &= \sqrt{\frac{v_p \Delta k}{2\pi}} \sum_l \hat{A}_l(t_1) e^{i\omega_l(t_1-t)}, \\ &\approx \sqrt{\frac{\rho_c}{2\pi}} \int_{\omega_{min}}^{\omega_{max}} \hat{A}_l(t_1) e^{i\omega(t_1-t)} d\omega, \end{aligned} \quad (2.3.14)$$

where the density $\rho_c = (v_p \Delta k)^{-1}$.

Similarly, the (classical) incoming field term of Eq. (2.3.2) can be written as:

$$\sum_{q \approx p} K_q \tilde{\alpha}_q e^{-i\omega_q t} \approx \frac{K_p \sqrt{2\pi}}{\sqrt{v_p \Delta k}} \alpha_{in}(t), \quad (2.3.15)$$

with:

$$\begin{aligned} \alpha_{in}(t) &= \sqrt{\frac{v_p \Delta k}{2\pi}} \sum_{q \approx p} \tilde{\alpha}_q e^{-i\omega_q t_0} e^{-i\omega_q(t-t_0)}, \\ &\approx \sqrt{\frac{\rho_c}{2\pi}} \int_{\omega_{min}}^{\omega_{max}} \tilde{\alpha}_q e^{-i\omega t_0} e^{-i\omega(t-t_0)} d\omega. \end{aligned} \quad (2.3.16)$$

α_{in} represents the classical average amplitude of the coherent incoming drive, having noticed that $\tilde{\alpha}_q e^{-i\omega_q t_0} = \langle \hat{A}_q(t_0) \rangle$, the expectation value of the incoming modes populated by the generator. The field $\hat{\xi}(t)$ thus represents the noise contribution of the incoming bosonic channels on top of the classical drive, with both thermal and quantum contributions. Note that these operators are defined in units of $\sqrt{\text{Rad/s}}$: these are traveling bosons [26]. We shall also define the coherent drive in the rotating frame by :

$$\tilde{\alpha}_{in}(t) = \alpha_{in}(t)e^{i\omega_p t}, \quad (2.3.17)$$

and correspondingly the input and output photonic fields, translated in frequency by ω_p (see Section 2.3.3).

INPUT-OUTPUT RELATIONS Defining $\kappa = 2\pi K_p^2 / (v_p \Delta k)$ and remembering the first Markov approximation, we can therefore derive a simplified expression for the bath term:

$$\begin{aligned} \sum_l K_l \hat{A}_l(t) &= \sqrt{\kappa} \hat{\xi}(t) + \frac{\kappa}{2} \hat{a}(t), \\ &= \sqrt{\kappa} \hat{a}_{out}(t) - \frac{\kappa}{2} \hat{a}(t), \end{aligned} \quad (2.3.18)$$

where we employ the useful following mathematical result based on the δ distribution properties, f being an arbitrary function of time t :

$$\begin{aligned} \int_{t_0}^t \delta(t-t') f(t') dt' &= \int_{t_0-t}^0 \delta(-\tau) f(t+\tau) d\tau = \int_{\mathbb{R}^-} \delta(-\tau) f(t+\tau) d\tau, \\ \int_t^{t_1} \delta(t-t') f(t') dt' &= \int_0^{t_1-t} \delta(-\tau) f(t+\tau) d\tau = \int_{\mathbb{R}^+} \delta(-\tau) f(t+\tau) d\tau, \end{aligned} \quad (2.3.19)$$

and:

$$\begin{aligned} \int_{\mathbb{R}^-} \delta(-\tau) f(t+\tau) d\tau &= \int_{\mathbb{R}^+} \delta(-\tau) f(t+\tau) d\tau, \\ &= \frac{1}{2} \int_{\mathbb{R}} \delta(-\tau) f(t+\tau) d\tau, \\ &= \frac{1}{2} f(t). \end{aligned} \quad (2.3.20)$$

Substituting equations, we finally obtain the input-output relation under the following form [26]:

$$\hat{a}_{out}(t) = \hat{\xi}(t) + \sqrt{\kappa} \hat{a}(t). \quad (2.3.21)$$

This equation appears to be very useful to calculate the output optical spectrum and to derive time reversal quantum langevin equations. Experimentally, this writing corresponds to a system with a single optical bath that is both the input and the output port: the field propagating away is thus composed of the incoming field plus the one radiated out by the optical mode via the coupling mechanism. The (more realistic) generic case considering more than one bath is discussed in the next Section.

The same treatment can be performed concerning the mechanical bath interaction, defining an input mechanical boson $\hat{\zeta}(t)$ of density ρ_m as the one used for the optical field:

$$\hat{\zeta}(t) = \sqrt{\frac{\rho_m}{2\pi}} \int_{\Omega_{min}}^{\Omega_{max}} \hat{B}_{\Omega}(t_0) e^{-i\Omega(t-t_0)} d\Omega. \quad (2.3.22)$$

Applying the same methods we finally end up with the following mechanical input equation:

$$\sum_k F_k \hat{B}_k(t) = \sqrt{\Gamma} \hat{\zeta}(t) + \frac{\Gamma}{2} \hat{b}(t), \quad (2.3.23)$$

where we defined the relaxation rate Γ for the mechanics similarly to κ for the optics. In analogy with the optical part, the first term of this equation is generated by the mechanical mode that radiates quanta into the mechanical heat bath via the coupling interaction whereas the second term comes from the free evolution of the mechanical heat bath.

2.3.3 Quantum Langevin equations (QLE)

We now use Eq. (2.3.2) and the two input-output relations for both fields to compute the quantum equations of motion of the overall system. We now generalize to the case where the optomechanical system is coupled to i different optical baths and j different mechanical baths. Applying the rotating wave transform to the right hand side of Eq. (2.3.18), and injecting it into Eq. (2.3.2), we obtain:

$$\begin{cases} \dot{\hat{a}} = i\Delta\hat{a} - \frac{\kappa}{2}\hat{a} + ig_0\hat{a}(\hat{b} + \hat{b}^\dagger) - \sqrt{\kappa_{ex}}\tilde{\alpha}_{in}\hat{1} - \sum_i \sqrt{\kappa_i}\hat{\zeta}_i(t), \\ \dot{\hat{b}} = -i\Omega_m\hat{b} - \frac{\Gamma_m}{2}\hat{b} + ig_0\hat{a}^\dagger\hat{a} - \sum_j \sqrt{\Gamma_j}\hat{\zeta}_j(t), \end{cases} \quad (2.3.24)$$

where the total decay rate of the cavity is $\kappa = \kappa_{ex} + \sum_{i \neq ex} \kappa_i$ and the total decay rate of the mechanical mode is $\Gamma_m = \sum_j \Gamma_j$. This is schematized in Fig. 2.1. We have defined $\kappa_{ex} = 2\pi K_p^2 / (v_p \Delta k)$ the coupling to the optical bath that serves both as input and output. Each bath is coupled with its own rate κ_i (for the optics, and Γ_j for the mechanics). The input/output one is called a port, in order to differentiate it from the others; this corresponds to a system with a single terminal, wired in reflection mode. The model is easily extended to a multi-terminal setup (see experimental Chapter 7 for details). In Eq. (2.3.24), $\tilde{\alpha}_{in}(t)$ corresponds to the excitation amplitude in the rotating frame, obtained from Eq. (2.3.16), and we make for commodity the substitution for the optical fields $\tilde{\zeta}_i(t) \rightarrow \zeta_i(t)e^{i\omega_p t}$, which represent the optical baths operators shifted in frequency by ω_p . It is worth to remind here that the terms depending on $\hat{\zeta}_j(t)$ and $\hat{\zeta}_i(t)$ [and respec-

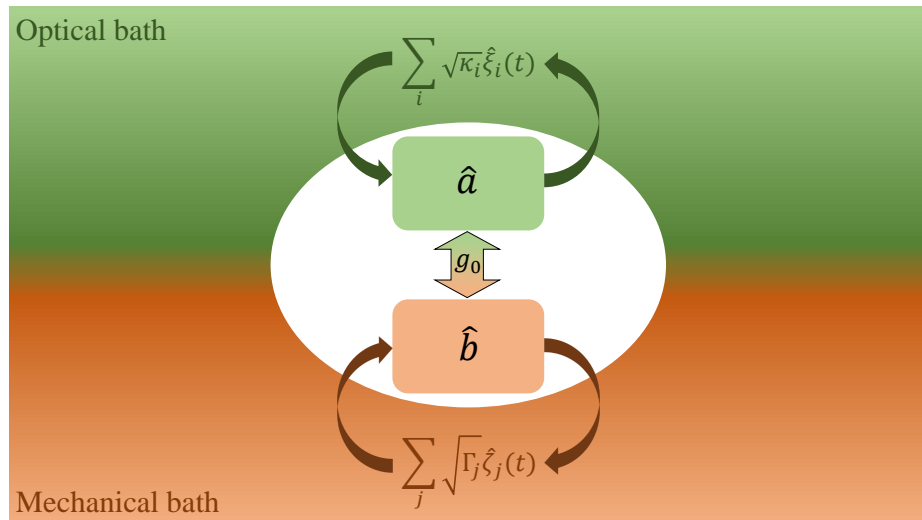


FIGURE 2.1 – Scheme of a completely generic optomechanical system coupled to its mechanical and optical environment. Note that the optical drive term ($i = ex$) is part of the optical bath.

tively on $\hat{\zeta}_j^\dagger(t)$ and $\hat{\zeta}_i^\dagger(t)$] are operators representing the noisy (quantum) environment interacting with the optomechanical system. Each bath is independent, and the initial state of the total system (at $t \rightarrow -\infty$ prior to interaction) is factorized. But these bath states, apart from the imposed (classical) drive, are not. If the statistics of these operators is thermal (i.e. high temperature limit), the input fields will be thermal noise. But at zero temperature, quantum noise always persists, arising from the zero point motion of the input field. With the use of the first Markov approximation, we consider these noises to be delta-correlated in time. Using the expected value operation $\langle \dots \rangle$ which means an average over all the possible quantum states of the Hilbert space, the noise correlators [26] are:

$$\begin{aligned} \langle \hat{\zeta}_i^\dagger(t) \hat{\zeta}_i(t') \rangle &= n_i \delta(t - t'), & \langle \hat{\zeta}_i(t) \hat{\zeta}_i^\dagger(t') \rangle &= (n_i + 1) \delta(t - t'), \\ \langle \hat{\zeta}_j^\dagger(t) \hat{\zeta}_j(t') \rangle &= \eta_j \delta(t - t'), & \langle \hat{\zeta}_j(t) \hat{\zeta}_j^\dagger(t') \rangle &= (\eta_j + 1) \delta(t - t'), \end{aligned} \quad (2.3.25)$$

where n_i represents an occupation number of photon, and η_j a number of phonons.

The commutation relations are :

$$\begin{aligned} \langle [\hat{\zeta}_i(t), \hat{\zeta}_i^\dagger(t')] \rangle &= \delta(t - t'), \\ \langle [\hat{\zeta}_j(t), \hat{\zeta}_j^\dagger(t')] \rangle &= \delta(t - t'). \end{aligned} \quad (2.3.26)$$

In the modeling, the baths are (quantum) thermal baths that we will assume thermalized to the same temperature T , thus the input fields correspond to thermal noise (plus quantum zero-point fluctuations) and, at equilibrium the thermal occupations follow the Planck distribution:

$$n_i(\omega_{cav}) = \left[\exp\left(\frac{\hbar\omega_{cav}}{k_B T}\right) - 1 \right]^{-1} \quad \text{and} \quad \eta_j(\Omega_m) = \left[\exp\left(\frac{\hbar\Omega_m}{k_B T}\right) - 1 \right]^{-1}. \quad (2.3.27)$$

Over the narrow bandwidth of interest, we can assume all bosons to have the same frequency ($\omega_i \approx \omega_{cav}$ for the optical and $\omega_j \approx \Omega_m$ for the mechanical baths, respectively).

2.4 SEMI-CLASSICAL LIMITS OF LANGEVIN EQUATIONS

2.4.1 Linearized equations of motion

The quantum optomechanical equations of motion Eq. (2.3.24) generate a nonlinear dynamics since they include a coupling term which is the product of the optical field \hat{a} and the mechanical displacement amplitude $\hat{x} \propto (\hat{b} + \hat{b}^\dagger)$. These equations are reliable in the high-Q limit for both mechanics and optics $\Gamma_m \ll \Omega_m$ and $\kappa \ll \omega_{cav}$, and for not too large amplitudes for both fields (since we neglected all nonlinearities). However, within the linear expansion the coupling strength g_0 is arbitrary and can be large [86]. To solve this set of coupled differential equations it is possible to linearize them around a steady state solution. In this sense we split the amplitude field of the optics into an average (classical) coherent amplitude and a noise (quantum) part:

$$\hat{a} = \alpha \hat{\mathbb{1}} + \delta\hat{a}, \quad (2.4.1)$$

where $\alpha = \langle \hat{a} \rangle$ is a complex number and where $\delta\hat{a}$ represents the operator of the optical fluctuations in steady state conditions. This assumption shall be relevant if $|\alpha| \gg 1$.

Inserting the previous statement in Eqs. (2.3.24) and dropping all higher order terms in $\delta\hat{a}$ and $\delta\hat{a}^\dagger$, the equations of motion become:

$$\begin{cases} \delta\dot{\hat{a}} = (i\Delta - \frac{\kappa}{2})\delta\hat{a} + ig(\hat{b} + \hat{b}^\dagger) - \sum_i \sqrt{\kappa_i}\hat{\xi}_i(t), \\ \dot{\hat{b}} = -\left(i\Omega_m + \frac{\Gamma_m}{2}\right)\hat{b} + ig(\delta\hat{a} + \delta\hat{a}^\dagger) - \sum_j \sqrt{\Gamma_j}\hat{\zeta}_j(t). \end{cases} \quad (2.4.2)$$

In these equations we introduced the enhanced optomechanical coupling strength $g = g_0\alpha$ which depends on the input optical drive amplitude α_{in} with:

$$-\dot{\alpha} + i\Delta\alpha - \frac{\kappa}{2}\alpha = \sqrt{\kappa_{ex}}\tilde{\alpha}_{in}(t). \quad (2.4.3)$$

Up to this point, g is a complex number which phase depends on the sign of g_0 (real number) and the time-reference that sets the phases of the $\tilde{\alpha}_q$ components within the definition of α_{in} . $\tilde{\alpha}_{in}$ is almost a constant, and will be discussed in Section 2.5.1. Compared to the other timescales of the problem, all terms depending on α will thus be treated as (quasi)-static. Note also that we have redefined the (quasi)-static position of the mechanical resonator by dropping a time-independent term proportional to $|\alpha|^2$. This static deflection is also responsible for a slight optical frequency shift which has been neglected; it originates in the average part of the radiation pressure force. When the mechanical motion amplitude becomes large, these assumptions may not be valid anymore; this is discussed in Section 2.7 in the framework of self-oscillating mechanical states.

2.4.2 Fourier domain solving

These kinds of coupled equations of motion are more convenient to solve in frequency domain. For this purpose we define the Fourier transform of a time-dependent operator \hat{f} by:

$$\hat{f}(t) = \frac{1}{2\pi} \int_{\mathbb{R}} \hat{f}[\omega] e^{-i\omega t} d\omega, \quad \hat{f}[\omega] = \int_{\mathbb{R}} \hat{f}(t) e^{+i\omega t} dt. \quad (2.4.4)$$

Using the relation $\hat{f}[\omega]^\dagger = \hat{f}^\dagger[-\omega]$, the linearized quantum Langevin equations become in frequency space:

$$\begin{cases} \chi_c^{-1}[\omega]\delta\hat{a}[\omega] = ig(\hat{b}[\omega] + \hat{b}^\dagger[\omega]) - \sum_i \sqrt{\kappa_i}\hat{\xi}_i[\omega], \\ \bar{\chi}_c^{-1}[-\omega]\delta\hat{a}^\dagger[\omega] = -ig^*(\hat{b}^\dagger[\omega] + \hat{b}[\omega]) - \sum_i \sqrt{\kappa_i}\hat{\xi}_i^\dagger[\omega], \\ \chi_m^{-1}[\omega]\hat{b}[\omega] = ig(\delta\hat{a}[\omega] + \delta\hat{a}^\dagger[\omega]) - \sum_j \sqrt{\Gamma_j}\hat{\zeta}_j[\omega], \\ \bar{\chi}_m^{-1}[-\omega]\hat{b}^\dagger[\omega] = -ig^*(\delta\hat{a}^\dagger[\omega] + \delta\hat{a}[\omega]) - \sum_j \sqrt{\Gamma_j}\hat{\zeta}_j^\dagger[\omega]. \end{cases} \quad (2.4.5)$$

We also precised the adjoint equations for both system operators. Here χ_c represents the response function of the optical cavity and χ_m the response function of the mechanical mode [136], both functions being defined as follows:

$$\begin{cases} \chi_c^{-1}[\omega] = \frac{\kappa}{2} - i(\Delta + \omega), \\ \bar{\chi}_c^{-1}[-\omega] = \frac{\kappa}{2} + i(\Delta - \omega), \\ \chi_m^{-1}[\omega] = \frac{\Gamma_m}{2} + i(\Omega_m - \omega), \\ \bar{\chi}_m^{-1}[-\omega] = \frac{\Gamma_m}{2} - i(\Omega_m + \omega). \end{cases} \quad (2.4.6)$$

The equations (2.4.5) obtained for optical and mechanical fields are perfectly symmetric. We now present the solution of this linear system of equations:

$$\begin{aligned}\delta\hat{a}[\omega] &= \left(-\bar{\chi}_c^{-1}[-\omega] \left[\text{i}g \sum_j \left(\chi_m[\omega] \sqrt{\Gamma_j} \hat{\xi}_j[\omega] + \bar{\chi}_m[-\omega] \sqrt{\Gamma_j} \hat{\xi}_j^\dagger[\omega] \right) + \sum_i \sqrt{\kappa_i} \hat{\xi}_i[\omega] \right] \right. \\ &\quad \left. + \text{i}\Sigma_m[\omega] \sum_i \sqrt{\kappa_i} \left(\hat{\xi}_i[\omega] + \frac{g}{g^*} \hat{\xi}_i^\dagger[\omega] \right) \right) \left(\bar{\chi}_c^{-1}[-\omega] \chi_c^{-1}[\omega] - 2\Delta\Sigma_m[\omega] \right)^{-1}, \quad (2.4.7) \\ \delta\hat{a}^\dagger[\omega] &= \left(\chi_c^{-1}[\omega] \left[\text{i}g^* \sum_j \left(\chi_m[\omega] \sqrt{\Gamma_j} \hat{\xi}_j[\omega] + \bar{\chi}_m[-\omega] \sqrt{\Gamma_j} \hat{\xi}_j^\dagger[\omega] \right) - \sum_i \sqrt{\kappa_i} \hat{\xi}_i^\dagger[\omega] \right] \right. \\ &\quad \left. - \text{i}\Sigma_m[\omega] \sum_i \sqrt{\kappa_i} \left(\frac{g^*}{g} \hat{\xi}_i[\omega] + \hat{\xi}_i^\dagger[\omega] \right) \right) \left(\bar{\chi}_c^{-1}[-\omega] \chi_c^{-1}[\omega] - 2\Delta\Sigma_m[\omega] \right)^{-1},\end{aligned}$$

for the optical field, and:

$$\begin{aligned}\hat{b}[\omega] &= \left(-\bar{\chi}_m^{-1}[-\omega] \left[\text{i} \sum_i \left(g^* \chi_c[\omega] \sqrt{\kappa_i} \hat{\xi}_i[\omega] + g \bar{\chi}_c[-\omega] \sqrt{\kappa_i} \hat{\xi}_i^\dagger[\omega] \right) + \sum_j \sqrt{\Gamma_j} \hat{\xi}_j[\omega] \right] \right. \\ &\quad \left. + \text{i}\Sigma_c[\omega] \sum_j \sqrt{\Gamma_j} \left(\hat{\xi}_j[\omega] + \hat{\xi}_j^\dagger[\omega] \right) \right) \left(\bar{\chi}_m^{-1}[-\omega] \chi_m^{-1}[\omega] + 2\Omega_m \Sigma_c[\omega] \right)^{-1}, \quad (2.4.8) \\ \hat{b}^\dagger[\omega] &= \left(\chi_m^{-1}[\omega] \left[\text{i} \sum_i \left(g^* \chi_c[\omega] \sqrt{\kappa_i} \hat{\xi}_i[\omega] + g \bar{\chi}_c[-\omega] \sqrt{\kappa_i} \hat{\xi}_i^\dagger[\omega] \right) - \sum_j \sqrt{\Gamma_j} \hat{\xi}_j^\dagger[\omega] \right] \right. \\ &\quad \left. - \text{i}\Sigma_c[\omega] \sum_j \sqrt{\Gamma_j} \left(\hat{\xi}_j[\omega] + \hat{\xi}_j^\dagger[\omega] \right) \right) \left(\bar{\chi}_m^{-1}[-\omega] \chi_m^{-1}[\omega] + 2\Omega_m \Sigma_c[\omega] \right)^{-1},\end{aligned}$$

for the mechanics, where we introduced the optomechanical "self-energies" (defined in Rad/s) [136]:

$$\begin{aligned}\Sigma_c[\omega] &= -\text{i}|g|^2 (\chi_c[\omega] - \bar{\chi}_c[-\omega]), \\ \Sigma_m[\omega] &= -\text{i}|g|^2 (\chi_m[\omega] - \bar{\chi}_m[-\omega]).\end{aligned} \quad (2.4.9)$$

2.4.3 Spectral densities of mechanics and optics

From the solutions of the linear system of equations Eq. (2.4.5), we can derive the relevant spectra from the canonical statistical properties of the quantum baths operators $\hat{\xi}_i$ and $\hat{\xi}_j$ (and their adjoint operators), Eqs. (2.3.25).

Classical measurements are performed on observables, which in our case shall be position $\hat{x} \propto \hat{b} + \hat{b}^\dagger$ or voltage $\hat{V} \propto \hat{a} + \hat{a}^\dagger$. Equivalently it could be momentum \hat{p} or current \hat{I} , the quantum conjugate variable [26]. We can thus write normalized operators such as:

$$\begin{aligned}\hat{O}_{\hat{a}} &= \hat{a}(t) + \hat{a}^\dagger(t), & \hat{O}_{\hat{b}} &= \hat{b}(t) + \hat{b}^\dagger(t), \\ \text{i}\hat{O}'_{\hat{a}} &= \hat{a}(t) - \hat{a}^\dagger(t), & \text{i}\hat{O}'_{\hat{b}} &= \hat{b}(t) - \hat{b}^\dagger(t),\end{aligned} \quad (2.4.10)$$

with: $[\hat{O}_{\hat{a}}, \hat{O}'_{\hat{a}}] = 2\text{i}$, $\hat{O}_{\hat{a}}^\dagger = \hat{O}_{\hat{a}}$ and $\hat{O}'_{\hat{a}}{}^\dagger = \hat{O}'_{\hat{a}}$ by definition (and same relations for mechanics).

Let us define $\mathcal{C}_{\hat{A}}(t-t') = \langle \hat{A}(t)\hat{A}^\dagger(t') \rangle$ the quantum correlator of any operator \hat{A} . We define the spectrum from the Fourier transform:

$$\mathcal{S}_{\hat{A}}[\omega] = \int_{\mathbb{R}} \mathcal{C}_{\hat{A}}(\tau) e^{+i\omega\tau} d\tau. \quad (2.4.11)$$

It is easy to show that:

$$\mathcal{C}_{\hat{O}_a}(\tau) = \mathcal{C}_{\hat{a}}(\tau) + \mathcal{C}_{\hat{a}^\dagger}(\tau) = \mathcal{C}_{\hat{O}_a'}(\tau), \quad (2.4.12)$$

which leads to a similar relation for the spectrum. The same obviously applies for the mechanics.

Using the Fourier transform definition already introduced in Section 2.4.2 we obtain:

$$\begin{aligned} 2\pi\delta(\omega - \omega') \mathcal{S}_{\hat{a}^\dagger}[\omega] &= \langle \hat{a}^\dagger[\omega] \hat{a}[-\omega'] \rangle, \\ 2\pi\delta(\omega - \omega') \mathcal{S}_{\hat{a}}[\omega] &= \langle \hat{a}[\omega] \hat{a}^\dagger[-\omega'] \rangle, \end{aligned} \quad (2.4.13)$$

and the same relations for \hat{b} and \hat{b}^\dagger operators.

We can therefore write:

$$\begin{aligned} \mathcal{S}_{\hat{O}_a}[\omega] &= \frac{1}{2\pi} \int_{\mathbb{R}} \langle \hat{a}^\dagger[\omega] \hat{a}[-\omega'] \rangle + \langle \hat{a}[\omega] \hat{a}^\dagger[-\omega'] \rangle d\omega', \\ \mathcal{S}_{\hat{O}_b}[\omega] &= \frac{1}{2\pi} \int_{\mathbb{R}} \langle \hat{b}^\dagger[\omega] \hat{b}[-\omega'] \rangle + \langle \hat{b}[\omega] \hat{b}^\dagger[-\omega'] \rangle d\omega', \end{aligned} \quad (2.4.14)$$

which define the quantum spectra in the laboratory frame [in units of Quanta/(Rad/s)]. From the rotating wave transformation we have:

$$\hat{a}(t) = [\alpha(t)\hat{\mathbb{1}} + \delta\hat{a}(t)]e^{-i\omega_p t}, \quad (2.4.15)$$

and the corresponding adjoint equation, which relates the photon field (in the laboratory frame) to the rotating wave calculated one.

Thus:

$$\begin{aligned} \mathcal{C}_{\hat{a}}(t-t') &= \langle [\alpha(t)\hat{\mathbb{1}} + \delta\hat{a}(t)]e^{-i\omega_p t} [\alpha^*(t')\hat{\mathbb{1}} + \delta\hat{a}^\dagger(t')]e^{i\omega_p t'} \rangle, \\ &= [\alpha(t)\alpha^*(t') + \mathcal{C}_{\delta\hat{a}}(t-t')]e^{i\omega_p(t-t')}, \end{aligned} \quad (2.4.16)$$

with: $\mathcal{C}_{\delta\hat{a}}(t-t') = \langle \delta\hat{a}(t)\delta\hat{a}^\dagger(t') \rangle$ and the conjugate expression for $\mathcal{C}_{\hat{a}^\dagger}(t-t')$. We thus obtain for the spectra:

$$\begin{aligned} \mathcal{S}_{\hat{a}}[\omega] &= \mathcal{S}_\alpha[\omega - \omega_p] + \mathcal{S}_{\delta\hat{a}}[\omega - \omega_p], \\ \mathcal{S}_{\hat{a}^\dagger}[\omega] &= \mathcal{S}_{\alpha^*}[\omega + \omega_p] + \mathcal{S}_{\delta\hat{a}^\dagger}[\omega + \omega_p], \end{aligned} \quad (2.4.17)$$

with $\mathcal{S}_\alpha[\omega]$ the contribution to the cavity field from the drive (which shall be discussed in Section 2.5.1).

Therefore, omitting the drive term we have:

$$\mathcal{S}_{\hat{O}_a}[\omega] = \mathcal{S}_{\delta\hat{a}}[\omega - \omega_p] + \mathcal{S}_{\delta\hat{a}^\dagger}[\omega + \omega_p]. \quad (2.4.18)$$

This is readily computed from:

$$\begin{aligned} \langle \delta \hat{a}[\omega] \delta \hat{a}^\dagger[-\omega'] \rangle = & \frac{\left| \bar{\chi}_c^{-1}[-\omega] - i \Sigma_m[\omega] \right|^2 \sum_i \kappa_i \langle \hat{\xi}_i[\omega] \hat{\xi}_i^\dagger[-\omega'] \rangle + \left| \Sigma_m[\omega] \right|^2 \sum_i \kappa_i \langle \hat{\xi}_i^\dagger[\omega] \hat{\xi}_i[-\omega'] \rangle}{\left| \bar{\chi}_c^{-1}[-\omega] \chi_c^{-1}[\omega] - 2 \Delta \Sigma_m[\omega] \right|^2}, \\ & + |g|^2 \left| \bar{\chi}_c^{-1}[-\omega] \right|^2 \left[\left| \bar{\chi}_m[-\omega] \right|^2 \sum_j \Gamma_j \langle \hat{\xi}_j^\dagger[\omega] \hat{\xi}_j[-\omega'] \rangle \right. \\ & \left. + \left| \chi_m[\omega] \right|^2 \sum_j \Gamma_j \langle \hat{\xi}_j[\omega] \hat{\xi}_j^\dagger[-\omega'] \rangle \right], \end{aligned} \quad (2.4.19)$$

$$\begin{aligned} \langle \delta \hat{a}^\dagger[\omega] \delta \hat{a}[-\omega'] \rangle = & \frac{\left| \chi_c^{-1}[\omega] + i \Sigma_m[\omega] \right|^2 \sum_i \kappa_i \langle \hat{\xi}_i^\dagger[\omega] \hat{\xi}_i[-\omega'] \rangle + \left| \Sigma_m[\omega] \right|^2 \sum_i \kappa_i \langle \hat{\xi}_i[\omega] \hat{\xi}_i^\dagger[-\omega'] \rangle}{\left| \bar{\chi}_c^{-1}[-\omega] \chi_c^{-1}[\omega] - 2 \Delta \Sigma_m[\omega] \right|^2}, \\ & + |g|^2 \left| \chi_c^{-1}[\omega] \right|^2 \left[\left| \chi_m[\omega] \right|^2 \sum_j \Gamma_j \langle \hat{\xi}_j[\omega] \hat{\xi}_j^\dagger[-\omega'] \rangle \right. \\ & \left. + \left| \bar{\chi}_m[-\omega] \right|^2 \sum_j \Gamma_j \langle \hat{\xi}_j^\dagger[\omega] \hat{\xi}_j[-\omega'] \rangle \right]. \end{aligned} \quad (2.4.20)$$

Similarly for the mechanics we have [86]:

$$\begin{aligned} \langle \hat{b}[\omega] \hat{b}^\dagger[-\omega'] \rangle = & \frac{\left| \bar{\chi}_m^{-1}[-\omega] - i \Sigma_c[\omega] \right|^2 \sum_j \Gamma_j \langle \hat{\xi}_j[\omega] \hat{\xi}_j^\dagger[-\omega'] \rangle + \left| \Sigma_c[\omega] \right|^2 \sum_j \Gamma_j \langle \hat{\xi}_j^\dagger[\omega] \hat{\xi}_j[-\omega'] \rangle}{\left| \bar{\chi}_m^{-1}[-\omega] \chi_m^{-1}[\omega] + 2 \Omega_m \Sigma_c[\omega] \right|^2}, \\ & + |g|^2 \left| \bar{\chi}_m^{-1}[-\omega] \right|^2 \left[\left| \bar{\chi}_c[-\omega] \right|^2 \sum_i \kappa_i \langle \hat{\xi}_i^\dagger[\omega] \hat{\xi}_i[-\omega'] \rangle \right. \\ & \left. + \left| \chi_c[\omega] \right|^2 \sum_i \kappa_i \langle \hat{\xi}_i[\omega] \hat{\xi}_i^\dagger[-\omega'] \rangle \right], \end{aligned} \quad (2.4.21)$$

$$\begin{aligned} \langle \hat{b}^\dagger[\omega] \hat{b}[-\omega'] \rangle = & \frac{\left| \chi_m^{-1}[\omega] + i \Sigma_c[\omega] \right|^2 \sum_j \Gamma_j \langle \hat{\xi}_j^\dagger[\omega] \hat{\xi}_j[-\omega'] \rangle + \left| \Sigma_c[\omega] \right|^2 \sum_j \Gamma_j \langle \hat{\xi}_j[\omega] \hat{\xi}_j^\dagger[-\omega'] \rangle}{\left| \bar{\chi}_m^{-1}[-\omega] \chi_m^{-1}[\omega] + 2 \Omega_m \Sigma_c[\omega] \right|^2}, \\ & + |g|^2 \left| \chi_m^{-1}[\omega] \right|^2 \left[\left| \chi_c[\omega] \right|^2 \sum_i \kappa_i \langle \hat{\xi}_i[\omega] \hat{\xi}_i^\dagger[-\omega'] \rangle \right. \\ & \left. + \left| \bar{\chi}_c[-\omega] \right|^2 \sum_i \kappa_i \langle \hat{\xi}_i^\dagger[\omega] \hat{\xi}_i[-\omega'] \rangle \right]. \end{aligned} \quad (2.4.22)$$

Note the symmetries between these relations, using the properties of the functions already defined.

The sought solutions for $\mathcal{S}_{\hat{a}}(\omega)$ and $\mathcal{S}_{\hat{b}}(\omega)$ are finally obtained from the baths properties; in Fourier space the equations Eqs. (2.3.25) write:

$$\begin{aligned} \langle \hat{\xi}_i[\omega] \hat{\xi}_i^\dagger[-\omega'] \rangle &= 2\pi \delta(\omega - \omega') (n_i + 1), \\ \langle \hat{\xi}_i^\dagger[\omega] \hat{\xi}_i[-\omega'] \rangle &= 2\pi \delta(\omega - \omega') (n_i), \end{aligned}$$

$$\begin{aligned}\langle \hat{\xi}_j[\omega] \hat{\xi}_j^\dagger[-\omega'] \rangle &= 2\pi\delta(\omega - \omega')(\eta_j + 1), \\ \langle \hat{\xi}_j^\dagger[\omega] \hat{\xi}_j[-\omega'] \rangle &= 2\pi\delta(\omega - \omega')(\eta_j),\end{aligned}\tag{2.4.23}$$

as a function of the populations n_i and η_j .

We can thus define:

$$\begin{aligned}\sum_i \kappa_i \langle \hat{\xi}_i[\omega] \hat{\xi}_i^\dagger[-\omega'] \rangle &= 2\pi\delta(\omega - \omega')\kappa(\bar{N}_c + 1), \\ \sum_i \kappa_i \langle \hat{\xi}_i^\dagger[\omega] \hat{\xi}_i[-\omega'] \rangle &= 2\pi\delta(\omega - \omega')\kappa(\bar{N}_c),\end{aligned}\tag{2.4.24}$$

with $\sum_i \kappa_i = \kappa$ and $\bar{N}_c = \sum_i \kappa_i n_i / \kappa$ the averaged photon bath population. Similar notation hold for the mechanics, introducing Γ_m and \bar{N}_m .

We end up with the final expressions:

$$\mathcal{S}_{\delta\hat{a}}[\omega] = \frac{\left| \bar{\chi}_c^{-1}[-\omega] - i\Sigma_m[\omega] \right|^2 \kappa(\bar{N}_c + 1) + \left| \Sigma_m[\omega] \right|^2 \kappa\bar{N}_c + |g|^2 \left| \bar{\chi}_c^{-1}[-\omega] \right|^2 \left[\left| \bar{\chi}_m[-\omega] \right|^2 \Gamma_m \bar{N}_m + \left| \chi_m[\omega] \right|^2 \Gamma_m (\bar{N}_m + 1) \right]}{\left| \bar{\chi}_c^{-1}[-\omega] \chi_c^{-1}[\omega] - 2\Delta\Sigma_m[\omega] \right|^2},\tag{2.4.25}$$

$$\mathcal{S}_{\delta\hat{a}^\dagger}[\omega] = \frac{\left| \chi_c^{-1}[\omega] + i\Sigma_m[\omega] \right|^2 \kappa\bar{N}_c + \left| \Sigma_m[\omega] \right|^2 \kappa(\bar{N}_c + 1) + |g|^2 \left| \chi_c^{-1}[\omega] \right|^2 \left[\left| \bar{\chi}_m[-\omega] \right|^2 \Gamma_m \bar{N}_m + \left| \chi_m[\omega] \right|^2 \Gamma_m (\bar{N}_m + 1) \right]}{\left| \bar{\chi}_c^{-1}[-\omega] \chi_c^{-1}[\omega] - 2\Delta\Sigma_m[\omega] \right|^2},\tag{2.4.26}$$

for the optics, and:

$$\begin{aligned}\mathcal{S}_{\hat{O}_b}[\omega] &= \frac{\left| \bar{\chi}_m^{-1}[-\omega] - i\Sigma_c[\omega] \right|^2 \Gamma_m (\bar{N}_m + 1) + \left| \Sigma_c[\omega] \right|^2 \Gamma_m \bar{N}_m + |g|^2 \left| \bar{\chi}_m^{-1}[-\omega] \right|^2 \left[\left| \bar{\chi}_c[-\omega] \right|^2 \kappa\bar{N}_c + \left| \chi_c[\omega] \right|^2 \kappa(\bar{N}_c + 1) \right]}{\left| \bar{\chi}_m^{-1}[-\omega] \chi_m^{-1}[\omega] + 2\Omega_m \Sigma_c[\omega] \right|^2} \\ &+ \frac{\left| \chi_m^{-1}[\omega] + i\Sigma_c[\omega] \right|^2 \Gamma_m \bar{N}_m + \left| \Sigma_c[\omega] \right|^2 \Gamma_m (\bar{N}_m + 1) + |g|^2 \left| \chi_m^{-1}[\omega] \right|^2 \left[\left| \bar{\chi}_c[-\omega] \right|^2 \kappa\bar{N}_c + \left| \chi_c[\omega] \right|^2 \kappa(\bar{N}_c + 1) \right]}{\left| \bar{\chi}_m^{-1}[-\omega] \chi_m^{-1}[\omega] + 2\Omega_m \Sigma_c[\omega] \right|^2},\end{aligned}\tag{2.4.27}$$

for the mechanics. Note that these are quantum spectra, i.e. they are not symmetric around $\omega = 0$, by construction. Output flux and measured quantities are discussed specifically in Sections 2.4.5 and 2.4.6 respectively. In the rest of the manuscript, we shall often omit the writing of the operator \hat{O} and only refer to the original operators $\delta\hat{a}$ and \hat{b} .

Eqs. (2.4.25-2.4.27) generalize the single-sided spectrum presented in Ref. [86] for the mechanics. The generic spectra $\mathcal{S}_{\delta\hat{a}}[\omega]$ and $\mathcal{S}_{\hat{O}_b}[\omega]$ contain all information about the optomechanical interaction, and represent the physical quantities that are relevant in an experiment. The first terms at the numerators of these expressions correspond to the noise seen by each field from its direct environment, while the second terms are due to

the interaction: the stochastic component of the back-action of one sub-system onto the other. Note that the quantum nature of the baths is actually contained in the asymmetry of these spectra, when the population $n_i, \eta_j < 1$.

Only for given values of Δ will the optics and the mechanics be in resonance, in the so-called resolved-sideband regime ($\kappa/\Omega_m \ll 1$). This defines the standard optomechanical schemes that will be useful in practice. We shall now describe the properties of these spectra, in specific limits, and how they are perceived by a (classical) measurement apparatus for a given scheme.

2.4.4 Dynamical back-action

The optical self-energy Σ_c can be split in real and imaginary parts, leading to the two fundamental optomechanical effects: the optical spring and the optical damping [136]. Fundamentally, they originate in the retarded nature of the back-action radiation pressure force with respect to the dynamics of the motion.

In Eq. (2.4.27), the self-energies combine with the response functions and modify them. Factorizing out $|\bar{\chi}_m^{-1}[-\omega]|^2$ in the expression of $\langle \hat{b}[\omega] \hat{b}^\dagger[-\omega'] \rangle$ (the first term), the denominator of the mechanical spectrum $\mathcal{S}_{\hat{O}_b}[\omega]$ is proportional to $|\chi_m^{-1}[\omega] + i\Sigma_c[\omega]|^2$. It leads to a peak around $\omega \approx \Omega_m$, in the high mechanical Q limit ($\Gamma_m/\Omega_m \ll 1$). The same reasoning can be performed factorizing $|\chi_m^{-1}[\omega]|^2$ in $\langle \hat{b}^\dagger[\omega] \hat{b}[-\omega'] \rangle$ (second term), and looking at the $\omega \approx -\Omega_m$ peak; see Section 2.5.2 for more details. We thus recognize the modulus squared of the effective mechanical response function, as defined in Ref. [136]. Introducing the effective mass m_{eff} of the mechanical mode, the response function is linked to the mechanical susceptibility (see Section 2.5.1). We then re-write:

$$\Sigma_c[\omega] = 2m_{eff}\omega \left(\delta\Omega_m[\omega] - i\frac{1}{2}\Gamma_{opt}[\omega] \right), \quad (2.4.28)$$

where we explicitly define the optical spring term $\delta\Omega_m[\omega] \propto \Re(\Sigma_c[\omega])$ corresponding to a frequency shift of the mechanical mode due to the optomechanical coupling:

$$\delta\Omega_m[\omega] = |g|^2 \frac{\Omega_m}{\omega} \left[\frac{\Delta + \omega}{(\Delta + \omega)^2 + (\frac{\kappa}{2})^2} + \frac{\Delta - \omega}{(\Delta - \omega)^2 + (\frac{\kappa}{2})^2} \right], \quad (2.4.29)$$

and the optomechanical damping term $\Gamma_{opt}[\omega] \propto \Im(\Sigma_c[\omega])$ related to additional mechanical dissipation induced by the optomechanical coupling:

$$\Gamma_{opt}[\omega] = |g|^2 \frac{\Omega_m}{\omega} \left[\frac{\kappa}{(\Delta + \omega)^2 + (\frac{\kappa}{2})^2} - \frac{\kappa}{(\Delta - \omega)^2 + (\frac{\kappa}{2})^2} \right]. \quad (2.4.30)$$

Within the hypothesis $\Gamma_m \ll \kappa$ (experimentally easily matched), we can evaluate the value of these two terms at the original mechanical resonance $\omega \approx \Omega_m$:

$$\begin{aligned} \delta\Omega_m[\Omega_m] &= \frac{1}{2\Omega_m m_{eff}} \Re(\Sigma_c[\Omega_m]), \\ &= |g|^2 \left[\frac{\Delta + \Omega_m}{(\Delta + \Omega_m)^2 + (\frac{\kappa}{2})^2} + \frac{\Delta - \Omega_m}{(\Delta - \Omega_m)^2 + (\frac{\kappa}{2})^2} \right], \end{aligned} \quad (2.4.31)$$

$$\begin{aligned}\Gamma_{opt}[\Omega_m] &= -\frac{1}{\Omega_m m_{eff}} \Im(\Sigma_c[\Omega_m]), \\ &= |g|^2 \kappa \left[\frac{1}{(\Delta + \Omega_m)^2 + (\frac{\kappa}{2})^2} - \frac{1}{(\Delta - \Omega_m)^2 + (\frac{\kappa}{2})^2} \right].\end{aligned}\quad (2.4.32)$$

A complementary reasoning has to be performed for the action of the mechanical field onto the optical field $\mathcal{S}_{\hat{O}_a}[\omega]$, through $\Sigma_m[\omega]$. This is required when discussing the output photon flux; we thus come back to this point in Section 2.5.2.

OPTICAL SPRING As expected from the expression of $\delta\Omega_m[\Omega_m]$, depending on the optical detuning Δ the mechanical mode resonance frequency $\Omega_{eff} = \Omega_m + \delta\Omega_m$ is spring-softened or spring-hardened depending on the actual value of Δ with respect to $\Delta = 0, \pm\Omega_m$ (see Fig. 2.2, example of two different devices).

We shall thus define three specific standard measurement schemes, depending on the detuning Δ . This is described in the following paragraph.

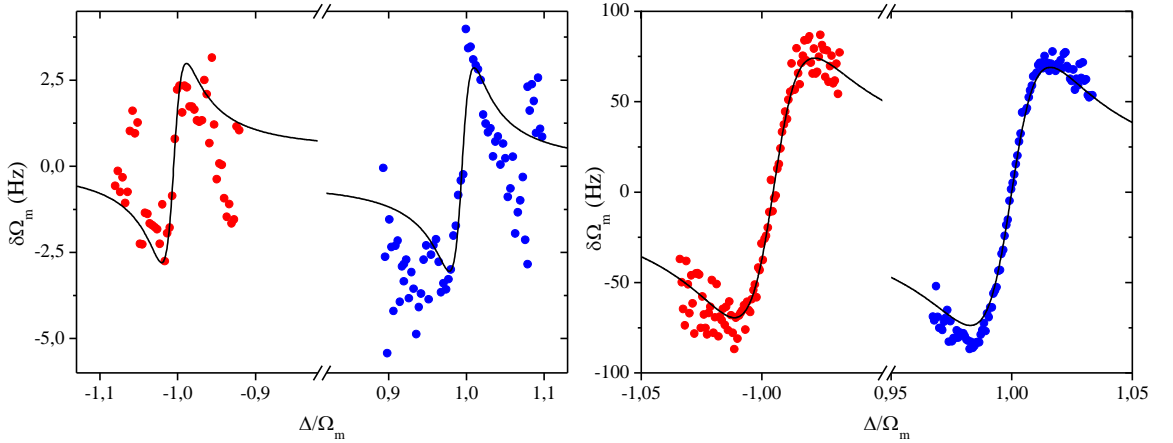


FIGURE 2.2 – Experimental data of optical spring effect obtained at 214 mK as a function of the normalized detuning of the pump signal. Blue dots: Stokes sideband pumping ($\Delta > 0$). Red dots: Anti-stokes sideband pumping ($\Delta < 0$). Black lines: theoretical fits. Left: Very small coupling beam device measured at $P_{in} \approx 20$ nW ($\Omega_m/2\pi \approx 3.8$ MHz, $\Gamma_m/2\pi \approx 18$ Hz, $g_0/2\pi \approx 0.5$ Hz, $\omega_{cav}/2\pi \approx 5.9$ GHz, $\kappa/2\pi \approx 120$ kHz, $\kappa_{ex}/2\pi \approx 95$ kHz). Right: Very high coupling drumhead device measured at $P_{in} \approx 71$ pW ($\Omega_m/2\pi \approx 15.1$ MHz, $\Gamma_m/2\pi \approx 490$ Hz, $g_0/2\pi \approx 230$ Hz, $\omega_{cav}/2\pi \approx 5.7$ GHz, $\kappa/2\pi \approx 500$ kHz, $\kappa_{ex}/2\pi \approx 250$ kHz).

OPTOMECHANICAL DAMPING We now define the effective damping of the mechanical mode by $\Gamma_{eff} = \Gamma_m + \Gamma_{opt}$. Depending on the detuning (Δ) sign, the optical part of the effective damping Γ_{eff} can cause either extra damping or antidamping on the mechanical mode. By pumping the Stokes sideband, i.e. applying a so-called "blue detuned" excitation tone ($\Delta \approx +\Omega_m$, blue dots in Fig. 2.3), amplification of the mechanical system displacement can be performed. In this case Γ_{opt} takes negative values meaning that antidamping is provided to the mechanical system. For sufficient drive powers, the total damping Γ_{eff} can reach zero: this is the parametric instability beyond which the system starts to self-oscillate. This regime is discussed in Section 2.7.

On the other hand, pumping on the anti-Stokes sideband by applying a "red detuned" excitation tone ($\Delta \approx -\Omega_m$, red dots in Fig. 2.3) provides extra damping to the mechanical system. In this case Γ_{opt} takes positive values and the mechanical mode is optically damped: this provides an active cooling scheme for the mechanical mode, see Section

2.5.2. Note that if $\Delta = 0$, the optical damping effect vanishes exactly. This is referred to as the "optimal" scheme in optomechanics, when the back-action is minimized [136].

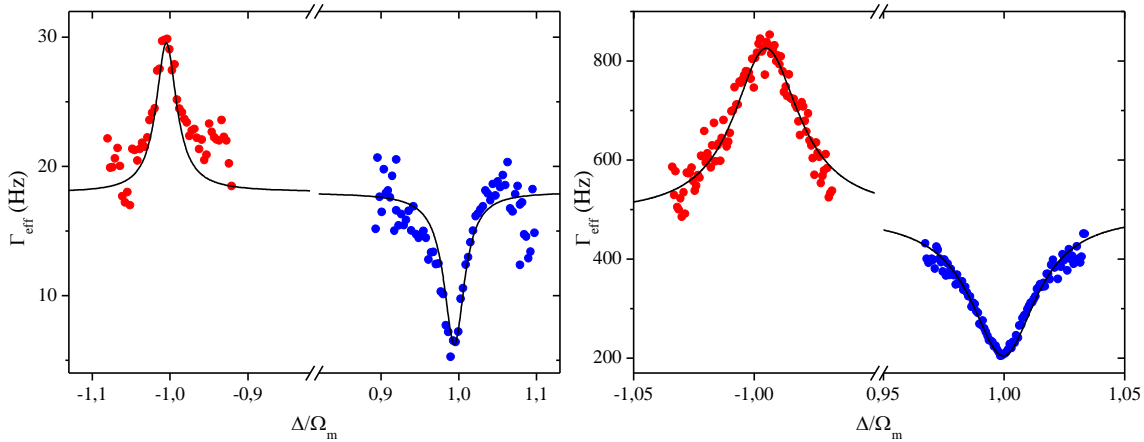


FIGURE 2.3 – Experimental data of the optomechanical damping effect obtained at 214 mK as a function of the normalized detuning of the pump signal. Same characteristics as Fig. 2.2, with fits (black lines).

SCATTERING PICTURE AND OPTICALLY INDUCED TRANSITIONS Due to the optomechanical coupling mechanism, the optical spectrum displays a series of sidebands spaced by multiple integers of the mechanical frequency Ω_m . In the development we presented, we considered only the first pair of sidebands which correspond to single-photon/phonon processes. The comb structure of the spectra shall be discussed in the framework of the self-oscillation regime (Section 2.7). The optical cavity acts as an effective density of output modes, meaning that detuning the pump signal from the optical cavity frequency provides scattering of photons to one of the sidebands preferentially. In the resolved sideband limit ($\kappa/\Omega_m \ll 1$), there will be clear resonant schemes depending on the actual value of Δ : imposed detuning around 0, $+\Omega_m$ and $-\Omega_m$.

As in Raman scattering processes, mechanical amplification and cooling phenomena are well described in the frequency picture by the imbalance of the Stokes (red) and anti-Stokes (blue) sidebands (see Fig. 2.4). Considering an amplification scheme (left part in Fig. 2.4), Blue detuned pumping leads to downward scattering of photons, leading to creating phonons in the mechanical mode, hence enhancing the Stokes sideband. Quantum mechanically if we represent the state of the optomechanical system by the ket $|n, \eta\rangle$ where n and η are the number of photons and number of phonons respectively, the pumping drive induces (red shifted) transitions of type $|n, \eta\rangle \rightarrow |n+1, \eta-1\rangle$ which de-energized into $|n, \eta+1\rangle$, absorbing a cavity photon at ω_{cav} . The mechanical mode goes from η to $\eta+1$ phonons (see Fig. 2.2 right). A similar reasoning can be made concerning the cooling scheme where the mechanical mode occupation goes from η to $\eta-1$ phonons (see Fig. 2.2 left).

In the case where the pumping is exactly on resonance with the cavity ($\Delta = 0$), the Stokes and Anti-stokes processes have the same weight: there is no exchange of energy between the two sub-systems (Fig. 2.4 center). We call this scheme the "green pumping", in analogy with the two other schemes.

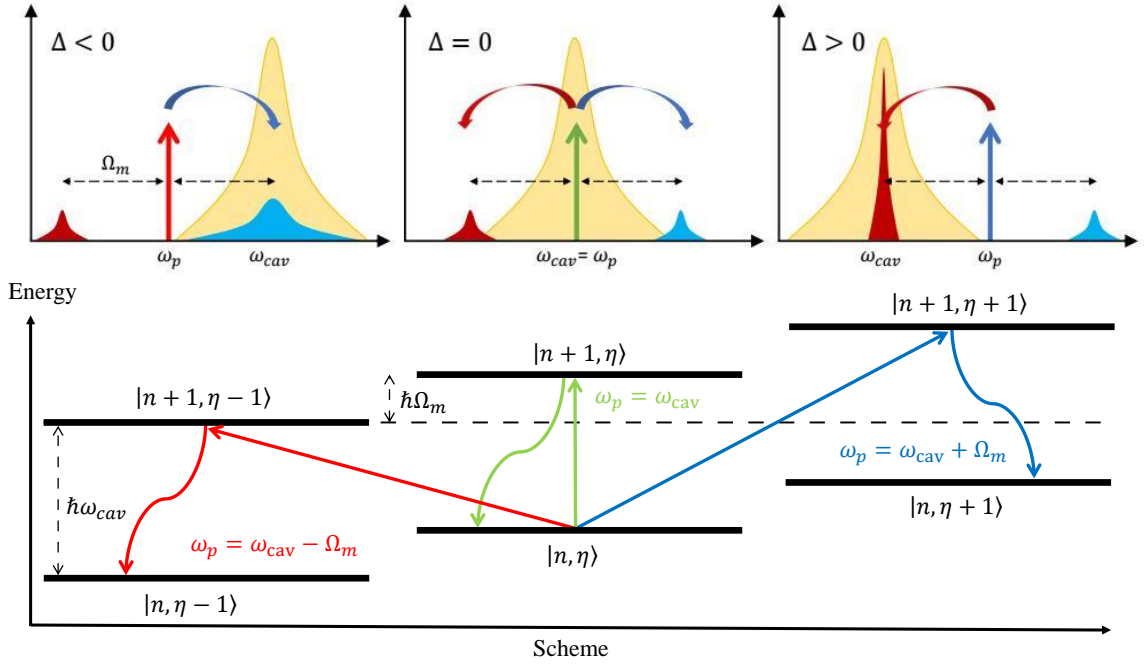


FIGURE 2.4 – Principle of cavity optomechanics. Top: scattering picture representations of the three standard optomechanical pumping schemes, visualized with the optical spectra. The orange curve represents the optical cavity mode, the blue curve the anti-Stokes peak and the red one the Stokes peak. The arrow models the pumping frequency position ω_p . From left to right: Anti-Stokes pumping (active modal cooling), in-cavity pumping (no optics-mechanics energy exchange), and Stokes pumping (active modal amplification or heating). Bottom: Transition diagram representing the three standard schemes exposed (for photons n and phonons η): Right: A photon can create a phonon. Center: a photon can be absorbed by the optical mode leaving the mechanical population unchanged. Left: A photon can annihilate a phonon.

2.4.5 Output optical power spectral density

The spectral density corresponding to the output optical fluctuations is obtained by applying the input-output relation Eq. (2.3.21). We write this expression and its corresponding adjoint form in the frequency space for the output fluctuation operator:

$$\begin{cases} \hat{a}_{out}[\omega] = \hat{\xi}_{ext}[\omega] + \sqrt{\kappa_{ex}}\hat{a}[\omega], \\ \hat{a}_{out}^\dagger[-\omega] = \hat{\xi}_{ext}^\dagger[-\omega] + \sqrt{\kappa_{ex}}\hat{a}^\dagger[-\omega], \end{cases} \quad (2.4.33)$$

where the field $\hat{\xi}_{ext}$ represents the fluctuations of the out-coming port connecting the optomechanical system to the detector (which is the same as the incoming one for a reflection measurement; but is different for a two-port setup). Hence we can write the output quantum optical spectral density under the following form (see Fig. 2.5):

$$\mathcal{S}_{\hat{a}_{out}}[\omega] = \mathcal{S}_{ext} + \kappa_{ex} \left(\mathcal{S}_{\hat{a}}[\omega] + \mathcal{S}_{\hat{\xi}_{ext}, \hat{a}}[\omega] \right), \quad (2.4.34)$$

where $\mathcal{S}_{ext} = \frac{1}{2\pi} \int_{\mathbb{R}} \langle \hat{\xi}_{ext}[\omega - \omega_p] \hat{\xi}_{ext}^\dagger[-\omega'] + \hat{\xi}_{ext}^\dagger[\omega + \omega_p] \hat{\xi}_{ext}[-\omega'] \rangle d\omega'$ represents the excess signal occupation from the output field. By definition, $\mathcal{S}_{ext} = N_{ext}$ (the occupation number of the output boson) for $\omega \approx -\omega_p$ and $\mathcal{S}_{ext} = N_{ext} + 1$ around $+\omega_p$. The term

$\mathcal{S}_{\hat{\xi}_{ext}, \hat{a}}[\omega]$ corresponds to the cross-correlations between the output field noise and the intra-cavity field. We can decompose it into:

$$\mathcal{S}_{\hat{\xi}_{ext}, \hat{a}}[\omega] = \mathcal{S}_{\hat{\xi}_{ext}, \delta\hat{a}}[\omega - \omega_p] + \mathcal{S}_{\hat{\xi}_{ext}, \delta\hat{a}^\dagger}[\omega + \omega_p] \quad (2.4.35)$$

by making use of the rotating wave transform. They write explicitly:

$$\mathcal{S}_{\hat{\xi}_{ext}, \delta\hat{a}}[\omega] = \frac{-2\Re \left[\left(1 - i\bar{\chi}_c[-\omega] \Sigma_m[\omega] \right) \left(\bar{\chi}_c^{-1}[\omega] - 2\Delta\bar{\chi}_c[-\omega] \Sigma_m[-\omega] \right) \right]}{\left| \bar{\chi}_c^{-1}[\omega] - 2\Delta\bar{\chi}_c[-\omega] \Sigma_m[\omega] \right|^2} \langle \hat{\xi}_{ext}[\omega] \hat{\xi}_{ext}^\dagger[-\omega] \rangle, \quad (2.4.36)$$

$$\mathcal{S}_{\hat{\xi}_{ext}, \delta\hat{a}^\dagger}[\omega] = \frac{-2\Re \left[\left(1 + i\chi_c[\omega] \Sigma_m[\omega] \right) \left(\chi_c^{-1}[-\omega] - 2\Delta\bar{\chi}_c[\omega] \bar{\Sigma}_m[\omega] \right) \right]}{\left| \bar{\chi}_c^{-1}[-\omega] - 2\Delta\bar{\chi}_c[\omega] \Sigma_m[\omega] \right|^2} \langle \hat{\xi}_{ext}^\dagger[\omega] \hat{\xi}_{ext}[-\omega] \rangle. \quad (2.4.37)$$

At that stage, it is useful to note that Eqs. (2.4.25) and (2.4.26) already contained a cross-correlation term between all the input fields (which obviously also contain the above mentioned $\hat{\xi}_{ext}$) and the back-action noise acting on the mechanics. To make it directly explicit, we rewrite:

$$\begin{aligned} |g|^2 & \left[\left| \chi_m[\omega] \right|^2 \sum_j \Gamma_j \langle \hat{\xi}_j[\omega] \hat{\xi}_j^\dagger[-\omega] \rangle + \left| \bar{\chi}_m[-\omega] \right|^2 \sum_j \Gamma_j \langle \hat{\xi}_j^\dagger[\omega] \hat{\xi}_j[-\omega] \rangle \right] \\ & + \left| 1 - i(\bar{\chi}_c[-\omega] - \chi_c[\omega]) \Sigma_m[\omega] \right|^2 \sum_i \kappa_i \langle \hat{\xi}_i[\omega] \hat{\xi}_i^\dagger[-\omega] \rangle \\ & + \left| \chi_c[\omega] \Sigma_m[\omega] \right|^2 \sum_i \kappa_i \langle \hat{\xi}_i[\omega] \hat{\xi}_i^\dagger[-\omega] \rangle + \left| \bar{\chi}_c[-\omega] \Sigma_m[\omega] \right|^2 \sum_i \kappa_i \langle \hat{\xi}_i^\dagger[\omega] \hat{\xi}_i[-\omega] \rangle \\ & + 2\Re \left[i \left(1 - i(\bar{\chi}_c[-\omega] - \chi_c[\omega]) \Sigma_m[\omega] \right) \bar{\chi}_c[\omega] \bar{\Sigma}_m[\omega] \right] \sum_i \kappa_i \langle \hat{\xi}_i[\omega] \hat{\xi}_i^\dagger[-\omega] \rangle \end{aligned}$$

$$\mathcal{S}_{\delta\hat{a}}[\omega] = \frac{\hspace{10em}}{\left| \bar{\chi}_c^{-1}[\omega] - 2\Delta\bar{\chi}_c[-\omega] \Sigma_m[\omega] \right|^2}, \quad (2.4.38)$$

$$\begin{aligned} |g|^2 & \left[\left| \chi_m[\omega] \right|^2 \sum_j \Gamma_j \langle \hat{\xi}_j[\omega] \hat{\xi}_j^\dagger[-\omega] \rangle + \left| \bar{\chi}_m[-\omega] \right|^2 \sum_j \Gamma_j \langle \hat{\xi}_j^\dagger[\omega] \hat{\xi}_j[-\omega] \rangle \right] \\ & + \left| 1 + i(\chi_c[\omega] - \bar{\chi}_c[-\omega]) \Sigma_m[\omega] \right|^2 \sum_i \kappa_i \langle \hat{\xi}_i^\dagger[\omega] \hat{\xi}_i[-\omega] \rangle \\ & + \left| \chi_c[\omega] \Sigma_m[\omega] \right|^2 \sum_i \kappa_i \langle \hat{\xi}_i[\omega] \hat{\xi}_i^\dagger[-\omega] \rangle + \left| \bar{\chi}_c[-\omega] \Sigma_m[\omega] \right|^2 \sum_i \kappa_i \langle \hat{\xi}_i^\dagger[\omega] \hat{\xi}_i[-\omega] \rangle \\ & + 2\Re \left[-i \left(1 + i(\chi_c[\omega] - \bar{\chi}_c[-\omega]) \Sigma_m[\omega] \right) \chi_c[-\omega] \Sigma_m[-\omega] \right] \sum_i \kappa_i \langle \hat{\xi}_i^\dagger[\omega] \hat{\xi}_i[-\omega] \rangle \end{aligned}$$

$$\mathcal{S}_{\delta\hat{a}^\dagger}[\omega] = \frac{\hspace{10em}}{\left| \bar{\chi}_c^{-1}[-\omega] - 2\Delta\bar{\chi}_c[\omega] \Sigma_m[\omega] \right|^2}, \quad (2.4.39)$$

In these equations, the terms involving Real Parts are the cross-correlation terms. Physically, they are non-zero because the fields that drive optics \hat{a} and mechanics \hat{b} through the back-action force are indeed the ones of the input baths i , including the connecting ports. The relevance of these terms shall be discussed in Section 2.6.

In practice, we perform an amplitude-and-phase measurement of the time-dependent voltage, from which the spectrum is calculated. The classical apparatus in use detects, by construction, only the symmetrized component of the output spectrum [37, 26], defined as:

$$S_{\hat{\delta}_{\hat{a}_{out}}}^{sym}[\omega] = \frac{1}{2} \left(S_{\hat{\delta}_{\hat{a}_{out}}}[\omega] + S_{\hat{\delta}_{\hat{a}_{out}}}[-\omega] \right). \quad (2.4.40)$$

We shall call for simplicity in the following $S_{\hat{\delta}_{\hat{a}_{out}}}[\omega]$ the signal component of this spectrum, in the frame rotating at ω_p (which is essentially our demodulation frequency in experiments, see Chapter 7), omitting thus both the pump and the background contributions. This spectrum is depicted in Fig. 2.5 for the two standard "red" and "blue" pumping schemes. Explicit expressions are given in the classical limit, omitting any back-action from the cavity in Section 2.5.2. The complete solution is discussed in Section 2.6.

Introducing $S_{\hat{a}_{out}} = \hbar\omega \mathcal{S}_{\hat{a}_{out}}$, we see that the measured spectra are then defined in photons ($\mathcal{S}_{\hat{a}_{out}}$) or in Joules ($S_{\hat{\delta}_{\hat{a}_{out}}}$): the latter is referred to as power spectral density. The other relevant variables (with proper units) to be measured are now introduced in the next Section.

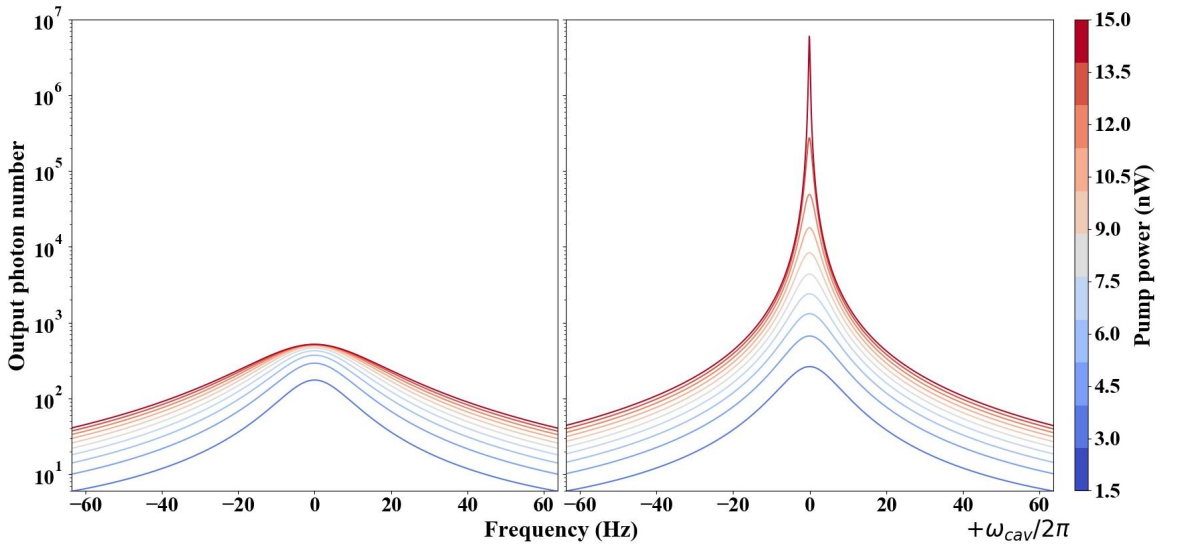


FIGURE 2.5 – Computed output optical power spectral density (PSD) as a function of the input pump power (at frequency $\omega_{cav} + \Delta$) in both cases of Stokes pumping $\Delta = +\Omega_m$ (left side) and anti-Stokes pumping $\Delta = -\Omega_m$ (right side). The calculation is performed with the low-coupled beam device parameters given in Fig. 2.2 using Eq. (2.4.34) for a temperature $T = 214$ mK.

2.4.6 Quanta flux and measured quantities

The effective output photon flux (units of photons per second) is directly the mean square fluctuation of $\delta\hat{a}_{out}$, which can be defined from the integral of the spectrum:

$$\langle \delta\hat{a}_{out}^2 \rangle = \frac{1}{2\pi} \int_{\mathbb{R}^+} \mathcal{S}_{\hat{a}_{out}}[\omega] d\omega. \quad (2.4.41)$$

What is measured is actually a power, the energy flowing out of the cavity: $\hbar\omega_{cav} \langle \delta\hat{a}_{out}^2 \rangle$. This quantity is the one that we want to fit to experimentally determine the mode temperature through its population (see Chapter 7).

Correspondingly, the effective phonon occupation (units of phonons) for the mechanical mode is:

$$\langle \hat{b}^2 \rangle = \frac{1}{2\pi} \int_{\mathbb{R}} \mathcal{S}_{\hat{O}_b}[\omega] d\omega. \quad (2.4.42)$$

Similarly, from the canonical expression (expressed in Fourier space):

$$\hat{x}[\omega] = x_{zpf} \left(\hat{b}[\omega] + \hat{b}^\dagger[\omega] \right), \quad (2.4.43)$$

with $x_{zpf} = \sqrt{\hbar/(2\Omega_m m_{eff})}$, we find the mean square displacement of the mechanical degree of freedom from the position spectrum:

$$S_{\hat{x}}[\omega] = x_{zpf}^2 \mathcal{S}_{\hat{O}_b}[\omega], \quad (2.4.44)$$

$$\langle \delta\hat{x}^2 \rangle = \frac{1}{2\pi} \int_{\mathbb{R}} S_{\hat{x}}[\omega] d\omega = x_{zpf}^2 \langle \hat{b}^2 \rangle. \quad (2.4.45)$$

Together with Eqs. (2.4.25-2.4.27) we thus have all mathematical tools to describe quantitatively our measurements.

2.5 CLASSICAL LIMITS

2.5.1 Zero coupling limit

AVERAGE INTRACAVITY OCCUPATION In the absence of any coupling ($g_0 \rightarrow 0$), the mechanical and optical fields are decoupled. The quantum Langevin equation for the optical mode \hat{a} [Eq. (2.3.24)] in the rotating frame can be written as follows:

$$\dot{\hat{a}} = i\Delta\hat{a} - \frac{\kappa}{2}\hat{a} - \sqrt{\kappa_{ex}}\tilde{\alpha}_{in} - \sum_i \sqrt{\kappa_i}\hat{\zeta}_i(t). \quad (2.5.1)$$

Inserting $\hat{a} = \alpha\hat{1} + \delta\hat{a}$ and taking the average, we recover the equation Eq. (2.4.3). In Fourier space, it writes:

$$\left(i(\Delta + \omega) - \frac{\kappa}{2} \right) \alpha[\omega] = \sqrt{\kappa_{ex}}\tilde{\alpha}_{in}[\omega], \quad (2.5.2)$$

with $\alpha[\omega]$ the Fourier transform of $\langle \hat{a}(t) \rangle$. This leads to the expression of the mean number of photons circulating inside the cavity:

$$n_{cav}(t) = \langle \hat{a}^\dagger(t)\hat{a}(t) \rangle \approx \alpha^*(t)\alpha(t), \quad (2.5.3)$$

to lowest order in $\delta\hat{a}$, and assuming $\omega \ll \Delta$ (valid if the coherent field is close enough to a Dirac peak):

$$n_{cav}[\omega] = \frac{\kappa_{ex}}{\Delta^2 + \left(\frac{\kappa}{2}\right)^2} \frac{1}{2\pi} (\tilde{\alpha}_{in}^*[-\omega'] * \tilde{\alpha}_{in}[\omega'])[\omega], \quad (2.5.4)$$

given in the Fourier space. We made use of the convolution product defined as:

$$(f[\omega'] * g[\omega'])[\omega] = \int_{\mathbb{R}} f[\omega - \omega']g[\omega']d\omega'. \quad (2.5.5)$$

Eq. (2.5.4) leads to the drive contribution \mathcal{S}_α appearing in the optical spectrum, Eq. (2.4.17). This expression can be put under a useful form by letting appear the input pump power P_{in} in units of Watts:

$$\bar{n}_{cav} = \frac{1}{2\pi} \int_{\omega} n_{cav}[\omega]d\omega = \kappa_{ex} \left| \chi_c[0] \right|^2 \frac{P_{in}}{\hbar\omega_p}, \quad (2.5.6)$$

having defined:

$$\begin{aligned} P_{in} &= \left(\frac{1}{2\pi} \right)^2 \int_{\mathbb{R}} \hbar\omega (\alpha_{in}^*[-\omega'] * \alpha_{in}[\omega'])[\omega]d\omega, \\ &\approx \hbar\omega_p \frac{1}{2\pi} \left(\int_{\mathbb{R}} \tilde{\alpha}_{in}^*[\omega']d\omega' \right) \frac{1}{2\pi} \left(\int_{\mathbb{R}} \tilde{\alpha}_{in}[\omega]d\omega \right). \end{aligned} \quad (2.5.7)$$

If the excitation field is perfectly monochromatic at ω_p , then $\tilde{\alpha}_{in}(t) = \tilde{\alpha}_0$ is a constant and $\tilde{\alpha}_{in}[\omega] = \tilde{\alpha}_0 2\pi\delta[\omega]$. We then recover the canonical result $P_{in} = \hbar\omega_p |\tilde{\alpha}_0|^2$. This leads to the simple expression $\bar{n}_{cav} = \kappa_{ex} \left| \chi_c[0] \right|^2 |\tilde{\alpha}_0|^2$; with a proper definition of the time reference t_0 , $\tilde{\alpha}_0$ can thus be chosen real positive and $g = g_0 \sqrt{\bar{n}_{cav}} > 0$ (with $g_0 > 0$, which implies as well a choice for the x-axis direction, see discussion in Section 2.7). This is the writing that will be extensively used in our experimental Chapters.

THE DAMPED HARMONIC OSCILLATOR In the case of zero coupling, the power spectral densities of mechanical and optical modes Eqs. (2.4.25-2.4.27) become:

$$\begin{aligned} S_{\hat{O}_a}[\omega] &= \hbar\omega \left[\left| \chi_c[\omega - \omega_p] \right|^2 \kappa(\bar{N}_c + 1) + \left| \bar{\chi}_c[\omega + \omega_p] \right|^2 \kappa\bar{N}_c \right], \\ S_{\hat{O}_b}[\omega] &= \hbar\omega \left[\left| \chi_m[\omega] \right|^2 \Gamma_m(\bar{N}_m + 1) + \left| \bar{\chi}_m[-\omega] \right|^2 \Gamma_m\bar{N}_m \right]. \end{aligned} \quad (2.5.8)$$

Hence, we recover the case of two independent damped (quantum) harmonic oscillators coupled to two different sets of baths. Note that from Eq. (2.4.34), because of the cross-correlation terms, if all the optical baths are at the same temperature the output photon flux reduces then to \mathcal{S}_{ext} : to "see" the cavity with a peak or a dip, a temperature difference should be created, leading to a flux of energy *in*, or *out*.

Within the classical limit, and considering that the mechanical oscillator is in thermal equilibrium with all the baths at the same temperature we get $\eta_j \rightarrow k_B T / \hbar\Omega_m \gg 1$. Replacing Eq. (2.5.8) in the definition of the displacement spectrum Eq. (2.4.44), we obtain:

$$\begin{aligned} S_{\hat{x}}[\omega] &= x_{zpf}^2 \left[\left| \chi_m[\omega] \right|^2 + \left| \bar{\chi}_m[-\omega] \right|^2 \right] \Gamma_m \frac{k_B T}{\hbar\Omega_m}, \\ &= \frac{1}{(2m_{eff}\Omega_m)^2} \left[\left| \chi_m[\omega] \right|^2 + \left| \bar{\chi}_m[-\omega] \right|^2 \right] 2m_{eff}\Gamma_m k_B T, \end{aligned} \quad (2.5.9)$$

having made use of the definition of the zero piont motion x_{zpf} , with m_{eff} the mechanical mode mass.

Introducing the mechanical susceptibility (in meter/Newton):

$$\chi_{mech}[\omega] = \frac{1}{(2m_{eff}\Omega_m)}\chi_m[\omega], \quad (2.5.10)$$

defined from the response function χ_m , we recover the classical version of the Fluctuation-Dissipation theorem: the spectrum is symmetric with two Lorentzian peaks at $\pm\Omega_m$, and $2m_{eff}\Gamma_mk_B T$ is the white Langevin force noise spectrum of the bath, linking thus fluctuations (i.e. $S_{\hat{x}}[\omega]$) to dissipation (i.e. Γ_m). We also recover the equipartition theorem: $\langle\delta x^2\rangle = k_B T / (m_{eff}\Omega_m^2)$.

2.5.2 Coupled system

The equations Eq. (2.4.25-2.4.27) giving the power spectral densities derived before can be put under a simplified form with some assumptions. We shall consider that the optical mode is in the quantum ground state while the mechanical mode is at high temperature $\bar{N}_m \approx k_B T / (\hbar\Omega_m) \gg 1$. We can thus neglect the mechanics quantum noise and the cavity thermal and quantum fluctuations, such that $\bar{N}_c, \bar{N}_c + 1 \rightarrow 0$; the back-action noise from the cavity (including the cross-correlation terms) shall be discussed later in the manuscript (Section 2.6). In this section, both spectra thus reduce to their (symmetric in frequency) classical limit, without stochastic back-action component.

The output optical spectrum can thus be written as follows (in the rotating frame, around ω_p):

$$\mathcal{S}_{\hat{a}_{out}}[\omega] = \kappa_{ex}|g|^2 \frac{\left[|\chi_m[\omega]|^2 + |\bar{\chi}_m[-\omega]|^2\right]}{\left|\chi_c^{-1}[\omega] - 2\Delta\bar{\chi}_c[-\omega]\Sigma_m[\omega]\right|^2} \Gamma_m \bar{N}_m. \quad (2.5.11)$$

Similarly, the mechanical spectrum is obtained as:

$$\begin{aligned} \mathcal{S}_{\hat{O}_b}[\omega] = & \frac{\left|1 - i\bar{\chi}_m[-\omega]\Sigma_c[\omega]\right|^2 + \left|\bar{\chi}_m[-\omega]\Sigma_c[\omega]\right|^2}{\left|\chi_m^{-1}[\omega] + 2\Omega_m\bar{\chi}_m[-\omega]\Sigma_c[\omega]\right|^2} \Gamma_m \bar{N}_m \\ & + \frac{\left|1 + i\chi_m[\omega]\Sigma_c[\omega]\right|^2 + \left|\chi_m[\omega]\Sigma_c[\omega]\right|^2}{\left|\bar{\chi}_m^{-1}[-\omega] + 2\Omega_m\chi_m[\omega]\Sigma_c[\omega]\right|^2} \Gamma_m \bar{N}_m. \end{aligned} \quad (2.5.12)$$

We recognize at the denominator the effective mechanical response function, for both $\omega \approx \pm\Omega_m$ peaks (see Section 2.4.4). Both expressions depend directly on Δ ; we should thus describe now the different useful schemes, which were already introduced in the framework of dynamical back-action (Section 2.4.4).

Let us start with the simple case $\Delta = 0$, the "green" pumping. Then $\Sigma_c \rightarrow 0$ (there is no dynamical back-action) and the two above expressions reduce to:

$$\begin{aligned}\mathcal{S}_{\hat{a}_{out}}[\omega] &= \kappa_{ex}|g|^2|\chi_c[\omega]|^2\left[|\bar{\chi}_m[-\omega]|^2+|\chi_m[\omega]|^2\right]\Gamma_m\bar{N}_m, \\ \mathcal{S}_{\hat{O}_b}[\omega] &= \left[|\chi_m[\omega]|^2+|\bar{\chi}_m[-\omega]|^2\right]\Gamma_m\bar{N}_m.\end{aligned}\quad (2.5.13)$$

The optical spectrum is imprinted by two peaks at $\pm\Omega_m$ around the pump tone, which are the image of the mechanical spectrum. The mechanics is unaltered by the optical drive (we recover Eq. (2.5.8) above, second line): thus the two imprinted peaks are exactly equivalent.

We now shall evaluate $\mathcal{S}_{\hat{a}_{out}}$ and $\mathcal{S}_{\hat{O}_b}$ for both "blue" and "red" detuned pumping cases, in the usual limits of resolved sideband $\kappa/\Omega_m \ll 1$ and small mechanical damping $\Gamma_{eff} \ll \Omega_m, \kappa$, implying both $\Gamma_m, |\Gamma_{opt}| \ll \kappa$; we thus develop the theory in the limit of weak coupling, which is the relevant limit for our experiments.

RED DETUNED PUMPING Let us first consider the "red" detuned pumping scheme with $\Delta = -\Omega_m$. In the high mechanical Q limit, $|\chi_m[\omega]|^2$ is peaked around $+\Omega_m$ while $|\bar{\chi}_m[-\omega]|^2$ is peaked around $-\Omega_m$. We thus compute both optical and mechanical spectra in the rotating wave approximation near this two particular points.

Concerning the lower sideband $\omega = -\Omega_m + \delta\omega$ we have:

$$\begin{aligned}\mathcal{S}_{\hat{a}_{out}}[\omega] &\approx \frac{\kappa_{ex}|g|^2}{4\Omega_m^2} \frac{|\bar{\chi}_m[-(\delta\omega - \Omega_m)]|^2}{\left|1 + \frac{4|g|^2}{\kappa\Gamma_m} \frac{1}{1-i\frac{\delta\omega}{\Gamma_m/2}}\right|^2} \Gamma_m\bar{N}_m, \\ &\approx \frac{\kappa_{ex}|g|^2}{4\Omega_m^2} |\chi_{eff}[\delta\omega]|^2 \Gamma_m\bar{N}_m,\end{aligned}\quad (2.5.14)$$

and similarly for the upper sideband $\omega = +\Omega_m + \delta\omega$ we obtain:

$$\begin{aligned}\mathcal{S}_{\hat{a}_{out}}[\omega] &\approx \frac{\kappa_{ex}|g|^2}{\left(\frac{\kappa}{2}\right)^2} \frac{|\chi_m[\delta\omega + \Omega_m]|^2}{\left|1 + \frac{4|g|^2}{\kappa\Gamma_m} \frac{1}{1-i\frac{\delta\omega}{\Gamma_m/2}}\right|^2} \Gamma_m\bar{N}_m, \\ &\approx \frac{\kappa_{ex}|g|^2}{\left(\frac{\kappa}{2}\right)^2} |\chi_{eff}[\delta\omega]|^2 \Gamma_m\bar{N}_m,\end{aligned}\quad (2.5.15)$$

where we defined an effective response function:

$$\chi_{eff}[\delta\omega] = \frac{1}{\frac{\Gamma_m}{2} + \frac{\Gamma_{opt}}{2} - i\delta\omega}, \quad \text{with} \quad \Gamma_{opt} = +\frac{4|g|^2}{\kappa}.\quad (2.5.16)$$

We thus see that the lower sideband (peak at $-\Omega_m + \delta\omega$) is suppressed by a factor:

$$\left(\frac{\kappa}{4\Omega_m}\right)^2 \ll 1.\quad (2.5.17)$$

Only the upper sideband (peak at $\Omega_m + \delta\omega$) is relevant and consequently:

$$\mathcal{S}_{\hat{a}_{out}}[\Omega_m + \delta\omega] \approx \kappa_{ex}|g|^2 \left| \chi_c[-\Delta] \right|^2 \left| \chi_{eff}[\delta\omega] \right|^2 \Gamma_m \bar{N}_m. \quad (2.5.18)$$

Let us now consider the mechanical spectrum. In Eq. (2.5.12), looking at the peak at $-\Omega_m + \delta\omega$ the first term can be neglected in a rotating wave approximation and only the second term appears relevant. On the other hand for the $+\Omega_m + \delta\omega$ peak, the reverse occurs and finally:

$$\mathcal{S}_{\hat{O}_b}[\omega] \approx \left[1 + \frac{2|g|^4}{(\kappa\Omega_m)^2} \right] \left| \chi_{eff}[\delta\omega] \right|^2 \Gamma_m \bar{N}_m, \quad (2.5.19)$$

for both positive $\omega = \Omega_m + \delta\omega$ and negative $\omega = -\Omega_m + \delta\omega$ peaks. The mechanical spectrum is thus symmetric as expected, and each peak is directly proportional to the peak measured in the output optical spectrum $\mathcal{S}_{\hat{a}_{out}}$ within a factor $1 + \frac{2|g|^4}{(\kappa\Omega_m)^2}$. Note that in the weak coupling limit valid for our experimental conditions $\frac{2|g|^4}{(\kappa\Omega_m)^2} = \frac{1}{8} \left(\frac{\Gamma_{opt}}{\Omega_m} \right)^2 \ll 1$ and this correction can be safely neglected. Thus:

$$\mathcal{S}_{\hat{a}_{out}}[\Omega_m + \delta\omega] \approx \kappa_{ex}|g|^2 \left| \chi_c[-\Delta] \right|^2 \mathcal{S}_{\hat{O}_b}[\Omega_m + \delta\omega]. \quad (2.5.20)$$

BLUE DETUNED PUMPING A similar calculation is applied for the "blue" detuned pumping scheme, i.e. for $\Delta = +\Omega_m$.

In this case for the lower sideband $\omega = -\Omega_m + \delta\omega$ we have:

$$\begin{aligned} \mathcal{S}_{\hat{a}_{out}}[\omega] &\approx \frac{\kappa_{ex}|g|^2 \left| \tilde{\chi}_m[-(\delta\omega - \Omega_m)] \right|^2}{\left(\frac{\kappa}{2} \right)^2 \left| 1 - \frac{4|g|^2}{\kappa\Gamma_m} \frac{1}{1 - i\frac{\delta\omega}{\Gamma_m/2}} \right|^2} \Gamma_m \bar{N}_m, \\ &\approx \frac{\kappa_{ex}|g|^2}{\left(\frac{\kappa}{2} \right)^2} \left| \chi_{eff}[\delta\omega] \right|^2 \Gamma_m \bar{N}_m, \end{aligned} \quad (2.5.21)$$

and similarly for the upper one, using the same hypotheses as before:

$$\begin{aligned} \mathcal{S}_{\hat{a}_{out}}[\omega] &\approx \frac{\kappa_{ex}|g|^2 \left| \chi_m[\delta\omega + \Omega_m] \right|^2}{4\Omega_m^2 \left| 1 - \frac{4|g|^2}{\kappa\Gamma_m} \frac{1}{1 - i\frac{\delta\omega}{\Gamma_m/2}} \right|^2} \Gamma_m \bar{N}_m, \\ &\approx \frac{\kappa_{ex}|g|^2}{4\Omega_m^2} \left| \chi_{eff}[\delta\omega] \right|^2 \Gamma_m \bar{N}_m, \end{aligned} \quad (2.5.22)$$

where we defined the effective susceptibility for "blue" detuned pumping the same way as for "red" detuned pumping:

$$\chi_{eff}[\delta\omega] = \frac{1}{\frac{\Gamma_m}{2} + \frac{\Gamma_{opt}}{2} - i\delta\omega}, \quad \text{with} \quad \Gamma_{opt} = -\frac{4|g|^2}{\kappa}. \quad (2.5.23)$$

Note the sign change in Γ_{opt} . Again, one peak is suppressed by $[\kappa/(4\Omega_m)]^2 \ll 1$, but now the situation is reversed (i.e. the upper sideband at $\Omega_m + \delta\omega$ is the suppressed peak). And similarly to the "red" detuned pumping, the output optical spectrum writes:

$$\mathcal{S}_{\hat{a}_{out}}[-\Omega_m + \delta\omega] \approx \kappa_{ex}|g|^2 \left| \chi_c[-\Delta] \right|^2 \left| \chi_{eff}[\delta\omega] \right|^2 \Gamma_m \bar{N}_m. \quad (2.5.24)$$

Note that in this case $\Gamma_{opt} < 0$, and therefore anti-damping is provided to the mechanical system (see Section 2.4.4).

Concerning the mechanical spectrum, one easily finds that the same conclusions apply for blue as for red detuned pumping. One recovers the same relation as Eq. (2.5.19):

$$\mathcal{S}_{\hat{O}_b}[\omega] \approx \left[1 + \frac{2|g|^4}{(\kappa\Omega_m)^2} \right] \left| \chi_{eff}[\delta\omega] \right|^2 \Gamma_m \bar{N}_m, \quad \text{but with} \quad \Gamma_{opt} = -\frac{4|g|^2}{\kappa}, \quad (2.5.25)$$

for both $\omega = \pm\Omega_m + \delta$.

Measuring the lower output optical sideband at $-\Omega_m + \delta\omega$ gives us a direct image of the mechanical spectrum:

$$\mathcal{S}_{\hat{a}_{out}}[-\Omega_m + \delta\omega] \approx \kappa_{ex}|g|^2 \left| \chi_c[-\Delta] \right|^2 \mathcal{S}_{\hat{O}_b}[-\Omega_m + \delta\omega]. \quad (2.5.26)$$

where we neglected again the $|g|^4$ correction.

QUANTA FLUX Integrating optical spectra over one sideband (the visible one for "red" or "blue" schemes, or any of the two for "green"), one obtains the main experimental measured quantity: the flux of photons exiting the cavity Eq. (2.4.41):

$$\langle \delta \hat{a}_{out}^2 \rangle_{(\Delta=0)} = \kappa_{ex} \frac{|g|^2}{\Omega_m^2} \frac{1}{2} \frac{k_B T}{\hbar \Omega_m}, \quad (2.5.27)$$

$$\langle \delta \hat{a}_{out}^2 \rangle_{(\Delta=\mp\Omega_m)} = 4\kappa_{ex} \frac{|g|^2}{\kappa^2} \frac{\Gamma_m}{\Gamma_m + \Gamma_{opt}} \frac{1}{2} \frac{k_B T}{\hbar \Omega_m}, \quad \text{with} \quad \Gamma_{opt} = \pm \frac{4|g|^2}{\kappa}, \quad (2.5.28)$$

the sign of Γ_{opt} depending on the sign of Δ (+ for "red", and - for "blue" pumping). Consequently in the weak coupling limit:

$$\langle \delta \hat{a}_{out}^2 \rangle_{(\Delta=0)} = \kappa_{ex} \frac{|g|^2}{\Omega_m^2} \frac{1}{2} \langle \hat{b}^2 \rangle_{(\Delta=0)}, \quad (2.5.29)$$

$$\langle \delta \hat{a}_{out}^2 \rangle_{(\Delta=\mp\Omega_m)} = 4\kappa_{ex} \frac{|g|^2}{\kappa^2} \frac{1}{2} \langle \hat{b}^2 \rangle_{(\Delta=\mp\Omega_m)}. \quad (2.5.30)$$

For "red" and "blue" pumping, we see that in $\langle \hat{b}^2 \rangle$ the temperature is replaced by the expression $T \rightarrow \frac{\Gamma_m}{\Gamma_m + \Gamma_{opt}} T$: this is the effective temperature of the mode, which is either increased (amplification) or reduced (cooling) depending on the sign of Γ_{opt} .

We now have all the tools required to define experimentally in Chapter 7 the mechanical mode temperature.

2.6 QUANTUM LIMITS

2.6.1 Cavity back-action

Eq. (2.4.27) giving the total mechanical spectrum includes the quantum contributions of both the mechanics and the optics. The first term corresponds to the positive peak (at $+\Omega_m + \delta\omega$) and the second to the negative one (at $-\Omega_m + \delta\omega$). For both peaks the optical cavity back-action contribution is identical and writes:

$$|g|^2\kappa \left[\left(|\bar{\chi}_c[-\omega]|^2 + |\chi_c[\omega]|^2 \right) \bar{N}_c + |\bar{\chi}_c[-\omega]|^2 \right], \quad (2.6.1)$$

where the first term $\propto \bar{N}_c$ is the thermal part and the second term the quantum contribution of the cavity back-action. We derive the quantum mechanical spectrum for the relevant schemes ("blue", "red", "green") in the following Section 2.6.2.

On the other hand, the presence of the cross-correlation terms in the optical field Eqs. (2.4.36-2.4.39) generate additional contributions that mimic an extra stochastic background for the mechanics: as such, the measured mechanical sidebands do not correspond exactly to the (quantum) mechanical spectrum. This has important implications like the nature of the so-called sideband asymmetry [37]. The full optical field is thus presented and discussed below in Section 2.6.3. The insightful comparison to the classical electric model is given in Chapter 3.

2.6.2 Mechanical field

"GREEN" PUMPING Concerning the in-cavity pumping scheme, i.e. for $\Delta = 0$ the mechanical spectrum Eq. (2.4.27) becomes in the usual resolved sideband regime $\kappa \ll \Omega_m$:

$$\begin{aligned} \mathcal{S}_{\hat{O}_b}[\omega] &= |\bar{\chi}_m[-\omega]|^2 \left[\frac{2|g|^2\kappa}{\Omega_m^2} \bar{N}_c + \frac{|g|^2\kappa}{\Omega_m^2} + \Gamma_m \bar{N}_m \right] \\ &+ |\chi_m[\omega]|^2 \left[\frac{2|g|^2\kappa}{\Omega_m^2} \bar{N}_c + \frac{|g|^2\kappa}{\Omega_m^2} + \Gamma_m (\bar{N}_m + 1) \right]. \end{aligned} \quad (2.6.2)$$

For both peaks, the cavity contribution (first thermal term and second quantum one) are the same. The only difference between both peaks occurs with the mechanical quantum zero-point-motion present in the positive peak [end of second line in Eq. (2.6.2)].

Defining (in order to match the "red" sideband pumping expressions):

$$\begin{cases} \Gamma_{opt} &= \frac{4|g|^2}{\kappa}, \\ n_c^{min} &= \left(\frac{\kappa}{4\Omega_m} \right)^2, \end{cases} \quad (2.6.3)$$

Eq. (2.6.2) can be recast in:

$$\mathcal{S}_{\hat{O}_b}[\omega] = |\bar{\chi}_m[-\omega]|^2 \Gamma_m \bar{N}_{eff} + |\chi_m[\omega]|^2 \Gamma_m (\bar{N}_{eff} + 1), \quad (2.6.4)$$

where we introduced an effective population which includes the cavity zero-point-fluctuation:

$$\bar{N}_{eff} = \frac{\Gamma_m \bar{N}_m + 4|\Gamma_{opt}| n_c^{min} (2\bar{N}_c + 1)}{\Gamma_m}. \quad (2.6.5)$$

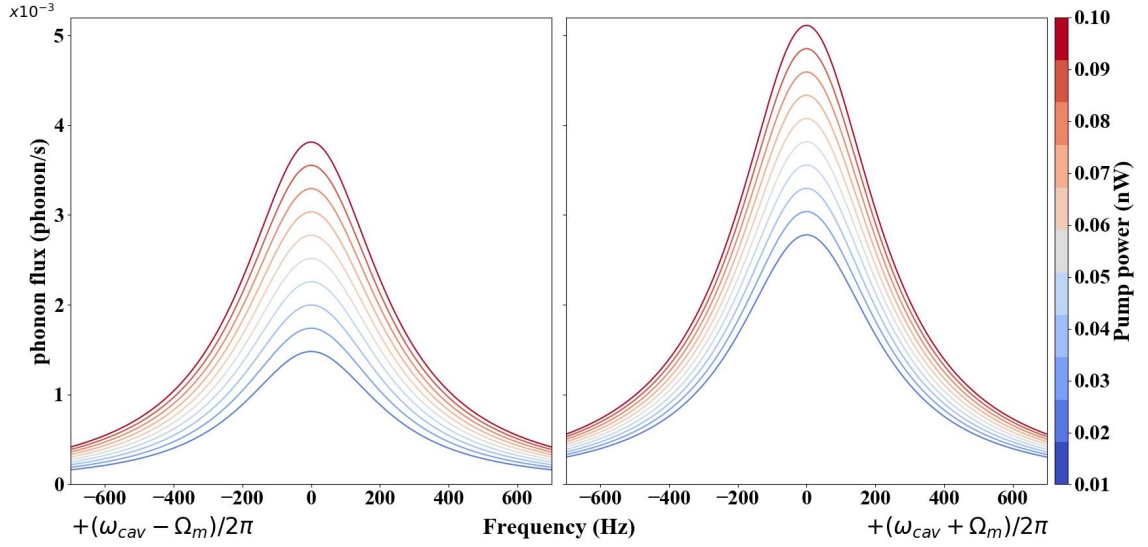


FIGURE 2.6 – Computed mechanical quantum spectra within the "green" pumping scheme ($\Delta = 0$) as a function of the injected power P_m . The calculation is performed with the highly-coupled drumhead device parameters given in Fig. 2.2 for a temperature $T = 1$ mK. The negative peak (left curve) has an area \bar{N}_{eff} whereas the positive one (right curve) has an area $\bar{N}_{eff} + 1$.

This expression will be discussed below when compared to the two other "red" and "blue" pumping schemes.

From the definitions:

$$\begin{cases} n_- = \frac{1}{2\pi} \int_{\mathbb{R}^-} \mathcal{S}_{\hat{O}_b}[\omega] d\omega, \\ n_+ = \frac{1}{2\pi} \int_{\mathbb{R}^+} \mathcal{S}_{\hat{O}_b}[\omega] d\omega, \end{cases} \quad (2.6.6)$$

as being the populations of the negative and positive portions of the spectrum respectively, we obviously obtain:

$$\begin{cases} n_- = \bar{N}_{eff}, \\ n_+ = \bar{N}_{eff} + 1. \end{cases} \quad (2.6.7)$$

Thus the only quantum signature for the mechanics is the asymmetry between both Stokes and Anti-Stokes peaks displayed on Fig. 2.6. Note that this feature completely disappears in the previously presented classical limit where $\bar{N}_{eff} \gg 1$.

Even at zero temperature a small population persists. This is due to the back-action of the quantum contribution of the optical cavity onto the mechanics:

$$\bar{N}_{eff}(T = 0) = 4 \frac{\Gamma_{opt}}{\Gamma_m} n_c^{min} = 16 \frac{g_0^2}{\kappa \Gamma_m} \bar{n}_{cav} n_c^{min}, \quad (2.6.8)$$

which increases as one increases the measurement power (i.e. \bar{n}_{cav}).

"RED" PUMPING For the "red" sideband pumping scheme, we consider $\Delta = -\Omega_m$. In this case and using the same hypotheses as before, the mechanical spectrum writes for both peaks at $\omega = \pm\Omega_m + \delta\omega$:

$$\begin{aligned} \mathcal{S}_{\hat{O}_b}[\omega] &= \left\{ \left[1 + \frac{2|g|^4}{\Omega_m^2 \kappa^2} \right] \Gamma_m \bar{N}_m + \frac{|g|^4}{\Omega_m^2 \kappa^2} \Gamma_m + \frac{4|g|^2}{\kappa} \left[\bar{N}_c + \frac{\kappa^2}{16\Omega_m^2} \right] \right\} |\tilde{\chi}_{eff}[-\delta\omega]|^2 \\ &+ \left\{ \left[1 + \frac{2|g|^4}{\Omega_m^2 \kappa^2} \right] \Gamma_m \bar{N}_m + \left[1 + \frac{|g|^4}{\Omega_m^2 \kappa^2} \right] \Gamma_m + \frac{4|g|^2}{\kappa} (\bar{N}_c + 1) \right\} |\chi_{eff}[\delta\omega]|^2, \end{aligned} \quad (2.6.9)$$

where we introduced (for a compact writing):

$$\chi_{eff}[\delta\omega] = \frac{1}{\frac{\Gamma_{eff}}{2} - i\delta\omega} \quad \text{with } \omega = +\Omega_m + \delta\omega \text{ (and 0 elsewhere)}, \quad (2.6.10)$$

$$\tilde{\chi}_{eff}[-\delta\omega] = \frac{1}{\frac{\Gamma_{eff}}{2} - i\delta\omega} \quad \text{with } \omega = -\Omega_m + \delta\omega \text{ (and 0 elsewhere)}, \quad (2.6.11)$$

with again $\Gamma_{eff} = \Gamma_m + \Gamma_{opt}$ and $\Gamma_{opt} = 4|g|^2/\kappa$. Using Eqs. (2.6.3), we can recast the mechanical spectrum under the following form:

$$\mathcal{S}_{\hat{O}_b}[\omega] = \Gamma_{eff} \bar{N}_{eff} |\tilde{\chi}_{eff}[-\delta\omega]|^2 + \Gamma_{eff} \left[\bar{N}_{eff} + 1 - n_c^{min} \frac{|\Gamma_{opt}|}{\Gamma_m + |\Gamma_{opt}|} \right] |\chi_{eff}[\delta\omega]|^2, \quad (2.6.12)$$

with, similarly to the "green pumping" case:

$$\bar{N}_{eff} = \frac{\left[1 + 2 \frac{|\Gamma_{opt}|^2}{\kappa^2} n_c^{min} \right] \Gamma_m (\bar{N}_m + \bar{n}_0) + |\Gamma_{opt}| (\bar{N}_c + n_c^{min})}{\Gamma_{eff}}, \quad (2.6.13)$$

where:

$$\bar{n}_0 = \frac{\frac{|\Gamma_{opt}|^2}{\kappa^2} n_c^{min}}{1 + 2 \frac{|\Gamma_{opt}|^2}{\kappa^2} n_c^{min}}. \quad (2.6.14)$$

In these expressions, the terms $\propto |\Gamma_{opt}|^2/\kappa^2$ correspond to the lowest order strong coupling corrections, which are very small for our experimental realizations.

Assuming the usual resolved sideband limit ($n_c^{min} \ll 1$), we recover the same quantum signature as for "green" pumping for the population of each peak:

$$\begin{cases} n_- = \bar{N}_{eff}, \\ n_+ \approx \bar{N}_{eff} + 1. \end{cases} \quad (2.6.15)$$

In this case, the mechanical spectrum looks very similar to Fig. 2.6 but with a different numerical value for \bar{N}_{eff} , and both peaks have a linewidth Γ_{eff} instead of Γ_m .

Assuming very high driving powers ($\Gamma_{opt} \gg \Gamma_m$) [86] and the cavity mode in the ground state ($\bar{N}_c \rightarrow 0$) we obtain:

$$\bar{N}_{eff} \approx n_c^{min} + \frac{\Gamma_{opt}}{\Gamma_m} \frac{\Gamma_m^2}{\kappa^2} n_c^{min} (1 + 2\bar{N}_m), \quad (2.6.16)$$

with the lowest order strong coupling correction. We recover the famous result of a minimum reachable population for the "red" sideband cooling scheme [86, 48].

"BLUE" PUMPING Within the "blue" sideband pumping scheme, i.e. for $\Delta = +\Omega_m$ the mechanical spectrum writes:

$$\begin{aligned} \mathcal{S}_{\hat{O}_b}[\omega] &= \left\{ \left[1 + \frac{2|g|^4}{\Omega_m^2 \kappa^2} \right] \Gamma_m \bar{N}_m + \frac{|g|^4}{\Omega_m^2 \kappa^2} \Gamma_m + \frac{4|g|^2}{\kappa} (\bar{N}_c + 1) \right\} \left| \bar{\chi}_{eff}[-\delta\omega] \right|^2 \\ &+ \left\{ \left[1 + \frac{2|g|^4}{\Omega_m^2 \kappa^2} \right] \Gamma_m \bar{N}_m + \frac{|g|^4}{\Omega_m^2 \kappa^2} \Gamma_m + \frac{4|g|^2}{\kappa} \left[\bar{N}_c + \frac{\kappa^2}{16\Omega_m^2} \right] \right\} \left| \chi_{eff}[\delta\omega] \right|^2, \end{aligned} \quad (2.6.17)$$

where similarly as for "red" pumping:

$$\chi_{eff}[\delta\omega] = \frac{1}{\frac{\Gamma_{eff}}{2} - i\delta\omega} \quad \text{with } \omega = +\Omega_m + \delta\omega \text{ (and 0 elsewhere)} \quad (2.6.18)$$

$$\bar{\chi}_{eff}[-\delta\omega] = \frac{1}{\frac{\Gamma_{eff}}{2} - i\delta\omega} \quad \text{with } \omega = -\Omega_m + \delta\omega \text{ (and 0 elsewhere)} \quad (2.6.19)$$

and $\Gamma_{eff} = \Gamma_m + \Gamma_{opt}$ with $\Gamma_{opt} = -4|g|^2/\kappa$.

We can recast $\mathcal{S}_{\hat{O}_b}$ into:

$$\mathcal{S}_{\hat{O}_b}[\omega] = \Gamma_{eff} \bar{N}_{eff} \left| \bar{\chi}_{eff}[-\delta\omega] \right|^2 + \Gamma_{eff} \left[\bar{N}_{eff} + 1 + n_c^{min} \frac{|\Gamma_{opt}|}{\Gamma_m - |\Gamma_{opt}|} \right] \left| \chi_{eff}[\delta\omega] \right|^2, \quad (2.6.20)$$

with:

$$\bar{N}_{eff} = \frac{\left[1 + 2 \frac{|\Gamma_{opt}|^2}{\kappa^2} n_c^{min} \right] \Gamma_m (\bar{N}_m + \bar{n}_0) + |\Gamma_{opt}| (\bar{N}_c + 1)}{\Gamma_{eff}}, \quad (2.6.21)$$

where \bar{n}_0, n_c^{min} are defined the same way as for "red" pumping. Within the same hypotheses as before, we recover the same asymmetric mechanical spectrum, signature of the quantum regime:

$$\begin{cases} n_- = \bar{N}_{eff}, \\ n_+ \approx \bar{N}_{eff} + 1. \end{cases} \quad (2.6.22)$$

Besides, we see that Eqs. (2.6.13) and (2.6.21) are very similar; with only the far right n_c^{min} term changed into 1 for the "blue" scheme expression. When compared to the "green" expression for \bar{N}_{eff} , Eq. (2.6.5), we also see that in the latter n_c^{min} appears in factor of \bar{N}_c : all the cavity noise is suppressed by the sideband resolved term $[\kappa/(4\Omega_m)]^2$, which is why this scheme is usually referred to as the optimal one for a position measurement. These aspects will be discussed further in Chapter 3 when comparing the quantum approach to the classical formalism.

2.6.3 Optical field

Concerning the optical field, we describe below the three usual schemes, with both the positive (around $+\omega_p$) and negative (around $-\omega_p$) regions of the quantum spectrum, as well as the symmetrized (classically measured) spectrum around $+\omega_p$.

"GREEN" PUMPING In the case of in-cavity pumping, i.e. for $\Delta = 0$ the positive part of the optical field around $+\omega_p$ becomes for both sidebands:

$$\begin{aligned} \mathcal{S}_{\delta\hat{a}}[\omega] = & \left| \chi_c[\omega] \right|^2 \left\{ \kappa(\bar{N}_c + 1) + |g|^2 \left| \chi_{eff}[\delta\omega] \right|^2 \Gamma_m \left[\bar{n} + \frac{|g|^2}{\Omega_m^2} \frac{\kappa}{\Gamma_m} (2\bar{N}_c + 1) \right] \right. \\ & \left. + |g|^2 \left| \chi_{eff}[\delta\omega] \right|^2 \Gamma_m \left[2 \frac{\delta\omega}{\Gamma_m} \frac{\kappa}{\Omega_m} (\bar{N}_c + 1) \right] \right\}, \end{aligned} \quad (2.6.23)$$

with:

$$\bar{n} = \begin{cases} \bar{N}_m, & \text{for the lower sideband around } -\Omega_m + \delta\omega, \\ \bar{N}_m + 1, & \text{for the upper sideband around } +\Omega_m + \delta\omega, \end{cases} \quad (2.6.24)$$

and where (similarly to the previous Section, for compact writing):

$$\left| \chi_{eff}[\delta\omega] \right|^2 = \frac{1}{\left(\frac{\Gamma_m}{2}\right)^2 + \delta\omega^2} \quad (\text{nonzero only around } \pm\Omega_m). \quad (2.6.25)$$

Note that in Eq. (2.6.23) the last term corresponds to the internal cross-correlation part. Concerning the extra external cross-correlation terms Eq. (2.4.36), they write in this case:

$$\begin{cases} \left| \chi_c[\omega] \right|^2 \left[-\kappa + |g|^2 \left| \chi_{eff}[\delta\omega] \right|^2 \Gamma_m \right] (N_{ext} + 1), & \text{for } -\Omega_m + \delta\omega, \\ \left| \chi_c[\omega] \right|^2 \left[-\kappa - |g|^2 \left| \chi_{eff}[\delta\omega] \right|^2 \Gamma_m \right] (N_{ext} + 1), & \text{for } +\Omega_m + \delta\omega. \end{cases} \quad (2.6.26)$$

The negative part of the optical spectrum around $-\omega_p$ writes:

$$\begin{aligned} \mathcal{S}_{\delta\hat{a}^\dagger}[\omega] = & \left| \bar{\chi}_c[-\omega] \right|^2 \left\{ \kappa\bar{N}_c + |g|^2 \left| \chi_{eff}[\delta\omega] \right|^2 \Gamma_m \left[\bar{n} + \frac{|g|^2}{\Omega_m^2} \frac{\kappa}{\Gamma_m} (2\bar{N}_c + 1) \right] \right. \\ & \left. - |g|^2 \left| \chi_{eff}[\delta\omega] \right|^2 \Gamma_m \left[2 \frac{\delta\omega}{\Gamma_m} \frac{\kappa}{\Omega_m} (\bar{N}_c + 1) \right] \right\}, \end{aligned} \quad (2.6.27)$$

with \bar{n} defined the same way as for the positive region, Eqs. (2.6.24). The extra external cross-correlation terms Eq. (2.4.37) write:

$$\begin{cases} \left| \bar{\chi}_c[-\omega] \right|^2 \left[-\kappa - |g|^2 \left| \chi_{eff}[\delta\omega] \right|^2 \Gamma_m \right] N_{ext}, & \text{for } -\Omega_m + \delta\omega, \\ \left| \bar{\chi}_c[-\omega] \right|^2 \left[-\kappa + |g|^2 \left| \chi_{eff}[\delta\omega] \right|^2 \Gamma_m \right] N_{ext}, & \text{for } +\Omega_m + \delta\omega. \end{cases} \quad (2.6.28)$$

The full symmetrized measured spectrum for both sidebands around $+\omega_p$ thus writes:

$$\begin{aligned} \mathcal{S}_{\delta\hat{a}}^{sym}[\omega] + \mathcal{S}_{\xi_{ext,\delta\hat{a}}}^{sym}[\omega] = & \left| \chi_c[\omega] \right|^2 \left\{ \kappa \left(\bar{N}_c + \frac{1}{2} \right) - \kappa \left(N_{ext} + \frac{1}{2} \right) \right. \\ & + |g|^2 \left| \chi_{eff}[\delta\omega] \right|^2 \Gamma_m \left[\left(\bar{N}_m + \frac{1}{2} \right) + \frac{|g|^2}{\Omega_m^2} \frac{\kappa}{\Gamma_m} (2\bar{N}_c + 1) \right. \\ & \left. \left. + 2 \frac{\delta\omega}{\Gamma_m} \frac{\kappa}{\Omega_m} \left(\bar{N}_c + \frac{1}{2} \right) \pm \left(N_{ext} + \frac{1}{2} \right) \right] \right\}, \end{aligned} \quad (2.6.29)$$

for $\omega = \mp\Omega_m + \delta\omega$; note the \pm sign change in the last line. This change is not a marginal feature, it is an essential signature present on the detected signal: on the lower sideband, noise quanta $N_{ext} + \frac{1}{2}$ are added from the microwave measurement port to the "measured effective mechanical bath", while they are subtracted on the upper one. This is responsible for both "sideband assymetry" [37] and "noise squashing" [200]. But obviously, these terms are not present in the mechanical spectrum. We shall comment this effect below, in the "blue" scheme paragraph. The term proportional to $\delta\omega$ mimics a tilted noise background, which in the sideband resolved limit ($\kappa/\Omega_m \ll 1$) can be safely neglected. The middle line is nothing but the effective mechanical bath with the back-action term. The first line is the cavity contribution. Again if $N_{ext} = \bar{N}_c$, the cavity peak itself is perfectly canceled.

"RED" PUMPING As for the "green" pumping scheme, we explicitly separate both optical sidebands (anti-Stokes and Stokes) in each spectral region (around $\omega \approx \pm\omega_p$). Looking at the positive part of the spectrum, for $\Delta = -\Omega_m$, the optical field for the upper sideband $\omega = +\Omega_m + \delta\omega$ writes:

$$\mathcal{S}_{\delta\hat{a}}[\omega] = \left| \chi_c[-\Delta] \right|^2 \left\{ \kappa(\bar{N}_c + 1) + |g|^2 \left| \chi_{eff}[\delta\omega] \right|^2 \left[\Gamma_m(\bar{N}_m + 1) + \Gamma_{opt}(\bar{N}_c + 1) + \Gamma_{opt} \left(\frac{\kappa}{4\Omega_m} \right)^2 \bar{N}_c - 2\Gamma_{eff}(\bar{N}_c + 1) \right] \right\}, \quad (2.6.30)$$

and

$$\mathcal{S}_{\delta\hat{a}}[\omega] = \left| \chi_c[+\Delta] \right|^2 \left\{ \kappa(\bar{N}_c + 1) + |g|^2 \left| \chi_{eff}[\delta\omega] \right|^2 \left[\Gamma_m\bar{N}_m + \Gamma_{opt}\bar{N}_c + \Gamma_{opt} \left(\frac{\kappa}{4\Omega_m} \right)^2 (\bar{N}_c + 1) + \delta\omega \frac{\kappa}{\Omega_m} (\bar{N}_c + 1) \right] \right\}, \quad (2.6.31)$$

for the lower one $\omega = -\Omega_m + \delta\omega$. The last terms $\propto \Gamma_{eff}$ and $\delta\omega$ in the above equations correspond to the the internal cross-correlation part. We also introduced similarly to the mechanical field calculation the quantities:

$$\Gamma_{eff} = \Gamma_m + \Gamma_{opt} \quad \text{with} \quad \Gamma_{opt} = +4 \frac{|g|^2}{\kappa}, \quad (2.6.32)$$

and

$$\left| \chi_{eff}[\delta\omega] \right|^2 = \frac{1}{\left(\frac{\Gamma_{eff}}{2} \right)^2 + \delta\omega^2}. \quad (2.6.33)$$

In this case the extra external cross-correlation terms write for both sidebands:

$$\begin{cases} \left| \chi_c[-\Delta] \right|^2 \left[-\kappa + |g|^2 \left(\Gamma_{eff} - \frac{\kappa\delta\omega}{2\Omega_m} \right) \left| \chi_{eff}[\delta\omega] \right|^2 \right] (N_{ext} + 1), & \text{for } +\Omega_m + \delta\omega, \\ \left| \chi_c[+\Delta] \right|^2 \left[-\kappa + |g|^2 \Gamma_{eff} \left| \chi_{eff}[\delta\omega] \right|^2 \right] (N_{ext} + 1), & \text{for } -\Omega_m + \delta\omega. \end{cases} \quad (2.6.34)$$

Note that expressions for the negative part of the optical spectrum (around $-\omega_p$) are symmetric with $(\bar{N}_c + 1) \rightarrow \bar{N}_c$ as well as $(N_{ext} + 1) \rightarrow N_{ext}$.

Similarly to the other schemes, we finally express the full symmetrized optical spectrum for "red" pumping:

$$\begin{aligned} \mathcal{S}_{\delta\hat{a}}^{sym}[\omega] + \mathcal{S}_{\hat{\xi}_{ext},\delta\hat{a}}^{sym}[\omega] &= \left| \chi_c[-\Delta] \right|^2 \left\{ \kappa \left(\bar{N}_c + \frac{1}{2} \right) - \kappa \left(N_{ext} + \frac{1}{2} \right) \right. \\ &+ |g|^2 \left| \chi_{eff}[\delta\omega] \right|^2 \Gamma_{eff} \left[\frac{\Gamma_m}{\Gamma_{eff}} \left(\bar{N}_m + \frac{1}{2} \right) + \frac{\Gamma_{opt}}{\Gamma_{eff}} \left(1 + \frac{\kappa^2}{16\Omega_m^2} \right) \left(\bar{N}_c + \frac{1}{2} \right) \right. \\ &\left. \left. - 2 \left(\bar{N}_c + \frac{1}{2} \right) + \left(N_{ext} + \frac{1}{2} \right) - 2 \frac{\delta\omega}{\Gamma_{eff}} \frac{\kappa}{4\Omega_m} \left(N_{ext} + \frac{1}{2} \right) \right] \right\}, \quad (2.6.35) \end{aligned}$$

defined for $\omega = +\Omega_m + \delta\omega$ only (we do not write the lower sideband, which is suppressed by a factor $(\frac{\kappa}{4\Omega_m})^2$). Similarly to the "green" scheme, we recognize in the first line the cavity contribution, in the second line the mechanical effective population with the back-action term, and finally in the last line the cross-correlation contributions. The last element proportional to $\delta\omega$ can be safely neglected for a sideband-resolved device. The term $-2(\bar{N}_c + \frac{1}{2}) + (N_{ext} + \frac{1}{2})$, responsible for "sideband asymmetry" and "noise squashing", will be discussed below in the "blue" scheme paragraph.

"BLUE" PUMPING Looking at the positive part of the spectrum, for $\Delta = +\Omega_m$, the optical field for the lower sideband $\omega = -\Omega_m + \delta\omega$ writes:

$$\begin{aligned} \mathcal{S}_{\delta\hat{a}}[\omega] &= \left| \chi_c[-\Delta] \right|^2 \left\{ \kappa (\bar{N}_c + 1) + |g|^2 \left| \chi_{eff}[\delta\omega] \right|^2 \left[\Gamma_m \bar{N}_m + \Gamma_{opt} (\bar{N}_c + 1) \right. \right. \\ &\left. \left. + \Gamma_{opt} \left(\frac{\kappa}{4\Omega_m} \right)^2 \bar{N}_c + 2\Gamma_{eff} (\bar{N}_c + 1) \right] \right\}, \quad (2.6.36) \end{aligned}$$

and

$$\begin{aligned} \mathcal{S}_{\delta\hat{a}}[\omega] &= \left| \chi_c[+\Delta] \right|^2 \left\{ \kappa (\bar{N}_c + 1) + |g|^2 \left| \chi_{eff}[\delta\omega] \right|^2 \left[\Gamma_m (\bar{N}_m + 1) + \Gamma_{opt} \bar{N}_c \right. \right. \\ &\left. \left. + \Gamma_{opt} \left(\frac{\kappa}{4\Omega_m} \right)^2 (\bar{N}_c + 1) + \delta\omega \frac{\kappa}{\Omega_m} (\bar{N}_c + 1) \right] \right\}, \quad (2.6.37) \end{aligned}$$

for the upper one at $\omega = +\Omega_m + \delta\omega$. The last terms $\propto \Gamma_{eff}$ and $\delta\omega$ in the above equations correspond, as for the "red" pumping case, to the internal cross-correlation part. Note that in this case:

$$\Gamma_{eff} = \Gamma_m + \Gamma_{opt} \quad \text{with} \quad \Gamma_{opt} = -4 \frac{|g|^2}{\kappa}. \quad (2.6.38)$$

The expression of $\left| \chi_{eff}[\delta\omega] \right|^2$ is unchanged from the previous paragraph. The extra external cross-correlation terms write for both sidebands:

$$\begin{cases} \left| \chi_c[-\Delta] \right|^2 \left[-\kappa - |g|^2 \left(\Gamma_{eff} + \frac{\kappa\delta\omega}{2\Omega_m} \right) \left| \chi_{eff}[\delta\omega] \right|^2 \right] (N_{ext} + 1), & \text{for } -\Omega_m + \delta\omega, \\ \left| \chi_c[+\Delta] \right|^2 \left[-\kappa - |g|^2 \Gamma_{eff} \left| \chi_{eff}[\delta\omega] \right|^2 \right] (N_{ext} + 1), & \text{for } +\Omega_m + \delta\omega. \end{cases} \quad (2.6.39)$$

Expressions for the negative part of the spectrum around $-\omega_p$ are deduced analogously to the others schemes.

We finally write the full symmetrized optical spectrum for "blue" pumping:

$$\begin{aligned} \mathcal{S}_{\delta\hat{a}}^{sym}[\omega] + \mathcal{S}_{\hat{\xi}_{ext},\delta\hat{a}}^{sym}[\omega] &= |\chi_c[-\Delta]|^2 \left\{ \kappa \left(\bar{N}_c + \frac{1}{2} \right) - \kappa \left(N_{ext} + \frac{1}{2} \right) \right. \\ &\quad + |g|^2 |\chi_{eff}[\delta\omega]|^2 \Gamma_{eff} \left[\frac{\Gamma_m}{\Gamma_{eff}} \left(\bar{N}_m + \frac{1}{2} \right) + \frac{|\Gamma_{opt}|}{\Gamma_{eff}} \left(1 + \frac{\kappa^2}{16\Omega_m^2} \right) \left(\bar{N}_c + \frac{1}{2} \right) \right. \\ &\quad \left. \left. + 2 \left(\bar{N}_c + \frac{1}{2} \right) - \left(N_{ext} + \frac{1}{2} \right) - 2 \frac{\delta\omega}{\Gamma_{eff}} \frac{\kappa}{4\Omega_m} \left(N_{ext} + \frac{1}{2} \right) \right] \right\}, \quad (2.6.40) \end{aligned}$$

for $\omega = -\Omega_m + \delta\omega$ (the other sideband being strongly suppressed, we do not give it explicitly). The last term ($\propto \delta\omega$) can be safely neglected in the sideband resolved limit. We recognize the same contributions as for the other schemes: the cavity (first line), the mechanical bath with back-action (middle) and the cross-correlation terms (last).

The cross-correlation terms in Eqs. (2.6.29,2.6.35,2.6.40) are essential to understand the phenomena of "noise squashing" and "sideband assymetry". Fundamentally, it means that the mechanical population measured through the sidebands *is not* strictly equivalent to the real population as determined from the mechanical spectrum. "Noise squashing" comes from the $-$ sign appearing in some of the cross-correlations: if the amount of noise that is fed from the output port is large enough, it can then create a "hole" in the noise level normally measured [200]. "Sideband assymetry" designates the fact that cross-correlations are fed onto the two sidebands with opposite signs. With "green" pumping, we have an extra population of $+(N_{ext} + \frac{1}{2})$ on the lower peak at $-\Omega_m$, and $-(N_{ext} + \frac{1}{2})$ at $+\Omega_m$: the assymetry being exactly $2N_{ext} + 1$. With "red" pumping, the measured (upper) sideband has a deficit $-(2\bar{N}_c - N_{ext} + \frac{1}{2})$ while for "blue" the lower one is increased by $(2\bar{N}_c - N_{ext} + \frac{1}{2})$. Again, the difference between the peaks measured in the two schemes, if the power is low enough to guarantee negligible dynamical back-action $\Gamma_{eff} \approx \Gamma_m$, is $2(2\bar{N}_c - N_{ext}) + 1$ [37]. If the optical baths have all the same temperature $\bar{N}_c = N_{ext}$, the two results are strictly equivalent.

Note also that if the optical fields are in their ground state, the assymetry is exactly one quantum. However, this quantum originates in cross-correlations from the zero point fluctuations of light; even if it looks like the quantum-mechanical spectrum, it has nothing to do with the zero-point-motion of the mechanics. The mechanics needs to be cold only to guarantee \bar{N}_m low enough to make the effect visible [37]. The link to classical physics will be discussed in Chapter 3.

2.7 BEYOND LINEAR COUPLING INTERACTION

The "blue-sideband" or Stokes pumping scheme leads to amplification of the mechanical motion. In this part of the manuscript, we study the optomechanical interaction beyond the threshold of the parametric instability ($\Gamma_{eff} = 0$), when the mechanical system enters the self-induced oscillation regime. Indeed because of anti-damping ($\Gamma_{opt} < 0$), when the total mechanical friction crosses zero and changes sign, any fluctuation of position becomes exponentially amplified instead of being damped; after a short period of time, the motion saturates and becomes limited by all the nonlinear effects of the system. Hence, in this case higher order optomechanical coupling terms need to be considered.

Note that the following derivation is performed in the framework of the semi-classical calculation presented before: the basics presented here are thus also valid below the parametric threshold. In the stable state calculation, we shall omit the Kerr effect of the cavity as well as the Duffing nonlinearity of the mechanics, since these two are proven experimentally to have a marginal impact on the dynamics (see Chapter 8). However, the Duffing term will generate a frequency shift on the mechanics, which can be measured (see Chapter 8).

2.7.1 Nonlinear optomechanical coupling dynamics

We now consider higher order nonlinear coupling terms [see Eq. (2.2.3)] and write the optomechanical Hamiltonian in the rotating frame under the following form:

$$\begin{aligned} \hat{H}_{RWT} = & -\hbar\Delta\hat{a}^\dagger\hat{a} + \hbar\Omega_m\hat{b}^\dagger\hat{b} - \hbar g_0\hat{a}^\dagger\hat{a}(\hat{b}^\dagger + \hat{b}) - \frac{1}{2}\sum_{k=1}^N \hbar g_k\hat{a}^\dagger\hat{a}(\hat{b}^\dagger + \hat{b})^{k+1} \\ & - i\hbar\sqrt{\kappa_{ex}}\left[\hat{a}^\dagger\alpha_{in}(t) - \alpha_{in}^*(t)\hat{a}\right] + \hat{H}_{baths}, \end{aligned} \quad (2.7.1)$$

where the non-linear expansion is taken up to order N .

In electromechanics, the signs of the g_k s depend on the topography of the electric field; in principle, they can be any (see Chapter 8). However, the choice of the direction of the x -axis (direction of the motion) being arbitrary, the choices $g_k \rightarrow (-1)^{k+1}g_k$ are equivalent. It is thus convenient to choose $g_0 > 0$ (Section 2.5.1), which fixes then the sign of all other terms.

Note that from the quantum Hamiltonian point of view, these g_k s correspond to processes involving $k + 1 > 1$ phonons and 1 photon.

\hat{H}_{baths} represents the external baths coupling Hamiltonian in the rotating frame as described in Eq. (2.2.18). As previously, the optical drive is considered to be coupled with a decay rate κ_{ex} and in this case the equations of motion for both the optics and the mechanics write:

$$\begin{cases} \langle \dot{\hat{a}} \rangle = \left(i\Delta - \frac{\kappa}{2}\right) \langle \hat{a} \rangle + ig_0 \langle (\hat{b} + \hat{b}^\dagger)\hat{a} \rangle + \frac{i}{2} \sum_{k=1}^N g_k \langle (\hat{b} + \hat{b}^\dagger)^{k+1}\hat{a} \rangle - \sqrt{\kappa_{ex}}\tilde{\alpha}_{in}, \\ \langle \dot{\hat{b}} \rangle = -\left(i\Omega_m + \frac{\Gamma_m}{2}\right) \langle \hat{b} \rangle + ig_0 \langle \hat{a}^\dagger\hat{a} \rangle + \frac{i}{2} \sum_{k=1}^N (k+1)g_k \langle (\hat{b} + \hat{b}^\dagger)^k\hat{a}^\dagger\hat{a} \rangle. \end{cases} \quad (2.7.2)$$

Considering the amplitude of both bosonic fields to be large enough, thermal and quantum fluctuations can be neglected. In this case we adopt the usual semiclassical approximation and write:

$$\begin{cases} \langle \hat{a} \rangle \rightarrow \alpha, \\ \langle \hat{b}^k \rangle \rightarrow \beta^k, \end{cases} \quad (2.7.3)$$

which leads to the following amplitude equations:

$$\begin{cases} \dot{\alpha} = \left(i\Delta - \frac{\kappa}{2}\right) \alpha + ig_0(\beta + \beta^*)\alpha + \frac{i}{2} \sum_{k=1}^N g_k(\beta + \beta^*)^{k+1}\alpha - \sqrt{\kappa_{ex}}\tilde{\alpha}_{in}, \\ \dot{\beta} = -\left(i\Omega_m + \frac{\Gamma_m}{2}\right) \beta + ig_0|\alpha|^2 + \frac{i}{2} \sum_{k=1}^N (k+1)g_k(\beta + \beta^*)^k|\alpha|^2. \end{cases} \quad (2.7.4)$$

Compared to Eqs. (2.4.2), we thus added the nonlinear terms but removed the fluctuating baths operators $\hat{\xi}_i, \hat{\xi}_j$. Their impact on self-oscillating states is explicitly studied in Ref. [28], in the simpler case of linear coupling.

2.7.2 Limit cycle solving

ANSATZ AND STATIC DEFLECTION This system of coupled equations is solved by means of the usual ansatz given for β :

$$\beta = \beta_c + B e^{-i\phi} e^{-i\omega t}, \quad (2.7.5)$$

where β_c is a term related to the static deflection of the average mechanical mode's position, and $B e^{-i\phi}$ corresponds to the complex-valued coherent motion. The angular frequency ω is yet undefined, but close to ω_m . Note that this form is generic and is also valid in the standard Brownian optomechanical case where we can write $\beta = \beta_c + B(t) e^{-i\omega t}$, $B(t)$ being a given (complex, and slow) stochastic variable. Injecting this ansatz into Eqs. (2.7.4) and keeping only non-rotating terms one can easily obtain the static term β_c by solving self-consistently the following polynomial equation (knowing $|\alpha|^2$ and B):

$$\Re[\beta_c] = \frac{g_0}{\Omega_m} \frac{\Omega_m^2}{\Omega_m^2 + \frac{\Gamma_m^2}{4}} \left[1 + \frac{1}{2} \sum_{k=1}^N (k+1) \frac{g_k}{g_0} \sum_{p=0}^{\lfloor \frac{k}{2} \rfloor} \frac{2^{k-2p} k!}{(p!)^2 (k-2p)!} \Re[\beta_c]^{k-2p} B^{2p} \right] |\alpha|^2. \quad (2.7.6)$$

From $\hat{x} = x_{zpf}(\hat{b} + \hat{b}^\dagger)$, we have $x_c = 2x_{zpf} \Re[\beta_c]$ for the static deflection. The symbol $\lfloor \cdot \rfloor$ refers to the (floor) integer part. In practice, one can show that only the first term of this series is relevant, higher order static terms being completely negligible. Besides, making the numerical estimate from this expression we see that x_c is always very small (see Chapter 8); in the following, we will thus simply neglect the impact of the static term β_c onto the dynamics.

OPTICAL DYNAMICS The optical amplitude equation takes now the form:

$$\dot{\alpha} = \left[i\Delta' - \frac{\kappa}{2} + ig_0 B \cos(\omega t + \phi) + i \sum_{k=0}^N G_k B^{k+1} \cos[(k+1)(\omega t + \phi)] \right] \alpha - \sqrt{\kappa_{ex}} \tilde{\alpha}_{in}, \quad (2.7.7)$$

with:

$$G_k = \sum_{p=0}^{\lfloor \frac{N-k}{2} \rfloor} \frac{(2p+k+1)!}{p!(p+k+1)!} g_{2p+k} B^{2p}, \quad (2.7.8)$$

and we also introduce for convenience a shifted detuning:

$$\Delta' = \Delta + \frac{1}{2} \sum_{k=1}^{\lfloor \frac{N+1}{2} \rfloor} \frac{(2k)!}{(k!)^2} g_{2k-1} B^{2k}. \quad (2.7.9)$$

Note that this means a slightly renormalized cavity resonance frequency. The solution of this equation can be found using the usual mathematical approach described in [85]:

We define $\tilde{\alpha} = \alpha e^{i\Theta}$ as:

$$\Theta(t) = -\frac{g_0 B}{\omega} \sin(\omega t + \phi) + \sum_{k=0}^N Z_k \sin[(k+1)(\omega t + \phi)], \quad (2.7.10)$$

with:

$$Z_k = -\frac{G_k B^{k+1}}{(k+1)\omega}, \quad (2.7.11)$$

leading to the following simpler form for the dynamics of $\tilde{\alpha}$:

$$\dot{\tilde{\alpha}} = \left(i\Delta' - \frac{\kappa}{2} \right) \tilde{\alpha} - \sqrt{\kappa_{ex}} \tilde{\alpha}_{in} e^{i\Theta}. \quad (2.7.12)$$

We now use the Jacobi-Anger expansion $N+1$ times (on the $N+1$ terms defining the function Θ) in order to write:

$$f(t) = e^{i\Theta(t)} = \sum_{n \in \mathbb{Z}} f_n e^{in(\omega t + \phi)}, \quad (2.7.13)$$

where f_n is defined as follows:

$$f_n = \sum_{q_N \in \mathbb{Z}} \dots \sum_{q_1 \in \mathbb{Z}} \prod_{k=1}^N (-1)^{q_k} J_{q_k}(Z_k) J_{Q_0(n)} \left(Z_0 - \frac{g_0 B}{\omega} \right), \quad (2.7.14)$$

with:

$$Q_0(n) = n + \sum_{p=1}^N (p+1)q_p, \quad (2.7.15)$$

and where we use the notation J_n to define the n^{th} -order Bessel function of the first kind.

Fourier transforming Eq. (2.7.12) we can write:

$$\tilde{\alpha}(t) = \sum_{n \in \mathbb{Z}} \tilde{\alpha}_n e^{in\omega t}, \quad (2.7.16)$$

with:

$$\tilde{\alpha}_n = \frac{-\sqrt{\kappa_{ex}} \tilde{\alpha}_{in} e^{in\phi} f_n}{i(n\omega - \Delta') + \frac{\kappa}{2}}. \quad (2.7.17)$$

From this form we can obtain a solution of the problem for α writing:

$$\begin{aligned} |\alpha|^2 &= |\tilde{\alpha}|^2 = \sum_{(n,n') \in \mathbb{Z}^2} \tilde{\alpha}_n \tilde{\alpha}_{n'}^* e^{i(n-n')\omega t}, \\ &= \sum_{(n,n') \in \mathbb{Z}^2} \kappa_{ex} |\tilde{\alpha}_{in}|^2 \frac{e^{i(n-n')\omega t} e^{i(n-n')\phi} f_n f_{n'}}{h_n h_{n'}^*}, \\ &= \sum_{q \in \mathbb{Z}} e^{-iq\omega t} \eta_q, \end{aligned} \quad (2.7.18)$$

with:

$$\eta_q = e^{-iq\phi} \kappa_{ex} |\tilde{\alpha}_{in}|^2 \left[\sum_{n \in \mathbb{Z}} \frac{f_n f_{n+q}}{h_n h_{n+q}^*} \right], \quad (2.7.19)$$

and $h_n = i(n\omega - \Delta') + \frac{\kappa}{2}$. Note the change of variable $q = n' - n$ in the previous equations. We can remark that in the standard linear optomechanical case where only g_0 is taken into account, we recover the usual following form:

$$f_n = J_n \left(-\frac{2g_0 B}{\omega} \right). \quad (2.7.20)$$

MECHANICAL DYNAMICS The equation for the mechanics can be solved injecting Eq. (2.7.19) into Eq. (2.7.4). Using a rotating wave approximation preserving only terms rotating at $-\omega$ the equation becomes:

$$\begin{aligned} \dot{\beta} = & - \left(i\Omega_m + \frac{\Gamma_m}{2} \right) \beta + ig_0 \eta_1 e^{-i\omega t} \\ & + \frac{i}{2} \sum_{k=1}^N g_k \sum_{p=0}^k \frac{(k+1)!}{p!(k-p)!} \beta^{k-p} (\beta^*)^p \eta_{1+2p-k} e^{-i(1+2p-k)\omega t}. \end{aligned} \quad (2.7.21)$$

This expression can now be recast introducing the optical back-action terms, the optical spring $\delta\Omega_m$ and optical damping Γ_{opt} :

$$\dot{\beta} = - \left[i\omega + \frac{1}{2}(\Gamma_m + \Gamma_{opt}) \right] \beta, \quad (2.7.22)$$

with $\omega = \Omega_m + \delta\Omega_m$ now explicitly defined, and:

$$\begin{aligned} \Gamma_{opt} &= -2\Re[X], \\ \delta\Omega_m &= -\Im[X], \end{aligned} \quad (2.7.23)$$

where the quantity X is expressed by:

$$X = i\kappa_{ex} |\tilde{\alpha}_{in}|^2 \left[\frac{g_0}{B} \sum_{n \in \mathbb{Z}} \frac{f_n f_{n+1}}{h_n h_{n+1}^*} + \frac{1}{2} \sum_{k=1}^N g_k \sum_{p=0}^k \frac{(k+1)!}{p!(k-p)!} B^{k-1} \sum_{n \in \mathbb{Z}} \frac{f_n f_{n+1+2p-k}}{h_n h_{n+1+2p-k}^*} \right]. \quad (2.7.24)$$

STABLE STATE COMPUTATION In order to find all the stable states, one needs now to solve self-consistently the equation which cancels the effective damping $\Gamma_m + \Gamma_{opt} = 0$, ensuring that:

$$\dot{B} = 0. \quad (2.7.25)$$

In general, it is sufficient to solve the limit cycle equation neglecting all kinds of mechanical shift assuming $\omega = \Omega_m$ in Eq. (2.7.14).

From Eq. (2.7.24), we see that the optical damping Γ_{opt} depends directly on the drive signal amplitude $|\tilde{\alpha}_{in}|$ (i.e. injected power P_{in}) and the detuning Δ .

The problem is solved numerically in order to find self-consistently a stable solution B to Eq. (2.7.25) for any couple (δ, P_{in}) , δ being the detuning of the pump signal from the optimal setting, $\Delta = \Omega_m + \delta$. Graphically, these stability points correspond to the intersection between the function $\Gamma_{opt}(B)/\Gamma_m + 1$ and the X-axis. This is illustrated in Fig. (2.7) for an expansion at second order $N = 2$, using values of g_1 and g_2 from the experimental Chapter 8. For small δ , the curves are always monotonous. At low power P_{in} there is no solution since $\Gamma_{opt}(B)/\Gamma_m + 1 > 0$ (orange line in Fig. 2.7). Increasing the power brings eventually the curve below the X-axis, creating a single intersection $\Gamma_{opt}(B)/\Gamma_m + 1 = 0$ (green circle on the red curve). For large positive δ , there is a range at

FIGURE 2.7 – Stability curves $\Gamma_{opt}/\Gamma_m + 1$ computed for $N = 2$ as a function of $(2g_0/\Omega_m) \times B$. These theoretical estimates are performed using the drumhead device parameters from Chapter 8 (see caption Fig. 2.8) for three different couples (δ, P_{in}) with $g_1 = +10^{-7}g_0$ and $g_2 = -10^{-13}g_0$. We show here the typical observed behaviors for this function: unstable (orange line), one stable state (red line) and unstable (blue circle) plus stable states highlighting hysteresis (magenta line). The self-consistent value of B corresponds to the (light and dark) green circles, see text.

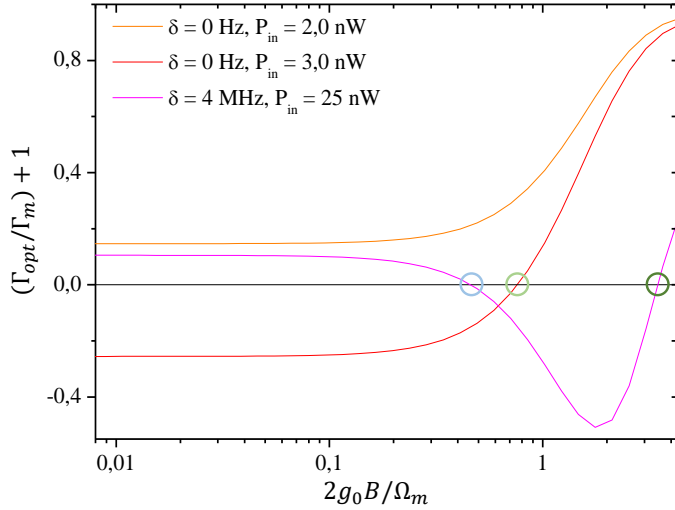
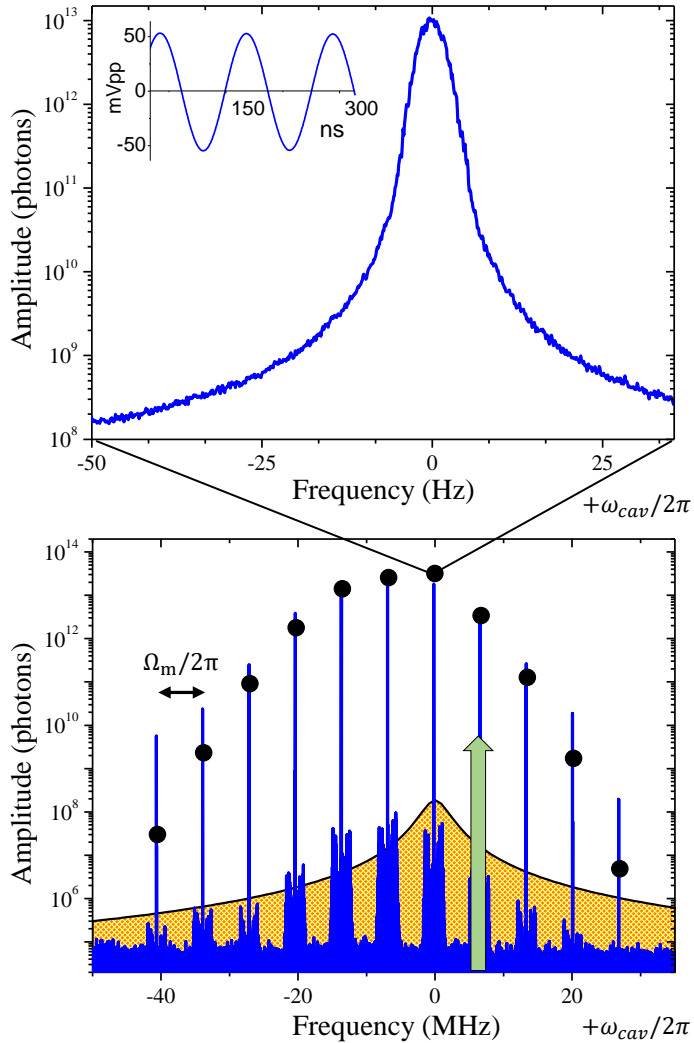


FIGURE 2.8 – Main top: Power spectral density (PSD) of the Stokes peak (i.e. at the cavity frequency ω_{cav}) measured in the self-sustained oscillation regime with a "badly-coupled" drumhead type device ($\Omega_m/2\pi \approx 6.7$ MHz, $\Gamma_m/2\pi \approx 150$ Hz at 50 mK, $g_0/2\pi \approx 10$ Hz, $\omega_{cav}/2\pi \approx 6.8$ GHz, $\kappa/2\pi \approx 4$ MHz, $\kappa_{ex}/2\pi \approx 2$ MHz, see Chapter 8) at 214 mK (blue-detuned pump power $P_{in} = 6$ nW and $\Delta = +\Omega_m$). The peak is not Lorentzian and its shape is defined by the phase noise present in the circuit. Inset: Time domain measurement of the coherent signal (raw data units). Bottom: PSD measurement of the comb produced by the strong applied power in same conditions (green arrow at drive frequency $(\omega_{cav} + \Omega_m)/2\pi$). The cavity resonance (orange area) is displayed with an arbitrary amplitude and its linewidth $\kappa/2\pi$ at scale. Black points are theoretical computation of the output amplitude of each measured peak [see Eq. (2.7.28)] for $N = 2$ with $g_1 = +10^{-7}g_0$ and $g_2 = -10^{-13}g_0$.



large P_{in} where the curve displays two intersections (magenta line in Fig. 2.7). Concerning the low- B value one, the derivative in this point being negative, the state displays anti-damping: it is unstable. On the other hand, for the high- B solution the slope being positive, the state is stable (dark green circle). However, this state has not been created by a smooth crossing of the X-axis from the whole curve, starting at the lowest $B \approx 0$: this means that it can be triggered only if one comes already from a high amplitude state and not from low- B ones (i.e Brownian motion regime). Such a stability function leads thus directly to a hysteretic behaviour in both δ and P_{in} . Moreover, due to the Bessel functions behaviour, higher amplitude B metastable states can appear, displaying more fancy hysteretic states (see Fig. 2.9).

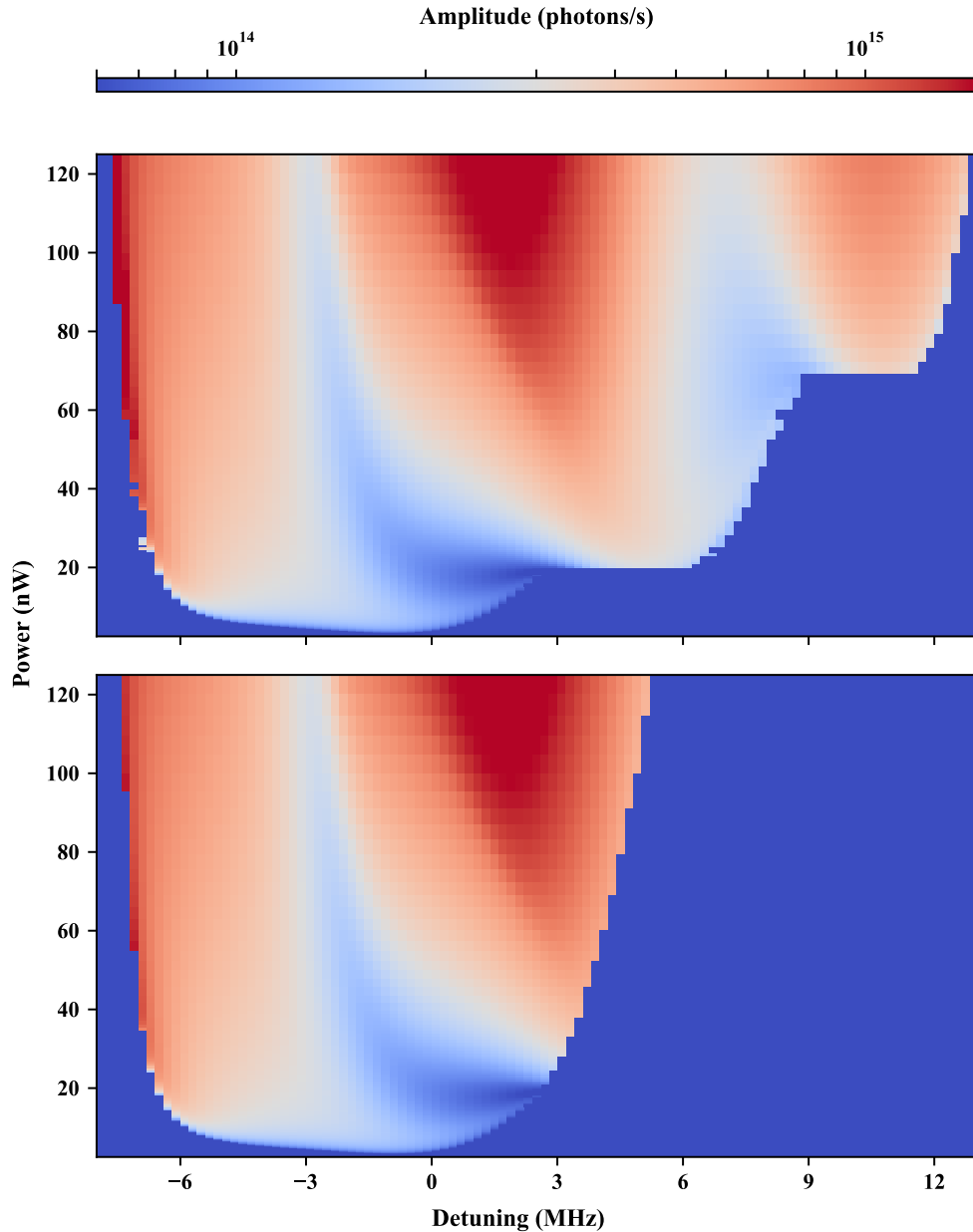


FIGURE 2.9 – Calculated colormaps of the output photon flux of the self-oscillating Stokes peak (at $\omega_{cav} + \delta$) as a function of both the input pump power P_{in} (applied at frequency $\omega_{cav} + \Omega_m + \delta$) and the detuning δ . The calculation is performed for $N = 2$ with the "badly-coupled" drumhead device parameters (see Fig.2.8) up-sweeping both P_{in} and δ (top) and down-sweeping (bottom). The top-right region (high power, high positive detuning) is bistable and exists only when entering from the self-oscillating state.

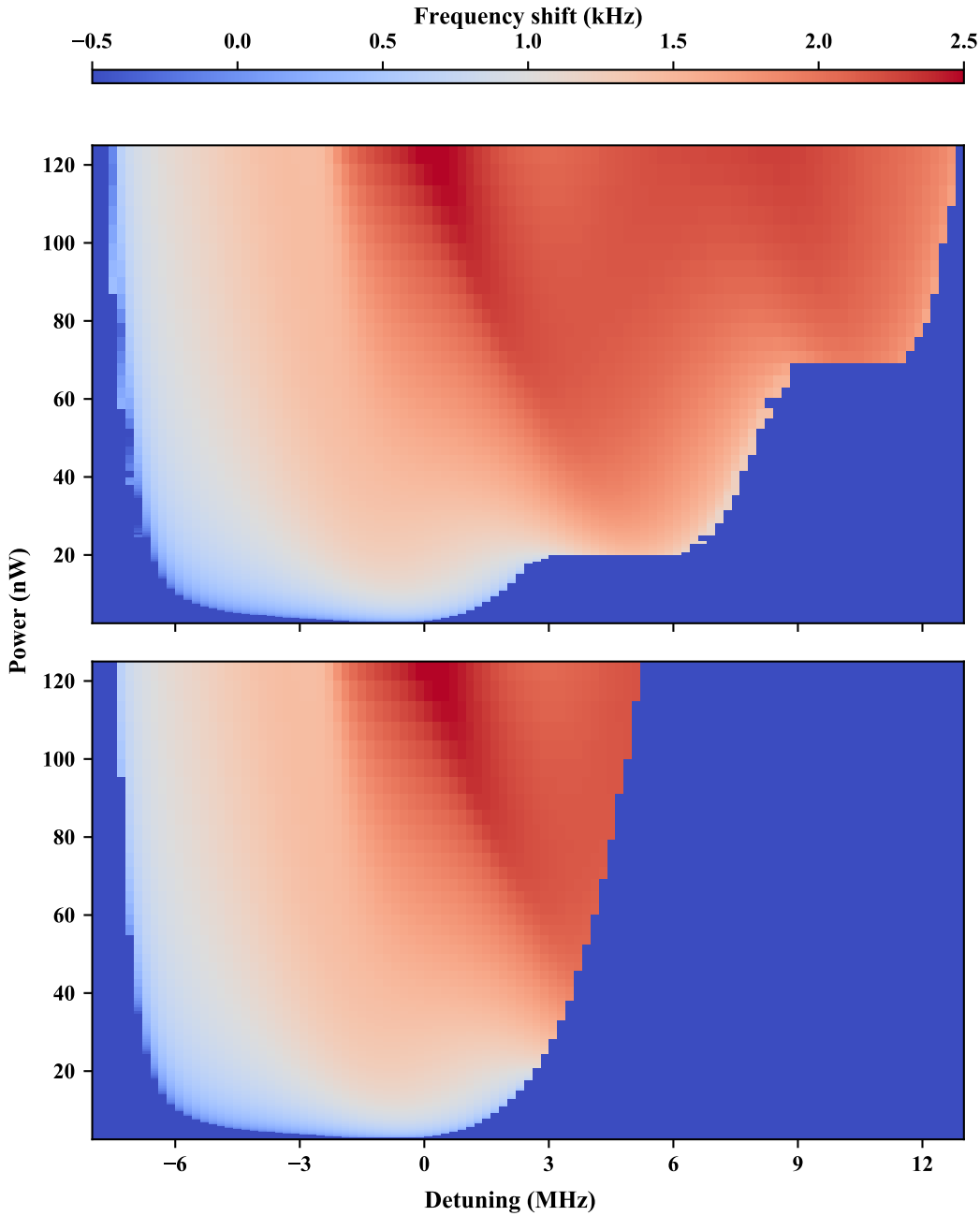


FIGURE 2.10 – Theoretical colormaps of the mechanical frequency shift of the self-oscillating Stokes peak (at $\omega_{cav} + \delta$) as a function of both the input pump power P_{in} (at frequency $\omega_{cav} + \Omega_m + \delta$) and the detuning δ . The calculation is performed in the same conditions as Fig. 2.9 with $3\beta_m \approx 2.1 \times 10^{-9}$ Hz up-sweeping space parameters (top) and down-sweeping space parameters (bottom).

OUTPUT AMPLITUDE OF THE COMB STRUCTURE Following the same procedure as for $\tilde{\alpha}$, the optical field amplitude in the cavity writes:

$$\alpha = \sum_{n \in \mathbb{Z}} \alpha_n e^{in\omega t}, \quad (2.7.26)$$

with:

$$\alpha_n = - \sum_{q \in \mathbb{Z}} \sqrt{\kappa_{ex}} \tilde{\alpha}_{in} \frac{f_q f_{q-n}}{h_q} e^{in\phi}. \quad (2.7.27)$$

This expression highlights the fact that the optomechanical coupling imprints a comb structure in the photon field (see Fig. 2.8 at $\delta = 0$). We can then compute the amplitude of the output photon flux $\dot{N}_{out,n}$ of each comb peak n as (see Fig. 2.9 for $n = -1$ as a function of δ and P_{in}):

$$\dot{N}_{out,n} = \kappa_{ex} |\alpha_n|^2, \quad (2.7.28)$$

where we make use of the well known input-output relation [see Eq. (2.3.21)] linking the intra-cavity fields to the output travelling fields. For instance, $n = 0$ corresponds to the pump tone at frequency $\omega_{cav} + \Omega_m$, $n = -1$ to the Stokes sideband at ω_{cav} and $n = 1$ to the anti-Stokes peak at $\omega_{cav} + 2\Omega_m$.

Note that the shape of the peaks (Fig. 2.8 top) is defined by the phase noise in the system; this is outside of the scope of this modeling since fluctuations have been neglected. Experimental details can be found in Chapter 8.

MECHANICAL DUFFING NONLINEARITY Since in the self-induced oscillation regime, the mechanical motion can be very large, the nonlinear stretching effect of the mechanical object has to be considered: this is the so-called Duffing nonlinearity (see Chapter 4), which shifts the mechanical resonance frequency by $3\beta_m B^2$ [see Eq. (2.2.5), the Duffing Hamiltonian $\hat{H}_{M,Duffing}$]. This term can be taken into account recursively in the calculation of the stable states (see discussion in Chapter 8), but the result is that it has only a marginal impact on the self-oscillating state definition. This is why it has been neglected in this Section, when calculating the dynamics. However, it dominates the mechanical frequency shift over all terms and in particular over the optical spring one $\delta\Omega_m$. One can thus fit the Duffing coefficient β_m on the data; besides, the frequency shift is thus an image of the mechanical motion amplitude B^2 , see Chapter 8.

The total mechanical frequency shift writes: $\Omega'_m = \Omega_m + \delta\Omega_m + 3\beta_m B^2$. For simplicity, we shall omit the prime on Ω_m in the experimental Chapter, reminding that the measured frequency shift includes all terms. In Fig. 2.10 we present the calculated total frequency shift for the same device as for Fig. 2.9, in the same parameter space (δ, P_{in}) . We refer to Chapter 8 for more experimental details.

2.8 CONCLUSION

In this chapter of the manuscript, we developed the basic quantum theory of generic cavity optomechanical systems modeled by one mechanical mode coupled to a single optical one. Each sub-system has been represented by a single harmonic oscillator coupled to an external heat bath himself modeled by a continuum of harmonic oscillators. We based all derivations on the usual quantum optics formalism, using the well-known input-output theory developed in the context of open quantum systems. In this framework, we presented the standard single-tone schemes used in optomechanics, the so-called phase-resolved weak continuous measurements [49]. We derived the theoretical spectra as well as the well-known optomechanical phenomena describing dynamical backaction and the radiation pressure force. The theoretical form of both optical and mechanical spectra indeed captures the relevant phenomena, and their knowledge is necessary for quantitative fits of the experimental data obtained within the single-pump protocols: Anti-Stokes "red-sideband" pumping, Stokes "blue-sideband" and the in-cavity "green" scheme (Chapter 7). Besides, the expressions obtained can be expanded into the classical limit, and compared

to the fully classical electric approach of Chapter 3. These constitute extremely useful grounds to understand what signatures are really quantum, or not.

We explored the optomechanical dynamics beyond the threshold of the parametric instability, in the so-called mechanical self-induced oscillation regime. In this high-amplitude mechanical motion state, the dynamics can be accurately described within the semi-classical approach, neglecting all fluctuations. It appears to be very sensitive to nonlinearities, especially nonlinearities in the coupling term which are today a subject of interest within the framework of quantum non-demolition measurements (QND). Our modeling and the use of the self-oscillating state can indeed be viewed as a new resource enabling to fit experimentally the nonlinearities of the system (see Chapter 8).

As a matter of fact, this theoretical work could be extended to more recent (and more complex) schemes that have been proposed, together with QND and other quantum protocols, to enrich the optomechanics toolbox. With two microwave tones applied at the same time, it is for instance possible to devise back-action evading schemes (BAE) [98, 63, 25]. Again, the quantum description of this Chapter could be compared to the classical model derived in Chapter 3. Especially, beyond the back-action noise evading aspect, a new type of parametric instability emerges [99].

2.9 RÉSUMÉ EN FRANÇAIS

Nous avons dédié cette partie du manuscrit au développement de la théorie quantique des systèmes optomécaniques génériques modélisés par un unique mode mécanique couplé à un mode optique. Chaque sous-système a été représenté par un unique oscillateur harmonique couplé à son bain extérieur, lui-même décrit comme un continuum d'oscillateurs harmoniques. Nous avons exploité le formalisme de l'optique quantique en utilisant la théorie entrée-sortie dans le contexte des systèmes quantiques ouverts. Avec ces bases théoriques, nous avons présenté le pompage standard simple ton utilisé en optomécanique; cette méthode est aussi connue sous le nom de mesure résolue en phase faible et continue [49]. Nous avons ainsi calculé la forme mathématique des spectres, ainsi que décrit les principaux phénomènes optomécaniques caractérisés par l'action en retour dynamique et la pression de radiation. Les expressions théoriques des spectres optiques et mécaniques capturent tous deux les phénomènes optomécaniques pertinents, et leur connaissance est indispensable pour effectuer des comparaisons quantitatives avec les données expérimentales obtenues lors de la mise en oeuvre des protocoles standards: pompage Anti-Stokes "bande latérale rouge", pompage Stokes "bande latérale bleue" et pompage en cavité "protocole vert" (voir Chapitre 7). En outre, les expressions obtenues peuvent être simplifiées en considérant la limite classique, et être comparées avec l'approche complètement classique basée sur la théorie des circuits électriques développée au Chapitre 3. Ceci étant très utile pour distinguer ce qui est de nature quantique de ce qui ne l'est pas.

Nous nous sommes également penchés sur la dynamique des systèmes optomécaniques au-delà de l'instabilité paramétrique, lorsque le système évolue dans le régime d'auto-oscillation. Dans cet état de forte amplitude mécanique, la dynamique peut être précisément capturée grâce à une approche semi-classique, en négligeant toutes fluctuations. Ce régime particulier apparaît très sensible aux nonlinéarités, et notamment aux nonlinéarités de couplage optomécanique qui suscitent aujourd'hui un grand intérêt dans le domaine des mesures QND (mesure quantique sans destruction). Notre approche théorique

ainsi que l'utilisation d'états auto-oscillants peuvent en effet être perçus comme une nouvelle ressource permettant de mesurer les nonlinéarités du système (voir Chapitre 8).

Enfin, ce travail théorique pourrait très bien être appliqué aux protocoles proposés plus récemment (de fait plus complexes), conjointement avec les mesures QND ainsi que d'autres protocoles quantiques dans le but d'enrichir la boîte à outils utilisée en optomécanique. Lorsque deux tons micro-ondes sont appliqués simultanément, il est par exemple possible d'envisager des protocoles BAE (échappant l'action en retour) [98, 63, 25]. De nouveau, la description quantique effectuée basée sur ce Chapitre pourrait être comparée au modèle classique détaillé dans le Chapitre 3. Plus spécifiquement, au delà de l'aspect BAE, un nouveau type d'instabilité paramétrique apparaît [99].

3

CLASSICAL ELECTRIC CIRCUIT ANALOGUE

In this chapter we report on the generic classical electric circuit modeling that describes standard single-tone microwave optomechanics. Based on a parallel RLC circuit in which a mechanical oscillator acts as a movable capacitor, derivations of analytical expressions are presented, including key features such as the back-action force, the input-output expressions, and the spectral densities associated, all in the classical regime. These expressions coincide with the standard quantum treatment performed in optomechanics when the occupation number of both cavity and mechanical oscillator are large (see Chapter 2). Besides, the derived analytics transposes optics into electronics terms, which is mandatory for quantitative measurement and design purposes. Finally, the direct comparison between the standard quantum treatment and the classical model addresses the bounds between quantum and classical regimes, highlighting the features which are truly quantum, and those which are not. This work is presented in Ref. [222].

CONTENTS

3.1	Modeling of the classical electric analogue	73
3.1.1	Generic microwave optomechanical circuit	73
3.1.2	Electrical dynamics equation	76
3.1.3	Solving the dynamics equation	78
3.1.4	Classical back-action of cavity onto mechanics	80
3.1.5	Spectral properties and input-output relationships	82
3.2	Classical versus Quantum	86
3.2.1	Planck's postulate	86
3.2.2	Sideband Assymetry	88
	"Blue" pumping	89
	"Red" pumping	89
	"Green" pumping	89
3.2.3	Heisenberg limit	90
	"Green" pumping	91
	"Blue" pumping	93
3.3	Conclusion	94
3.4	Résumé en français	94

3.1 MODELING OF THE CLASSICAL ELECTRIC ANALOGUE

3.1.1 Generic microwave optomechanical circuit

In the electromechanical version of optomechanics, the mechanical element of the circuit is a movable capacitor which is part of an RLC resonator. A schematic comparison is shown in Fig. 3.1 in the reflection mode. The input laser is replaced by the microwave signal (orange), entering the optical cavity (green) through a semi-reflecting mirror for the former (blue), and the RLC resonator (green) through a capacitor C_c for the latter (blue). The movable element (grey) modulates the resonance frequency ω_{cav} of the optical/microwave mode considered at a frequency Ω_m . Part of the confined energy eventually leaks out at a rate κ_{ex} , back to the input (green sinusoidal arrow).

In practice, this resonant circuit can be realized in many ways: a quarter-wave coplanar waveguide (CPW) element [54], a microfabricated superconducting inductor-capacitor meander [111], or even a parallel plate capacitor shunted by a spiral inductor [112]. Any resonator can be described by equivalent lumped RLC elements near a resonance; see e.g. Ref. [142] for the case of CPW resonators, providing analytic expressions. For complex geometries however, finite element analysis is required (like e.g. in Ref. [223]); see Chapter 4. In most experiments, the coupling to the outside is capacitive [54, 111, 112, 142, 223]: the resonator is almost isolated from the outside world, while the electromagnetic field from input/output waveguides is allowed to "leak in-and-out" through weakly coupled ports. This defines the microwave cavity element, in which the motion $x(t)$ of the mechanical object modulates the effective capacitance C .

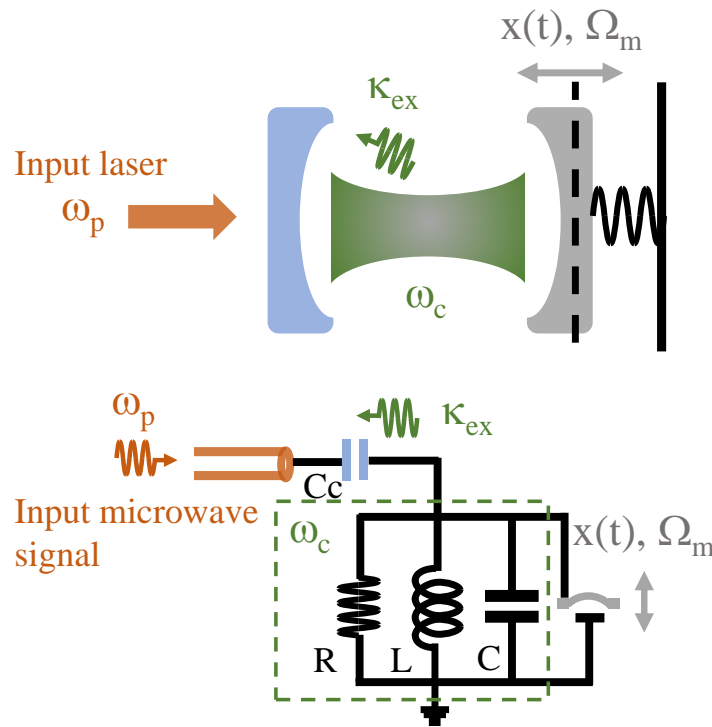


FIGURE 3.1 – Schematic diagram comparing a generic optomechanical system (top) and an electrical RLC circuit (bottom). See text for the color code.

In Fig. 3.2 we thus show the three standard microwave setups. The top one is a two-port scheme, in which a lumped RLC parallel circuit couples to distinct input and output ports through different capacitors C_{c1} and C_{c2} , yielding effective coupling rates κ_1 and κ_2 respectively; they quantify how energy decays over time from the resonator to each port [109, 53]. The total coupling rate to the outside is thus defined as $\kappa_{ex} = \kappa_1 + \kappa_2$. The internal damping rate of the circuit is modeled through R_{in} , leading to a κ_{in} decay rate (measuring the decay toward internal degrees of freedom). The total decay rate of the microwave mode is then $\kappa = \kappa_{ex} + \kappa_{in}$. The ports are realized by coaxial cables of characteristic impedance Z_0 connected to adapted elements, i.e. the outside impedance seen from the port is also Z_0 (see Fig. 3.2 top input and output): the voltage source $V_{rf}(t) = V_p \cos(\omega_p t)$ on the left has an output load of Z_0 , while the detection of the V_{out} voltage on the right is realized by an amplifier of input load Z_0 as well. ω_p is the (angular) microwave drive frequency, while V_p is the applied amplitude. In Fig. 3.2 center we show the electric schematic of a bi-directional coupling: the RLC resonator

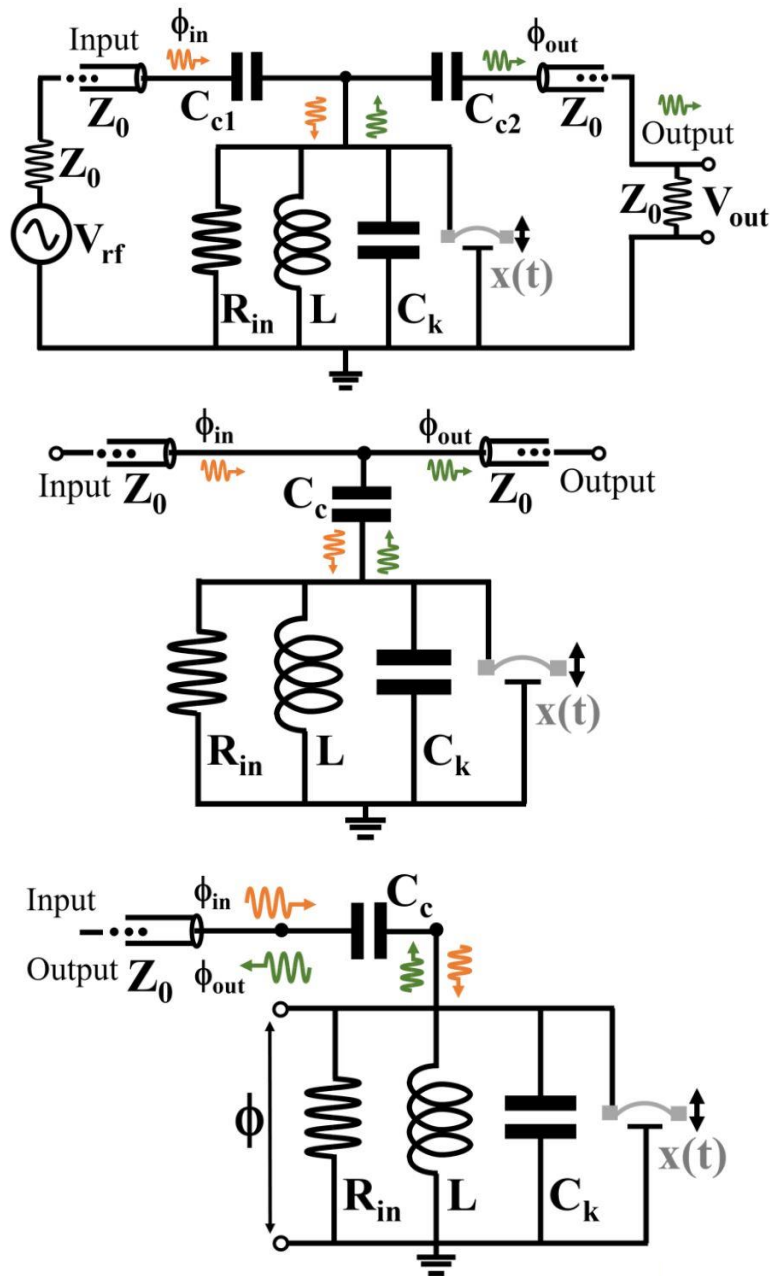


FIGURE 3.2 – The three equivalent electric circuits for microwave optomechanics with different input and output designs. In each, a mechanical element $x(t)$ capacitively couples to a parallel RLC circuit. Top is two-port, center is bi-directional and bottom is single-port (reflection design, a specific component is then required to separate incoming and outgoing waves). The defined electric elements are discussed in the text, and the outside world, as seen from the circuit, is depicted only in the top two-port scheme.

couples evanescently to a nearby transmission line with an effective capacitance C_c [111, 223, 202]. This is strictly equivalent to the two-port scheme (Fig. 3.2 top) when imposing $C_{c1} = C_{c2} = C_c/2$ (and thus $\kappa_2 = \kappa_1 = \kappa_{ex}/2$). At last, the third scheme is shown in Fig. 3.2 bottom. Only one port is connected to the device, requiring thus the use of a specific nonreciprocal component (e.g. like a circulator) to separate the drive signal from the response (reflection mode) [87]. This is again equivalent to the two-port scheme with

$C_{c1} = C_c$ and no C_{c2} (i.e. $\kappa_2 = 0, \kappa_{ex} = \kappa_1$). The problem at hand is solved below in terms of generalized fluxes [26]:

$$\phi(t) = \int_0^t V(t') dt'. \quad (3.1.1)$$

The dynamics equation will be written for the ϕ corresponding to the RLC node, see Fig. 3.2 bottom. Incoming and outgoing traveling waves (equivalent to the laser signals in conventional optomechanics) are thus defined as ϕ_{in} (the tone pump, orange) and ϕ_{out} (the response, green) in Fig. 3.2 [222].

3.1.2 Electrical dynamics equation

We shall consider in the following a single port configuration (Fig. 3.2 bottom), the extension to the other models being straightforward from what has been said above (the two-port scheme with $C_{c1} = C_{c2} = C_c/2$ gives equivalent results to the bi-directional one). We shall discuss the correspondence between schemes at the end of the Section.

The circuits shown in Fig. 3.2 are a combination of transmission lines (the coaxial cables) and lumped elements (RLC , Z_0 impedances, and source). The first step of the modeling is thus to get rid of the coaxial elements, in order to model an ideal lumped circuit. To start with, we consider the source V_{rf} which generates the incoming wave ϕ_{in} . In the two-port (top) and single port (bottom) schemes of Fig. 3.2, the drive port is terminated by an (almost) open circuit since the coupling capacitance is very small ($C_c \omega Z_0 \ll 1$). The incoming wave is thus almost fully reflected, and the standing wave voltage on the input capacitor is $V_d \approx 2V_{rf}$ [232]. On the other hand for the bi-directional scheme (center), the transmission line is almost unperturbed by the coupling element C_c , and the incoming wave travels toward the output port (almost) preserving its magnitude; on the coupling capacitor we have $V_d \approx V_{rf}$.

Applying Norton's theorem, we transform the series voltage source input circuit into a parallel RC , which drives a total current I_d across it. This is shown in Fig. 3.3 top, with finally the total loaded RLC resonator in Fig. 3.3 bottom. The effective components of the Norton drive circuit are defined from the real and imaginary parts of the complex admittance:

$$Y_c[\omega] = \frac{iC_c\omega}{1 + iC_c\omega Z_0}, \quad (3.1.2)$$

in the weak coupling limit ($C_c \omega Z_0 \ll 1$):

$$\Re(Y_c[\omega]) = \frac{1}{R_{ex}} \approx (C_c \omega_{cav})^2 Z_0, \quad (3.1.3)$$

$$\Im(Y_c[\omega]) \approx iC_c \omega_{cav}, \quad (3.1.4)$$

with the approximation $\omega \approx \omega_{cav}$.

The current I_d flowing into the resonator then writes:

$$I_d \approx iC_c \omega_{cav} V_d. \quad (3.1.5)$$

The detected voltage is calculated from the current flowing through the amplifier's impedance Z_0 . For circuits Fig. 3.3 top and bottom, this simply leads to:

$$V_{out} \approx -\omega_{cav}^2 C_c Z_0 \phi, \quad (3.1.6)$$

assuming again $\omega \approx \omega_{cav}$ (we do not report here the contribution from the incoming wave that eventually travels to the amplifier). For the bi-directional circuit, the evanescent coupling leads to a loading composed of two impedances Z_0 in parallel (half of the signal is fed back to the voltage source):

$$V_{out} \approx -\omega_{cav}^2 C_c \frac{Z_0}{2} \phi. \quad (3.1.7)$$

From our definitions of κ_{ex} , the subtlety of these different writings shall obviously be accounted for in our final expressions (see discussion of Section 3.1.5).

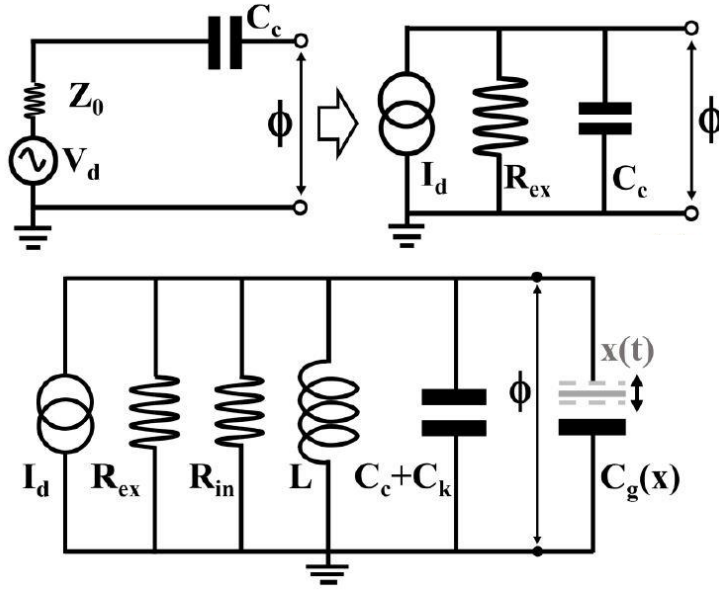


FIGURE 3.3 – Top: Circuit schematics converting the series voltage source V_d (impedance Z_0) that loads the capacitor C_c into a parallel current source I_d ; the equivalent resistance R_{ex} is defined from Z_0 and C_c (see text). Bottom: Equivalent parallel RLC circuit with current source for the one-port optomechanical circuit (replacing Fig. 3.2 bottom). The mechanical contribution to the capacitance is explicitly defined as $C_g(x)$.

From Kirchhoff's circuit laws, the classical dynamics equation that describes this problem writes:

$$I_d + I_{noise} = \frac{1}{L} \phi + \left(\frac{1}{R_{ex}} + \frac{1}{R_{in}} \right) \frac{d\phi}{dt} + \frac{d}{dt} \left[(C_c + C_k + C_g(x)) \frac{d\phi}{dt} \right]. \quad (3.1.8)$$

In Eq. (3.1.8), the fraction of the capacitance modulated by the mechanics is defined as $C_g(x)$ [see Fig. 3.3 bottom]. the Johnson-Nyquist electric noise (at temperature T_c) seen by the cavity is modeled as a source I_{noise} , in parallel with the imposed drive circuit generating I_d [26].

In the following, we will consider small motion. We therefore write:

$$C_g(x) \approx C_g(0) + x(t) \frac{dC_g(0)}{dx}, \quad (3.1.9)$$

defining the total (static) capacitance $C_{tot} = C_c + C_k + C_g(0)$. $C_g(0)$ corresponds to the contribution of the mobile element when at rest, while C_c comes from the slight leakage

of the cavity mode into the coaxial lines. The rates are then defined from the electronic components:

$$\kappa_{ex} = \frac{1}{R_{ex}C_{tot}}, \quad (3.1.10)$$

$$\kappa_{in} = \frac{1}{R_{in}C_{tot}}. \quad (3.1.11)$$

In the two-port case, one simply defines R_1 and R_2 leading to $1/R_{ex} = 1/R_1 + 1/R_2$, and similarly $1/R_{tot} = 1/R_{ex} + 1/R_{in}$; we write the corresponding quality factors $Q_i = \omega_{cav}/\kappa_i$ (with $i = in, ex$ or blank). Besides, the microwave resonance of the loaded RLC circuit is given by $\omega_{cav} = 1/\sqrt{LC_{tot}}$.

Introducing as usual the coupling strength:

$$G = -\frac{d\omega_{cav}}{dx} = -\frac{d\omega_{cav}}{dC_g} \frac{dC_g}{dx}, \quad (3.1.12)$$

Eq. (3.1.8) can be re-written in the more compact form:

$$\frac{I_d + I_{noise}}{C_{tot}} = \omega_c^2 \phi + \left(\kappa + \frac{2G}{\omega_c} \dot{x} \right) \dot{\phi} + \left(1 + \frac{2G}{\omega_c} x \right) \ddot{\phi}, \quad (3.1.13)$$

which we will now solve.

3.1.3 Solving the dynamics equation

The drive current writes:

$$I_d(t) = \frac{1}{2} \left(I_p e^{-i\omega_p t} + I_p^* e^{+i\omega_p t} \right), \quad (3.1.14)$$

with ω_p the frequency at which the microwave pumping is applied and I_p its (complex) amplitude. From Eq. (3.1.5), I_p is derived from the input voltage drive amplitude V_p . Note that impedances are expressed in the standard electronics language assuming $A_0 e^{+i\omega t}$ time dependencies. The writing should be adapted for full $A_0 e^{-i\omega t} + c.c.$ expressions. The mechanical displacement is written as:

$$x(t) = \frac{1}{2} \left(x_0(t) e^{-i\Omega_m t} + x_0^*(t) e^{+i\Omega_m t} \right), \quad (3.1.15)$$

with $x_0(t)$ the (complex) motion amplitude translated in frequency around Ω_m , the mechanical resonance frequency of the movable element. This amplitude is a stochastic variable: the Brownian motion of the moving element thermalized at temperature T_m (see Chapter 2).

The terms where motion $x(t)$ multiplies flux $\phi(t)$ in Eq. (3.1.13) then generate harmonics at $\omega_n = \omega_p + n\Omega_m$, with $n \in \mathbb{Z}$: this phenomenon is known as nonlinear mixing.

We can thus find an exact solution using the ansatz:

$$\phi(t) = \sum_{n \in \mathbb{Z}} \phi_n(t) = \frac{1}{2} \sum_{n \in \mathbb{Z}} \left[\mu_n(t) e^{-i\omega_n t} + \mu_n^*(t) e^{+i\omega_n t} \right], \quad (3.1.16)$$

which, when injected in Eq. (3.1.13) generates a system of coupled equations for the μ_n (complex) amplitudes. In order to match the decomposition, the white noise component is thus naturally written as:

$$I_{noise} = \frac{1}{2} \sum_{n \in \mathbb{Z}} \left[\delta I_n(t) e^{-i\omega_n t} + \delta I_n^*(t) e^{+i\omega_n t} \right], \quad (3.1.17)$$

with $\delta I_n(t)$ the (complex) amplitude translated at frequency ω_n .

Injecting Eqs. (3.1.14, 3.1.17, 3.1.16) in Eq. (3.1.13), we obtain for all amplitudes $\phi_n(t)$ the harmonic form:

$$\begin{aligned} \frac{\delta_{n,0} I_p + \delta I_n(t)}{C_{tot}} &= (\omega_{cav}^2 - \omega_n^2 - i\kappa\omega_n) \phi_n(t) \\ &+ \frac{G}{\omega_{cav}} \left[-x_0(t) \Omega_m \omega_{n-1} \phi_{n-1}(t) + x_0^*(t) \Omega_m \omega_{n+1} \phi_{n+1}(t) \right. \\ &\quad \left. - x_0(t) \omega_{n-1}^2 \phi_{n-1}(t) - x_0^*(t) \omega_{n+1}^2 \phi_{n+1}(t) \right], \end{aligned} \quad (3.1.18)$$

which represent the optical comb produced with all amplitudes imbricated, identical to the solution of the self-oscillation calculation made in Chapter 2.

In practice, we are interested only in schemes where $\Delta = \omega_p - \omega_{cav} \approx 0$, $+\Omega_m$ and $-\Omega_m$. The resonant feature brought in by the *RLC* element implies that only the spectral terms the closest to ω_{cav} in Eq. (3.1.16) will be relevant when $\kappa \ll \Omega_m$; this is known as the resolved sideband limit (see Chapter 2). From the full comb Eq. (3.1.18) which is directly the electric analogue of the optical formalism of Chapter 2, we thus keep only $n = -1, 0, +1$ which correspond respectively to the lower sideband (or Stokes), to the pump tone and to the upper sideband (anti-Stokes). Considering $\Omega_m \ll \omega_{cav}$, we also justify the assumption $\omega \approx \omega_{cav}$ used in Eqs. (3.1.3 - 3.1.7).

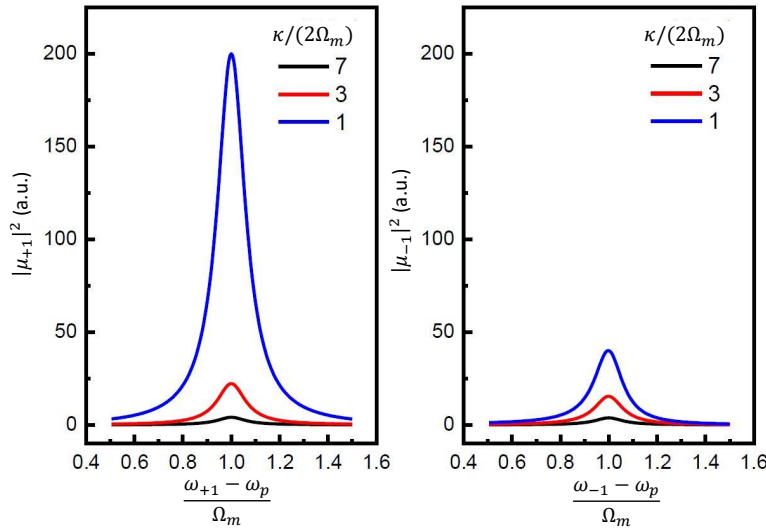


FIGURE 3.4 – Schematic frequency dependence of the μ_{-1} (right) and μ_{+1} (left) components, under "blue" sideband pumping. Each curve corresponds to a different ratio of $\kappa/(2\Omega_m)$ (see legend: not in the sideband resolved limit), in the small μ_0 drive limit (see text).

Eq. (3.1.13) is solved by mimicking a rotating wave approximation (see Chapter 2). For our classical treatment, it simply means that we are concerned by the dynamics of each

component of Eq. (3.1.16) only around its main frequency ω_n (what is called a rotating frame, as opposed to the laboratory frame for the full signal), assuming time-variations of x and Φ_n to be slow (valid for high- Q microwave and mechanical resonances). Reminding $\omega_{-1} \approx \omega_0 \approx \omega_1 \approx \omega_{cav}$, the flux amplitudes inside the cavity acting on the mechanical oscillator are:

$$\mu_0(t) = \frac{i I_p + \delta I_0(t)}{2 C_{tot} \omega_{cav}} \chi_c[0] \quad \text{for the pump,} \quad (3.1.19)$$

$$\mu_{-1}(t) = \frac{i}{2} \left(G x_0^*(t) \mu_0(t) + \frac{\delta I_{-1}(t)}{C_{tot} \omega_{cav}} \right) \chi_c[-\Omega_m] \quad \text{for the Stokes,} \quad (3.1.20)$$

$$\mu_{+1}(t) = \frac{i}{2} \left(G x_0(t) \mu_0(t) + \frac{\delta I_{+1}(t)}{C_{tot} \omega_{cav}} \right) \chi_c[+\Omega_m] \quad \text{for the anti-Stokes,} \quad (3.1.21)$$

with $\chi_c[\omega]$ defined as usual:

$$\chi_c[\omega] = \frac{1}{\frac{\kappa}{2} - i(\Delta + \omega)}, \quad (3.1.22)$$

the cavity susceptibility. We did not write conjugate expressions for simplicity.

When $\Delta \approx 0$, the pump tone for $n = 0$ is resonant with the cavity; the scheme is symmetric and the two $n = -1$ and $n = +1$ amplitudes are equivalent. We choose to call this the "green" pumping scheme in the following as in Chapter 2. When $\Delta \approx -\Omega_m$, the $n = +1$ component is resonant with the cavity and the $n = -1$ one is greatly suppressed. This is known as the "red" side-band pumping scheme. When $\Delta \approx +\Omega_m$, the situation is reversed and $n = -1$ is resonant with the cavity and $n = +1$ suppressed. This is the "blue" scheme. All schemes are explicitly schematized in Fig. 2.4.

The two satellite signals μ_{+1} and μ_{-1} at frequencies $\omega_p \pm \Omega_m$ generated by the pump tone μ_0 are schematized in Fig. 3.4 for an arbitrary Brownian noise x , in the small drive limit. They correspond to energy up-converted from the pump $n = 0$ (for $n = +1$), or down-converted (for $n = -1$). When the drive μ_0 (i.e. I_p or V_p) becomes large enough, back-action of the cavity onto the mechanical element has to be taken into account. This is derived in the next Section.

3.1.4 Classical back-action of cavity onto mechanics

The voltage bias on the mechanical element is responsible for a force F_{BA} , defined as the gradient of the electromagnetic energy:

$$F_{BA}(t) = + \frac{d}{dx} \left[\frac{1}{2} C_{tot} \left(\frac{d\phi(t)}{dt} \right)^2 \right], \quad (3.1.23)$$

using our notations (see Fig. 3.3). This is the so-called back-action of the cavity onto the mechanical element. The sign definition corresponds to the fixed electrode acting upon the mobile part. We are interested only in the component of this force that can drive the mechanics; we therefore define:

$$F_{BA}(t) = \frac{1}{2} \left(F_{BA,0}(t) e^{-i\Omega_m t} + F_{BA,0}^*(t) e^{+i\Omega_m t} \right), \quad (3.1.24)$$

with $F_{BA,0}(t)$ the (complex) force amplitude acting in the frame rotating at the mechanical frequency Ω_m . Re-writing ϕ in terms of the defined flux amplitudes, and keeping only the lowest order for the spatial derivative (small motion limit), we get:

$$F_{BA,0}(t) \approx C_{tot}\omega_{cav}G[\mu_0(t)\mu_{-1}^*(t) + \mu_0^*(t)\mu_{+1}(t)]. \quad (3.1.25)$$

From Eqs. (3.1.19-3.1.21), we immediately see that $F_0(t)$ will depend on both the motion amplitude $x_0(t)$ and the current noise components of the cavity $\delta I_n(t)$. Eq. (3.1.25) is thus recasted in:

$$F_{BA,0}(t) \approx -\Sigma[\Omega_m]x_0(t) + i\frac{G}{2}\left[\delta I_{+1}(t)\mu_0^*\chi_c[+\Omega_m] - \delta I_{-1}^*(t)\mu_0\chi_c^*[-\Omega_m]\right], \quad (3.1.26)$$

with the first term the so-called dynamic component (proportional to x_0), and the last term the stochastic component that is fed back from the cavity onto the mechanical degree of freedom. In Eq. (3.1.26), the term δI_0 has been dropped at lowest order and:

$$\mu_0 \approx \frac{i}{2}\frac{I_p}{C_{tot}\omega_{cav}}\chi_c[0] \quad (3.1.27)$$

is now time-independent; only the noise current at the two sidebands is relevant. We introduced the optical "self-energy" Σ [136] already discussed in Chapter 2 defined here in terms of electrical variables:

$$\Sigma[\omega] = -i\frac{G^2}{2}C_{tot}\omega_{cav}|\mu_0|^2\left[\chi_c[\omega] - \chi_c^*[-\omega]\right]. \quad (3.1.28)$$

The governing equation for the mechanical motion is expressed in the rotating frame as (neglecting again the slow dynamics):

$$-2i\dot{x}_0(t) - i\Gamma_m x_0(t) = \frac{F_{th,0}(t) + F_{BA,0}(t)}{m\Omega_m}, \quad (3.1.29)$$

with as usual Γ_m the mechanical damping rate, and $Q_m = \Omega_m/\Gamma_m$ the mechanical quality factor. m is the mass of the moving element. We write $F_{th}(t)$ the Langevin force (at temperature T_m), with $F_{th,0}(t)$ the component acting in the frame rotating at Ω_m . Injecting Eq. (3.1.26) into Eq. (3.1.29) and taking the Fourier transform, the solution can be written in the simple usual form:

$$x_0[\omega] = \chi_{m,eff}[\omega](F_{th,0}[\omega] + \delta F_{BA,0}[\omega]) \quad (3.1.30)$$

where we have defined:

$$\chi_{m,eff}[\omega] = \frac{1}{-2m\Omega_m\left(\omega + i\frac{\Gamma_m}{2}\right) + \Sigma[\omega]}, \quad (3.1.31)$$

$$\delta F_{BA,0}[\omega] = i\frac{G}{2}\left[\delta I_{+1}[\omega]\mu_0^*\chi_c[+\Omega_m] - \delta I_{-1}^*[\omega]\mu_0\chi_c^*[-\Omega_m]\right]. \quad (3.1.32)$$

Eq. (3.1.31) is the mechanical susceptibility of the moving element. The mechanical linear response is thus modified by the interaction with the microwave field through the term $\Sigma[\omega]$. Matching the expressions of Ref. [136], note the difference in the definition of susceptibilities between mechanical and optical fields: an i factor has been incorporated in

between. The last Eq. (3.1.32) corresponds to the stochastic component of the back-action: noise originating from the Johnson-Nyquist current that adds up with the Langevin force.

In the following Section we shall discuss the spectra associated to Eq. (3.1.30) with their specific properties. The link between injected power, Brownian motion and measured spectrum of the voltage V_{out} is finally presented.

3.1.5 Spectral properties and input-output relationships

Taking real and imaginary parts of Σ , we see from Eq. (3.1.31) that the optomechanical interaction is responsible for a frequency shift $\delta\Omega_m$ and an additional damping term Γ_{opt} , analogously to Eqs. (2.4.31) and (2.4.32) written with the quantum optics formalism, and we obtain:

$$\delta\Omega_m = G^2 \frac{C_{tot}\omega_c}{4m\Omega_m} |\mu_0|^2 \left[\frac{\Delta + \Omega_m}{(\Delta + \Omega_m)^2 + (\frac{\kappa}{2})^2} + \frac{\Delta - \Omega_m}{(\Delta - \Omega_m)^2 + (\frac{\kappa}{2})^2} \right], \quad (3.1.33)$$

$$\Gamma_{opt} = G^2 \frac{C_{tot}\omega_c}{4m\Omega_m} |\mu_0|^2 \left[\frac{\kappa}{(\Delta + \Omega_m)^2 + (\frac{\kappa}{2})^2} - \frac{\kappa}{(\Delta - \Omega_m)^2 + (\frac{\kappa}{2})^2} \right]. \quad (3.1.34)$$

The former expression above is referred to as the optical spring and the latter the optical damping effects (see Chapter 2). Physically, these effects originate in the radiation pressure exerted on the movable capacitor by the electromagnetic field confined inside it. The spectrum of the stochastic back-action term [Eq. (3.1.32)] writes:

$$S_{\delta F_{BA,0}}[\omega] = \frac{1}{4} G^2 R_{tot} C_{tot} |\mu_0|^2 \left[\frac{\kappa}{(\Delta + \Omega_m)^2 + (\frac{\kappa}{2})^2} + \frac{\kappa}{(\Delta - \Omega_m)^2 + (\frac{\kappa}{2})^2} \right] S_{\delta I_n}, \quad (3.1.35)$$

as a function of the white current noise spectrum $S_{\delta I_n} = S_{\delta I_{-1}}[\omega] = S_{\delta I_{+1}}[\omega]$, with $n = -1$ and $n = +1$ components uncorrelated; therefore $S_{\delta F_{BA,0}}$ is also white.

As a result, the displacement spectrum deduced from Eq. (3.1.30) is:

$$S_{x_0}[\omega] = \left| \chi_{m,eff}[\omega] \right|^2 [S_{F_{th,0}} + S_{\delta F_{BA,0}}], \quad (3.1.36)$$

with $S_{F_{th,0}}$ the white force spectrum associated to Brownian motion. This result is a Lorentzian peak with full-width $\Gamma_{eff} = \Gamma_m + \Gamma_{opt}$ and position $\delta\Omega_m$ (in the frame rotating at Ω_m); the total area is proportional to the total white noise force felt by the mechanics, namely $S_{\mathcal{F}_{th,0}} = S_{F_{th,0}} + S_{\delta F_{BA,0}}$. Equivalently, Eq. (3.1.36) writes with the original spectra in the laboratory frame:

$$S_x[\omega] = \left[\left| \chi_{m,eff}[\omega - \Omega_m] \right|^2 + \left| \chi_{m,eff}[\omega + \Omega_m] \right|^2 \right] S_{\mathcal{F}_{th}}, \quad (3.1.37)$$

defined for ω ranging from $-\infty$ to $+\infty$; the classical spectrum is even with two identical peaks $S_x^-[\omega]$ and $S_x^+[\omega]$ located at $\omega \approx \pm\Omega_m$. From the rotating wave transform, we have $S_{F_{th,0}}/4 = S_{F_{th}} = 2k_B m T_m \Gamma_m$ and $S_{\delta I_n}/4 = S_{I_{noise}} = 2k_B T_c / R_{tot}$ [136, 26]; by construction, each fluctuating current $\delta I_n(t)$ is defined over a bandwidth of order Ω_m (while I_{noise} covers \mathbb{R}). The stochastic force acting on the mechanics can thus be recasted in the simple form:

$$\frac{1}{4} S_{F_{th,0}} = S_{F_{th}} = 2k_B m \Gamma_{eff} T_{eff}, \quad (3.1.38)$$

with:

$$T_{eff} = \frac{T_m \Gamma_m + T_c \Gamma'_{opt}}{\Gamma_{eff}}, \quad (3.1.39)$$

$$\Gamma'_{opt} = G^2 \frac{C_{tot}}{4m} |\mu_0|^2 \left[\frac{\kappa}{(\Delta + \Omega_m)^2 + (\frac{\kappa}{2})^2} + \frac{\kappa}{(\Delta - \Omega_m)^2 + (\frac{\kappa}{2})^2} \right]. \quad (3.1.40)$$

The term T_{eff} in Eq. (3.1.38) is thus interpreted as an effective temperature for the mechanical mode, created by the combination of the force fluctuations around Ω_m (in the radio-frequency domain) and the current fluctuations around ω_c (in the microwave domain), both derived within the same physical framework: the fluctuation-dissipation theorem (see Chapter 2). Besides, we see that the magnitudes of optical spring, optical damping, and back-action noise are all governed by a single parameter:

$$g = G \sqrt{\frac{C_{tot} \omega_c |\mu_0|^2}{4m \Omega_m}}. \quad (3.1.41)$$

Replacing g in the above expressions, they are formally equivalent to the quantum optics results [136] (see Chapter 2); this fact shall be discussed in Section 3.2.

Depending on the scheme used, Eqs. (3.1.33) and (3.1.5) behave differently. When $\omega \approx +\Omega_m$, the second term in the brackets of these expressions dominate and $\delta\Omega_m \approx 4g^2(\Delta - \Omega_m)/\kappa^2$ and $\Gamma_{opt} \approx -4g^2/\kappa$ (resolved sideband limit). The optical damping is negative, therefore the mechanical response is enhanced (Γ_{eff} decreases and the mechanical Q factor grows), and the effective temperature T_{eff} is increased: energy is pumped into the mechanical mode, a mechanism called Stokes scattering in optics [135]. We adopt the language used in Chapter 2 and call this scheme the "blue" sideband pumping. When $\Gamma_{eff} = 0$ the system reaches an instability and starts to self-oscillate [136, 85, 197]. When $\omega \approx -\Omega_m$ the situation is reversed and $\delta\Omega_m \approx 4g^2(\Delta + \Omega_m)/\kappa^2$ and $\Gamma_{opt} \approx +4g^2/\kappa$. The optical damping is now positive, the mechanical response is damped (Γ_{eff} increases and the mechanical Q factor decreases) and the temperature T_{eff} is reduced: energy is pumped out of the mechanical mode, a mechanism called Anti-Stokes scattering in optics [135]. This scheme, known as sideband cooling is also referred to as "red" sideband pumping. At last, when $\Delta \approx 0$ the situation is symmetric: no energy is pumped in or out, and $\delta\Omega_m \approx 2g^2\Delta/\Omega_m^2$ and $\Gamma_{opt} \approx 0$. In order to distinguish it from the two other schemes, we named it "green" sideband pumping. Note that this scheme has the smallest back-action contribution; it is thus also referred to as the optimal scheme in optics [136] (see Chapter 2).

The final step of the modeling requires to link the input (the V_{rf} source) to the measured spectrum of the output voltage $S_{V_{out}[\omega]}$.

From Eq. (3.1.6), and including the voltage noise on the detector $V_{noise}(t)$, we have:

$$S_{V_{out}[\omega]} = S_{V_{noise}} + \omega_{cav}^4 (C_c Z_0)^2 \sum_{n \in \mathbb{Z}} \left[\frac{S_{\mu_n}[\omega - \omega_n]}{4} + \frac{S_{\mu_n}[\omega + \omega_n]}{4} \right] - \omega_{cav}^2 C_c Z_0 \sum_{n \in \mathbb{Z}} \left[\frac{S_{\mu_n, \delta V_n}[\omega - \omega_n]}{4} + \frac{S_{\mu_n, \delta V_n}[\omega + \omega_n]}{4} \right], \quad (3.1.42)$$

reminding $\omega_n = \omega_p + n\Omega_m$, with $S_{\mu_n}[\omega]$ the spectrum of the n^{th} component of the flux $\phi(t)$ decomposition, Eq. (3.1.16), and $S_{\mu_n, \delta V_n}$ the cross-correlations between flux and voltage noise components (with $V_{noise}(t) = \sum_n \frac{1}{2} \delta V_n(t) e^{-i\omega_n t} + c.c.$, same decomposition as

for the current I_{noise}). By construction, from the admittance Y_c introduced previously [Eq. (3.1.2)], we have:

$$V_{noise} \approx +i\omega_{cav}C_cZ_0R_{ex}I_{noise}, \quad (3.1.43)$$

which defines the output voltage noise from the cavity current noise. We have:

$$S_{\mu_0, \delta V_0}[\omega] = \frac{1}{2}Z_0R_{ex}\frac{C_c}{C_t}\left[\chi_c[0] + \chi_c^*[0]\right]S_{\delta I_n}, \quad (3.1.44)$$

$$S_{\mu_{-1}, \delta V_{-1}}[\omega] = \frac{1}{2}Z_0R_{ex}\frac{C_c}{C_t}\left[\chi_c[-\Omega_m] + \chi_c^*[-\Omega_m]\right]S_{\delta I_n} \\ + \frac{i}{4}|\mu_0|^2G^2\omega_{cav}C_cZ_0R_{ex}\left[\chi_c[-\Omega_m]^2\chi_{m,eff}^*[\omega] - \chi_c^*[-\Omega_m]^2\chi_{m,eff}[\omega]\right]S_{\delta I_n}, \quad (3.1.45)$$

$$S_{\mu_{+1}, \delta V_{+1}}[\omega] = \frac{1}{2}Z_0R_{ex}\frac{C_c}{C_t}\left[\chi_c[\Omega_m] + \chi_c^*[\Omega_m]\right]S_{\delta I_n} \\ + \frac{i}{4}|\mu_0|^2G^2\omega_{cav}C_cZ_0R_{ex}\left[\chi_c[\Omega_m]^2\chi_{m,eff}[\omega] - \chi_c^*[\Omega_m]^2\chi_{m,eff}^*[\omega]\right]S_{\delta I_n}, \quad (3.1.46)$$

using the properties of the Johnson-Nyquist current. On the right-hand-side, the first term involves only the microwave cavity; for Eqs. (3.1.46, 3.1.46) the last term involves the mechanics. These terms are nonzero since the same current noise generating the detection background also drives the cavity, and is fed back to the mechanics from Eq. (3.1.32). The total spectrum $S_{V_{out}}[\omega]$ is composed of identical combs around $\omega \approx \pm\omega_p$. What is measured by any classical apparatus (say, a spectrum analyzer) is the power spectral density [in W/(rad/s)]:

$$S_{PSD}[\omega] = \frac{2S_{V_{out}}[\omega > 0]}{Z_0}, \quad (3.1.47)$$

$$S_{PSD}[\omega] = 2R_{ex}S_{I_{noise}} + \frac{\omega_{cav}^4C_c^2Z_0}{2}\sum_{n=\{-1,0,+1\}}S_{\mu_n}[\omega - \omega_n] \quad (3.1.48)$$

$$- \frac{\omega_{cav}^2C_c}{2}\sum_{n=\{-1,0,+1\}}S_{\mu_n, \delta V_n}[\omega - \omega_n], \quad (3.1.49)$$

with all power folded in the $\omega > 0$ range. Similarly to the cavity itself, we defined a temperature for the detection port as $R_{ex}S_{I_{noise}} = R_{ex}S_{\delta I_n}/4 = k_B T_{ex}$, ensuring that the background noise in Eq. (3.1.48) reduces to $2k_B T_{ex}$, as it should. In the sum of Eq. (3.1.42), only the $n = \{-1, 0, +1\}$ terms have been kept: the measured spectrum is composed of three peaks, defined from Eqs. (3.1.19, 3.1.20, 3.1.21):

$$S_{\mu_0}[\omega] = |\mu_0|^2 2\pi\delta_0[\omega] + \frac{\kappa}{C_{tot}\omega_{cav}^2}\frac{R_{tot}S_{\delta I_n}}{4}\left|\chi_c[0]\right|^2, \quad (3.1.50)$$

$$S_{\mu_{-1}}[\omega] = \left(|\mu_0|^2 G^2 \frac{S_{x_0}[\omega]}{4} + \frac{\kappa}{C_{tot}\omega_{cav}^2} \frac{R_{tot}S_{\delta I_n}}{4} \right. \\ \left. + i|\mu_0|^2 G^2 \frac{\kappa}{2\omega_{cav}} \left[\chi_{m,eff}^*[\omega]\chi_c[-\Omega_m] - \chi_{m,eff}[\omega]\chi_c^*[-\Omega_m] \right] \frac{R_{tot}S_{\delta I_n}}{4} \right) \left| \chi_c[-\Omega_m] \right|^2, \quad (3.1.51)$$

$$S_{\mu_{+1}}[\omega] = \left(|\mu_0|^2 G^2 \frac{S_{x_0}[\omega]}{4} + \frac{\kappa}{C_{tot} \omega_{cav}^2} \frac{R_{tot} S_{\delta I_n}}{4} \right. \\ \left. + i |\mu_0|^2 G^2 \frac{\kappa}{2\omega_{cav}} \left[\chi_{m,eff}[\omega] \chi_c[\Omega_m] - \chi_{m,eff}^*[\omega] \chi_c^*[\Omega_m] \right] \frac{R_{tot} S_{\delta I_n}}{4} \right) |\chi_c[\Omega_m]|^2, \quad (3.1.52)$$

applying again the properties of the Johnson-Nyquist current (δ_0 is the Dirac function). The second terms in each expressions correspond to the cavity alone, being driven by the current noise. Eq. (3.1.50) is due to the pump tone signal; Eqs. (3.1.52,3.1.52) include the two sidebands, proportional to the mechanical motion spectrum and $|\mu_0|^2 = \left(\frac{|I_0|}{2C_{tot}\omega_{cav}} \right)^2 |\chi_c[0]|^2$. The last terms in Eqs. (3.1.52,3.1.52) correspond to cross-correlations between the cavity noise current and the motion.

We should now clarify the energy flow in this system. The power injected P_{in} by the traveling wave ϕ_{in} (see Fig. 3.2) is by definition $P_{in} = \frac{1}{2} \frac{|V_0^2|}{Z_0}$, and the energy E_c stored in the microwave resonator writes:

$$E_c = \frac{1}{2} C_{tot} \omega_{cav}^2 |\mu_0|^2 = P_{in} \kappa_{ex} |\chi_c[0]|^2, \quad (3.1.53)$$

where we made use of Eqs. (3.1.3,3.1.5,3.1.10).

The pump power P_{pump} measured in the output spectrum at ω_p is then:

$$P_{pump} = \frac{\omega_{cav}^4 (C_{tot} Z_0)^2}{2Z_0} |\mu_0|^2 = E_c \kappa_{ex}. \quad (3.1.54)$$

Replacing Eq. (3.1.53) in Eq. (3.1.54) leads to $P_{pump} = P_{in} \kappa_{ex}^2 |\chi_c[0]|^2$; the ratio P_{pump}/P_{in} is thus a straightforward calibration of the quantity κ_{ex} .

The power spectral density can thus be recasted in the compact form:

$$S_{PSD}[\omega] = 2k_B T_{ex} + P_{pump} 2\pi \delta_0[\omega - \omega_0] + \kappa_{ex} \kappa k_B (T_c - T_{ex}) |\chi_c[0]|^2 \Pi[\omega - \omega_p] \\ + \kappa_{ex} g^2 \frac{S_x^-[\omega - \omega_p]}{\bar{x}^2} |\chi_c[-\Omega_m]|^2 + \kappa_{ex} \kappa k_B (T_c - T_{ex}) |\chi_c[-\Omega_m]|^2 \Pi[\omega - \omega_{-1}] \\ + \kappa_{ex} g^2 \frac{S_x^+[\omega - \omega_p]}{\bar{x}^2} |\chi_c[\Omega_m]|^2 + \kappa_{ex} \kappa k_B (T_c - T_{ex}) |\chi_c[\Omega_m]|^2 \Pi[\omega - \omega_{+1}], \quad (3.1.55)$$

having defined $\bar{x}^2 = 1/(2m\omega_{cav}\Omega_m)$ (in m^2/J). $\Pi[\omega]$ denotes the door function (here, of width $\approx \Omega_m$), reminding that each cavity component is defined around a precise angular frequency ω_n . Note that to detect the cavity as a peak or a dip, one requires $T_c \neq T_{ex}$; T_{ex} also defines the background noise level that ultimately limits a measurement. Eq. (3.1.41) then reads $g = G\bar{x}\sqrt{E_c}$ (in rad/s). The last terms of Eqs. (3.1.46,3.1.52) and (3.1.46,3.1.52), which correspond to the cross-correlations involving the mechanics, affect the measurement by mimicking an extra force noise $\delta F_-, \delta F_+$ which depends on the sideband [136, 37]:

$$S_x^-[\omega] = S_x[\omega] + \left| \chi_{m,eff}[\omega - \Omega_m] \right|^2 S_{\delta F_-}, \quad (3.1.56)$$

$$S_x^+[\omega] = S_x[\omega] + \left| \chi_{m,eff}[\omega + \Omega_m] \right|^2 S_{\delta F_+}. \quad (3.1.57)$$

These shall not be confused with the true back-action force noise $S_{\delta F}$: $\delta F_- \delta F_+$ do not actually affect the mechanical degree of freedom. Their relevance is discussed in Section 3.2, on the basis of the three standard measuring schemes (with i.e. $\Delta = \{0, \pm\Omega_m\}$). Notwithstanding this fact, the two sidebands are thus the image of the two peaks of the mechanical spectrum, translated around ω_p (one being thus at $\omega_p - \Omega_m = \omega_{-1}$ and the other at $\omega_p + \Omega_m = \omega_{+1}$, with an amplitude proportional to g^2 and modulated by the susceptibilities $|\chi_c[-\Omega_m]|^2, |\chi_c[+\Omega_m]|^2$). Integrating the peaks, we obtain an area proportional to the observed variance of the displacement:

$$(\sigma_x^\pm)^2 = \frac{1}{2\pi} \int_{\mathbb{R}} S_x^\pm[\omega] d\omega, \quad (3.1.58)$$

including thus the cross-correlation contribution. The above applies to the reflection setup, Fig. 3.2 (bottom). For the two-port one Fig. 3.2 (top), one should replace $\kappa_{ex} \rightarrow \kappa_1$ in Eq. (3.1.53) and $\kappa_{ex} \rightarrow \kappa_2$ in Eqs. (3.1.54, 3.1.55). In the case of a bi-directional arrangement Fig. 3.2 (middle), one should replace $\kappa_{ex} \rightarrow \kappa_{ex}/2$ in all expressions. Up to this point, we relied only on classical mechanics, and all optomechanical properties (at fixed Δ) depend only on g (tuned experimentally through P_{in}) and $T_m; T_c; T_{ex}$. We shall now explicitly link our results to the quantum formalism of Chapter 2.

3.2 CLASSICAL VERSUS QUANTUM

3.2.1 Planck's postulate

Quantum mechanics tells us that energy comes in quanta, thus in order to link the classical writing to the quantum expressions derived in Chapter 2, we have to introduce the following populations:

$$n_c = \frac{E_c}{\mathcal{E}_{0,c}} \quad \text{and} \quad n_c^{th} = \frac{k_B T_c}{\mathcal{E}_{0,c}}, \quad (3.2.1)$$

with respectively the microwave drive number of quanta in the cavity n_c and the cavity thermal population n_c^{th} . We also introduce:

$$n_{ex}^{th} = \frac{k_B T_{ex}}{\mathcal{E}_{0,c}} \quad \text{and} \quad n_m^{th} = \frac{k_B T_m}{\mathcal{E}_{0,m}}, \quad (3.2.2)$$

with respectively the external microwave port (thermal) population n_{ex}^{th} and the number of thermal mechanical quanta n_m^{th} . In the above expressions, we use the notation $\mathcal{E}_{0,c}$ in order to define the energy per microwave quanta (and respectively $\mathcal{E}_{0,m}$ the energy per mechanical quanta). This brings us also readily the so-called zero-point fluctuation and single-photon coupling:

$$x_{zpf}^2 = \bar{x}^2 \mathcal{E}_{0,c} \quad \text{in units of m}^2/\text{quanta}, \quad (3.2.3)$$

$$g_0 = G x_{zpf} \quad \text{in units of Rad/s}. \quad (3.2.4)$$

We can now recast the total Langevin force on the mechanics in the form:

$$S_{\mathcal{L}} = 2m\Gamma_{eff} \mathcal{E}_{0,m} n_{m,eff}, \quad (3.2.5)$$

where $n_{m,eff}$ is the effective number of mechanical quanta defined as:

$$n_{m,eff} = \frac{k_B T_{eff}}{\mathcal{E}_{0,m}} = \frac{\Gamma_m n_m^{th} + \tilde{\Gamma}_{opt} n_c^{th}}{\Gamma_{eff}}, \quad (3.2.6)$$

$$\tilde{\Gamma}_{opt} = \Gamma'_{opt} \frac{\mathcal{E}_{0,c}}{\mathcal{E}_{0,m}}. \quad (3.2.7)$$

Equivalently the back-action stochastic force Eq. (3.1.35) can be recast into:

$$S_{\delta F_{BA,0}} = n_c n_c^{th} \frac{G^2 \mathcal{E}_{0,c}^2}{\omega_{cav}^2} \left[\frac{\kappa}{(\Delta + \Omega_m)^2 + (\frac{\kappa}{2})^2} + \frac{\kappa}{(\Delta - \Omega_m)^2 + (\frac{\kappa}{2})^2} \right]. \quad (3.2.8)$$

Fially we rewrite the measured spectrum under the following form:

$$\begin{aligned} S_{PSD}[\omega] = & 2\mathcal{E}_{0,c} n_{ex}^{th} + \mathcal{E}_{0,c} \kappa_{ex} \left[n_c 2\pi \delta_0[\omega - \omega_p] + (n_c^{th} - n_{ex}^{th}) \kappa |\chi_c[0]|^2 \right] \Pi[\omega - \omega_p] \\ & + \mathcal{E}_{0,c} \kappa_{ex} |\chi_c[-\Omega_m]|^2 \left[\frac{g^2}{x_{zpf}^2} S_x^-[\omega - \omega_p] + (n_c^{th} - n_{ex}^{th}) \kappa \right] \Pi[\omega - \omega_{-1}] \\ & + \mathcal{E}_{0,c} \kappa_{ex} |\chi_c[+\Omega_m]|^2 \left[\frac{g^2}{x_{zpf}^2} S_x^+[\omega - \omega_p] + (n_c^{th} - n_{ex}^{th}) \kappa \right] \Pi[\omega - \omega_{+1}]. \end{aligned} \quad (3.2.9)$$

In classical mechanics, the energy in both mechanical peaks is given by the equipartition theorem, remembering Eq. (3.1.58): $\langle \sigma_x^\pm \rangle^2 = \frac{1}{2} \sigma_x^2$. We do not consider yet back-action and sideband asymmetry, which leads to:

$$\sigma_x^2 = \langle \delta x^2 \rangle \frac{\Gamma_m}{\Gamma_{eff}}, \quad (3.2.10)$$

$$\langle \delta x^2 \rangle = \frac{k_B T_m}{2m\Omega_m} = x_{zpf}^2 n_m^{th} \frac{\omega_{cav}}{\Omega_m} \frac{\mathcal{E}_{0,m}}{\mathcal{E}_{0,c}}, \quad (3.2.11)$$

with $\langle \delta x^2 \rangle$ the half-variance of the motion (computed on one sideband only), having defined $g = g_0 \sqrt{n_c}$. Note that we have the same expressions with $n_{m,eff}$ for the effective temperature T_{eff} . The Γ_m/Γ_{eff} factor comes from the dynamical part of the back-action, causing optical damping/anti-damping, with $\Gamma_{eff} = \Gamma_m + \Gamma_{opt}$ for "blue" and "red" pumping schemes, and $\Gamma_{eff} = \Gamma_m$ for "green". We shall thus write here:

$$\Gamma_{opt} = g_0^2 n_c \left[\frac{\kappa}{(\Delta + \Omega_m)^2 + (\frac{\kappa}{2})^2} - \frac{\kappa}{(\Delta - \Omega_m)^2 + (\frac{\kappa}{2})^2} \right], \quad (3.2.12)$$

in terms of n_c .

Eq. (3.2.11) coincides exactly with the quantum mechanical high-temperature limit. But when $T \rightarrow 0$ K, $n_m^{th} \rightarrow 0$ and n_m^{th} should be replaced by the factor 1/2 which corresponds to the vacuum noise predicted by quantum mechanics [26, 136]. In the following, the same treatment shall be performed for n_c^{th} in the so-called quantum ($T \rightarrow 0$ K) limit.

Any measurement comes with an acquisition imprecision. In the literature, one finds a discussion focused on the phase of the optical "green" readout [136]. An equivalent

discussion can be performed on the amplitude of the signal; this is what we will present in the following. A position fluctuation δx transduces into a cavity frequency shift:

$$\delta\omega_{cav} = G\delta x \left| \frac{\frac{\kappa}{2}}{-i\omega + \frac{\kappa}{2}} \right|, \quad (3.2.13)$$

taking into account the finite response time of the microwave mode. This shift $\delta\omega_{cav}$ will in turn modify the output signal energy:

$$\frac{\delta E}{E} \approx -4 \frac{\delta\omega_{cav}^2}{\kappa^2} = -4 \frac{G^2 \delta x^2}{\kappa^2} \frac{1}{1 + 4 \frac{\omega^2}{\kappa^2}}, \quad (3.2.14)$$

or equivalently modify the phase θ of the sideband signal:

$$\delta\theta \approx -2 \frac{\delta\omega_{cav}}{\kappa}. \quad (3.2.15)$$

Both quantities correspond to the relative error on what is measured experimentally. In our case we decide to do the reasoning on the sideband energy. This energy variation can be expressed in terms of detection noise quanta $n_{det} = \delta E / \mathcal{E}_{0,c}$ with $\delta E / E = n_{det} / (n_c \kappa t)$ measured during a time t . For an ideal quantum detector the measurement is shot-noise limited with $n_{det} = 1$ [136, 26]; in the classical case, $n_{det} \mathcal{E}_{0,c}$ corresponds to the noise background (in Joules) affecting the detection, arising from the whole amplification chain (with obviously $n_{det} \gg 1$). The imprecision in position resulting from the finite n_{det} can be interpreted as the integral of a flat noise S_x^{imp} (over a bandwidth t^{-1}) [15]:

$$S_x^{imp}[\omega] = \frac{\kappa^2 n_{det}}{16 G^2 n_c \kappa_{ex}} \left(1 + 4 \frac{\omega^2}{\kappa^2} \right), \quad (3.2.16)$$

where ω is set by the measuring scheme, "blue", "red" or "green".

Note that up to this point we only postulated that energy was quantized. Eqs. (3.2.16) match the high-temperature limit of the quantum mechanics writing, with the following hypothesis described in Chapter 2:

$$\hat{a} = \alpha + \delta\hat{a} \quad (\text{linearization}), \quad (3.2.17)$$

$$n_c = |\alpha|^2 \gg 1, \quad (3.2.18)$$

$$\langle \delta\hat{a}^\dagger \delta\hat{a} \rangle = n_c^{th} \gg 1, \quad (3.2.19)$$

$$\langle \hat{b}^\dagger \hat{b} \rangle = n_m^{th} \gg 1, \quad (3.2.20)$$

if and only if we impose:

$$\frac{\mathcal{E}_{0,m}}{\Omega_m} = \frac{\mathcal{E}_{0,c}}{\omega_{cav}} = cste, \quad (3.2.21)$$

since this reasoning applies to any of mechanical and optical modes. We recover here precisely Planck's postulate and we can already write $cste = \hbar$ even if we have no way to evaluate quantitatively this constant.

3.2.2 Sideband Assymetry

Cross-correlations between the cavity current noise and the mechanics, Eqs. (3.1.52, 3.1.52) and cross-correlations between the detection background and the cavity noise Eqs.

(3.1.46,3.1.46) can be recast into apparent stochastic force components that depend on the sideband, Eqs. (3.1.56,3.1.57) for the $n = \pm 1$ ones respectively.

"BLUE" PUMPING For the "blue" pumping scheme, only the $n = -1$ sideband is measurable in the sideband-resolved limit. Injecting $\Delta = +\Omega_m$ in the above mentioned equations, we obtain:

$$S_{\delta F_-} = 2m\Gamma_{eff}k_B(2T_c - T_{ex})\frac{\Omega_m}{\omega_{cav}} = 2m\Gamma_{eff}\hbar\Omega_m(2n_c^{th} - n_{ex}^{th}), \quad (3.2.22)$$

with T_c and T_{ex} the temperatures of the cavity and the detection port respectively, as introduced in the preceding Section.

"RED" PUMPING Similarly for the "red" scheme, with $\Delta = -\Omega_m$ and looking at the $n = +1$ sideband we have:

$$S_{\delta F_+} = 2m\Gamma_{eff}k_B(T_{ex} - 2T_c)\frac{\Omega_m}{\omega_{cav}} = 2m\Gamma_{eff}\hbar\Omega_m(n_{ex}^{th} - 2n_c^{th}). \quad (3.2.23)$$

In both expressions, $\Gamma_{eff} = \Gamma_m + \Gamma_{opt}$ but Γ_{opt} is different: negative for the "blue" scheme, and positive for the "red" one. However, for low drive powers $\Gamma_{opt} \approx 0$ and $\Gamma_{eff} \approx \Gamma_m$. In this case, a very simple result emerges: the two apparent force noises are opposite, a result referred to in the literature as sideband asymmetry [136, 37].

"GREEN" PUMPING In the case of a "green" pumping scheme, $\Delta = 0$ and both sidebands can be measured at the same time. The resulting expressions for the cross-correlation apparent stochastic force components are:

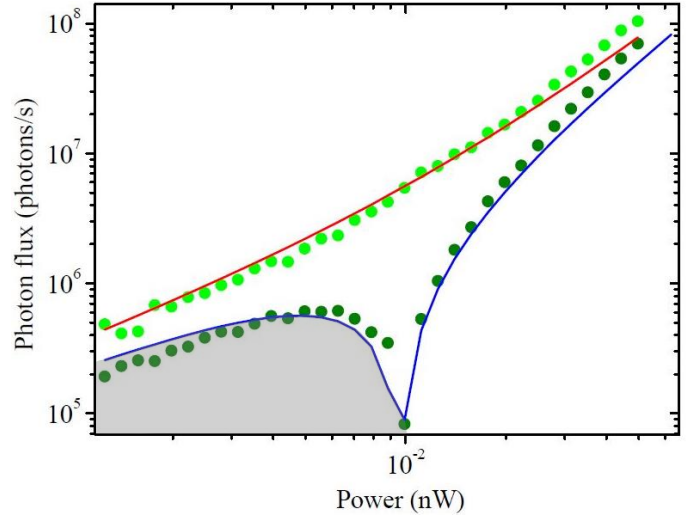
$$S_{\delta F_-} = 2m\Gamma_{eff}k_B T_{ex} \frac{\Omega_m}{\omega_{cav}} = 2m\Gamma_{eff}\hbar\Omega_m n_{ex}^{th}, \quad (3.2.24)$$

$$S_{\delta F_+} = -S_{\delta F_-}, \quad (3.2.25)$$

again in the sideband-resolved limit. Eqs. (3.2.24,3.2.25) are very similar to Eqs. (3.2.22, 3.2.23): again the two forces are opposite, but this time they depend only on n_{ex}^{th} .

Let us consider the case of an ideally thermalized system were $T_c = T_{ex} = T_m$. Then in the limit $\Gamma_{opt} \approx 0$ sideband asymmetry measured by comparing the $n = -1$ peak in "blue" pumping Eq. (3.2.22) with the $n = +1$ peak in "red" Eq. (3.2.23) gives strictly the same result as the direct comparison of the two sidebands Eqs. (3.2.24,3.2.25) observed with a "green" scheme. Besides, the sideband asymmetry effect simply renormalizes the observed mechanical temperature by $T_m \rightarrow T_m(1 + \Omega_m/\omega_{cav})$ on the $n = -1$ side, and by $T_m \rightarrow T_m(1 - \Omega_m/\omega_{cav})$ on the $n = +1$ side; since $\Omega_m/\omega_{cav} \ll 1$, this effect can be safely neglected in this case. One needs to artificially create a situation where $T_m \ll T_{ex}$ to make the sideband asymmetry detectable (e.g. by sideband cooling the mechanical mode, and injecting noise through the microwave port) [37]. This is illustrated in Fig. 3.5 for one of our sample, injecting microwave noise at ω_{cav} to mimic a high-temperature (thus classical) situation [220]. As soon as $T \rightarrow 0$ K, the classical picture breaks down and all features should be interpreted in the framework of quantum mechanics (see Chapter 2); including sideband asymmetry. The direct link between the two theories shall be discussed in Section 3.2.3.

FIGURE 3.5 – Experimental measurements of the output photon flux as a function of the injected microwave power performed on the highly-coupled drum device. Presented data are obtained for the "green" pumping scheme measuring both sidebands with $T_m = 100$ mK, $T_{ex} = 220$ K and thus $T_c = (T_{ex} + T_m)/2 = 110$ K (remembering that for this chip $\kappa/\kappa_{ex} \approx 2$). Dark green dots correspond to the upper sideband data whereas light green dots are the lower sideband data. In the shaded area, the peak is actually reversed, and appears as a dip (this is called noise squashing; we plot the absolute value of the area). The blue line is a theoretical fit for the upper sideband whereas the red line is a theoretical fit for the upper one. Note the great visibility of the noise squashing phenomenon [220].



3.2.3 Heisenberg limit

We now calculate the standard product of the imprecision on the measurement S_x^{imp} and the back-action force $S_{\delta F_{BA,0}}$:

$$S_x^{imp} \cdot S_{\delta F_{BA,0}} = \frac{1}{16} \frac{\kappa}{\kappa_{ex}} \frac{\mathcal{E}_{0,c}^2}{\omega_{cav}^2} n_c^{th} n_{det} \left[1 + 4 \frac{\omega^2}{\kappa^2} \right] \left[\frac{\kappa^2}{(\Delta + \Omega_m)^2 + (\frac{\kappa}{2})^2} + \frac{\kappa^2}{(\Delta - \Omega_m)^2 + (\frac{\kappa}{2})^2} \right] \quad (3.2.26)$$

Focusing on each of the three standard schemes, this leads to the following results:

$$S_x^{imp} \cdot S_{\delta F_{BA,0}} = \frac{\hbar^2}{4} \frac{\kappa}{\kappa_{ex}} 2 n_c^{th} n_{det} \quad \text{for } \Delta = 0, \text{ with } \omega \approx \pm \Omega_m, \quad (3.2.27)$$

$$S_x^{imp} \cdot S_{\delta F_{BA,0}} = \frac{\hbar^2}{4} \frac{\kappa}{\kappa_{ex}} n_c^{th} n_{det} \quad \text{for } \Delta = +\Omega_m, \text{ with } \omega \approx 0, \quad (3.2.28)$$

$$S_x^{imp} \cdot S_{\delta F_{BA,0}} = \frac{\hbar^2}{16} \frac{\kappa}{\kappa_{ex}} \left(1 + 16 \frac{\Omega_m^2}{\kappa^2} \right) n_c^{th} n_{det} \quad \text{for } \Delta = -\Omega_m, \text{ with } \omega \approx 2\Omega_m. \quad (3.2.29)$$

At $T \rightarrow 0$ K, $n_c^{th} \rightarrow 0$ and quantum mechanics predicts that:

$$n_c^{th} \xrightarrow{\text{replaced}} \frac{1}{2} \quad \text{for } \Delta = 0, \quad (3.2.30)$$

$$n_c^{th} \xrightarrow{\text{replaced}} 1 \quad \text{for } \Delta = +\Omega_m, \quad (3.2.31)$$

$$n_c^{th} \xrightarrow{\text{replaced}} \frac{\kappa^2}{4\Omega_m^2} \quad \text{for } \Delta = -\Omega_m. \quad (3.2.32)$$

Note that this last one corresponds to the usual sideband cooling limit [136]. Thus for a shot-noise limited detection ($n_{det} = 1$) and in the usual resolved sideband limit we recover from Eqs. (3.2.27-3.2.29) the famous Heisenberg limit:

$$S_x^{imp} \cdot S_{\delta F_{BA,0}} \geq \frac{\hbar^2}{4}, \quad (3.2.33)$$

reached only for an overcoupled cavity $\kappa \approx \kappa_{ex}$. This means that each of the three schemes are at the quantum limit.

It is enlightening to evaluate the minimal mechanical displacement which can be detected with such a microwave optomechanical scheme. The imprecision noise Eq. (3.2.16) can be taken into account by adding it up with S_x^\pm in Eq. (3.2.9). Subtracting the $2k_B T_{ex}$ background and integrating each sideband over a bandwidth $\Delta\omega$ large enough to cover the peaks, we are led to define a signal component \mathcal{S}_{ig} , and a noise component \mathcal{N}_{oise} , for each sideband $n = \pm 1$:

$$\mathcal{S}_{ig} = \hbar\omega_{cav}\kappa_{ex}G^2n_c \left| \chi_c[\pm\Omega_m] \right|^2 \frac{\Gamma_m}{\Gamma_{eff}} \left[\langle \delta x^2 \rangle + \frac{S_{\delta F_\pm}}{(2m\Omega_m)^2\Gamma_m} \right], \quad (3.2.34)$$

$$\begin{aligned} \mathcal{N}_{oise} = \hbar\omega_{cav}\kappa_{ex} \left| \chi_c[\pm\Omega_m] \right|^2 & \left\{ \kappa \frac{\Delta\omega}{2\pi} \left[\frac{n_{det}}{16} \frac{\kappa}{\kappa_{ex}} \left(1 + 4 \frac{\omega^2}{\kappa^2} \right) + n_c^{th} - n_{ex}^{th} \right] \right. \\ & \left. + \frac{G^4 n_c^2 x_{zpf}^4 \kappa}{\Gamma_m} n_c^{th} \left(\left| \chi_c[+\Omega_m] \right|^2 + \left| \chi_c[-\Omega_m] \right|^2 \right) \frac{\Gamma_m}{\Gamma_{eff}} \right\}, \end{aligned} \quad (3.2.35)$$

where \mathcal{N}_{oise} contains both imprecision (former term, with also cavity noise $n_c^{th} - n_{ex}^{th}$) and back-action (latter). We now wrote explicitly the sideband asymmetry contribution $S_{\delta F_\pm}$ in Eq. (3.2.34).

Note that $\Delta\omega$ is the bandwidth of the filter, which should be big enough to capture S_x^{imp} but not too much to minimize the noise contribution, thus: $\Delta\omega = a\Gamma_{eff}$ with a a small number. Considering the error function for a Lorentz shaped curve:

$$E_{ri}(a) = 1 - \frac{2}{\pi} \int_{-\frac{a}{2}}^{+\frac{a}{2}} \frac{1}{1+4x^2} dx = 1 - \frac{2}{\pi} \arctan(a), \quad (3.2.36)$$

in order to obtain $E_{ri}(a) \leq 5\%$, $a = 12$ is typically good enough.

"GREEN" PUMPING Considering the "green" scheme, we have $\langle \delta x^2 \rangle \Gamma_m / \Gamma_{eff} = x_{zpf}^2 n_m^{th}$ and $\left| \chi_c[-\Omega_m] \right|^2 = \left| \chi_c[+\Omega_m] \right|^2$. Eqs. (3.2.24,3.2.25) demonstrate that the extra term in Eq. (3.2.34) modifies the measured peaks from Eq. (3.2.11) into Eq. (3.2.34) by substituting $n_m^{th} \rightarrow n_m^{th} + n_{ex}^{th}$ on the $n = -1$ side, and $n_m^{th} \rightarrow n_m^{th} - n_{ex}^{th}$ on the $n = +1$ side; this is sideband asymmetry in the quantum mechanics language. The difference $(\sigma_x^-)^2 - (\sigma_x^+)^2$ is then proportional to $2n_{ex}^{th}$, which tends towards 1 in quantum mechanics at $T \rightarrow 0$ K; a similar result can be obtained comparing the $n = \pm 1$ peaks obtained in "blue" and "red" pumping schemes respectively [37]. However from $((\sigma_x^-)^2 + (\sigma_x^+)^2)/2$, the "green" scheme leads to a quantity insensitive to sideband asymmetry, which is directly the image of the mechanical motion. Discussing now on this quantity, our signal is then $\mathcal{S}_{ig} \propto \langle \delta x^2 \rangle$.

Carrying out the substitution $\Gamma_{eff} = \Gamma_m$ valid for "green" pumping in Eqs. (3.2.34,3.2.36), we can define a signal-to-noise ratio $\mathcal{S}_{ig}/\mathcal{N}_{oise}$ that illustrates our sensitivity to the quantity $\langle \delta x^2 \rangle$. We obtain in the "green" pumping case:

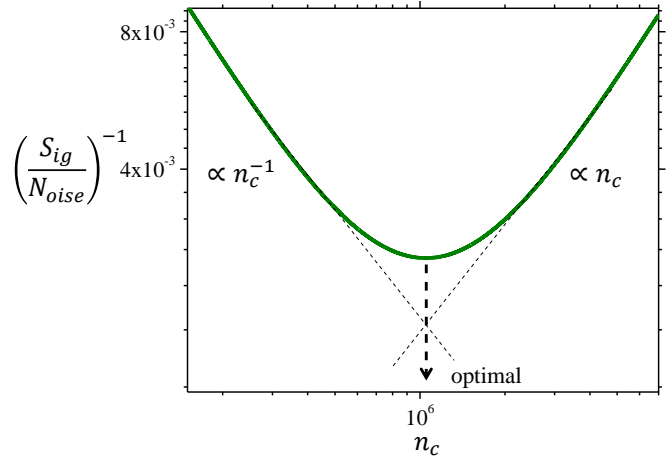
$$\frac{\mathcal{S}_{ig}}{\mathcal{N}_{oise}}(n_c) = \frac{1}{2} \frac{n_m^{th} \Omega_m}{n_c^{th} \kappa} \frac{X_g}{\frac{a}{2\pi} \left(1 + \frac{\Omega_m^2 n_{det}}{4\kappa_{ex} n_c^{th}} - \frac{n_{ex}^{th}}{n_c^{th}} \right) + X_g^2} \quad \text{with} \quad X_g = \frac{g_0^2 n_c}{\Omega_m \Gamma_m}, \quad (3.2.37)$$

and for $n_{ex}^{th} = n_c^{th}$:

$$\frac{\mathcal{S}_{ig}}{\mathcal{N}_{oise}}(n_c) = \frac{g_0^2 n_c n_m^{th}}{\frac{\Gamma_m \Omega_m^2}{\kappa_{ex}} \frac{a}{8\pi} n_{det} + 2g_0^4 n_c^2 n_c^{th} \frac{\kappa}{\Gamma_m \Omega_m^2}}. \quad (3.2.38)$$

This is represented in Fig. 3.6 as a function of drive power with the parameter n_c ; similar

FIGURE 3.6 – Illustration of inverse signal-to-noise ratio $\mathcal{N}_{oise}/\mathcal{S}_{ig}$ in the "green" pumping scheme, as a function of photon number n_c inside the cavity. Driven at optimal n_c , the best signal-to-noise ratio can be obtained for the detection of $\langle \delta x^2 \rangle$ (so-called standard classical limit, see text). Curve computed with the badly-coupled drum parameters but with $\kappa = \kappa_{ex} = 4$ MHz and $n_{det} = 100$, $n_{ex}^{th} = n_c^{th} = 6 \times 10^3$ and $n_m^{th} = 6 \times 10^5$. At the quantum limit, the optimum point (the minimum of the curve) reaches $\mathcal{N}_{oise}/\mathcal{S}_{ig} \approx 2$ (standard quantum limit, see text).



plots can be found in Refs. [136, 111, 26]. On the left, the sensitivity is lost $\propto n_c^{-1}$ because of our finite detection noise n_{det} . On the right, the measurement is dominated by back-action $\propto n_c$ arising from n_c^{th} . There is an optimum defined by:

$$\frac{d}{dn_c} \left(\frac{\mathcal{S}_{ig}}{\mathcal{N}_{oise}} \right) = 0. \quad (3.2.39)$$

This point verifies:

$$n_c^{op} \approx \frac{\Gamma_m \Omega_m^2}{4\kappa g_0^2} \sqrt{\frac{a}{\pi} \frac{\kappa}{\kappa_{ex}} \frac{n_{det}}{n_c^{th}}}, \quad (3.2.40)$$

with:

$$\frac{\mathcal{S}_{ig}}{\mathcal{N}_{oise}}(n_c^{op}) \approx n_m^{th} \sqrt{\frac{\pi \kappa_{ex}}{a} \frac{1}{\kappa n_{det} n_c^{th}}}. \quad (3.2.41)$$

At the $T \rightarrow 0$ K quantum limit n_c^{th}, n_m^{th} are replaced by $1/2$; with a shot-noise limited detector $n_{det} = 1$, we reach at best $\frac{\mathcal{S}_{ig}}{\mathcal{N}_{oise}} \approx 1/2$ (for $\kappa \approx \kappa_{ex}$ and $\Delta\omega \approx \Gamma_m$): the signal is about half the total detected noise [26]. This is called the standard quantum limit, which reaches the ultimate physical limit when simultaneously measuring two non-commuting quadratures of the motion. In contrast, the classical optimum which we shall call standard classical limit (SCL) is relative and depends both on n_{det} (quality of classical detector) and n_c^{th} (Johnson-Nyquist noise of the cavity). The main optomechanical results applying to the "green" pumping scheme are compared in Tab. 3.1 in the classical and quantum

regimes. The key point revealed by the classical modeling is that all features have a classical analogue; only the $T \rightarrow 0$ K quantities are a true signature of quantumness, which highlights the importance of calibrations in all conducted experiments.

Quantity	Quantum limit	Classical limit
$S_x^{imp} \cdot S_{\delta F_{BA,0}}$	$\frac{\kappa}{\kappa_{ex}} \hbar^2 / 4$	$\frac{1}{2} \frac{\kappa}{\kappa_{ex}} k_B T_c \delta E / (\omega_{cav}^2)$
\mathcal{S}_{ig}	$\propto x_{zpf}^2 / 2$	$\propto k_B T_m / (2 m \Omega_m^2)$
\mathcal{N}_{oise}	$\propto x_{zpf}^2$	$\propto \sqrt{\delta E k_B T_c} / (\sqrt{2} m \Omega_m \omega_{cav})$
$\mathcal{S}_{ig} / \mathcal{N}_{oise}$	$1/2$	$k_B T_m \omega_{cav} / (\sqrt{2} \sqrt{\delta E k_B T_c} \Omega_m)$

TABLE 3.1 – $S_x^{imp} \cdot S_{\delta F_{BA,0}}$ product, signal \mathcal{S}_{ig} , noise \mathcal{N}_{oise} and signal-to-noise ratio in the quantum and classical limits (the latter are given at the optimal n_c for the "green" pumping scheme; δE energy detection resolution and T_c cavity temperature, see text).

"BLUE" PUMPING A similar reasoning can be performed for the "blue" pumping scheme. Carrying out the valid substitutions for the "blue" pumping case: $\Gamma_{eff} = \Gamma_m + \Gamma_{opt}$ with $\Gamma_{opt} = -4g^2/\kappa$, one obtains for the signal-to-noise ratio:

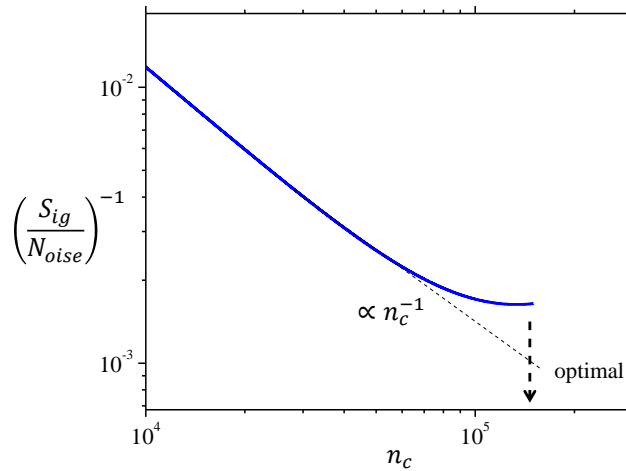
$$\frac{\mathcal{S}_{ig}}{\mathcal{N}_{oise}}(n_c) = \frac{n_m^{th}}{n_c^{th}} \frac{X_b}{\frac{2a}{\pi} \left(1 + \frac{\kappa}{16\kappa_{ex}} \frac{n_{det}}{n_c^{th}} - \frac{n_{ex}^{th}}{n_c^{th}} \right) (1 - X_b)^2 + X_b^2} \quad \text{with} \quad X_b = \frac{4g_0^2 n_c}{\kappa \Gamma_m}. \quad (3.2.42)$$

Similarly to the "green" pumping the optimum of this function is verified by:

$$n_c^{op} \approx \frac{\kappa \Gamma_m}{4g_0^2} \sqrt{\frac{\frac{a}{8\pi} \frac{\kappa}{\kappa_{ex}} \frac{n_{det}}{n_m^{th}}}{\frac{n_c^{th}}{n_m^{th}} + \frac{a}{8\pi} \frac{\kappa}{\kappa_{ex}} \frac{n_{det}}{n_m^{th}}}}. \quad (3.2.43)$$

We illustrate the case of "blue" pumping in Fig. 3.7. The parametric instability occurring with this scheme implies that the system cannot go further than $X_b \rightarrow 1^-$. At the $T \rightarrow 0$ K quantum limit $\{n_c^{th}, n_m^{th}\} \rightarrow 1/2$ with a shot-noise limited detector $n_{det} = 1$, we reach at best $\frac{\mathcal{S}_{ig}}{\mathcal{N}_{oise}} \approx \frac{n_m^{th}}{n_c^{th}} = 1$ (for $\kappa \approx \kappa_{ex}$ and $\Delta\omega \approx \Gamma_m$).

FIGURE 3.7 – Illustration of inverse signal-to-noise ratio $\mathcal{N}_{oise}/\mathcal{S}_{ig}$ in the "blue" pumping scheme, as a function of photon number n_c inside the cavity. Driven at optimal n_c , the best signal-to-noise ratio can be obtained for the detection of $\langle \delta x^2 \rangle$. Curve computed with the badly-coupled drum parameters but with $\kappa = \kappa_{ex} = 4$ MHz and $n_{det} = 100$, $n_{ex}^{th} = n_c^{th} = 6 \times 10^3$ and $n_m^{th} = 6 \times 10^5$. At the quantum limit, the optimum point (the minimum of the curve) reaches $\mathcal{N}_{oise}/\mathcal{S}_{ig} \approx 1$.



Note that this scheme is classically better than the "green" one because in classical physics $n_{det} \gg n_c^{th}$. It is also independent of the small corrections κ/κ_{ex} and $\Delta\omega$. While

the measurement is limited by the parametric instability for n_c , the signal-to-noise ratio can be recast into $T_m \omega_{cav} / (T_c \Omega_m) \gg 1$ close to it. This makes it a very practical technique to perform thermometry [223].

3.3 CONCLUSION

In summary, we have presented the generic classical electric circuit model which is analogous to the standard optomechanics quantum treatment (see Chapter 3). The developed analytics provides the bridge between circuit parameters and quantum optics quantities, a mandatory link for design and optimization. The two approaches are strictly equivalent, provided temperatures are high enough for both the mechanical and the electromagnetic degrees of freedom.

Besides, a thorough comparison of the two models gives a profound understanding of what measured properties are fundamentally quantum. To match the mathematics of the two computation methods, we introduce populations by means of an energy per quanta proportional to the mode resonance frequency: the early Planck postulate. Sideband asymmetry is derived in classical terms, and we distinguish the temperatures of the mechanical mode T_m from the one of the microwave mode T_c and the microwave (detection) port T_{ex} . Considering the measurement protocol in itself, we derive the resolution limit of a classical experiment performed with the optimal optomechanical scheme. We obtain the classical (and relative) analogue of the (absolute) standard quantum limit (SQL) fixed by the Heisenberg principle in quantum mechanics; we shall name it the standard classical limit (SCL). Only the $T_m, T_c, T_{ex} \rightarrow 0$ K measured quantities appear to be specific to quantum mechanics, since all features present a classical analogous counterpart.

3.4 RÉSUMÉ EN FRANÇAIS

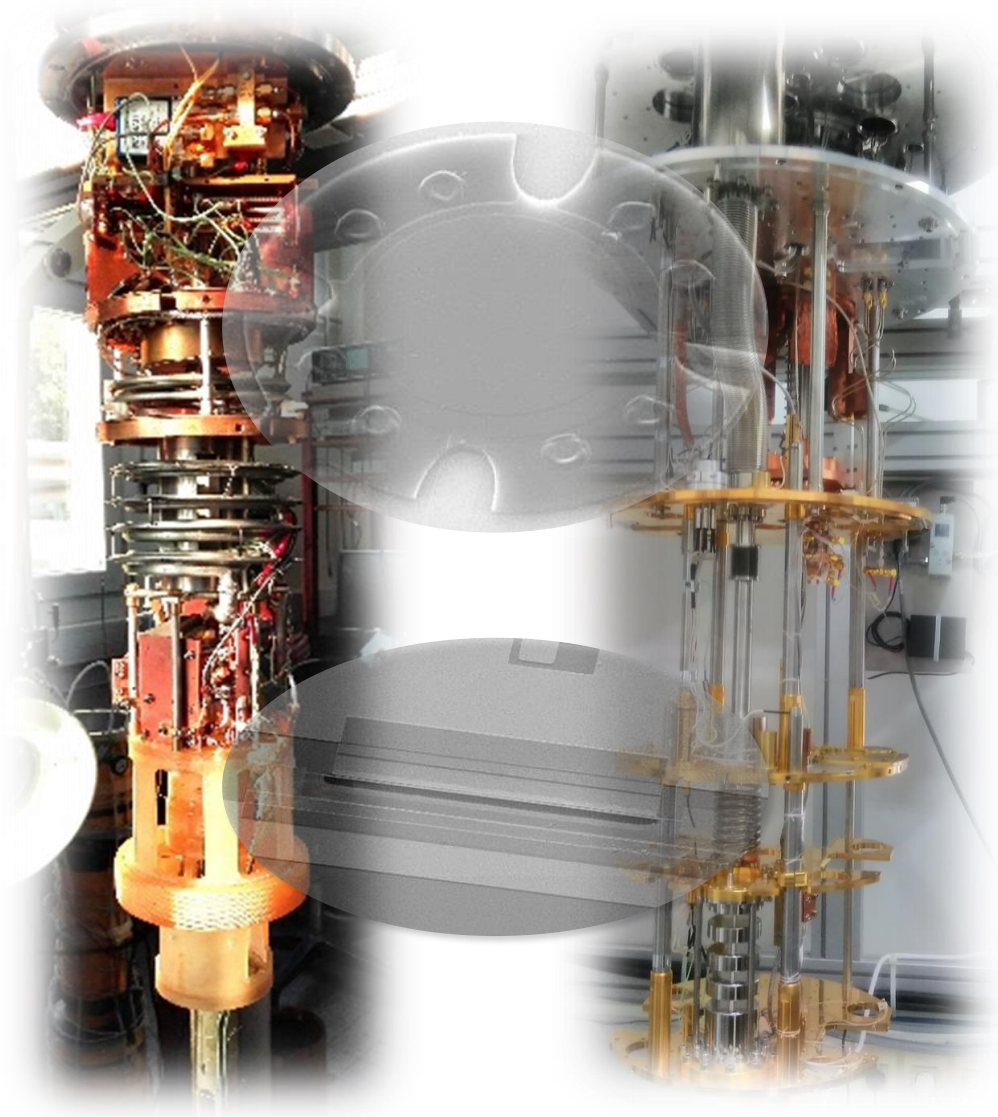
En conclusion, dans ce chapitre nous avons présenté le modèle électrique classique générique analogue au traitement standard de l'optomécanique quantique (voir Chapitre 3). Le développement analytique fournit la passerelle entre les paramètres électriques et les quantités relatives à l'optique quantique, un lien fondamental nécessaire au design et à l'optimization. Les deux approches sont strictement équivalentes dans le cas où les températures des degrés de liberté mécanique et électromagnétique sont suffisamment élevées.

De plus, une comparaison approfondie des deux modèles aboutit à une profonde compréhension de quelles propriétés mesurées sont finalement fondamentalement quantiques. Pour faire correspondre les mathématiques des deux méthodes de calcul, nous introduisons les populations par l'intermédiaire d'une énergie par quanta proportionnelle à la fréquence modale de résonance: à savoir le postulat de Planck. L'asymétrie des bandes latérales est décrite en terme classique, et nous distinguons la température du mode mécanique T_m de celle du mode micro-onde T_c ainsi que de celle du port de détection micro-onde T_{ex} . Considérant le protocole de mesure lui-même, nous calculons la limite de résolution en terme classique du protocole optomécanique optimal. Nous obtenons l'analogue classique (et relatif) de la limite quantique standard (et absolue) fixée par le principe d'Heisenberg en mécanique quantique; nous nommons cela la limite classique standard. Les quantités mesurées s'avèrent spécifiques à la mécanique quantique seule-

ment lorsque $T_m, T_c, T_{ex} \rightarrow 0$ K, en effet toutes les caractéristiques présentent un analogue classique.

Part III

MEASURING BENCHMARK DEVICES: BEAMS AND DRUMS



Experiments at cryogenic temperatures.

4

MECHANICAL STRUCTURES

The nanomechanical device is the central element of the experiments. In this chapter we briefly describe the mechanical structures of our standard NEMS in the framework of classical continuum mechanics [226]. In particular we focus on the two geometrical structures used in the presented experimental work: beams and drumheads devices. In both cases, we remind the modal decomposition analysis and the usual vibration eigenmodes necessary for the understanding of measured mechanical properties. Geometrical nonlinearities are also discussed, and the specific case of drum-head devices is presented in Ref. [217].

CONTENTS

4.1	1D beam structure	99
4.1.1	Beam modal decomposition	99
	Beam's dynamics	99
	Bending limit	100
	String limit	101
4.1.2	Beam nonlinear behaviour	102
4.2	2D drumhead structure	104
4.2.1	Drum modal decomposition	104
	Drum's dynamics	104
	Plates limit	105
	Membranes limit	106
4.2.2	Drum nonlinear behaviour	107
4.3	Conclusion	108
4.4	Résumé en français	109

4.1 1D BEAM STRUCTURE

4.1.1 Beam modal decomposition

The first mechanical structure studied is the most elementary and simple mechanical element one could think of: the well-known one-dimensional rectangular beam device. It gathers an ensemble of natural resonance modes and in particular of longitudinal, flexural, and torsional kinds. We will focus the analysis on doubly-clamped beams, as being the structure studied experimentally here, and specifically on out-of-plane and in-plane flexure excitation [245] which are the modes we measure. Indeed, even if torsional and longitudinal motion exists, they do not couple to the detection scheme used in the experiment.

BEAM'S DYNAMICS Let us consider our object as being an isotropic long-and-thin ($L \ll e$) [238] beam as shown on Fig. 4.1. The beam is assumed homogeneous with a constant cross section over its length L . Applying the least action principle to the displacement field $f(z, t)$ (Euler-Lagrange equations), one can derive the equation describing the re-

relationship between one-dimensional deflection and the corresponding applied load, the so-called Euler-Bernoulli equation [246]:

$$E_z I_z \frac{\partial^4 f(z, t)}{\partial z^4} + S_{z,0} \frac{\partial^2 f(z, t)}{\partial z^2} = -\rho A_z \frac{\partial^2 f(z, t)}{\partial t^2}, \quad (4.1.1)$$

with E_z the Young's modulus, $I_z = le^3/12$ the second moment of area, $S_{z,0} = A_z \sigma_0$ the in-built axial force load (with σ_0 the uniaxial stress), ρ the mass density and $A_z = le$ the section area (l is width and e is thickness). Here $S_{z,0}$ is taken negative for tensile. The z index refers to the axis pointing along the beam, see Fig. 4.1. The function $f(z, t)$ describes the transverse motion of the structure (in the x direction), with the proper boundary conditions. This equation essentially neglects rotational inertia of beam elementary elements δz , and all shearing forces (in contrast with Timoshenko's theory). In this 1D modeling, we neglected so far all nonlinear effects (as well as friction), which shall be discussed later in Section 4.1.2.

For such a doubly-clamped geometry, we are left with the boundary conditions:

$$f(z = [0, L], t) = 0, \quad (4.1.2)$$

$$\left. \frac{\partial f(z, t)}{\partial z} \right|_{z=[0, L]} = 0, \quad (4.1.3)$$

the first one characterizing zero z -displacement at each clamp, and the second one describing clamps as being ideal.

When dealing with small displacements, Eq. (4.1.1) is solved by a linear superposition of eigenmodes $f_n(z, t)$ i.e. writing the solution as a stationary wave, separating the spatial and temporal components:

$$f_n(z, t) = x_n(t) \psi_n(z), \quad (4.1.4)$$

with $\psi_n(z)$ the mode shape of mode n (no units), with corresponding mode resonance frequency ω_n . $x_n(t)$ is the time-dependent motion associated with the mode; by means of a Rotating-Frame Transform, it writes $a_n(t) \cos(\omega t + \phi)$ with $a_n(t)$ a slow varying amplitude variable, nonzero only for $\omega \approx \omega_n$ (resonance condition). Note that the quantitative value of $x_n(t)$ depends on the normalization choice of $\psi_n(z)$; here we will always normalize modal functions to the maximum displacement amplitude, such that at this abscissa z_n one gets $\psi_n(z_n) = 1$. Eq. (4.1.1) is exempted of a generic analytical solution, since we are concerned only by the steady-state result. The problem is then solved analytically in engineer's beam theory distinguishing two limiting cases depending on the contribution of bending rigidity and tensile stress in the mechanical object.

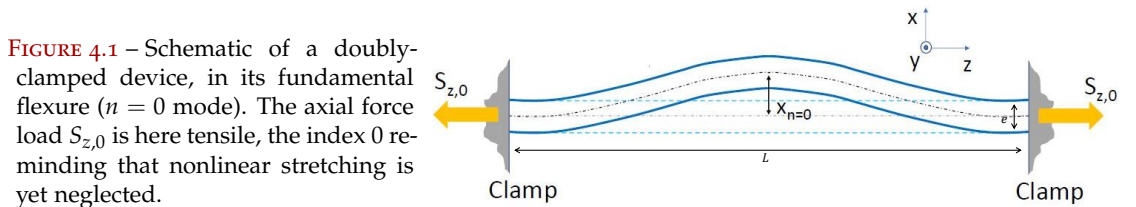


FIGURE 4.1 – Schematic of a doubly-clamped device, in its fundamental flexure ($n = 0$ mode). The axial force load $S_{z,0}$ is here tensile, the index 0 reminding that nonlinear stretching is yet neglected.

BENDING LIMIT In the low-stress (or bending) limit, the energy coming from the bending moment is much bigger than the potential energy due to stress. In this case, for

infinitely small tensile load $S_{z,0}$, the term representing the potential energy due to the external load $\propto S_{z,0}$ in Eq. (4.1.1) vanishes. The resulting "free vibration" equation writes:

$$E_z I_z \frac{\partial^4 f(z, t)}{\partial z^4} = -\rho A_z \frac{\partial^2 f(z, t)}{\partial t^2}. \quad (4.1.5)$$

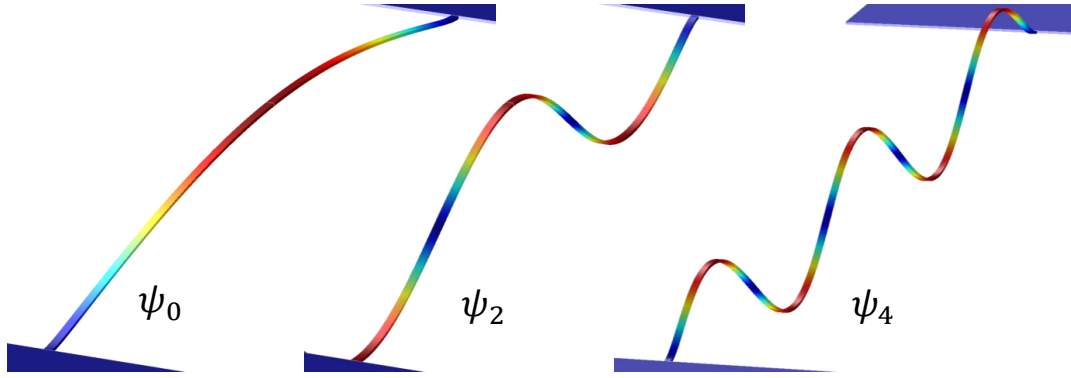


FIGURE 4.2 – Numerical simulations performed for one of our devices (bilayer aluminium/high-stress silicon-nitride doubly-clamped beam). The (symmetric) modes shown are: first, third, fifth out-of-plane flexural modes (from left to right). Beam parameters used for calculation are given in Tab. 6.1. Color scale displays the arbitrary amplitude of each eigenmode.

This equation is easily solved in the Fourier domain. The solution for the displacement field $f_n(z, t)$ depends on the frequency ω_n :

$$\psi_n(z) = C_1 \sinh\left(\lambda_n \frac{z}{L}\right) + C_2 \cosh\left(\lambda_n \frac{z}{L}\right) + C_3 \sin\left(\lambda_n \frac{z}{L}\right) + C_4 \cos\left(\lambda_n \frac{z}{L}\right), \quad (4.1.6)$$

with λ_n the mode parameter directly linked to ω_n by the dispersion relation:

$$\omega_n = \sqrt{\frac{E_z I_z}{\rho A_z}} \left(\frac{\lambda_n}{L}\right)^2. \quad (4.1.7)$$

The coefficients C_1, C_2, C_3 and C_4 are constants which depend directly on the set of boundary conditions. The dispersion relation is quadratic in λ_n , with $\lambda_0 \approx 4.730$, $\lambda_2 \approx 10.996$, and $C_2 = -C_4$, $C_1 = -C_3$, and $C_4/C_3 \approx 1$ [226].

STRING LIMIT The high-stress (or string) limit corresponds to the case where the potential energy coming from the bending moment is much smaller than the one due to the tensile stored stress. In such situation, we recover the "vibrating string" equation:

$$S_{z,0} \frac{\partial^2 f(z, t)}{\partial z^2} = -\rho A_z \frac{\partial^2 f(z, t)}{\partial t^2}. \quad (4.1.8)$$

In this case the solution of the modal profile is:

$$\psi_n(z) = C_1 \sin\left(\lambda_n \frac{z}{L}\right) + C_2 \cos\left(\lambda_n \frac{z}{L}\right), \quad (4.1.9)$$

with the natural resonance frequencies ω_n following:

$$\omega_n = \sqrt{\frac{|S_{z,0}|}{\rho A_z} \frac{\lambda_n}{L}} = \frac{(n+1)\pi}{L} \sqrt{\frac{|S_{z,0}|}{\rho A_z}}. \quad (4.1.10)$$

The dispersion relation is then linear with mode parameter λ_n . One set of boundary conditions, Eq. (4.1.3), has to be relaxed; we have $C_2 = 0$ and $C_1 = 1$. Most of the beam devices used in this thesis, and in particular the $50 \mu\text{m}$ long beam, are made of high-stress silicon-nitride (SiN). For these devices Eq. (4.1.10) is appropriate for the evaluation of modal resonance frequencies ω_n . On Fig. 4.2 we present numerical finite element simulations (eigenfrequency analysis) of the bilayer doubly-clamped beam used experimentally (parameters displayed in Tab. 6.1 and Fig. 6.3). The vibration profiles are displayed for the three first out-of-plane modes. The bilayer nature of the beam device is modeled in the simulation, but in the previous section, analytical expressions do not take into account this property. Analytically, this fact implies only very small corrections [74], as the stress is mostly present in the silicon-nitride layer. Experimentally we measured the first out-of-plane mode (ψ_1) and an example of measured Brownian spectrum displaying the mechanical resonance is shown on Fig. 4.3 left side.

4.1.2 Beam nonlinear behaviour

Flexural oscillations of the mechanical object produce an elongation, as such, some additional stretching appears in the structure. This phenomenon is called a geometric nonlinearity, because it originates in the structure of the device: a cantilever does not experience stretching.

The total stretching writes $S_{z,0} \rightarrow S_{z,0} + \Delta S$ with $|\Delta S| = E_z A_z \Delta L / L$ and ΔL the extension [242]:

$$\Delta L = \frac{1}{2} \int_0^L \left(\frac{\partial f(z,t)}{\partial z} \right)^2 dz, \quad (4.1.11)$$

expanded at lowest order in f . Note that from Eq. (4.1.4) this expression is quadratic in motion amplitudes $x_n(t)$, thus a simple Rotating-Wave Approximation leads to an extension $\Delta L \propto a_n^2 / 2$ (the slow variables): the nonlinear stretching is essentially a static effect, which is why there is no time-delay in the relationship between ΔS and ΔL . Considering a superposition of modes in f leads to nonlinear mode coupling [152]; we shall not consider this situation here.

The basic nonlinear modeling consists then in reinjecting Eq. (4.1.11) into Eq. (4.1.1), and neglecting any other alterations due to the large motion amplitude, e.g. higher order terms in the radius of curvature of the distorted shape or the modification of the mode shape $\psi_n(z)$ itself [242, 44]. While the validity of these assumptions is questionable, it has been found experimentally that this modeling describes very well experimental results [119, 152, 169].

For a single mode $f \rightarrow f_n$, the projection of Eq. (4.1.1) onto it (i.e. multiplying the equation by ψ_n and integrating over the beam length) leads to the definition of modal parameters:

$$m_n = \rho A_z \int_0^L [\psi_n(z)]^2 dz, \quad (4.1.12)$$

$$k_n = E_z I_z \int_0^L \left[\frac{d^2 \psi_n(z)}{dz^2} \right]^2 dz - S_z \int_0^L \left[\frac{d\psi_n(z)}{dz} \right]^2 dz, \quad (4.1.13)$$

$$\tilde{k}_n = \frac{E_z A_z}{2L} \left(\int_0^L \left[\frac{d\psi_n(z)}{dz} \right]^2 dz \right)^2, \quad (4.1.14)$$

with m_n the mode mass, k_n the mode spring constant and \tilde{k}_n the so-called Duffing nonlinear parameter [225]. The resonance frequency verifies $\omega_n = \sqrt{k_n/m_n}$. In the particular case of high stress doubly-clamped beams where the mode profile writes:

$$\psi_n(z) = \sin \left[\frac{(n+1)\pi}{L} z \right], \quad (4.1.15)$$

the Duffing nonlinear parameter is considerably simplified:

$$\frac{\tilde{k}_n}{m_n} = \frac{E_z}{2\rho} \left[\frac{(n+1)\pi}{L} \right]^4. \quad (4.1.16)$$

Including in Eq. (4.1.1) a damping Γ and a drive term $F(t)$ is straightforward [242]. The obtained equation of motion for x_n is then the one of a driven harmonic oscillator plus a purely cubic nonlinear restoring term:

$$\ddot{x}_n + \Gamma \dot{x}_n + \omega_0 x_n + \frac{\tilde{k}_n}{m_n} x_n^3 = \frac{F(t)}{m_n}. \quad (4.1.17)$$

Note that from the fluctuation-dissipation theorem (see Chapter 2), the force $F(t)$ should contain a stochastic component which is defined from the damping parameter Γ . This shall be neglected here. They are a variety of models describing the origin of mechanical damping Γ [226]. One microscopic origin usually referred to for MEMS and NEMS is the coupling of phonons to localized two-level-systems [118, 221]. These material-dependent aspects shall not be discussed here.

Eq. (4.1.17) has a well-known solution in the case of a coherent driving force $F(t) = F_0 \cos(\omega t + \phi)$ [237]. In the high- Q limit, the resultant mechanical susceptibility is a Lorentzian peak at small drive amplitudes. When F_0 is increased, the susceptibility is distorted and the peak deforms into a triangular shape.

Note that \tilde{k}_n is always positive, because of stretching (the mode "hardens"); in the steady-state ($a_n = \text{constant}$), the resonant response measured while sweeping the drive frequency upwards will be pulled up, with the frequency at maximum amplitude a_n^{max} given by [242, 73]:

$$\omega_n^{\text{res}} = \omega_n + \beta_n (a_n^{\text{max}})^2, \quad (4.1.18)$$

with:

$$\beta_n = \frac{3}{8} \omega_n \frac{\tilde{k}_n}{k_n}. \quad (4.1.19)$$

A simple quadratic fit of the frequency pulling is thus enough to extract the Duffing parameter. While this cannot be performed in-situ in our optomechanical setups because we do not have an RF gate connected to the device (Chapter 6), it can be done on separate purely electro-mechanical devices. The free-decay solution can also be analytically produced [73].

A very similar modeling can be applied to 2D objects; we will thus now present a brief description of the mechanics of drumhead devices, which are the second type of NEMS used in this thesis.

4.2 2D DRUMHEAD STRUCTURE

4.2.1 Drum modal decomposition

The second type of mechanical structures we are interested in is the two-dimensional circular membrane under tension, also known as the drumhead NEMS structure. Similarly to the beam mechanical object, circular membranes gather an ensemble of natural internal resonances. The detection scheme used experimentally couples only to transverse vibrations of the drum device, therefore we will focus the analysis on this particular family of modes.

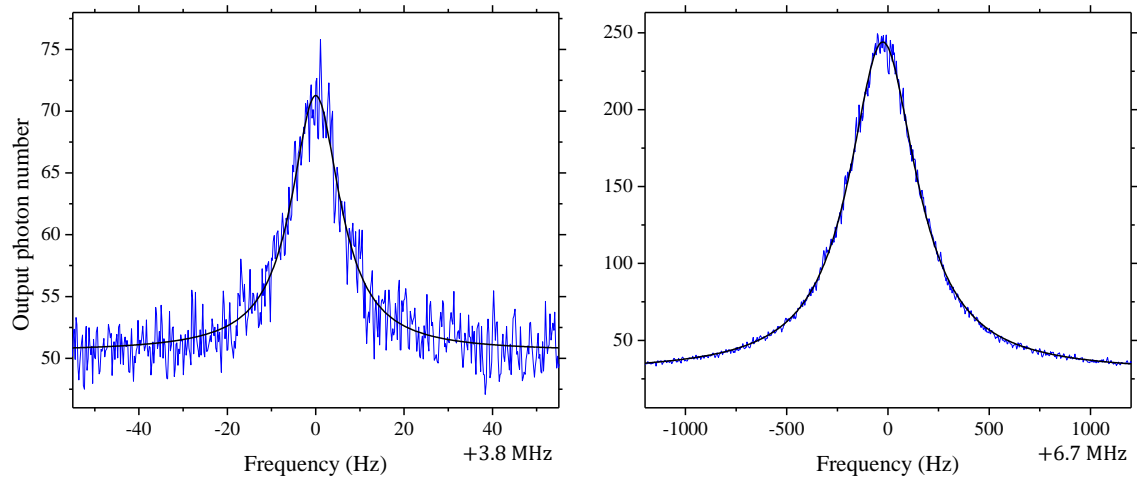


FIGURE 4.3 – Power spectral densities of thermomechanical noise measured with the first out-of-plane mode of the beam device (left side) at 214 mK ($P_{in} \approx 1.5$ nW) and with the first mode of the badly-coupled drumhead NEMS (right side) at 25 mK ($P_{in} \approx 1.2$ nW). Both measurements have been performed in the linear regime of optomechanics [where $\Gamma_{opt} = 0$ (see Chapter 2)]. Blue noisy curves are experimental measurements and black lines are lorentzian fits. Note that the two sets of data have a different SNR due to the significantly different coupling strengths.

DRUM'S DYNAMICS For 2D circular structures we now consider the same hypothesis as for beam devices: let us consider our isotropic drum as being infinitely thin ($R_d \gg e$), see Fig. 4.4. The generic formalism applied to thin drums obtained within the same continuum mechanics reasoning that leads to the Euler-Bernoulli equation [244, 247], Eq. (4.1.1), is known as the Kirchhoff-Love equation [31]:

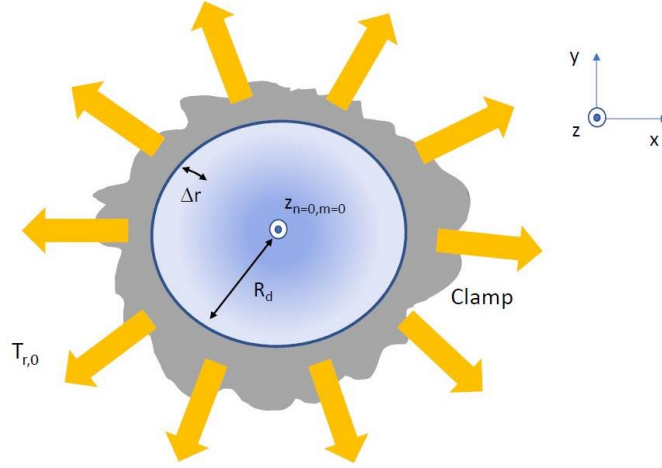
$$D_r \Delta^2 f(r, \theta, t) + T_{r,0} \Delta f(r, \theta, t) = -\rho e \frac{\partial^2 f(r, \theta, t)}{\partial t^2}, \quad (4.2.1)$$

with $\Delta \cdot = \frac{1}{r} \partial_r (r \partial_r \cdot) + \frac{1}{r^2} \partial_\theta^2 \cdot$ the Laplacian operator in polar coordinates and:

$$D_r = \frac{1}{12} \frac{e^3 E_r}{1 - \nu_r^2}, \quad (4.2.2)$$

the flexural rigidity (bending stiffness) in the plane of the drum (ν_r being Poisson's ratio), $2\pi R_d T_{r,0} = 2\pi R_d e \sigma_0$ the tension within the drum (σ_0 being the biaxial stress), e its thickness and R_d its radius. We assume materials properties E_r , ν_r , ρ , σ_0 and thickness e to be homogeneous and isotropic over the device. Note that in Eq. (4.2.1) the $T_{r,0}$ term resulting from the biaxial stress σ_0 is taken negative for tensile load. The Dirichlet boundary

FIGURE 4.4 – Schematic of a drum device, in its fundamental flexure ($n = 0, m = 0$ mode). The biaxial force $2\pi R_d T_{r,0}$ is here tensile. R_d is the radius of the drum of thickness e . Δr is the nonlinear stretching discussed in the following.



conditions for such a structure writes:

$$f(r = R_d, \theta, t) = 0, \quad (4.2.3)$$

$$\left. \frac{\partial f(r, \theta, t)}{\partial r} \right|_{r=R_d} = 0. \quad (4.2.4)$$

Similarly to the Euler-Bernoulli beam theory, in the limit of small displacements, we separate temporal and spatial parts of the displacement field $f(r, \theta, t)$ and write:

$$f_{n,m}(r, \theta, t) = z_{n,m}(t) \psi_{n,m}(r, \theta), \quad (4.2.5)$$

with $\psi_{n,m}(r, \theta) = \phi_{n,m}(r) \cos(n\theta)$ the mode shape and $z_{n,m}(t)$ the motion amplitude. Note that now two indexes are necessary to label all 2D flexural modes of the circular structure. As for beam theory, the problem is solved analytically in two simple limits: high or low stress cases [217].

PLATES LIMIT In the low-stress (or plates) limit the term $\propto T_{r,0}$ vanishes in Eq. (4.2.1) and taking into account boundary conditions, the solution writes:

$$\phi_{n,m}(r) = \frac{I_n\left(\frac{\lambda_{n,m} r}{R_d}\right) - \frac{I_n(\lambda_{n,m})}{J_n(\lambda_{n,m})} J_n\left(\frac{\lambda_{n,m} r}{R_d}\right)}{I_n\left(\frac{\lambda_{n,m} r_{n,m}}{R_d}\right) - \frac{I_n(\lambda_{n,m})}{J_n(\lambda_{n,m})} J_n\left(\frac{\lambda_{n,m} r_{n,m}}{R_d}\right)}, \quad (4.2.6)$$

where J_n defines the n^{th} -order Bessel function of the first kind and $I_n(\cdot) = i^{-n} J_n(i \cdot)$ the n^{th} -order modified Bessel function of the first kind. $\lambda_{n,m}$ is as usual the mode parameter and $r_{n,m}$ the radial position of the maximum amplitude (occurring for given angles θ when $n \neq 0$). In this case the natural resonance frequencies $\omega_{n,m}$ follow the following dispersion relation:

$$\omega_{n,m} = \sqrt{\frac{D_r}{\rho e}} \left(\frac{\lambda_{n,m}}{R_d} \right)^2. \quad (4.2.7)$$

The dispersion relation is quadratic in $\lambda_{n,m}$, as for low-stress beams. The first axisymmetric modes verify $\lambda_{0,0} = 3.19622$, $\lambda_{0,1} = 6.30644$, $\lambda_{0,2} = 9.43950$ with $r_{0,m} = 0$.

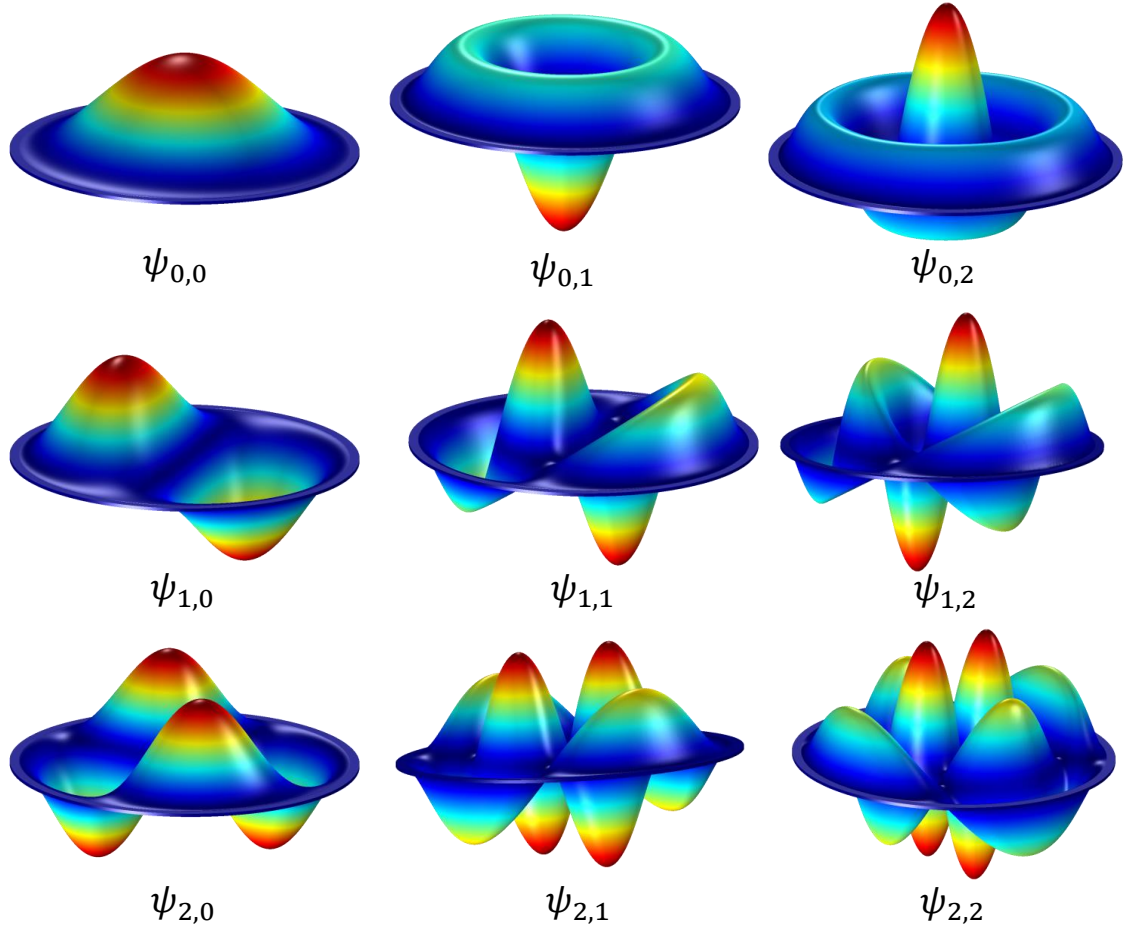


FIGURE 4.5 – Numerical simulations performed for one of our devices (drumhead structure). The nine first modes of a circular membrane are displayed in matrix form. Drum parameters used for calculation given in Tab. 6.1. The color scale displays the arbitrary amplitude of each eigenmodes.

MEMBRANES LIMIT In the high-stress (or membranes) limit the term $\propto D_r$ vanishes in Eq. 4.2.1 and taking into account boundary conditions, the solution writes ($T_{r,0} < 0$):

$$\phi_{n,m}(r) = \frac{J_n\left(\frac{\lambda_{n,m}r}{R_d}\right)}{J_n\left(\frac{\lambda_{n,m}r_{n,m}}{R_d}\right)}, \quad (4.2.8)$$

and the natural resonance frequencies $\omega_{n,m}$ follow:

$$\omega_{n,m} = \sqrt{\frac{|T_{r,0}|}{\rho e}} \left(\frac{\lambda_{n,m}}{R_d}\right). \quad (4.2.9)$$

The dispersion relation is now linear, with $\lambda_{0,0} = 2.40483$, $\lambda_{0,1} = 5.52008$, and $\lambda_{0,2} = 8.65373$, with $r_{0,m} = 0$. Numerical simulations [217] for first modes of circular structures show that both high and low stress calculated topographies are very similar and differ by small corrections. On Fig. 4.5 we present finite element simulations of the first nine modes of a typical drumhead NEMS used experimentally for $(n,m) \in [0,1,2]^2$. On the first line we display the three first axisymmetric vibration profiles. For both measured

drumhead devices, we exploited the first mode $\psi_{0,0}$ and an example of such measured thermomechanical spectrum in the case of the badly-coupled drum NEMS is displayed on Fig. 4.3.

4.2.2 Drum nonlinear behaviour

The nonlinear behaviour of drumhead mechanical structures is very similar to the one already introduced for beam devices. In this case the derivation of the expression of the Duffing nonlinear parameter is much more complex. There is an extremely vast literature on the subject, which is not easily tractable for our purpose. We therefore developed a modeling based on the very same ideas as for beams, which leads to simple analytic expressions which require only the knowledge of the mode shapes [217]. We summarize the results of this work below (see [217] for analytic calculations and numerical estimations of geometric nonlinearities for drum based NEMS).

Similarly to the beam case, the stretching in 2D is a change of surface area per unit angle. This writes mathematically:

$$\frac{\delta S}{\delta \theta} = \frac{1}{2} \int_0^{R_d} \left[\left(\frac{\partial f(r, \theta, t)}{\partial r} \right)^2 + \frac{1}{r^2} \left(\frac{\partial f(r, \theta, t)}{\partial \theta} \right)^2 \right] r dr, \quad (4.2.10)$$

at lowest order in f . Geometrically, this quantity is directly linked to the radial strain $\epsilon = \Delta r / R_d$ experienced by the drum at its edge $\delta S = R_d \delta \theta \Delta r$, i.e. $\delta S(\theta, t) / \delta \theta = R_d^2 \epsilon(\theta, t)$, see Fig. 4.4. Injecting the mode shape Eq. (4.2.5) into Eq. (4.2.10), one obtains:

$$\epsilon_{n,m}(\theta, t) = \left(\frac{z_{n,m}(t)}{R_d} \right)^2 \left[\frac{C_{n,m}^{(1)} + C_{n,m}^{(2)}}{2} + \frac{C_{n,m}^{(1)} - C_{n,m}^{(2)}}{2} \cos(2n\theta) \right], \quad (4.2.11)$$

where we have defined (constants with no dimensions):

$$C_{n,m}^{(1)} = \frac{1}{2} \int_0^{R_d} \left(\frac{d\phi_{n,m}(r)}{dr} \right)^2 r dr, \quad (4.2.12)$$

$$C_{0,m}^{(2)} = C_{0,m}^{(1)} \quad (4.2.13)$$

$$C_{n,m}^{(2)} = \frac{1}{2} \int_0^{R_d} \left[\frac{n}{r} \phi_{n,m}(r) \right]^2 r dr, \quad (n \neq 0). \quad (4.2.14)$$

For $n = 0$, the problem is isotropic and the solution rather straightforward. However for $n \neq 0$, the stress within the drum has an extra angle-dependent component $\cos(2n\theta)$. The Kirchhoff-Love differential equation (Eq. (4.2.1)) has thus to be modified to:

$$D_r \Delta^2 f + \int_{-\frac{\epsilon}{2}}^{+\frac{\epsilon}{2}} \left[\frac{1}{r} \frac{\partial}{\partial r} \left(\sigma_r r \frac{\partial f}{\partial r} \right) + \frac{1}{r^2} \frac{\partial}{\partial \theta} \left(\sigma_\theta \frac{\partial f}{\partial \theta} \right) \right] dz = -\rho e \frac{\partial^2 f}{\partial t^2}, \quad (4.2.15)$$

with $\sigma_r(r, \theta, z, t)$ and $\sigma_\theta(r, \theta, z, t)$ the superposition of the initial biaxial stress σ_0 plus the elastic response of the drum to the strain ϵ , Eq. (4.2.11). As for beams, we neglect any other nonlinear contribution arising from the large motion amplitude. Shear stresses (e.g. the $\sigma_{r,\theta}$ component) are not taken into account in the Kirchhoff-Love theory, as in the Euler-Bernoulli beam theory.

One can thus compute the stress field (arising from the two-dimensional problem), and project Eq. (4.2.15) on a given mode n, m and define the modal parameters in a similar fashion to Eqs. (4.1.12, 4.1.13):

$$M_{n,m} = \rho e \int_0^{2\pi} \int_0^{R_d} [\psi_{n,m}(r, \theta)]^2 r dr d\theta, \quad (4.2.16)$$

$$K_{n,m} = \int_0^{2\pi} \int_0^{R_d} \left[D_r \psi_{n,m}(r, \theta) \Delta^2 \psi_{n,m}(r, \theta) + T_{r,0} \psi_{n,m}(r, \theta) \Delta \psi_{n,m}(r, \theta) \right] r dr d\theta, \quad (4.2.17)$$

where $M_{n,m}$ and $K_{n,m}$ corresponds in this case to the mode mass and mode spring constant respectively. As usual the resonance frequency verifies $\omega_{n,m} = \sqrt{K_{n,m}/M_{n,m}}$.

Beyond the usual linear coefficients, the Duffing term analogous to Eq. (4.1.14) finally writes:

$$\begin{aligned} \tilde{K}_{n,m} = & -\frac{eE_r}{R_d^2} \left[\frac{C_{n,m}^{(1)} + C_{n,m}^{(2)}}{2} \eta^{(0)}(\nu_r) \int_0^{2\pi} \int_0^1 [\psi_{n,m}(\tilde{r}, \theta) \Delta \psi_{n,m}(\tilde{r}, \theta)] \tilde{r} d\tilde{r} d\theta \right. \\ & + \frac{C_{n,m}^{(1)} - C_{n,m}^{(2)}}{2} \left(\eta_r^{(n)}(\nu_r) \frac{\pi}{2} \int_0^1 \phi_{n,m}(\tilde{r}) \frac{1}{\tilde{r}} \frac{d}{d\tilde{r}} \left(\tilde{r}^{2n+1} \frac{d\phi_{n,m}(\tilde{r})}{d\tilde{r}} \right) \tilde{r} d\tilde{r} \right. \\ & \left. \left. + \eta_\theta^{(n)}(\nu_r) n^2 \frac{\pi}{2} \int_0^1 \tilde{r}^{2(n-1)} [\phi_{n,m}(\tilde{r})]^2 \tilde{r} d\tilde{r} \right) \right], \quad (4.2.18) \end{aligned}$$

with the integrals written in normalized units $\tilde{r} = r/R_d$ (no dimensions). We defined $\eta^{(0)}(\nu_r) = (1 - \nu_r)^{-1}$ and the two functions $\eta_r^{(n)}(\nu_r)$ and $\eta_\theta^{(n)}(\nu_r)$ for $n \neq 0$ as [217]:

$$\eta_r^{(n \neq 0)}(\nu_r) = \frac{1 + 2n - 2(1 + n)\nu_r}{(1 + 2n)(1 + \nu_r)}, \quad (4.2.19)$$

$$\eta_\theta^{(n \neq 0)}(\nu_r) = -\frac{3 + 4n}{(1 + 2n)(1 + \nu_r)}. \quad (4.2.20)$$

Note that for the beam device, Eq. (4.1.14) leads to a scaling of the Duffing parameter $\propto E_z A_z / L^3$ whereas here, for the drum device Eq. (4.2.18) leads to a similar scaling $\propto E_r (2\pi e R_d) / R_d^3$. In both cases, the Duffing effect is a stiffening.

4.3 CONCLUSION

In this Chapter we succinctly present the two types of mechanical structures used experimentally in this thesis: the 1-dimensional beam geometry and the 2-dimensional drumhead one. For both types of devices, we remind the basics of the continuum mechanics theory and introduce the standard modal analysis describing vibrations eigenmodes. Whether for beams or drumhead NEMS, we consider two simple limits where the eigenvalue problem can be solved analytically: the high and low stress limits. Furthermore, in this context we introduce the concept of geometrical nonlinearity, which originates in the stretching of the devices. This is the major source of mechanical nonlinearity for our beam and drum structures, which have clamped boundary conditions. We thus present the usual modeling of the Duffing stretching that can be found in books [242], and the analog development that we adapted to 2D structures [217]. All these results make the

basic analytic library that is required for the modeling of the mechanical devices used in our experiments, Chapter 6.

4.4 RÉSUMÉ EN FRANÇAIS

Dans ce chapitre, nous présentons succinctement les deux types de structures mécaniques utilisées expérimentalement: les poutres unidimensionnelles et les membranes (deux dimensions). Pour ces deux géométries différentes, nous rappelons les équations de base de la mécanique des milieux continus et introduisons l'analyse modale dans le but de décrire les résonances mécaniques. Dans ces deux cas, nous pouvons considérer deux limites dans lesquelles le problème peut être résolu analytiquement: cas de forte ou faible tension. Dans ce contexte nous introduisons le concept de non-linéarité géométrique, ayant pour origine l'élongation des structures mécaniques. Pour nos structures de types poutres et tambours encastrées sur les bords, ces non-linéarités géométriques sont dominantes. Nous présentons ici la modélisation usuelle du Duffing qui peut être trouvée dans l'ouvrage [242], ainsi que notre développement analogue adapté aux structures 2D [217]. Ces résultats forment la librairie analytique requise pour modéliser les structures mécaniques utilisées dans nos travaux expérimentaux (voir Chapitre 6).

5

MICROWAVE CIRCUIT PROPERTIES

In this chapter, we present the basic steps necessary for the modeling and characterization of our microwave resonators. Numerical simulations and measurements obtained from the scattering matrix are presented. We also discuss a method based on electromechanical numerical simulations that enables us to predict the coupling strength g_0 of our actual beam design.

CONTENTS

5.1	Superconducting microwave resonators	111
5.1.1	Idealized resonator	111
5.1.2	Microwave cavity characterization	114
5.2	Modeling optomechanical coupling	117
5.3	Conclusion	118
5.4	Résumé en français	118

5.1 SUPERCONDUCTING MICROWAVE RESONATORS

5.1.1 Idealized resonator

Superconducting microwave optomechanical systems are usually based on transmission line type resonators, typically coplanar wave-guide (CPW) cavities (e.g. $\lambda/4$ resonators) or lumped element circuits made up of capacitive and inductive elements. Typical superconducting lumped element devices [223] can be designed with dimensions much smaller than a wavelength whereas transmission line resonators have usually only one dimension of the order of the wavelength [239].

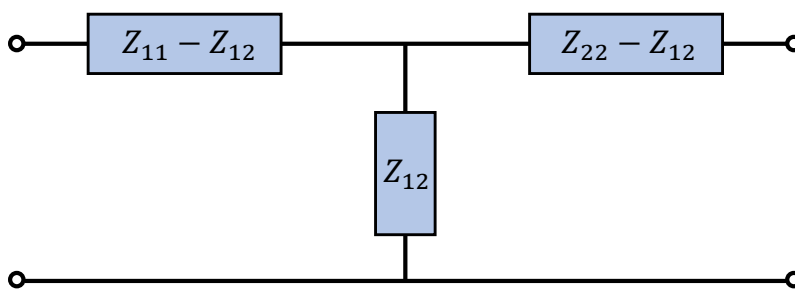


FIGURE 5.1 – T equivalent impedance circuit model for a reciprocal generic two-port network [232].

On Fig 5.1 we present the theoretical generic modeling of such an electrical element using the impedance matrix $[Z_{ij}]$ formalism [232]. This generic T-shape scheme enables to model both two-port and one-port microwave cavity design. Using the network formalism [232, 156] one can derive the expression of the full scattering matrix and in particular the transmission coefficient:

$$S_{12} = \frac{2Z_{12}Z_0}{\Delta Z}, \quad (5.1.1)$$

and the reflection one:

$$S_{11} = \frac{(Z_{11} - Z_0)(Z_{22} + Z_0) - Z_{12}^2}{\Delta Z}, \quad (5.1.2)$$

where we introduce $\Delta Z = (Z_{11} + Z_0)(Z_{22} + Z_0) - Z_{12}^2$ and Z_0 as being the usual circuit characteristic impedance (for us, 50 Ohm). For a typical two-port bidirectionally coupled microwave cavity design, Z_{11} and Z_{22} represent imperfections in the circuitry, in particular impedance mismatch. We will assume here a completely symmetric model, writing for the two ports:

$$Z_{11} = Z_{12} + Z_0(\epsilon_R + i\epsilon_I), \quad (5.1.3)$$

$$Z_{22} = Z_{12} + Z_0(\epsilon_R + i\epsilon_I), \quad (5.1.4)$$

where ϵ_R and ϵ_I represent dissipative-like and dispersive-like electrical impedances respectively (which should be zero in the ideal case). In the literature ϵ_I is sometimes attributed, with no really clear proofs, to the bonding wires [167, 162]. The resonant part of the microwave circuits are modeled in the literature as ideal parallel RLC circuits, shorting the ports (via R) at resonance. In our case we will write the electrical impedance of the resonator at first order in $\omega = \omega_{cav} + \Delta\omega$ as:

$$Z \approx \left[\frac{1}{R} + 2iC_t\Delta\omega \right]^{-1}, \quad (5.1.5)$$

where C_t is the total capacitance of the circuit and the cavity resonance frequency verifies $\omega_{cav} = 1/\sqrt{LC_t}$. In the bidirectional case, transmission and reflection can be rewritten under the following forms in decibel units:

$$S_{12}[\omega]_{dB} = -10 \log \left| (1 + \epsilon_R^2) \left[1 + \left(\frac{Q_{exR}}{Q_{exI}} \right)^2 \right] \right| + 20 \log \left| 1 - \frac{Q(Q_{exR}^{-1} + iQ_{exI}^{-1})}{1 + 2iQ\frac{\Delta\omega}{\omega_{cav}}} \right|, \quad (5.1.6)$$

$$S_{11}[\omega]_{dB} = 20 \log \left| \frac{\epsilon_R + i\epsilon_I}{1 + \epsilon_R + i\epsilon_I} - \frac{1}{1 + \epsilon_R} \frac{QQ_{exR}^{-1}}{1 + 2iQ\frac{\Delta\omega}{\omega_{cav}}} \right|, \quad (5.1.7)$$

where $Q = \omega_{cav}/\kappa$ is the total microwave quality factor, $Q_{exR} = \omega_{cav}/\kappa_{ex}$ is the (total) external coupling contribution to the quality factor, representing the quality of the photons transfer between the standing intracavity wave and the travelling wave in the two-port capacitively coupled feeding line (with $\kappa_{ex}/2$ associated to each port). Note that for a design with two *distinct* ports, this expression would read differently [12]. Q_{exI} corresponds to the imaginary component of the external impedance, attributed to all microwave circuit imperfections [167, 162]. This Q_{exI} has the additional effect of renormalizing the cavity resonance frequency $\omega_{cav} \rightarrow \omega_{cav} \left(1 - (2Q_{exI})^{-1} \right)$. Note that the imperfections introduced ϵ_R and ϵ_I renormalize the measured backgrounds in both S_{12} and S_{11} . We point out that for $\epsilon_R, \epsilon_I \rightarrow 0$, we recover the standard relation $S_{12} = 1 + S_{11}$.

On Fig. 5.2 we present our design made for the beam motion detection. The cavity is made by a meandering wire, which is capacitively coupled on one side to a transmission line. The cavity is here made of niobium. This design is significantly much more compact than the transmission line type resonators. All internal losses are represented by the $R = R_{in}$ element included in the model, see Chapter 3 for the electric circuit description.

Concerning our design, electromagnetic finite element simulation have been performed for modal characterization (see Fig. 5.2).

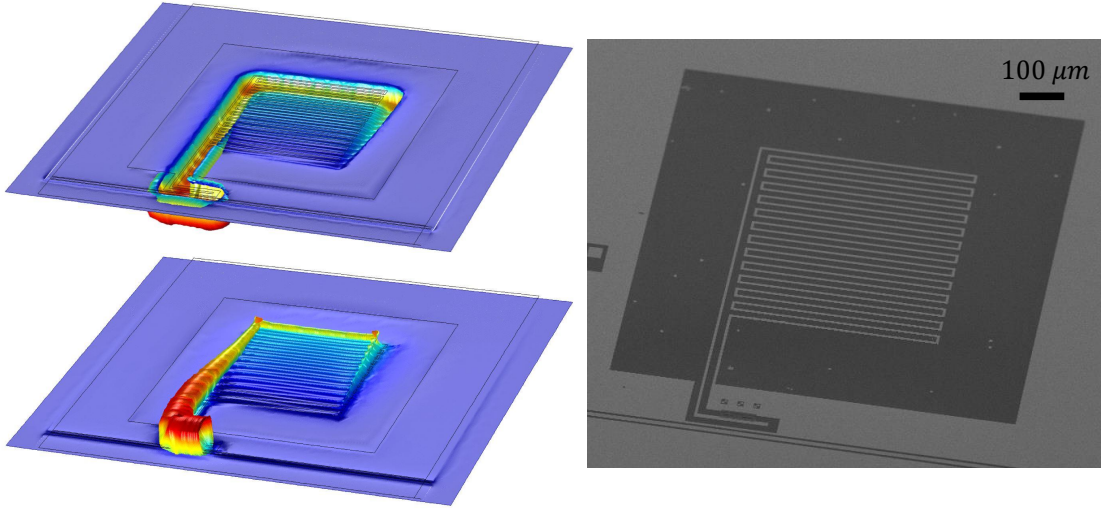


FIGURE 5.2 – Left: Numerical simulation of the lumped element type microwave resonator designed for the beam device motion detection. We display the shape of the first intra-cavity mode at about 6 GHz, the simulated damping being linked to material losses and depending on boundary conditions chosen to resolve the problem. Color displays the absolute value of the concentrated electric field in arbitrary units (at the two extremes of an oscillation period). Right: Corresponding SEM picture of the micro-fabricated microwave cavity resonator. One can see the coupled transmission line at the bottom of the image.

On Fig. 5.3, we compare both transmission and reflection measurements performed on our beam-based bidirectional design. Linear response measurements of the microwave cavity for S_{12} and S_{11} are perfectly fit with Eq. (5.1.6) and Eq. (5.1.7) respectively. Both fits are in agreement with a relative error of 15% for both Q and Q_{exR} parameters. In this bidirectional configuration, the fit background of S_{11} is non zero because of imperfections; it is therefore rather arbitrary and has been shifted to zero dB for clarity in the figure. On Fig. 5.3 bottom, we compare microwave optomechanical measurements performed in both transmission and reflection configurations. Perfect agreement is obtained for the output amplitude and for the effective damping within ± 2 dBm error bars in both injection and detection lines.

Both drum-based chips are designed in a one-port way. For such reflection schemes we assume electrical imperfections on one arbitrary side only writing:

$$Z_{11} = Z_{12} + Z_0(\epsilon_R + i\epsilon_I), \quad (5.1.8)$$

$$Z_{22} \rightarrow +\infty, \quad (5.1.9)$$

which enables to recover the standard reflection coefficient from S_{11} . With these assumptions, the reflection component of the scattering matrix in decibel units then writes:

$$S_{11}[\omega]_{db} = 20 \log \left| 1 - \frac{2}{1 + \epsilon_R} \frac{QQ_{exR}^{-1}}{1 + 2iQ \frac{\Delta\omega}{\omega_{cav}}} \right|, \quad (5.1.10)$$

with the same convention. Note that here Q_{exI} has the same frequency renormalization as in the bidirectional scheme, $\omega_{cav} \rightarrow \omega_{cav} \left(1 - (2Q_{exI})^{-1} \right)$.

Drum chips have been made in Aalto university. Simulations and characterizations have been performed at Aalto, and are not reproduced here. They also have been designed with lumped element type cavities [57], but for reflection measurements. The cavities are here made of aluminum. For this purpose we use an additional circulator, separating the input and output fields into two physical ports. On Fig. 5.4, we present a linear response measurement in reflection on the chip containing the badly-coupled drumhead device. Data are perfectly fit with Eq. (5.1.10). Note that with this specific configuration, the measured S_{11} is essentially a symmetric Lorentzian lineshape.

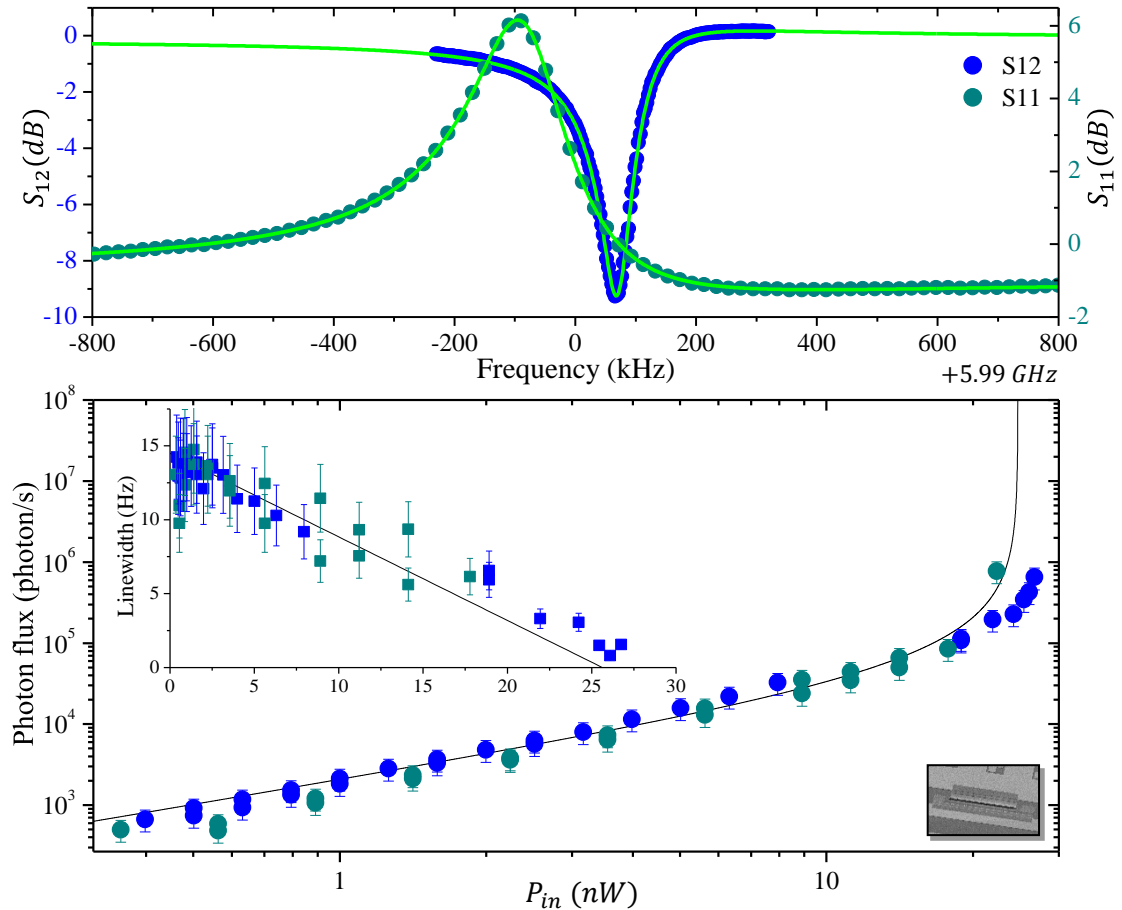


FIGURE 5.3 – Comparison of transmission and reflection measurements on the two-port bidirectional beam-based design at 215 mK. Top: Microwave cavity linear response measurements performed in transmission (S_{12} in blue) and reflection (S_{11} in dark cyan). Backgrounds are arbitrarily shifted for convenience and green lines are theoretical fits from Eq. (5.1.6) for S_{12} (with $Q \approx 49000$, $Q_{exR} \approx 78000$ and $Q_{exI} \approx -2000$) and Eq. (5.1.7) for S_{11} (with $Q \approx 42000$, $Q_{exR} \approx 67000$, $\epsilon_R \approx -0.26$ and $\epsilon_I \approx -0.049$). Note that resonance frequencies are slightly different between S_{12} and S_{11} as they have been measured during two different runs. Main bottom: Output photon flux as a function of power P_{in} measured in S_{12} (blue dots) and S_{11} circuit configurations (dark cyan dots). The black curve is a theoretical fit (see Chapter 2). Bottom inset: Mode effective damping as a function of P_{in} measured in S_{12} (blue squares) and S_{11} (dark cyan squares).

5.1.2 Microwave cavity characterization

For all measurements we use a lock-in detection in order to obtain phase resolved data of the microwave cavity resonances. With this method we can resolve the background, and can carefully subtract it. This enables us to avoid the introduction of an ad-oc Q_{exI}

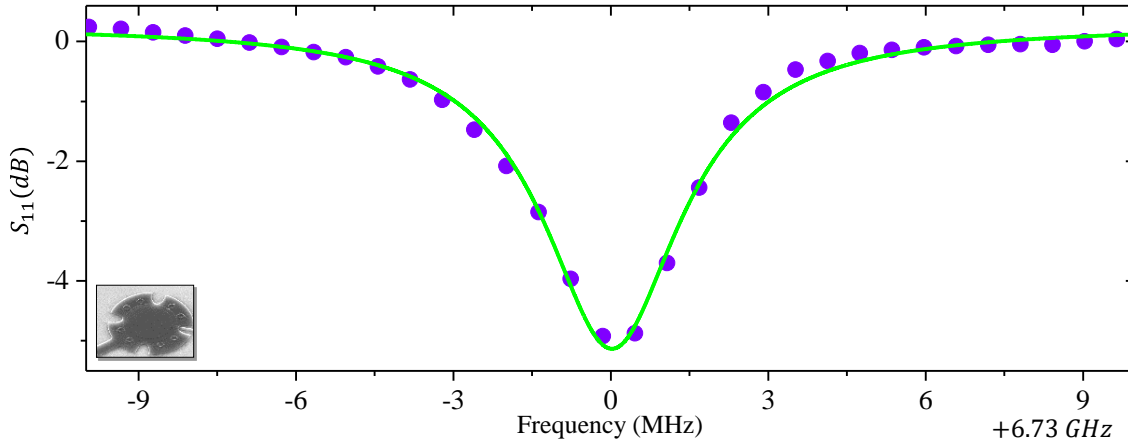


FIGURE 5.4 – Microwave cavity linear response (violet dots) measured in reflection on a one-port chip containing the badly-coupled drumhead device at 215 mK. The green line is a theoretical fit from Eq. (5.1.10) (with $Q \approx 1500$, $Q_{exR} \approx 3300$ and $\epsilon_R \approx -0.3$).

term; but relevant fit parameters are unchanged. However, with such a method the main drawback is that we lose the information linked to Q_{exR} . Such a linear response measurement is presented in Fig. 5.5 (left) for our cavity shown in Fig. 5.2. The response is a clear phase-resolved Lorentzian peak (see fit), with no asymmetries.

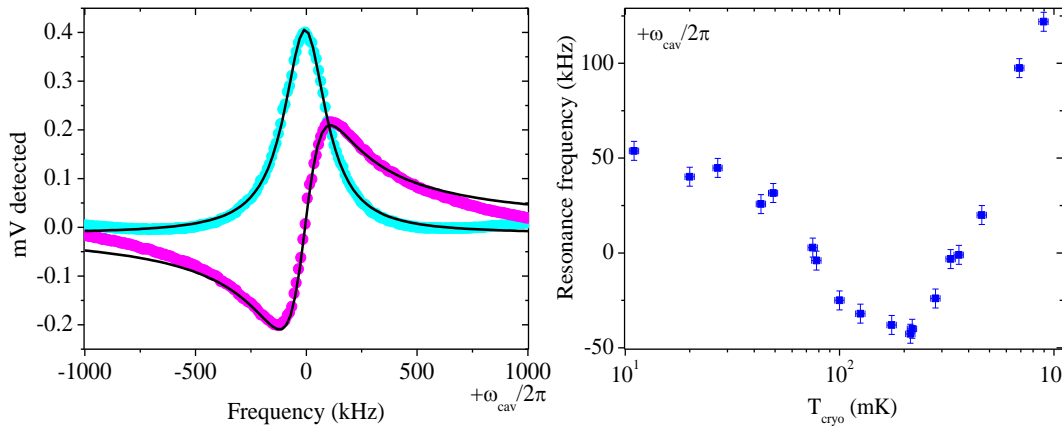


FIGURE 5.5 – Left: Transmission linear response measurement of the niobium microwave cavity coupled to the beam device at 250 mK with only the probe tone injecting extremely low power. We present a phase-resolved measurement displaying X (cyan curve) and Y (pink curve) at $\omega_{cav} \approx 6$ GHz. Black lines are Lorentzian fits. Right: Resonance frequency temperature dependence of this microwave cavity measured with a blue-detuned pump power of 0.2 nW, the total linewidth κ being constant over the full measured temperature range.

For each resonator we characterized their temperature dependencies. At AC frequencies, superconducting materials are not perfectly lossless. Cooper pairs transport current without losses, but their thermal excitations (quasi-particles) do create losses [240]. As well, Two-Level Systems (TLS) present in the materials do limit the highest reachable quality factors [219]. These sources of dissipation are represented by the internal quality factor $Q_{in}^{-1} = Q^{-1} - Q_{exR}^{-1}$. The quasi-particle contribution is directly proportional to the quasi-particle density, which decreases exponentially at very low temperatures. The cavity used for the beam detection is made of niobium which has a $T_c \approx 9$ K, its total κ is thus stable below 1 K, it only varies between typically 120 kHz and 190 kHz from one cool-down to the other (for unknown reasons). Concerning the temperature dependence

of the niobium cavity resonance frequency presented in Fig. 5.5, the situation is rather complex. This is certainly linked to the physics of TLS present in the material. κ_{ex} being intrinsically linked to the geometry of the design (distance to the feedline), it is very stable and reproducible, and does not vary by more than about $\pm 5\%$ from one cooldown to the other.

FIGURE 5.6 – Main: Total microwave cavity linewidth κ (or equivalently inverse optical quality factor) temperature dependence measured for the aluminum microwave cavity of the badly-coupled drum device (reflection measurements). Inset: Corresponding resonance frequency temperature dependence. Both measured sets of data should follow the well-known Mattis-Bardeen theory [68].

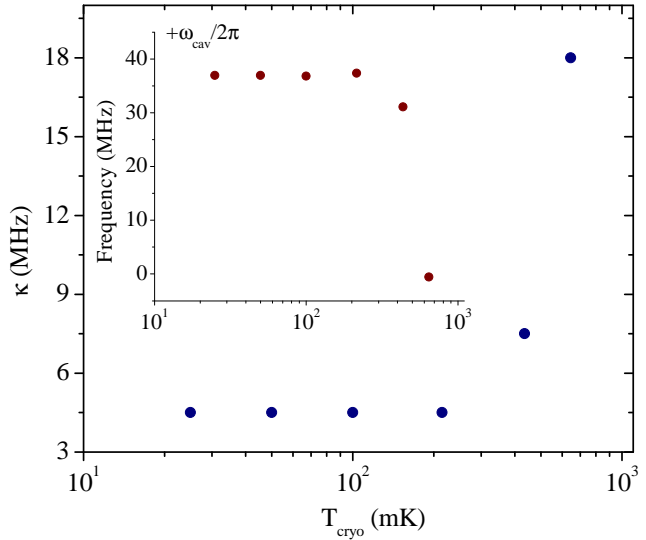
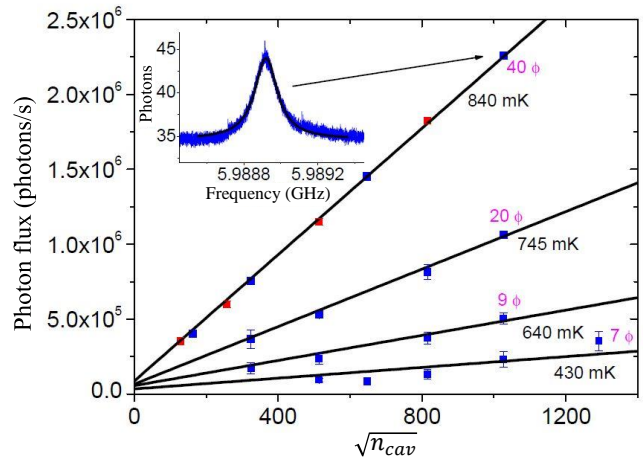


FIGURE 5.7 – Photon flux due to occupation of the cavity mode in excess of that expected from the cryostat temperature. The x axis is $\sqrt{n_{cav}}$ (blue-detuned pump scheme for blue symbols, red-detuned pump for red). Inset: example of resonance peak obtained from spectrum analyzer. The lines are guides to the eye. The numbers in magenta correspond to the calculated intra-cavity population for the last point of each temperature series from the fitted value of κ_{ex} .



In the case of both drum chips, lumped element cavities are made of aluminum which has a $T_c \approx 1.2$ K. Concerning the cavity used for the detection of the badly-coupled drum device, we present data of frequency shift as well as total κ in Fig. 5.6. These experimental measurements should follow the so-called Mattis-Bardeen theory [68] which yields to the expressions of superconductors' complex conductivities from BCS theory. The $T = 0$ K value of κ reflects a strong contribution from defects, namely TLS [167, 162]. The temperature dependence of the real part of the superconductor conductivity causes cavity frequency shifts whereas the imaginary part produces internal quality factor variations.

In each experiment we also characterized the effect of the applied injected pump power onto the microwave cavity. The properties of the cavity are too complex to allow an analysis of the type of Fig. 5.6 (performed for the NEMS), which could tell us by how much the microwave mode (and/or the chip) heats at a given pump power. We therefore

measured directly the population of the cavity with respect to P_{in} . We present these data in Fig. 5.7 as a function of $\sqrt{n_{cav}}$: on pure phenomenological grounds, the dependence seems then to be linear (see guides for the eyes in Fig. 5.7). We could not perform this measurement below typically 400 mK because the signal was too weak. The power-dependence is rather different from Fig. 5.6 and does not seem to be a true heating of the chip itself; it has thus to be noise fed into the cavity by the pump generator. Indeed, similar features but with different levels of cavity populations have been measured using different brands of generators (and other cavities). The relevant outcome of this graph is the extra (out-of-equilibrium) cavity population induced by the strong pump; this is the number quoted in magenta in Fig. 5.7 for each temperature, at the largest powers displayed. This number is obtained by dividing the photon flux by $\kappa_{ex}/2$ (bi-directional coupling). Injecting it in the theoretical expressions [136], we find out that this effect remains always negligible with respect to other experimental problems.

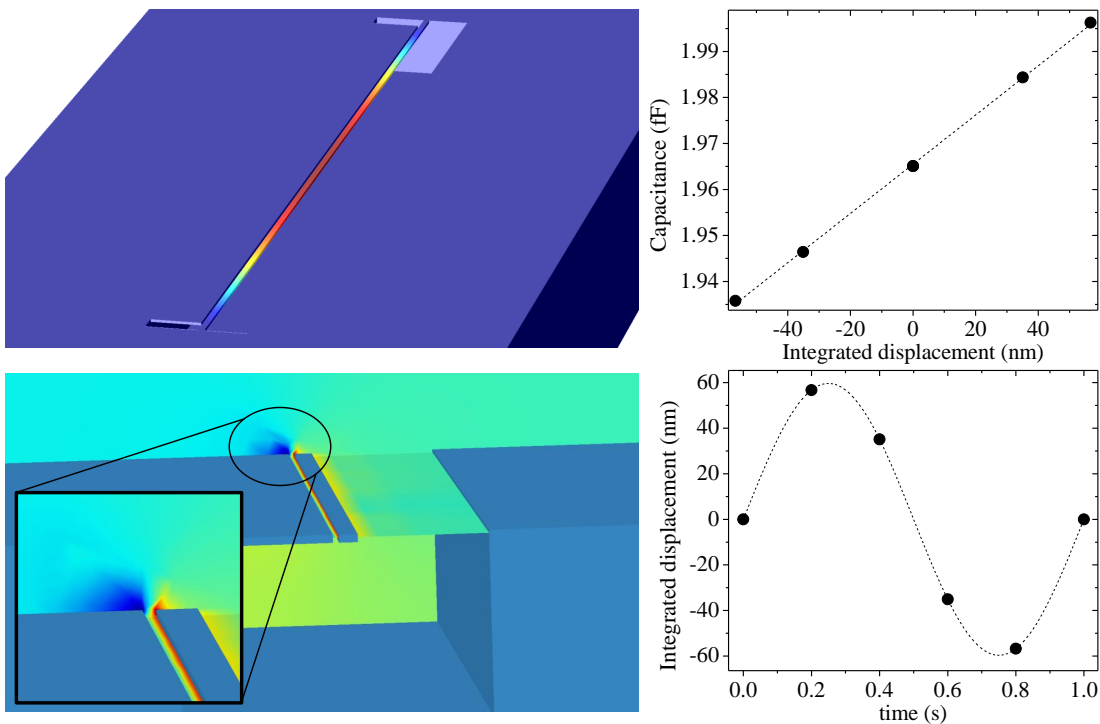


FIGURE 5.8 – Top left: Electromechanical simulation of our studied beam device (characteristics given in Tab. 6.1). Colors display the mechanical out-of-plane deformation from blue (zero deformation) to red (deformation of order 15 μm). Bottom left: Electromechanical simulation displaying in color the local electric field from blue (0 V on the gate side) to red (0.1V on the NEMS side). Top right: Simulated capacitance as a function of the integrated position of the beam NEMS: dashed black line is linear fit of slope $\propto dC/dx$. Bottom right: Resulting simulated beam displacement as a function of an arbitrary time: dashed black curve is sine shape function.

5.2 MODELING OPTOMECHANICAL COUPLING

Predicting the optomechanical coupling strength of a particular optomechanical design is crucial in order to build the right system for the right application. Concerning our design based on the beam motion detection, we performed electromechanical finite element

simulation. The coupling strength can be expressed as a function of electromechanical parameters by Taylor expanding the cavity resonance frequency:

$$g_0 = \frac{1}{2} \omega_{cav}^2 Z_{eq} \frac{\partial C}{\partial x} x_{zpf}, \quad (5.2.1)$$

where Z_{eq} corresponds to the equivalent impedance of the microwave cavity, calculated from the equivalent inductance and capacitance. This quantity is determined fitting the full scattering matrix extracted from microwave simulations of our particular cavity design (see Fig. 5.2). We obtained for our lumped element design $Z_{eq} \approx 600 \text{ Ohms} \pm 20\%$.

In order to model the mechanical part, we choose to apply an oscillating force on the center of the beam device, mimicking thus the deformation of the first vibration mode. We numerically simulated the out-of-plane motion by applying this force on the top of the NEMS and the in-plane motion by applying it on the side of the beam. In Fig. 5.8, we present the numerical calculations for the out-of-plane motion. The value of the force is chosen to obtain a maximum displacement of the device of the order of 15 pm (see Fig. 5.8 bottom-right), consistent with measured thermal noise motion. The time scale is arbitrary as we performed an adiabatic displacement of the NEMS. We thus simulate the capacitance for several positions of the mechanical object to determine the quantity $\partial C / \partial x$ (slope of the linear fit in Fig. 5.8 top-right). We ended up with a linear optomechanical coupling strength g_0 of about 0.5 Hz for the out-of-plane motion, value consistent with experimental measurements (see Chapters 6, 7 and 8). The in-plane motion has also been simulated and we predicted a coupling strength about 10 times greater than for the out-of-plane motion.

5.3 CONCLUSION

As a conclusion, in this technical chapter we succinctly detail the modeling and characterization of our microwave parameters. In particular we presented numerical simulations of our lumped element design used for the beam detection as well as experimental measurements necessary for the characterization of our built systems. We finally present a method based on finite element simulation that enables us to determine the optomechanical coupling strength of a particular mode NEMS displacement. This method can obviously also be applied for drum designs.

5.4 RÉSUMÉ EN FRANÇAIS

En conclusion, dans ce chapitre technique, nous avons succinctement détaillé la modélisation et la caractérisation de nos paramètres micro-onde. En particulier, nous avons présenté des simulations numériques de nos cavités micro-onde fabriquées pour la détection du mouvement de notre NEMS de type poutre ainsi que des mesures expérimentales nécessaires à la caractérisation de nos systèmes. Nous avons finalement décrit une méthode basée sur des simulations éléments finis qui nous a permis de déterminer la force du couplage optomécanique dans un cas particulier de mouvement de NEMS. Cette méthode peut bien sûr être appliquée aux conceptions basées sur des NEMS de type tambour.

6

CRYOGENIC TECHNIQUES: SIDEBAND MEASUREMENTS DOWN TO BELOW 1 mK

In this chapter we present the technical aspects of the experiments. We give the key elements that enabled us to build a microwave optomechanical platform on a nuclear adiabatic demagnetization cryostat in order to perform sideband pumping schemes down to the lowest achievable temperature. Building such a microwave/microkelvin experimental platform is challenging and requires expertise in Nano-Electro-Mechanical System technologies (NEMS), cryogenic techniques, thermometry at ultra-low temperature as well as microwave engineering. At the laboratory, two platforms are equipped with the same microwave setup and have been well calibrated: one on a commercial BlueFors[®] dry machine devoted to preliminary experiments, calibrations and tests. The other setup is installed into a home-made wet dilution cryostat with a nuclear demagnetization stage which is used for brute force cooling down to below 1 mK. Particular care has been taken in the construction of the two cryostats' temperature scales.

CONTENTS

6.1	On-chip design	120
6.1.1	Multiplexed readout design	120
6.1.2	Measured NEMS	121
	Beam device	121
	Drumhead devices	121
6.2	The BlueFors [®] machine: base temperature 7.5 mK	122
6.2.1	Working principle of dilution refrigerator	122
6.2.2	Thermometry	123
6.3	The nuclear adiabatic demagnetization cryostat: down to 400 μ K	124
6.3.1	Nuclear Entropy and heat capacity	124
6.3.2	High temperature approximation	125
6.3.3	Electronic heat capacity	125
6.3.4	Phonon heat capacity	126
6.3.5	The case of copper	126
6.3.6	Adiabaticity of the demagnetization process	126
6.3.7	Thermodynamic cycle of the demagnetization process	127
6.3.8	Nuclei-Phonons coupling	128
6.3.9	The home-made refrigerator	129
	The superconducting heat switch	129
	The demagnetization stage	130
	The adiabatic demagnetization process	130
	Thermometry	130
6.4	³ He thermometry	131
6.5	Microwave experimental platform	132
6.6	Conclusion	134
6.7	Résumé en français	134

6.1 ON-CHIP DESIGN

6.1.1 Multiplexed readout design

The on-chip part of the circuit is shown on Fig. 6.1. Our design has been processed at the Nanofab facility in the Néel Institute. It is made in a multiplexed way where three microfabricated microwave cavities are coupled capacitively to a coplanar waveguide. Typically microwave cavity structures are transmission lines (λ , $\lambda/2$, $\lambda/4$) or lumped elements. In our case we need to detect the motion of a NEMS, and the capacitive coupling $\delta C(x)$ being very weak, the cavity is made of an LC lumped element circuit and the nanomechanical element is directly embedded inside. This reduces the stray capacitance to ground in the effective mode capacitance C_0 (or equivalently increases the characteristic impedance), which enhances the coupling $\propto \delta C/C_0$. The chip is designed in order to perform transmission measurements (see Chapter 3). In order to obtain high quality factor cavities, our circuits are realized through laser lithography and RIE (Reactive Ion Etching) of a 120 nm thick superconducting niobium (Nb) layer patterned on silicon nitride. To be superconducting, the circuit has to be cooled down to $T \ll 8$ K, but to make sure that the cavity is not populated by thermal photons we need $T \ll \hbar\omega_{cav}/k_B$ (see Tab. 6.1 for experimental parameters). Usually we perform experiments below 200 mK, and in this range of temperatures the microwave cavity is indeed operating in the quantum regime (photon thermal population smaller than 1). Note that our fabrication process allowed us to process several beams for a single cavity and also beams in several cavities at the same time allowing us to design multiple experiments on the same chip (see Fig. 6.1).

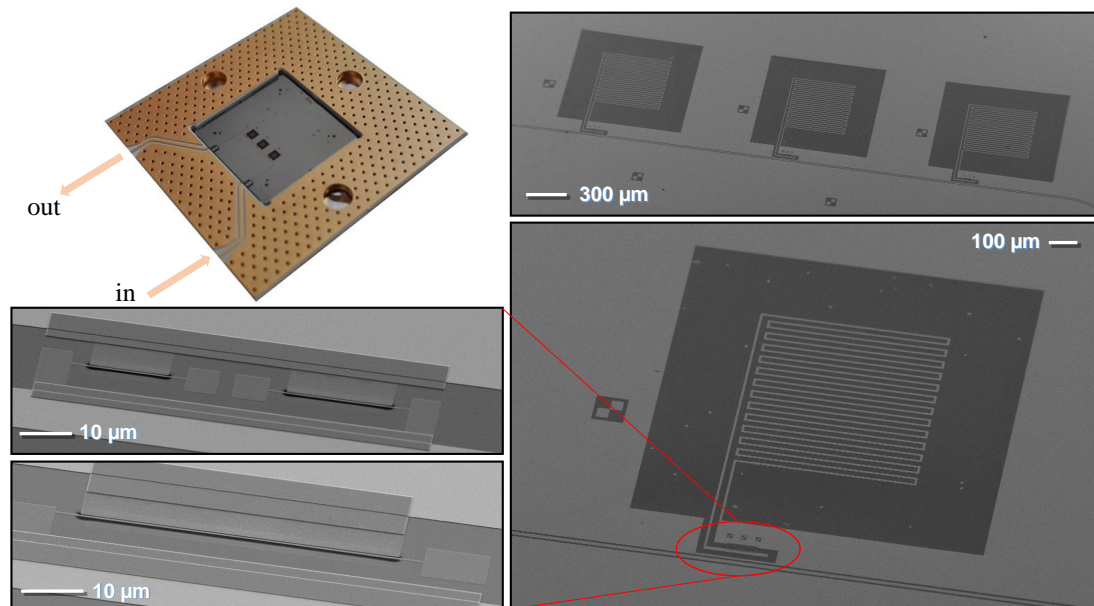


FIGURE 6.1 – Chip arrangement. Clockwise from PCB: Chip before bonding in PCB (microwave circuit board), displaying a coplanar transmission line coupled to three microwave cavities. SEM pictures of the three multiplexed microwave cavities, a zoom-in on one cavity, a zoom-in on its capacitively coupled $50 \mu\text{m}$ beam NEMS, and another on a multiplexed beam design with two beam NEMS designed in parallel (coupled to another cavity).

6.1.2 Measured NEMS

BEAM DEVICE The beam NEMS studied in this thesis has been designed and processed at the Néel Institute. The NEMS mechanical element we use is made from 80 nm thick high-stress silicon-nitride (SiN, 0.9 GPa), grown on top of silicon. It is a $50\ \mu\text{m}$ long doubly-clamped beam of width 300 nm (see Fig. 6.2 and Tab. 6.1). It is covered by a 30 nm layer of aluminum (Al), capacitively coupled to the cavity through a 100 nm gap. The aluminum part has been patterned using standard e-beam lithography and lift-off, while the beam was released through RIE etching of the silicon-nitride followed by a selective XeF_2 silicon etching [140]. The silicon-nitride has not been removed below the niobium layer. The mechanical resonance of the first flexural mode we use is shown in Fig. 4.3 left, around $\Omega_m/(2\pi) \approx 4$ MHz, with damping rate $\Gamma_m/(2\pi)$ of order 10 Hz at this temperature (200 mK). Such a mechanical mode still hosts about 6 thermal phonons around 1 mK, large enough to be considered in the classical limit and thus well adapted to mode thermometry (see Chapter 7).

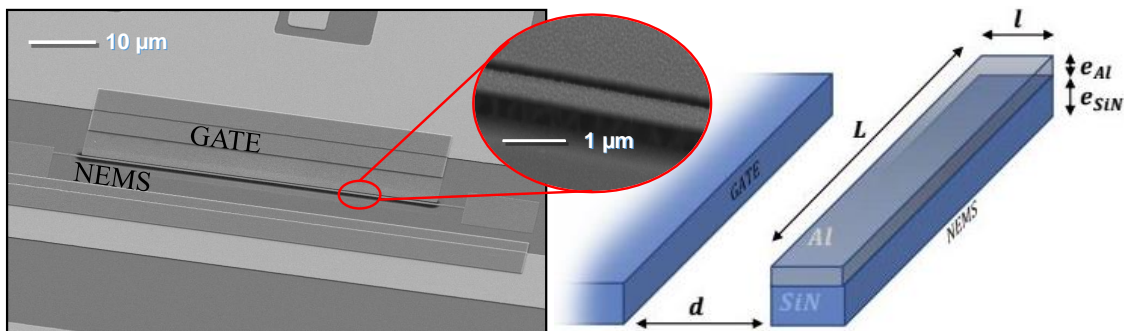


FIGURE 6.2 – Left: SEM picture of the NEMS beam structure used in the experiment and zoom-in on the 300 nm width beam. Right: Schematic diagram of the doubly-clamped beam with its gate. The two ends of the beam are clamped. Beam dimensions given in Tab. 6.1.

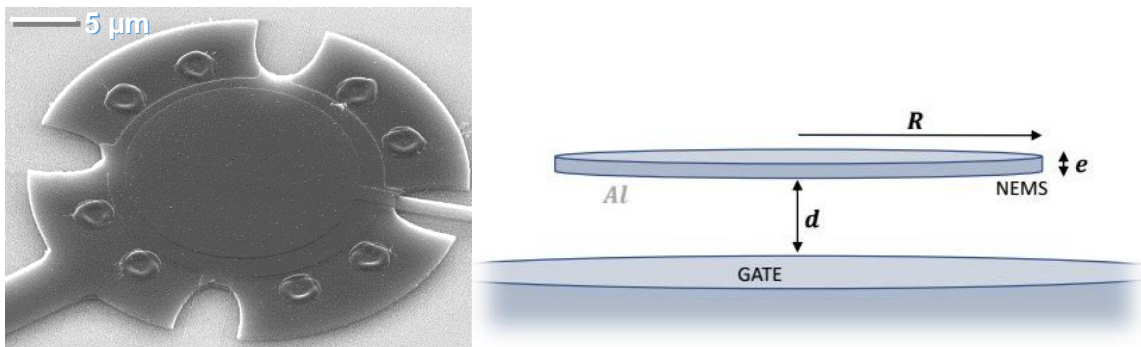


FIGURE 6.3 – Left: SEM picture of a typical drumhead NEMS structure used in the experiment; the gate is below the drumhead NEMS and is not visible on this picture. Right: Schematic diagram of a typical drum with its gate. The periphery is clamped. Drum dimensions given in Tab.6.1 for both drum devices used in this thesis.

DRUMHEAD DEVICES The chips containing the drumhead devices used in the experiments have been designed and processed at Aalto University in Finland. They are designed for reflection measurements. For both chips, the aluminum microfabricated lumped microwave cavity resonators resonate at $\omega_{cav}/(2\pi) \approx 6$ GHz (see Tab. 6.1 for details) and are coupled to aluminum drumhead NEMS [57] (see Fig. 6.3). We

performed the experiments using the fundamental mode of both drum NEMS devices which resonate around $\Omega_m/(2\pi) \approx 6.7$ MHz for the "badly-coupled" one and around $\Omega_m/(2\pi) \approx 15$ MHz for the other, "highly-coupled" (see Tab. 6.1 for details on the geometry and measured parameters). The mechanical resonance of the badly-coupled drum resonator is shown in Fig. 4.3 right. The badly-coupled drum is fabricated on quartz and the highly-coupled one on sapphire. The beam chip has been clamped directly onto the copper cell while the drums are glued using G-varnish.

NEMS estimated dimensions

Device	$L(\mu m)$	$l(nm)$	$R_d(\mu m)$	$d(nm)$	$e_{Al}(nm)$	$e_{SiN}(nm)$
Beam	≈ 50	≈ 300		≈ 100	≈ 30	≈ 80
badly-coupled drum			≈ 8.5	≈ 150	≈ 170	
Highly-coupled drum			≈ 7.3	≈ 50	≈ 100	

NEMS measured parameters (at 100 mK)

Device	$\Omega_m/2\pi(MHz)$	$\Gamma_m/2\pi(Hz)$	$g_0/2\pi(Hz)$
Beam	≈ 3.8	≈ 18	≈ 0.5
badly-coupled drum	≈ 6.7	≈ 150	≈ 10
Highly-coupled drum	≈ 15.1	≈ 490	≈ 230

Cavity measured characteristics (at 100 mK)

Device	$\omega_{cav}/2\pi(GHz)$	$\kappa/2\pi(MHz)$	$\kappa_{ex}/2\pi(MHz)$
Beam	≈ 5.9	≈ 0.12	≈ 0.095
badly-coupled drum	≈ 6.8	≈ 4	≈ 2
Highly-coupled drum	≈ 5.7	≈ 0.5	≈ 0.25

TABLE 6.1 – Summary of the experimental parameters for the three devices measured in this thesis: we present the dimensions and parameters of each NEMS and the characteristics of their own corresponding microwave cavity (drumheads parameters from Tabs. 8.2 and 7.1). Note that each mechanical device is subject to an in-built internal stress: beam structures (≈ 0.9 GPa), typical drumhead structures (50 – 250 MPa).

6.2 THE BLUEFORS[®] MACHINE: BASE TEMPERATURE 7.5 mK

6.2.1 Working principle of dilution refrigerator

Obtaining temperatures in the milliKelvin range can be achieved using a dilution refrigerator. Such a machine exploits the properties of the $^3He - ^4He$ mixture to cool down to about 10 mK [234, 241]. In Fig. 6.4 we present a scheme of such a dilution refrigerator with a picture of the dilution stage of the BlueFors[®] machine.

This new generation of dry fridge uses a pulse-tube cooler as cold source in order to pre-cool the helium mixture. The oldest wet machines such as our demagnetization cryostat use a 1K pot (a pumped 4He volume filled from the main bath) to thermalise and condense the 3He coming from the main pump.

Once the calorimeter (IVC) of the cryostat is pumped below 10^{-3} mbar to avoid heat leaks, the refrigerator is pre-cooled down to about 3K. At this temperature a compressor helps to condense the mixture in the dilution circuit by increasing the pressure up to 2 bar. Due to specific properties of the mixture phase diagram, below about 0.87 K the liquid separates into two distinct phases. This separation should occur in the coldest part of the dilution stage, the mixing chamber. The heavier phase is the one very poor

in ^3He (6.6% concentration), this is the dilute phase. On the other hand the lightest, the concentrated one, is very rich in ^3He (almost pure ^3He below typically 200 mK) and floats on the top of the dilute phase, both forming an interface. Pumping on the dilute phase through the still which is kept around 0.7 K allows to circulate more than 90% of ^3He and thus generates a flow \dot{n}_3 of ^3He atoms from the concentrated phase towards the dilute phase (an osmotic pressure being created between the mixing chamber and the still). The cooling mechanism comes from the dilution of ^3He atoms into the ^4He rich phase, a process which is endothermic with cooling power $\propto \dot{n}_3 T_{\text{mix}}^2$.

The ^3He being pumped outside from the still, it is re-injected to the concentrated phase in the mixing chamber within a closed cycle. The injection line involves a flow impedance in order to increase the pressure for the condensation (with a Joule-Thompson expansion) cooling further the fluid as well as a sequence of heat exchangers connected to the still for thermalisation of the injected ^3He rich phase. Actually, the amount of heat exchangers determines the lowest achievable temperature of such a machine, by reducing the heat losses.

The cooling power of the dilution stage being proportional to the flow rate of ^3He in the pumping line, a still heater is used to regulate this flow and achieve optimal cooling power by balancing the flow rate with the heat losses.

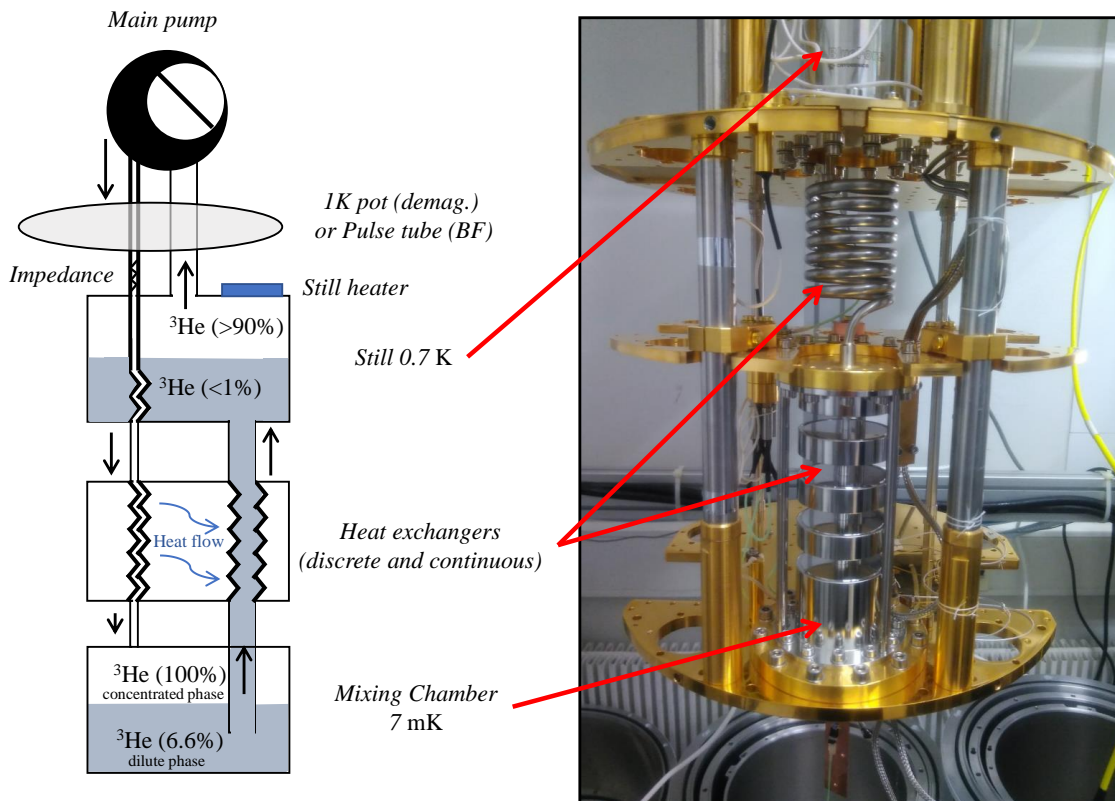


FIGURE 6.4 – Left: scheme of a dilution refrigerator. Right: picture of the dilution stage of the BlueFors[®] refrigerator.

6.2.2 Thermometry

In our case, the BlueFors[®] cryostat has been equipped with a Magnicon[®] MFFT (Magnetic Field Fluctuation Thermometer) noise thermometer and a CMN paramagnetic salt

(Cerium Magnesium Nitrate) thermometer. The MFFT is a noise SQUID-based (Superconducting QUantum Interference Device) thermometer [17] and is bolted at mixing chamber level while the CMN is directly mounted on the cold finger. Obviously we also used resistive thermometers (RuO₂, carbon Speer-type) calibrated against primary devices (mostly a Coulomb Blockade Thermometer), and our almost-primary thermometers (MFFT and CMN which do follow known temperature dependencies) are calibrated at a single point in temperature for practical reasons.

6.3 THE NUCLEAR ADIABATIC DEMAGNETIZATION CRYOSTAT: DOWN TO 400 μ K

The only practical known way to reach temperatures below 1 mK is to use adiabatic nuclear demagnetization. Indeed the best dilution cryostats can reach temperatures of order 2 – 5 mK, and electronic demagnetization is limited to much higher temperatures of order tens of mK, with much smaller cooling powers. The purpose of this part is the thermodynamic derivation of nuclear heat capacity and entropy, and their interpretations. Finally we present the structure of the demagnetization cryostat used for the microwave optomechanical experiment.

6.3.1 Nuclear Entropy and heat capacity

We consider here a nuclear magnetic moment originating in an angular momentum I . At a finite temperature T the $2I + 1$ energy levels are populated according to the following probability distribution [234]:

$$P(m) = \frac{e^{-\frac{\epsilon_m}{k_B T}}}{\sum_{-I}^{+I} e^{-\frac{\epsilon_m}{k_B T}}}, \quad (6.3.1)$$

where $\epsilon_m = m\mu_N g_L B$ denotes the energy of the nuclear Zeeman level of angular quantum number m . We use g_L as being the Landé factor, μ_N the nuclear magneton and B the magnetic field.

If we consider an ensemble of N nuclear spins, the corresponding partition function can be written as:

$$Z = \left(\sum_{-I}^{+I} \exp \left[-\frac{\epsilon_m}{k_B T} \right] \right)^N. \quad (6.3.2)$$

Using thermodynamic properties we can now write the entropy S and the heat capacity C_B as follows:

$$\begin{aligned} \frac{S}{k_B} &= \frac{\partial(T \ln Z)}{\partial T}, \\ C_B &= T \left(\frac{\partial S}{\partial T} \right)_B, \end{aligned} \quad (6.3.3)$$

where the index B means at constant magnetic field and $k_B \approx 1.38 \times 10^{-23} \text{J.K}^{-1}$ represents the Boltzmann constant.

For the purpose of our study we consider the magnetic dipoles to be independent and we use the notation $x = \frac{\mu_N g_L B}{2k_B T}$. The partition function can be expressed by:

$$Z = \left(\frac{\sinh([2I+1]x)}{\sinh(x)} \right)^N. \quad (6.3.4)$$

Using the equations Eqs. (6.3.3) we obtain the following expressions for the entropy and nuclear heat capacity:

$$\begin{aligned} \frac{S(B, T)}{k_B} &= x [\coth(x) - (2I+1) \coth(x(2I+1))] + \ln \left[\frac{\sinh(x[2I+1])}{\sinh(x)} \right], \\ \frac{C_B(B, T)}{k_B} &= x^2 \sinh^{-2}(x) - [x(2I+1)]^2 \sinh^{-2}[x(2I+1)]. \end{aligned} \quad (6.3.5)$$

Note that $x \propto B/T$ and both functions depend only on this ratio, in the limit of ideal paramagnetic nuclear magnetic susceptibility.

6.3.2 High temperature approximation

Usually, the demagnetization process is started at an initial temperature very close to the base temperature of the dilution stage which corresponds to about 10 mK. At this temperature, the thermal energy is much bigger than the magnetic interaction energy of the nuclear spins $\mu_N B \ll k_B T$. Following this condition, we can write the heat capacity and entropy of the nuclear spins Eqs. (6.3.5) in the high temperature limit ($x \ll 1$):

$$\begin{aligned} S(B, T) &= k_B \ln(2I+1) - \frac{NI(I+1)\mu^2 g^2}{6k_B} \left(\frac{B}{T} \right)^2 \\ C_B(B, T) &= \frac{NI(I+1)\mu^2 g^2}{3k_B} \left(\frac{B}{T} \right)^2 \end{aligned} \quad (6.3.6)$$

Where N is the number of spins. The second relation is the so-called Schottky law. For copper, the two stable isotopes are ^{63}Cu and ^{65}Cu , with natural abundance 70%/30% respectively. Both have $I = 3/2$, with $g_L \approx 1.48$ for the former and $g_L \approx 1.59$ for the latter. For numerical estimates, we shall simply take $g_L = 1.5$.

6.3.3 Electronic heat capacity

The conduction electrons in a metal are considered as a gas of free fermions [228]. Interactions are taken into account (when they are weak enough) through renormalized parameters (mass, etc...) within the Landau theory of fermi liquids. Thus, at low temperature the heat capacity drops linearly with temperature and can be expressed as follows (for an ensemble containing N electrons):

$$C_e(T) = N\gamma T, \quad (6.3.7)$$

where $\gamma = 6.7 \times 10^{-4} \text{J.K}^{-2}$ represents the Sommerfeld constant for copper metal.

6.3.4 Phonon heat capacity

At very low temperature, when the thermal energy becomes comparable to the energy necessary for excitation of lattice vibrations, deviations from the Dulong-Petit law appears. Indeed, in this regime, not all the lattice vibrations are necessarily excited. In order to derive the phonons heat capacity, the Debye model needs to be applied to compute the energy of the lattice vibrations [228]. The phonon heat capacity has a cubic dependence in temperature and is expressed with the Debye temperature θ_D by (for an ensemble of N atoms):

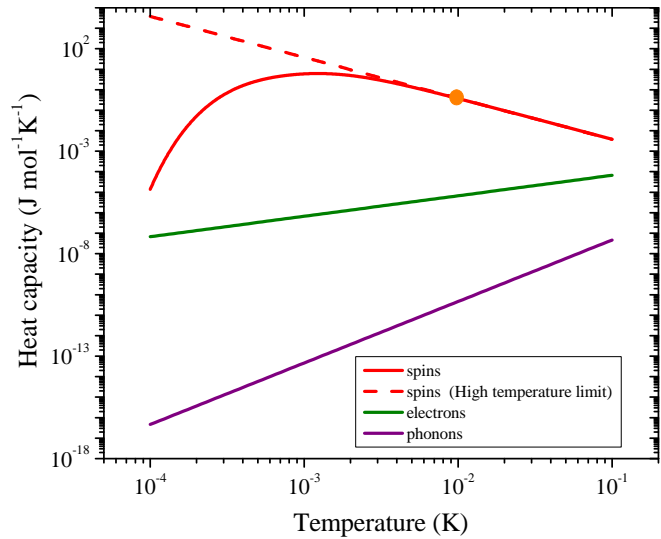
$$C_{ph}(T) = \frac{12}{5}\pi^4 Nk_B \left(\frac{T}{\theta_D}\right)^3 \quad (6.3.8)$$

For copper metal, we can consider the Debye temperature in the low temperature limit as being: $\theta_D = 347\text{K}$.

6.3.5 The case of copper

The workhorse of nuclear demagnetization is copper, but other materials are also used like PrNi_5 [234]. We thus show, based on the numbers introduced in the preceding Sections, the different contributions to the heat capacity of copper in Fig. 6.5. We can clearly see that in this range of low temperatures, and for a given magnetic field of 7 Tesla (typical for nuclear demagnetization cryostats), the nuclear spins have the biggest heat capacity. In our calculations we can thus safely neglect all other contributions, and focus on the nuclear spins only.

FIGURE 6.5 – Heat capacities as a function of temperature for copper ($I = 3/2$, $g_L = 1.5$, $\mu_N = 5.05 \times 10^{-27} \text{J}\cdot\text{T}^{-1}$) at a magnetic field of 7T. Red line: Nuclear spin heat capacity. Red dashed line: Nuclear spin heat capacity in the high temperature approximation ($\mu B \ll k_B T$). Green line: Electronic heat capacity. Purple: Phonons heat capacity. Orange dot: base temperature dilution cryostat.



In the following, we shall thus describe the basics of nuclear demagnetization cooling.

6.3.6 Adiabaticity of the demagnetization process

We now assume that the demagnetization process is adiabatic and reversible, which means in other words that the demagnetization is isentropic. In this ideal case, the final state of the system is entirely determined by the initial conditions; we will come back to this hypothesis below. We denote the state variable of the initial state with the index i

and the state variable of the final state with the index f respectively. From this isentropic condition, we can write:

$$S(B_i, T_i) = S(B_f, T_f). \quad (6.3.9)$$

Using the entropy relation given previously (which depends only on $x \propto B/T$), it follows that:

$$\frac{B_i}{T_i} = \frac{B_f}{T_f}. \quad (6.3.10)$$

This fundamental result means that during adiabatic demagnetization, the ratio of magnetic field and temperature is constant $B/T = \text{constant}$. Another consequence is that the magnetization is unchanged during an adiabatic process (again, it depends only on $x \propto B/T$). A microscopic analysis can also be used to explain magnetic refrigeration by looking at the behavior of the Zeeman energy levels. Due to the imposed magnetic field, the occupation of the lowest Zeeman levels are larger than the upper ones. The process being considered adiabatic, the occupation of each level is constant during the demagnetization, but the energy difference between the levels is changing, leading to a temperature change.

6.3.7 Thermodynamic cycle of the demagnetization process

The demagnetization is better understood in the T-S diagram plotted in Fig. 6.6 using the entropy equation Eq. (6.3.5 first line). The copper mass is brought into contact with a precooling bath (the mixing chamber of the dilution unit) to cool it down to the starting point A in the graph where the copper is at an initial temperature $T = T_A = T_B$. The magnetic field is then applied to perform an isothermal magnetization ($A \rightarrow B$) from $B = B_A$ to $B = B_B > B_A$.

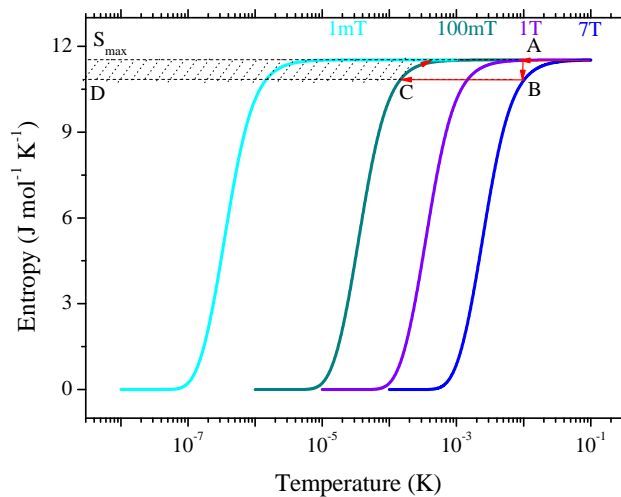


FIGURE 6.6 – T-S thermodynamic diagram: Entropy as function of temperature for copper ($I = 3/2$, $g_L = 1.5$, $\mu_N = 5.05 \times 10^{-27} \text{J}\cdot\text{T}^{-1}$) at different values of magnetic field. An example of demagnetization thermodynamic cycle is drawn by the red arrows describing the path ABC.

We note that during this process the heat of magnetization coming from the fact that entropy is removed from the system has to be absorbed by the cold bath. The copper mass is then isolated from its environment and an isentropic demagnetization is performed ($B \rightarrow C$) by reducing the external applied magnetic field from $B = B_B$ to $B = B_C \ll B_B$. The temperature decreases proportionally from $T = T_A$ down to $T = T_C \ll T_A$. The final step is the warming up of the copper mass along the entropy curve at a constant magnetic field $B = \text{Constant}$ due to the external heat leaks. We can point out that the energy of magnetization is directly related to the integral of the thermodynamic cycle, represented

by the area of the rectangle $ABDS_{max}$ in Fig. 6.6. S_{max} represents the point at zero field and maximal disorder where the nucleus are in their $2I + 1$ possible orientations: $S(T = \infty) = k_B \ln 4$. The total heat which can be absorbed by the copper mass after the demagnetization process is represented by the hatched area in Figure 16. This cooling energy is expressed by the following integral:

$$Q(B_C) = \int_{T_c}^{+\infty} T \left(\frac{\partial S}{\partial T} \right)_{B_c} dT. \quad (6.3.11)$$

6.3.8 Nuclei-Phonons coupling

In nuclear demagnetization refrigeration the temperature of the nuclear spins is decreased and at the end the ensemble of nuclear spins is considered in thermal equilibrium. Taking into account that in our experiments we are interested in the phonon temperature of our devices, let us consider the coupling between nuclear spins and the electron baths as well as the coupling between electron and phonon baths. Indeed, the nuclear spins interact very weakly with the lattice vibrations, but are well coupled to the conduction electrons. The cooling power is thus transferred to the phonons in the following way: nuclei \rightarrow electron \rightarrow phonon.

The nature of the interaction between nuclei and the conduction electrons is an electromagnetic coupling. This coupling mechanism is caused by hyperfine interactions. The microscopic mechanism which couples nuclei and conduction electrons is a mutual spin-flip coupling. Only the electrons which are close to the Fermi energy can interact with the nuclei, and the time of thermalization τ between both can be written in the following form [234]:

$$\tau T_n^{-1} = (T_e^{-1} - T_n^{-1}), \quad (6.3.12)$$

where T_e represents the electron bath temperature and T_n the nuclear spin bath temperature.

The Korringa law is then expressed by:

$$\tau = \frac{\kappa}{T_e}, \quad (6.3.13)$$

where κ is the Korringa constant. It is a constant of the material which represents the coupling strength between nuclei and conduction electrons. The Korringa constant has to be as small as possible to have the smallest possible thermalization time between nuclear spins and electrons. For instance, for copper $\kappa = 1.27$ K.s which is rather small for a non superconducting metal in this range of temperature.

Concerning the coupling mechanism between conduction electrons and the lattice vibrations, the coupling mechanism is mainly due to scattering and is governed by the Bloch-Grüneisen relation which relates the electrical resistivity to the temperature. The heat flow between the conduction electron bath and the phonon bath can thus be expressed by: $\dot{Q} \propto \Delta T^5$, where ΔT is the temperature gradient between the two baths. The thermal coupling is also proportional to the volume, which makes thermalization between electrons and phonons particularly difficult in nanostructures around 10 mK (this point is discussed also in Chapter 7) [124]. For a bulk metal, this is however not an issue.

In order to perform nuclear demagnetization and be able to exploit the cooling power for any experiments, one has to build a nuclear stage by making a compromise between the lowest possible Korringa constant, the highest thermal conductivity, and the lowest

superconductivity transition temperature of the material. Historically, copper has been chosen in many laboratories, and this is also the case for our refrigerator.

6.3.9 The home-made refrigerator

The microwave setup was installed into a home made refrigerator having a nuclear demagnetization stage [47] which has already demonstrated μ -Kelvin temperature by platinum nuclear magnetic resonance and by ^3He thermometry measurements.

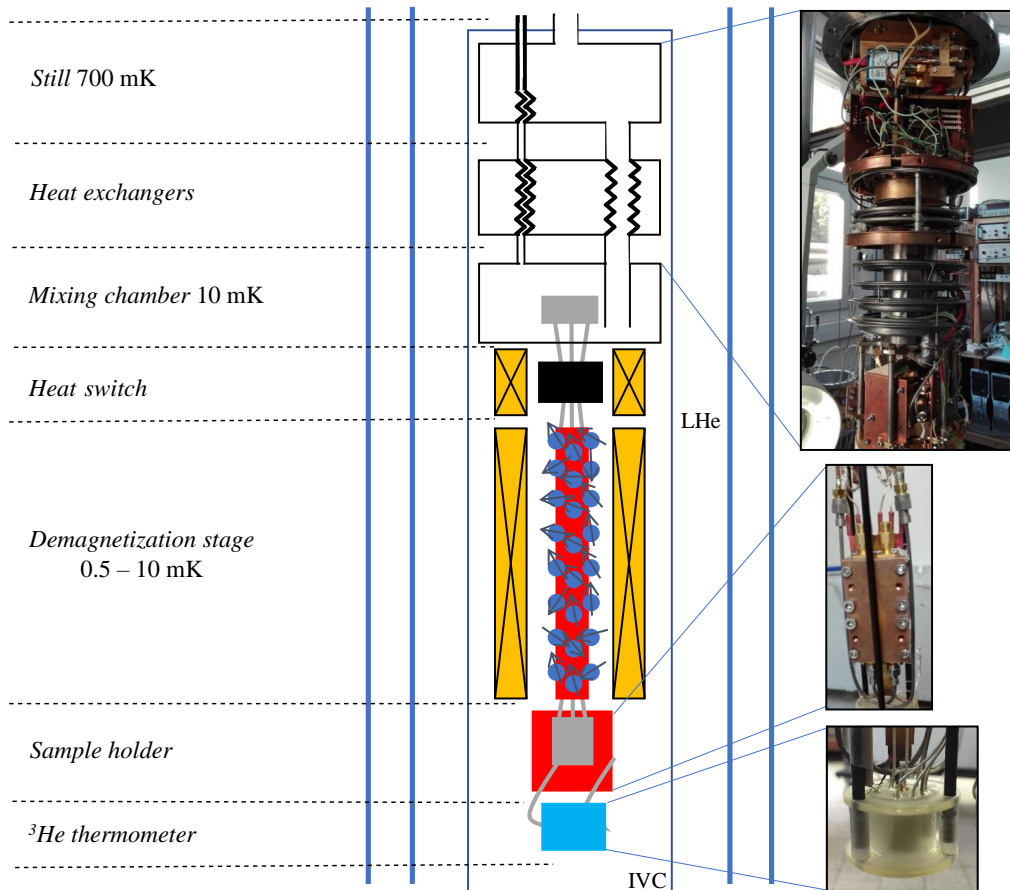


FIGURE 6.7 – Scheme of the nuclear demagnetization cryostat with the 7 T coil, the experimental cell and the ^3He thermometer. The random directions arrows represented on the copper stage schematize disordered nuclear copper spins before the magnetization process.

THE SUPERCONDUCTING HEAT SWITCH The home made dilution unit and the nuclear demagnetization stage are connected by a Lancaster-made Al heat switch [165] (see Fig. 6.7). This system is composed of a superconducting niobium coil with a core composed by an i block. Below 1.2 K the aluminum becomes superconducting, which means that the nuclear stage is thermally isolated from the mixing chamber. By passing a small current of about 100 mA in the coil, the magnetic field applied to the aluminum block leads to the normal state transition. The nuclear stage is thus thermally connected to the dilution unit and the nuclear stage energy can be absorbed by the mixing chamber constituting a cold bath.

THE DEMAGNETIZATION STAGE The nuclear stage is of laminar type and built with 1 kg of ultra-pure copper [47] assembled in plates to avoid Foucault currents. Particular care has been taken in thermalization issues. The experimental cell is thus made of annealed high-purity copper. It is mounted on a cold finger connected through silver wires to the bottom of the nuclear stage of the demagnetization cryostat (see Fig. 6.7). Concerning our 8 T magnet, it is compensated on both sides, but nonetheless small stray fields are present when it is magnetized (represented in Fig. 6.12 by the small boxed coil).

THE ADIABATIC DEMAGNETIZATION PROCESS Experimentally, the nuclear copper spins of the nuclear stage are magnetized up to 7 T and then precooled by the dilution unit (see Fig. 6.7) down to 7 – 10 mK (base temperature depending on the cooling power settings). This precooling phase can last several days in order to absorb the heat of magnetization from the nuclear stage. Then the copper stage is disconnected from the mixing chamber by means of the heat switch and the magnetic field is decreased adiabatically down to about 100 mT. The entropy being constant during the process, the decreasing in temperature is the same as the decreasing in magnetic field. In this thesis we worked down to 400 μ K. At this temperature the cryostat can then stay cold over a week (heat leak < 100 pW); another cycle needs then to be initiated with a pre-cooling of the system (see Fig. 6.8 right side). On Fig. 6.8 (left side) we present experimental measurements characterizing the adiabaticity of the home made demagnetization fridge at relatively high temperatures. At the lowest temperatures, we seem to be limited by a lack of adiabaticity due to our current source (American Magnetics), see Fig. 6.9.

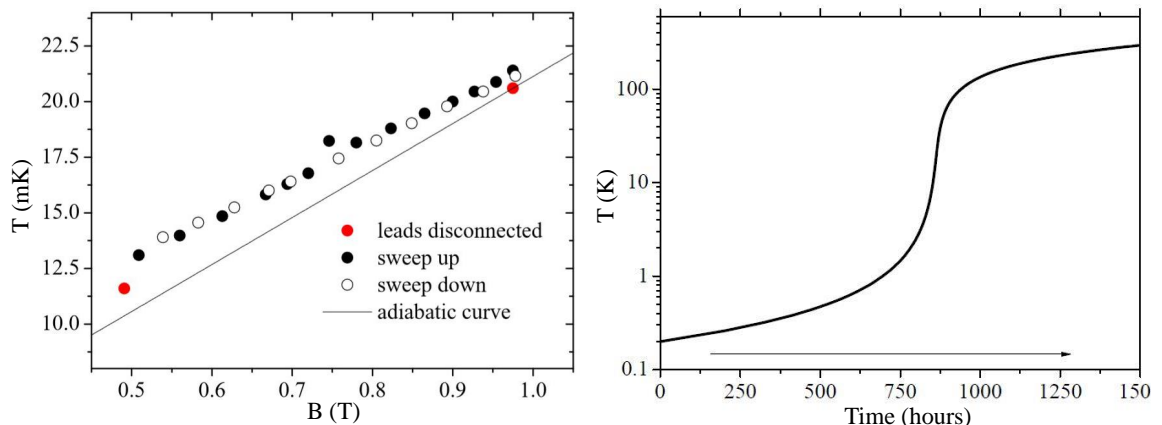


FIGURE 6.8 – Left: Temperature of the nuclear stage versus magnetic field; Experimental data in down and up-sweep of the magnetic field compared to the theoretical adiabatic curve. This is a demonstration of the adiabaticity of the demagnetization process. It is performed at particularly high temperatures, in order to use our "conventional" carbon resistor thermometers. The slight deviation to adiabaticity is certainly due to their saturation at low temperatures. Adiabatic field sweeps up and down are presented, corrected for a slight overheating of thermometers due to noise picked up by the current leads (extremes with leads disconnected in red, as a comparison). Right: Simulated warming up curve for the nuclear demagnetization cryostat.

THERMOMETRY On the demagnetization cryostat, an MFFT is mounted on the mixing chamber at the top of the nuclear stage while a ^3He thermometer is connected at the bottom of the nuclear stage; the experimental cell is actually between the nuclear stage and this thermometer. When their working range overlap, the thermometers agree within typically 2 – 5%. As for the BlueFors[®] fridge, we also used resistive thermometers (RuO_2 , carbon Speer-type) calibrated against primary devices.

6.4 ^3He THERMOMETRY

Previously, we used to measure the temperature of the nuclear stage by a Platinum NMR thermometer, but this method needs a magnetic field, which can cause a huge problems when dealing with superconducting resonant circuits. In order to perform thermometry measurements without using magnetic fields and hence without disturbing the microwave measurements, we choose to build a ^3He thermometer for the lowest part of our temperature scale (see Fig. 6.7).

It is based on the viscosity measured in the fluid with an immersed probe, a mechanical resonator. Indeed, viscous drag produces damping on the resonator motion, and its measurement gives directly access to the temperature of the fluid through the tabulated fluid viscosity. In the past, vibrating wires were the best choice for this task [39, 55]. Today, people use quartz tuning forks (see picture in Fig. 6.9) which are more practical [181, 70, 69]. Our thermometer is thus a nested cell (see picture in Fig. 6.7) containing two tuning forks (one in the outside cell, the other in the inside), filled with silver sinters connected to the nuclear stage by silver wires. The outside cell serves as a thermal shield for the inner one, and does not cool down below typically 1 mK. The inner cell is directly connected to the cold finger that hosts the microwave cell.

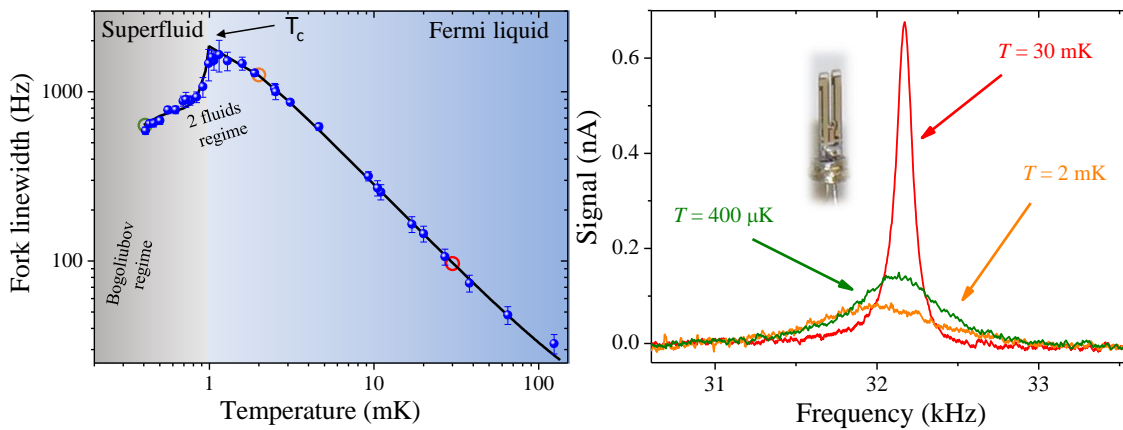
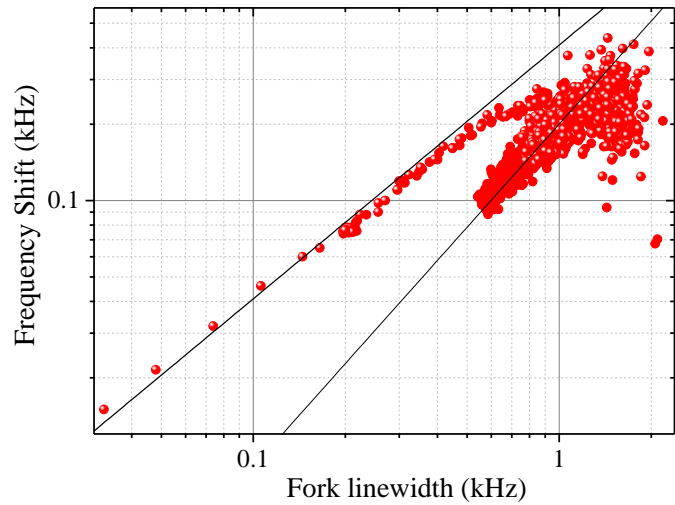


FIGURE 6.9 – Left: Calibration measurements performed on the ^3He thermometer, from the lowest operated temperature $400\ \mu\text{K}$ to about $100\ \text{mK}$. The superfluid transition T_c is clearly visible around $1\ \text{mK}$ and can be used as a temperature fixed point; the line is the expected behavior from ^3He viscosity and blue dots with error bars are experimental data (x-axis obtained from magnetic field, see text). Right: Measured raw data fork resonance curves for three different temperatures (corresponding to colored circles in left panel). The inset is a picture of a typical tuning fork.

Three regimes can be distinguished concerning the behavior of the fork in liquid ^3He depending on the temperature range (see Fig. 6.9). Above the superfluid transition of ^3He at about $1\ \text{mK}$ the fluid can be considered classically and the Navier-Stokes equations for a viscous fluid can be applied, it corresponds to the Fermi liquid zone. Below $1\ \text{mK}$, two different regimes exist. Above approximately $200\ \mu\text{K}$ the two fluid model can be used, which means that we can consider two kinds of flow on the fork, a viscous one and a superfluid one (see Fig. 6.10). Below $200\ \mu\text{K}$ the main part of the damping comes from broken Cooper pairs, the Bogoliubov quasiparticles, which density decreases exponentially leaving only the renormalized vacuum of the Bose Einstein condensate. At $0\ \text{bar}$ pressure, $0\ \text{T}$ field this state is called $^3\text{He} - B$, and the properties of this amazing fluid have been extensively studied over the years [230]. For instance, the viscosity of ^3He is well known for both normal and superfluid states, see e.g. [66, 67]. In principle, from

the knowledge of the geometry of the immersed object and its surface rugosity, one can calculate the friction and thus the broadening of the resonance. In practice, it is much more efficient to calibrate the device by scaling its properties on known measurements [70, 69].

FIGURE 6.10 – Experimental measurements giving the frequency shift of the tuning fork resonance as a function of its linewidth. Measurements are performed while continuously changing the stage temperature; both hydrodynamic regimes are explicitly distinguished (upper line is Fermi liquid whereas bottom line corresponds to superfluid).



In order to perform this scaling, we measured the damping of the quartz tuning fork thermometer (inner cell) as a function of the final field of the demagnetization process B_f . The protocol was to demagnetize by steps, and then remagnetize to B_i in order to verify that the process was indeed adiabatic (by recovering the initial temperature T_i). This works down to about 500 μ K, but fails below, presumably because of the equipment used for driving the current in the coil. It is then straightforward to calculate the temperature of the nuclear spins of copper for each step, which should be in equilibrium with electrons (and finally ^3He) if one waits long enough. The result is shown in Fig. 6.9. The line is the expected behavior from published results. Note that the superfluid transition T_c also acts as a fixed point in the temperature scale. We can consider this technique as an almost primary thermometry measurement, the calibration curve being entirely tabulated.

6.5 MICROWAVE EXPERIMENTAL PLATFORM

We have thus built a microwave platform for optomechanics on a nuclear adiabatic demagnetization cryostat. The microwave circuitry has been kept as basic as possible so far for demonstration purposes. It represents the simplest circuit possible and it is entirely compatible with quantum electronic devices. Neither JPA (Josephson Parametric Amplifier) nor qubits have been used up to date, and we rely only on intrinsic properties of optomechanics for the measurement. The microwave setup has been carefully calibrated by electronic means on both the demagnetization cryostat and the BlueFors[®] machine.

Two similar microwave setups have been used in these experiments. Their common features are described in Fig. 6.12. This wiring is basic and can also be found within the literature [54]. Essentially, they are built around a cryogenic HEMT (High Electron Mobility Transistor) placed at about 4 K and two circulators mounted on the mixing chamber of the dilution units (see Fig. 6.11). Circulators are essential in order to isolate as much as possible the chip from the HEMT noise. On the BlueFors[®] machine, the HEMT is a Low Noise Factory[®] 4 – 8 GHz bandwidth, with a measured noise temperature of

about 3 K (≈ 10 photons) at 6 GHz. On the nuclear adiabatic demagnetization cryostat, it is a Caltech 1 – 12 GHz bandwidth with a measured noise temperature of about 15 K (≈ 50 photons at 6 GHz). The noise background as seen from the detector is about 15 – 20 photons on the BlueFors[®], and about 100 – 150 photons on the demagnetization machine.

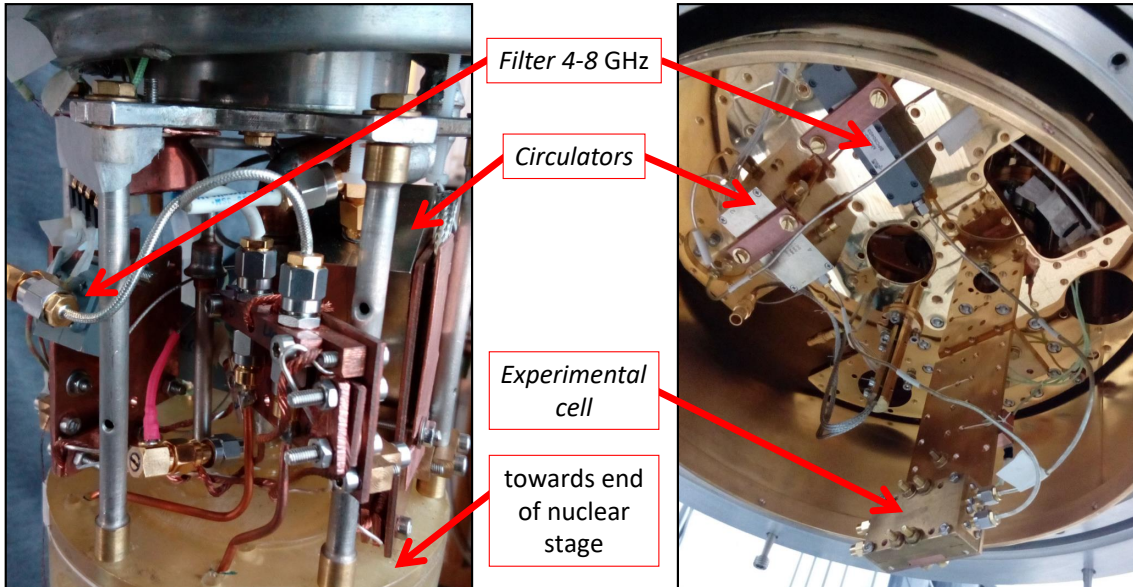


FIGURE 6.11 – Pictures of the mixing chamber stage for the demagnetization cryostat (left picture), about 10 cm diameter, and for the BlueFors[®] machine (right picture), about 30 cm diameter. On the demagnetization cryostat the experimental cell is located at the bottom of the nuclear demagnetization stage well below the mixing chamber. Note the difference in available space.

The (dashed green) boxed component below the HEMT in Fig. 6.12 represents a power combiner used to realize an opposition line (of major importance to protect the room temperature HEMT amplifier). On the BlueFors[®] setup, it is mandatory to put it at low temperature to avoid saturation of the cryogenic HEMT from the strong blue-detuned pump tone. On the demagnetization cryostat, the cryogenic HEMT is linear enough so this protection is not necessary; the opposition line can be put at room temperature. This choice has been made because of space constraints: feeding an extra microwave opposition line in the nuclear adiabatic demagnetization cryostat would be very demanding. The attenuation and filtering (see Fig. 6.11) of the injection lines (DC and microwave) is also described in Fig. 6.12, mandatory to protect the experimental cell from room temperature noise.

Gains and noise levels of the full chain have been carefully checked with respect to HEMT working point. Besides, each component has been tested at 4 K prior to mounting. The whole setup has then been calibrated, using an Agilent[®] microwave generator EXG N5173B and an Agilent[®] spectrum analyser MXA N9020A. The measurements presented in this thesis have been realized using a Zurich Instruments[®] UHFLLI lockin detector operating in spectrum mode by an heterodyne detection. The signal is mixed down with a Local Oscillator (LO) and detected at frequency $\pm\Omega_m + 2$ MHz (the shift avoiding overlap of Stokes/Anti-Stokes signals). The generators used were from Agilent[®], Keysight[®] brands leading to equivalent data quality. We also used an Anapico[®] 2-channels microwave generator for demodulation. The absolute error in the calibrations is estimated at about

± 2 dB (absolute) over the whole set of realized runs; within these error bars, the two cryogenic platforms gave the same quantitative results.

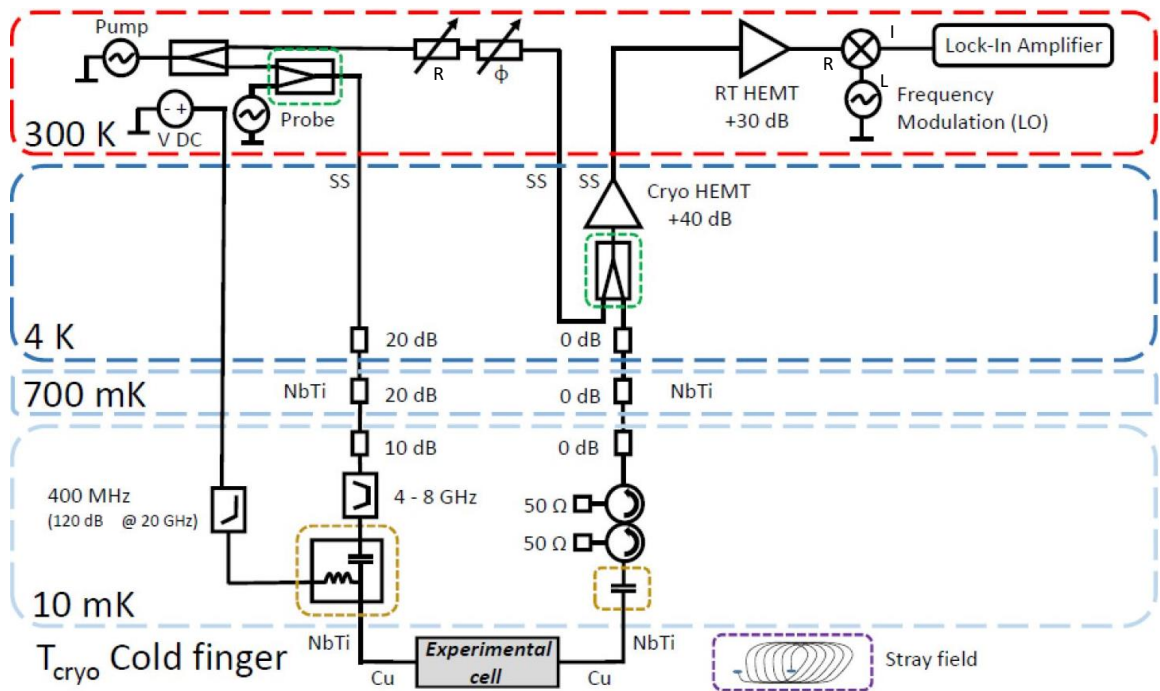


FIGURE 6.12 – Simplified common wiring of the experimental platforms; the different levels within the cryostats (BlueFors[®] and demagnetization fridge) are shown with their respective temperature. SS stands for Stainless-Steel, NbTi for Niobium-Titanium and Cu for Copper coaxial cables (50 Ohms impedance). The boxed elements have been added/removed depending on the experimental run (see text for details).

6.6 CONCLUSION

This part is a technical account on how our NEMS devices and cryogenic/microwave setups are made. Indeed we explain how to build a microwave optomechanical system on a nuclear demagnetization cryostat in order to perform brute force cooling experiments. We briefly present the three different chip designs measured in this thesis as well as the two available cooling platforms: the dry commercial fridge and the homemade demagnetization machine equipped with a handmade ³He primary thermometer. Both platforms are independently calibrated and give identical results down to dilution temperatures (see Chapter 7 and 8). In this chapter we give all needed information to understand how we had built and calibrated our microwave optomechanical circuit.

6.7 RÉSUMÉ EN FRANÇAIS

Ce chapitre explique brièvement comment nos systèmes nano-électromécaniques ont été réalisés. Il donne également les bases technologiques nécessaires à la réalisation d'une plateforme cryogénique micro-ondes. En effet, nous expliquons ici comment implémenter un système optomécanique micro-ondes sur un cryostat à désaimantation nucléaire dans le but de réaliser des expériences de refroidissement brute force. Nous présentons brièvement nos trois différents systèmes optomécaniques mesurés durant cette thèse ainsi que

les deux plateformes cryogéniques utilisées: le réfrigérateur commercial BlueFors[®] et la machine à désaimantation équipée du thermomètre ^3He . Ces deux plateformes ont été indépendamment calibré et donnent ainsi des résultats proche de l'identique jusqu'aux températures de dilution (voir Chapitre expérimentaux 7 et 8). Dans ce chapitre nous donnons donc toute l'information nécessaire pour comprendre comment nous avons construit notre circuit optomécanique micro-ondes.

7

STOKES SIDEBAND: AMPLIFICATION FOR THERMOMETRY

We present microwave optomechanics measurements performed on the nuclear adiabatic demagnetization cryostat, whose temperature is determined by accurate thermometry from below 500 μK to about 1 Kelvin (see Chapter 6). These data are completed by measurements performed on a BlueFors[®] dilution unit, demonstrating perfect agreement between runs: both microwave calibrations and thermometry above 10 mK are consistent. We describe a method for accessing the on-chip temperature, building on the blue-detuned parametric instability and a standard microwave setup. The capabilities and sensitivity of both the experimental arrangement and the developed technique are demonstrated with the 3 different devices presented in Chapter 6. We report on an unstable intrinsic driving force in the coupled microwave-mechanical system acting on the mechanics that appears below typically 100 mK. The origin of this phenomenon remains unknown, and deserves theoretical input. It prevents us from performing reliable experiments below typically 10 – 30 mK for low-coupled devices; however no evidence of thermal decoupling is observed. These results are presented in Ref. [223]. We discovered that the same features are present in all types of devices sharing the microwave technology, at different levels of strengths, depending of the number of driving photons used to perform the measurements. We further demonstrate empirically how most of the unstable features can be annihilated, and speculate how the mechanism could be linked to atomic-scale two level systems. Finally, we demonstrate state-of-the-art motional ground state cooling of a highly-coupled drumhead structure [218], a necessary step towards in-equilibrium quantum experiments.

CONTENTS

7.1	In built parametric amplifier	137
7.1.1	Optomechanical interaction calibration	137
7.1.2	Blue-detuned pumping method	138
7.2	Optomechanical thermometry	140
7.2.1	Phononic and Two-Level Systems (TLS) thermometry	140
7.2.2	In-equilibrium results	142
7.3	Unstable Stochastic driving force	146
7.4	Ground state cooling	150
7.4.1	Sideband asymmetry thermometry	151
7.4.2	Thermodynamic equilibrium below 1 mK	154
7.5	Conclusion	160
7.6	Résumé en français	161

7.1 IN BUILT PARAMETRIC AMPLIFIER

7.1.1 Optomechanical interaction calibration

We choose to perform blue-detuned pumping to amplify the Brownian motion and thus use the parametric instability to extrapolate the thermal occupation of the mechanical mode at zero optical anti-damping effect (i.e. zero injected power). We start by calibrating the optomechanical interaction. The optical damping and anti-damping are

linear in applied power P_{in} , see Fig. 7.1 (top left). From a fit [Eq. (7.1.4) below], we can infer the so-called single photon coupling strength:

$$g_0 = \frac{1}{2} \omega_{cav} \frac{1}{C} \frac{dC}{dx} x_{zpf}, \quad (7.1.1)$$

with x_{zpf} the zero-point-motion [136]. This is essentially a geometrical parameter, arising from the modulation dC/dx of the microwave mode capacitance C by the mechanical motion [54] (see Chapter 3). We find for the three different devices presented in Chapter 6 the value of g_0 presented in Tab. 6.1 within 20% error bars. Concerning the first measured device, the 50 μm long beam, we use its out-of-plane flexure. The coupling of this particular motion is particularly small [$g_0/(2\pi) \approx 0.5$ Hz, see Chapter 5], the idea being to take advantage of that to demonstrate the sensitivity of our method. The magnitude of the output power is fit to theory leading to a calibration of the measured phonon mode population/temperature [performed at 210 mK for each device, parameter \mathcal{M} in Eq. (7.1.2) and Fig. 7.1 (top right)].

7.1.2 Blue-detuned pumping method

The method we propose builds on the parametric instability of the blue-detuned pumping scheme. When the pump tone is applied at ω_{cav} , the size of the two equivalent sideband peaks (their measured area \mathcal{A}_0 , in photons/s) is simply proportional to injected power P_{in} and mode temperature T_{mode} [136]:

$$\mathcal{A}_0 = \mathcal{M} P_{in} T_{mode}. \quad (7.1.2)$$

This "green" scheme alters neither the measured position of the sideband peaks (detuned by $\pm\Omega_m[T_{NEMS}]$), nor their linewidth $\Gamma_m[T_{NEMS}]$: both are determined by mechanical properties, which depend on the NEMS temperature T_{NEMS} . The lineshapes are Lorentzian as shown in Fig. 4.3. We introduce the number of stored photons in the cavity n_{cav} function of both P_{in} and Δ (see Chapter 2):

$$n_{cav}(P_{in}) = \frac{P_{in}}{\hbar(\Delta + \omega_{cav})} \frac{\kappa_{ex}}{\Delta^2 + \frac{\kappa^2}{4}}. \quad (7.1.3)$$

Note that this formula is valid for both chips containing drum devices, as they are measured in reflection. In the case of the beam chip, the measurement is performed in transmission and we make the substitution $\kappa_{ex} \rightarrow \kappa_{ex}/2$ in the previous expression.

On the other hand for blue-detuned pumping, as we increase the injected power P_{in} (but keep it below the instability threshold), the area \mathcal{A} of the Stokes peak is amplified. The blue/red-detuned pumping expressions write:

$$\Gamma_{eff}(P_{in}) = \Gamma_m - \text{Sign}(\Delta) \frac{4g_0^2}{\kappa} n_{cav}(P_{in}), \quad (7.1.4)$$

$$\mathcal{A} = \mathcal{A}_0 \frac{\Gamma_m}{\Gamma_{eff}(P_{in})}, \quad (7.1.5)$$

in the limit of negligible cavity thermal population. For $\Delta > 0$, the last term in Eq. (7.1.5) after the Sign is a gain, illustrated in Fig. 7.1 (bottom right). It arises from the anti-damping, with Γ_{eff} the linewidth of the Lorentzian peak. Controlling the applied power P_{in} , from the knowledge of system parameters one can straightforwardly recalculate the

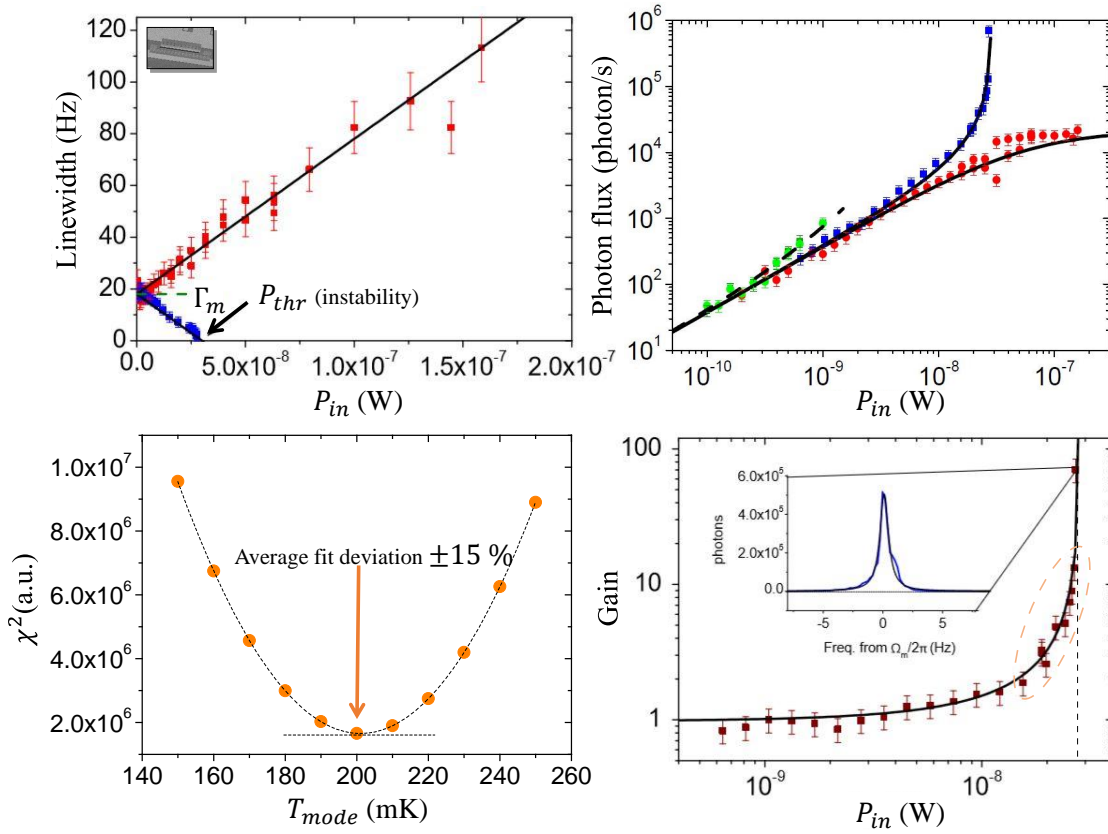


FIGURE 7.1 – Experimental data of the beam device. Top left: Effective damping/anti-damping Γ_{eff} measured for the blue and the red-detuned pumping schemes as a function of power (at 210 mK, blue and red squares respectively). The slope of the fit (black line) leads to the definition of g_0 [fit with Eq. (7.1.4)], while the $P_{in} \approx 0$ corresponds to Γ_m . The arrow indicates the position of the threshold P_{thr} towards self-sustained oscillations, which is simply proportional to Γ_m (see text). Top right: Measured signal amplitude for the 3 schemes used at 210 mK: blue-detuned pump, red-detuned pump and "in-cavity" ("green", the square and circle symbols stand for Stokes and Anti-Stokes peaks respectively). For blue/red pumping, the fits correspond to Eqs. (7.1.5), defining the coefficient \mathcal{M} . The dashed line corresponds to the heating measured in Fig. 7.3. Bottom left: χ^2 function of the output photon flux computed in the parametric amplification region only (orange region in Bottom right figure) demonstrating the ability to evaluate a modal temperature T_{mode} using the thermomechanical noise amplification method. Bottom right: Main: gain of the parametric amplification method based on the blue-detuned pumping scheme (210 mK data, brown squares), as a function of P_{in} . The asymptote indicates the position of the threshold P_{thr} towards self-sustained oscillations (see Chapter 8 for details on this particular regime). Inset: resonance line (blue trace) measured at very large gains, demonstrating its Lorentzian lineshape (linewidth of order 0.9 Hz, close to instability). The black lines are fits, and we report about 20 dB amplification of the Brownian signal. Finite error from both statistics and fluctuation in mechanical parameters (see text).

value of \mathcal{A}_0 , and thus of T_{mode} (i.e. the temperature of the mode in absence of optomechanical pumping). In Fig. 7.1 (bottom right) we demonstrate 18.5 dB gain with the beam device, which is greater than the previously reported maximum for a similar setup using a graphene device [206]. This setup is thus an in situ parametric amplifier with gains comparable to a standard HEMT amplifier. Essentially only Γ_m depends on temperature, and has to be known to apply Eq. (7.1.5). It can be obtained easily from a measurement of the mechanical effective damping [the linewidth of the Lorentzian Stokes peak, Fig. 7.1 (top left)], by either extrapolating to $P_{in} \rightarrow 0$ or defining the position of the threshold $P_{thr} \propto \Gamma_m$ [with Eq. (7.1.4) at $\Gamma_{eff} = 0$, see Figs. 7.1]. Obviously, the main requirement for this T_{mode} estimate is the stability of experimental parameters. The mechanical mode

itself happens to be the limiting element, leading to finite error bars at large gains in Fig. 7.1 (bottom right); fluctuations are further discussed in following Sections. On Fig. 7.1 (bottom right) we demonstrate by plotting the χ^2 function calculated in the parametric amplification region (from the curve giving \mathcal{A}) that it is possible to extract a fitted modal temperature T_{mode} by using the parametric instability. This method should work down to 1 mK for this beam device (limited by microwave absorption heating), and well below for higher-coupling devices such as our drumhead NEMS.

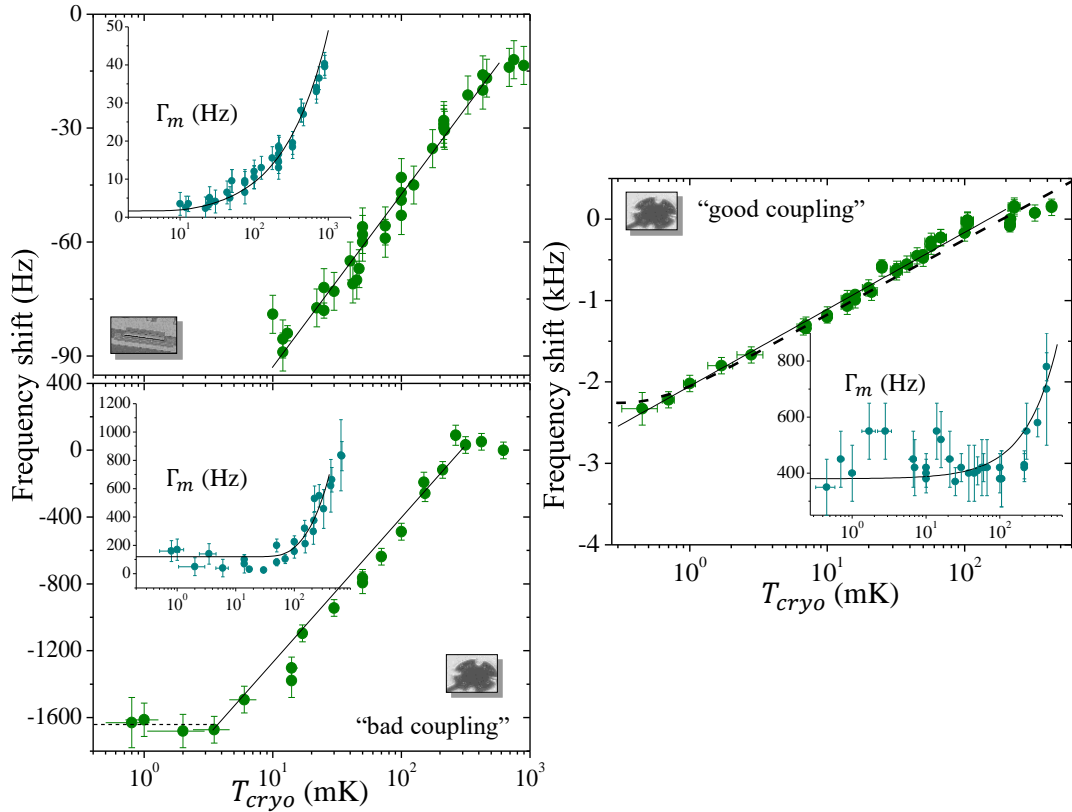


FIGURE 7.2 – Mains: Mechanical resonance frequency shift from $\Omega_m [T^*]$ as a function of the cryostat temperature T_{cryo} of the flexural mode of the beam device from 3.8 MHz (Top left), of the first mode of the badly-coupled drum device from 6.7 MHz (Bottom left) and of the first mode of the highly-coupled drum device from 15.1 MHz (Right). Insets: Corresponding mechanical damping parameter Γ_m as a function of cryostat temperature T_{cryo} for each device. The black lines are fits following the TLS model (power laws plus constant for the damping, and logarithmic for the frequency shift; the dashed line in the right panel is from the digamma function expression [211], see text). Parameter $T^* \approx 1.1$ K, $\alpha \approx 0.65$ for the beam, and $1 \pm 10\%$ for the two drums. Note the scatter in the data, and the range covered by the temperature axis. The dashed horizontal for the badly coupled device frequency shifts illustrates a saturation discussed in the text.

7.2 OPTOMECHANICAL THERMOMETRY

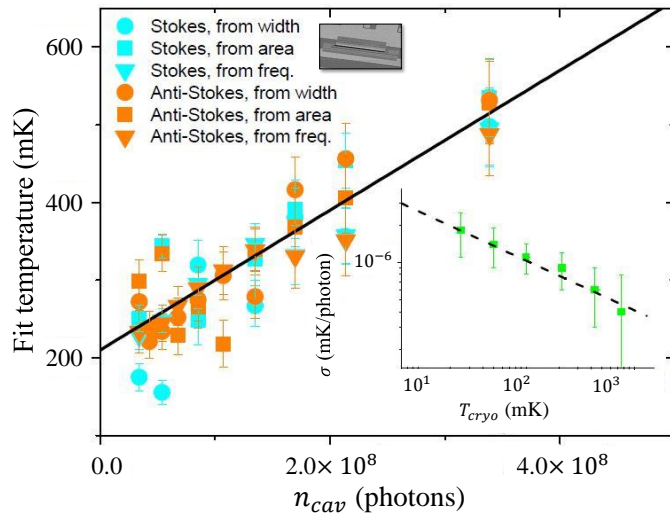
7.2.1 Phononic and Two-Level Systems (TLS) thermometry

The measured mechanical damping rates Γ_m and resonance frequencies Ω_m are shown in Fig. 7.2 for the first out-of-plane flexural mode of the beam device and for the first modes of the drumhead devices. The displayed dependencies are characteristic of NEMS devices in the millikelvin range: a damping $\Gamma_m \propto T^\alpha$ with $0.3 < \alpha < 2.5$ (eventually

saturating at the lowest temperatures) and a logarithmic frequency shift $\propto \ln(T/T^*)$ with T^* a characteristic temperature (see fits in Fig. 7.2). For all materials (from monocrystalline to amorphous) this behavior is understood as a signature of TLSs (Two-Level Systems) [211, 221, 46, 118, 174, 19, 143]: either defects (e.g. for monocrystalline Si, or polycrystalline Al), or constitutive of the atomic arrangement (for amorphous SiN). The logarithmic frequency shift is actually the high-temperature expansion of a more complex expression involving the digamma function [211] (see dashed line, right panel Fig. 7.2). Direct coupling of the first flexural mode to the phonon bath (i.e. clamping losses) [151] is negligible for beam structures at millikelvin temperatures, but clearly visible for the drums (saturation).

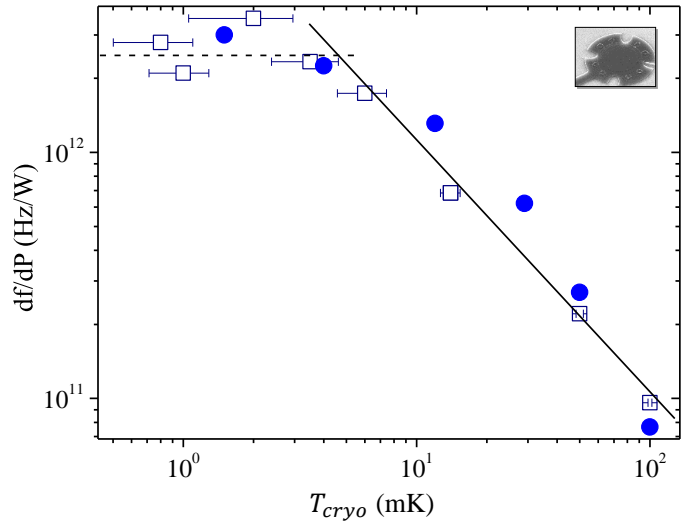
Within the TLS model the mechanical mode is coupled to the two level systems, which are themselves coupled to the external bath: the electrons and the (thermal) phonons present in the moving structure [118]. For superconducting materials, the electronic contribution is negligible and the TLSs temperature should reflect the phononic temperature in the NEMS structure (i.e. the temperature of high frequency modes well-coupled to the clamping ends), which we simply defined as T_{NEMS} . By inverting the fits in Fig. 7.2 it is thus straightforward to extract T_{NEMS} . The aim of our work is thus to compare the

FIGURE 7.3 – Main: microwave heating as a function of n_{cav} performed at 210 mK with the beam device, with temperatures recalculated from the measured width and position (corresponding to T_{NEMS}) and peak area (T_{mode}). The line is a linear fit, leading to the microwave-heating coefficient σ . Inset: heating coefficient σ versus cryostat temperature T_{cryo} ; the dashed line is a power law $T^{-0.4}$ guide to the eye.



temperature of the cryostat T_{cryo} to T_{NEMS} and T_{mode} . These results are analyzed in Section 7.2.2; however it is mandatory to quantify beforehand the impact of the microwave pump power on the defined temperatures for each studied mechanical structure. For this purpose we use the "in-cavity" pumping scheme ("green" pumping). We measure, at a given temperature T_{cryo} , the mechanical characteristics Γ_m, Ω_m and the area \mathcal{A}_0 of the two sideband peaks as a function of injected microwave power P_{in} . Using respectively the fits of Fig. 7.2 and Eq. (7.1.2), we can recalculate the expected temperatures T_{NEMS} and T_{mode} under microwave irradiation. Since the local heating should be proportional to the local electric field squared confined onto the NEMS, we discuss these results as a function of n_{cav} . A typical result obtained at 210 mK is shown in Fig. 7.3 (main graph) in the case of the beam device. Both T_{NEMS} (obtained equivalently from damping and frequency shift) and T_{mode} extracted from photon flux fits display the same linear dependence on n_{cav} , and the two sidebands are equivalent: this demonstrates that the effect is indeed thermal. Defining the slope of the fit as σ , we can extract this coefficient as a function of T_{cryo} (Fig. 7.3 inset). This temperature-dependence is non-trivial, and no heating model is provided here: such a model should take into account the microwave absorption in

FIGURE 7.4 – df/dP as a function of the temperature of the cryostat T_{cryo} measured down to demagnetization temperatures with the badly-coupled drum device (see Fig. 7.2 bottom left). The heating effect measured demonstrates thermalisation down to about 3 mK, with a similar saturation (dashed line) as the frequency shift presented in Fig. 7.2 bottom left. The full line is a $1/T$ guide. Blue dots represent theoretical calculations based on a simple microwave-induced heating (see text).



the materials, the energy flow in the mechanical structure plus the clamping zone slab (suspended by the fabrication undercut), and finally the anchoring to the bulk of the chip. Nonetheless, we can use this graph to estimate the NEMS heating for a given T_{cryo} and n_{cav} in the blue-detuned pumping scheme. For instance, we extrapolate that applying a power of order P_{thr} at 1 mK would heat the beam device by about 1 mK; above 10 mK, the heating is essentially negligible. Knowing the smallness of the coupling g_0 of the beam employed here, this demonstrates the capabilities of the method. Furthermore, because of this microwave-heating it is obviously meaningless to report experiments below about $T_{cryo} \approx 1$ mK for this first ultimate cooling attempt. A similar heating analysis can be performed for the drum devices. This is reported in Fig. 8.1 of Chapter 8 using the population measured with a red pumping scheme, down to 10 mK, on the badly-coupled device. In Fig. 7.4 we show the power-induced frequency shift through the slope df/dP down to the lowest temperatures for the same device. Similarly to the inset of Fig. 7.3 (beam case), we report on a power law dependence. However a saturation is observed below about 3 mK, reminiscent of the one of the frequency shift of Fig. 7.2 (bottom left panel). Using the fit of the heating effect from Fig. 8.2 (i.e. the coefficient dT/dP) and the temperature derivative of the frequency shift df/dT (from the fit of Fig. 7.2, bottom left), we can work out the theoretical points (in blue) in Fig. 7.4 representing a simple microwave-induced heating. From this, it appears that with the smallest microwave power we can use for the measurements of the badly coupled drum (about 10^{-10} W, in order to limit the averaging times), we calculate a *decoupling temperature* of about 3 mK; which is precisely the saturation observed. We thus conclude that this effect is of pure thermal origin, due to the measurement scheme itself. Indeed, this saturation is not observed with the highly coupled drum (Fig. 7.2 right), where no heating signatures could be detected.

7.2.2 In-equilibrium results

From fits to Eq. (7.1.5) of the power-dependent Stokes peak area, we thus extract T_{mode} . These fits are presented as an example with experimental data for two of our NEMS devices on Fig. 7.5. Reversing the fits of the mechanical parameters Γ_m, Ω_m (Fig. 7.3) we obtain T_{NEMS} . Both temperatures are displayed as a function of T_{cryo} in Fig. 7.6, for our three NEMS characterized in this thesis. Reported lowest thermodynamic temperatures

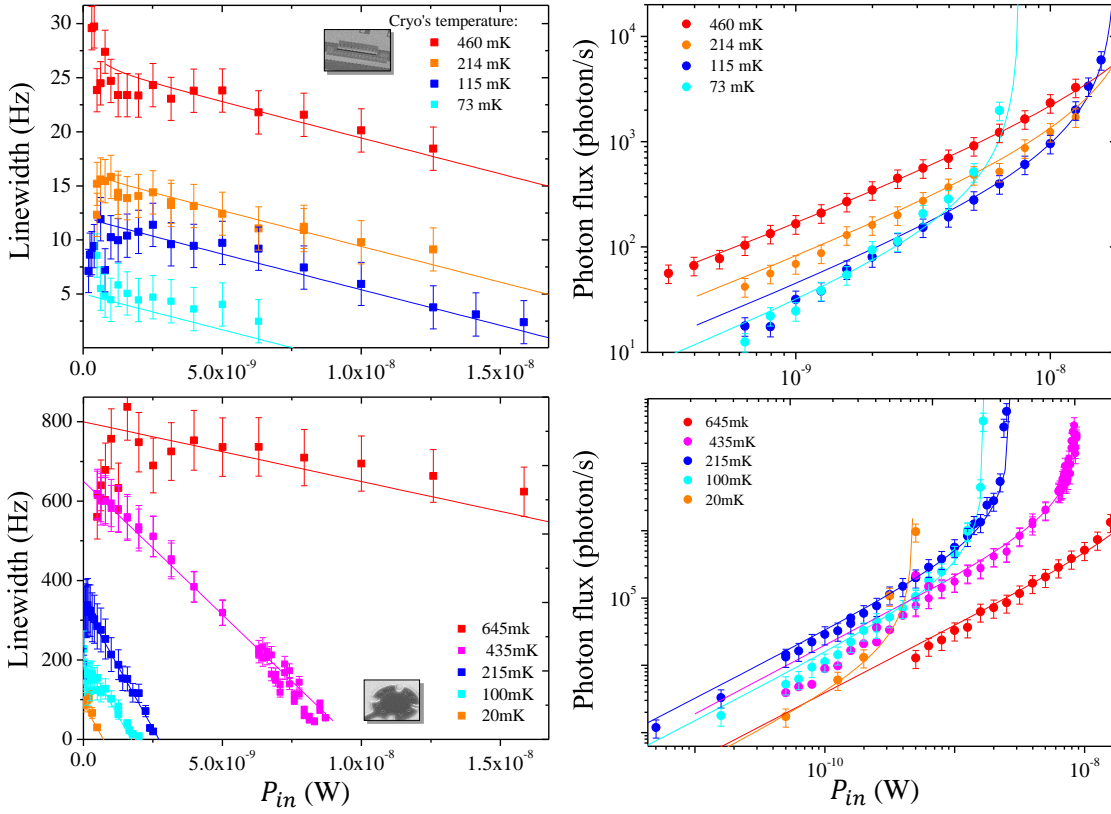


FIGURE 7.5 – Top left: Effective linewidth Γ_{eff} of the flexural mode of the beam device as a function of the input power P_{in} at different cryostat temperatures T_{cryo} in the case of Stokes pumping. Top right: Corresponding output photon flux (area of the Stokes sideband \mathcal{A}) as a function of the input power P_{in} for the beam at different cryostat temperatures T_{cryo} . In this case we are always in the resolved sideband regime, the cavity being made of niobium which has a T_c of 9 K. Dots are experimental measurements and lines correspond to theoretical fits [Eq. (7.1.4) for Γ_{eff} and Eq. (7.1.5) for \mathcal{A}]. Bottom: Same plots realized with the badly-coupled drum device. In this case, the cavity being made of aluminum which has a T_c around 1.2 K, the optical quality factor $\propto 1/\kappa$ decreases at high temperature and we are not always in the resolved sideband regime. It is the reason why the slope of the effective damping Γ_{eff} is not always the same and that there is a loss of signal \mathcal{A} at high temperature (red dots).

in the literature lie all within the range 10 – 30 mK [30, 202, 113, 54, 57, 77, 185, 163, 206, 112]; however one work reports a potential mode temperature for an Al-drum of order 7 mK, consistent with base temperature of dry dilution cryostats [107]. Similarly, a lowest temperature of 7 mK is reported for a gigahertz phononic crystal [94]; but obviously such a mode cannot be used for phonon thermometry at millikelvin temperatures.

For the 3 mechanical structures studied, we demonstrate a thermalisation from about 10 mK to 1 K of the mode and of the whole device; in particular the beam and the badly coupled drum are in thermal equilibrium over 2 orders of magnitude in T_{cryo} . In the case of the badly-coupled drum, we even demonstrate a frequency shift following temperature down to $T_{NEMS} \approx 3$ mK (see Figs. 7.2 and 7.3). Finally for our best device, the highly-coupled drum, we were able to measure at very low photon drives inside the cavity (smaller than 1000) down to the lowest achievable temperatures, below 1 mK, extracting *both* the phonon mode temperature T_{mode} and the environment temperature T_{NEMS} .

Our results are summarized in Fig. 7.6, going beyond today's state-of-art. However concerning the beam device, we did not measure better than others even though the

cryostat cools well below 7 mK. For the badly coupled drum, the same is true for the mode temperature T_{mode} , even though the frequency shift could be tracked to even lower temperatures. The reason for this is discussed in Section 7.3: below a certain temperature (typically 100 mK for the beam device and about 30 mK for drum devices), the system displays huge amplitude fluctuations which hinder the measurements (Fig. 7.7). These features have been seen by other groups for beam-based microwave optomechanical devices containing an Aluminum layer, but never reported so far. Until recently, this essentially prevented experiments from being performed on these types of devices below physical temperatures of order 100 mK [88, 111, 200]; remarkably however, (Al covered) ladder-type Si beams [185] seem to be less susceptible to this problem than simple doubly clamped beams. On the other hand, we are the first to report large signal fluctuations with (Al) drum-like structures. These large amplitude fluctuations do not show up in schemes which do not involve microwaves (e.g. magnetomotive measurements of SiN and Al beams [82], or laser-based measurements of Si beams [46]). This is what enabled nano-mechanical experiments to be conducted at base temperature of dilution cryostats. For our highly-coupled device where measurements are performed at very low powers, these fluctuations have not been seen with red and blue pumping schemes. However, with in-cavity pumping (which confines much more photons in the optical mode) the same problem seemed to appear again.

Up to now, the only possibility to deal with these large events was post-selection (see shaded areas in Fig. 7.6), which is extremely time consuming and even stops being usable at all at the lowest temperatures. The origin of this phenomenon remains unknown, and we can only speculate on it in Section 7.3 hereafter. Note that this behavior has nothing to do with a thermal decoupling, as shall be discussed below. On Fig. 7.6 (bottom), we present the state-of-the-art measurements obtained with the highly-coupled drum device, in particular we demonstrate that both its fundamental mode (T_{mode}) as well as its TLS environment temperature (T_{NEMS}) follow the cryostat temperature down to about 500 μ K. The specific features related to ground-state cooling will be discussed in Section 7.4. This 15 MHz device being of relatively high frequency, in this range of very low temperatures one needs to take into account the proper quantum expression for the mode population in the fitting. From the measured area of the peak obtained in the blue sideband scheme (see Chapter 4), we actually define:

$$T_{mode} \rightarrow T_{eff} = \frac{\hbar\Omega_m}{k_B}(n + 1), \quad (7.2.1)$$

with:

$$n = \frac{1}{e^{\frac{\hbar\Omega_m}{k_B T_{cryo}}} - 1}, \quad (7.2.2)$$

the Bose expression. At high temperatures, we indeed recover $T_{eff} \approx T_{cryo}$, ensuring $T_{eff} = T_{mode}$ ($y = x$ lines in Fig. 7.6). This law is always valid for modes with low enough resonance frequencies. However, for the highly coupled device around 1 mK, we observe a clear deviation of T_{eff} from the classical behavior (see magenta line, bottom right panel). This deviation cannot be interpreted as a thermal decoupling, since data-points lie on the theory line and the frequency shifts follow temperature nicely. However, extracting the proper T_{mode} value from the data (with relevant accuracy) is more difficult than for the classical limit, and shall be discussed in Section 7.4.

More conventional frequency Ω_m and damping Γ_m fluctuations [170] are also present (see e.g. Fig. 7.7). These features have been reported for essentially all micro/nano me-

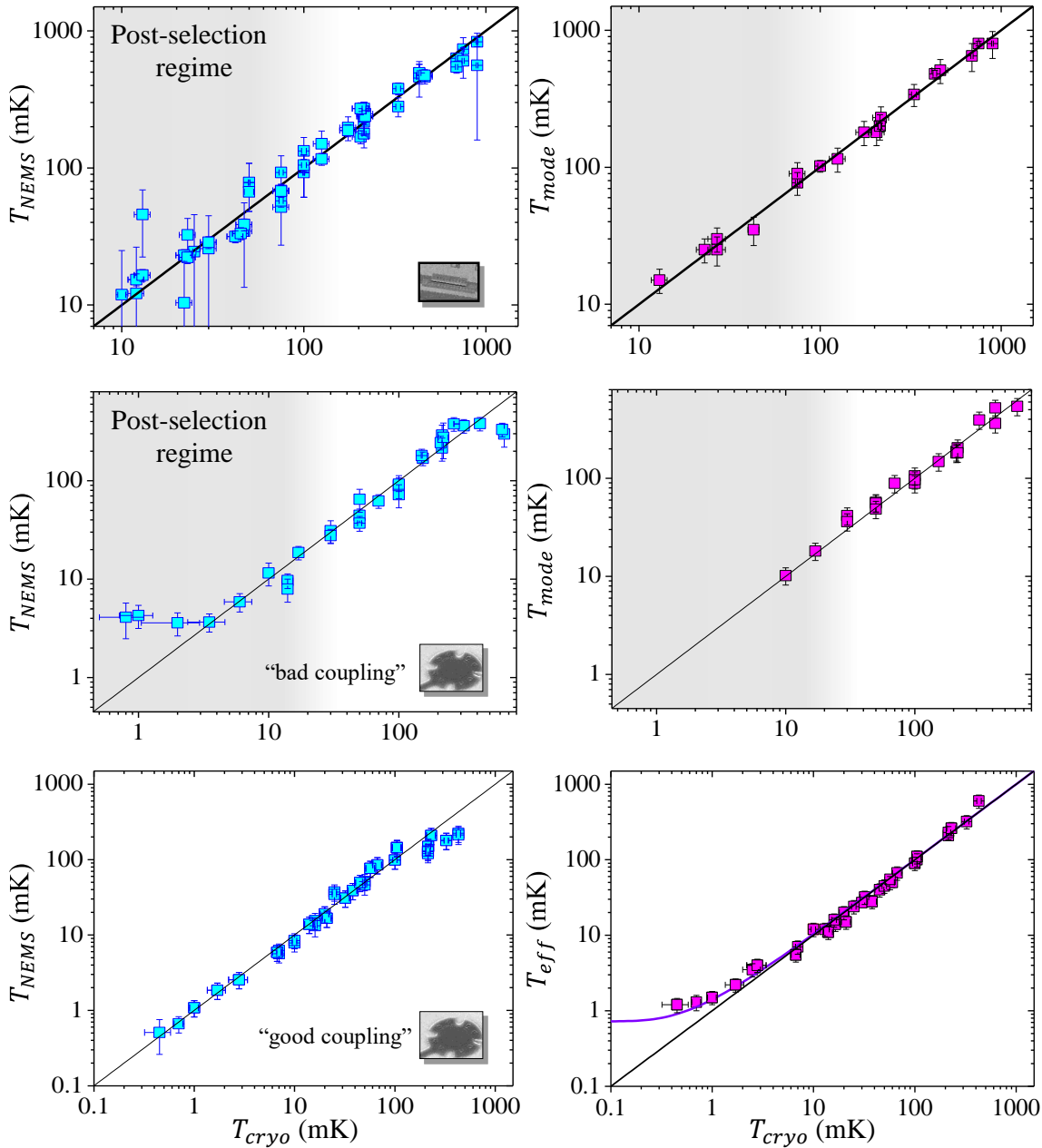


FIGURE 7.6 – Top left: NEMS temperature T_{NEMS} of the beam device inferred from the TLS bath as a function of cryostat temperature T_{cryo} . Top right: mode temperature T_{mode} of the out-of-plane flexural mode of the beam as a function of T_{cryo} . Middle: Same plots for the badly-coupled drum structure (for T_{mode} , the decrease of κ near 1 K has been taken into account). Bottom: Same plots for the highly coupled drum NEMS, with T_{mode} replaced by T_{eff} (see text). The black lines are the $y = x$ functions, whereas the purple curve (bottom right graph) corresponds to the theoretical quantum calculation which is necessary for this higher frequency mode (see text).

chanical devices, as soon as they were looked for; their nature also remains unexplained, and their experimental magnitude is much greater than all theoretical expectations [145]. Frequency noise essentially leads to inhomogeneous broadening [168]. It does not alter the area \mathcal{A} measurement, but does corrupt both frequency and linewidth estimates. This noise comes in with a $1/f$ -type component [170, 145], plus telegraph-like jumps (see also end of Chapter 8). It leads to the finite error bars in Fig. 7.2 insets; below 10 mK, for the beam device, the mechanical parameters Ω_m and Γ_m cannot be measured accurately.

Similar damping fluctuations [170] are more problematic, since the amplification gain Eq. (7.1.5) depends on Γ_m . The error bars of Fig. 7.2 (main graph) are essentially due to this; they translate into a finite error for the estimate of the gain, Fig. 7.1, which itself limits the resolution on T_{mode} (see Fig. 7.6).

7.3 UNSTABLE STOCHASTIC DRIVING FORCE

In Figs. 7.7 and 7.8 we show a typical series of spectral acquisitions as a function of time, around 1 and 5 mK measured with the more sensitive device, the beam structure. We see very large amplitude fluctuations which start to appear around 100 mK for this device, and get worse for lower temperatures (regardless of the scheme used): the "spikes" grow even larger, but more importantly their occurrence increases. We studied these events in the whole temperature range accessible to our experiment for our three different devices. Their statistics seems to be rather complex as we show in Fig. 7.10. Key features are summarized in this Section. For blue-detuned pumping the spikes worsen as pump power increases, while for red-detuned pumping it is more or less the opposite, suggesting that the effective damping of the mode Γ_{eff} plays an important role. With in-cavity pumping, spiky features are also present at very low powers, but not at high powers when the beam physical temperature exceeds about 100 mK. The recorded heights can be as large as equivalent mode temperatures in the Kelvin range. Around 10 – 30 mK, post-selection becomes impossible.

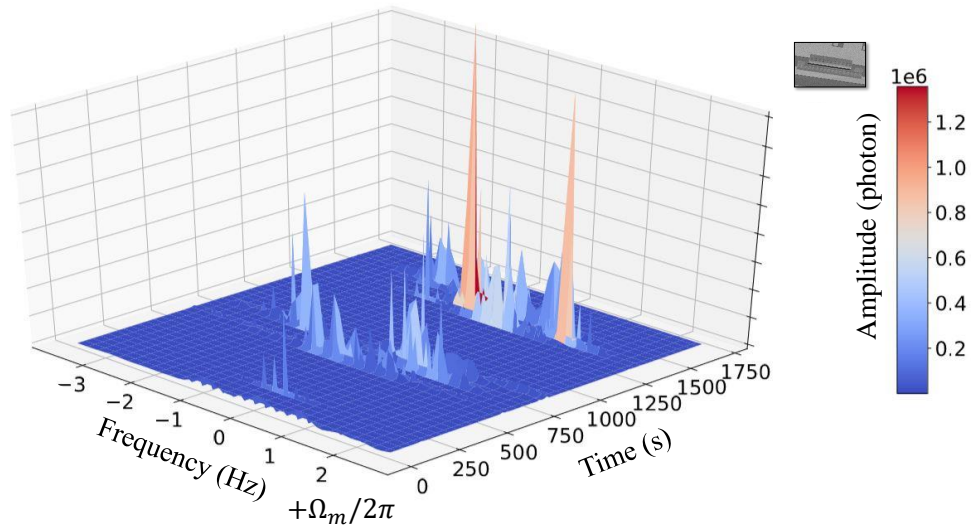
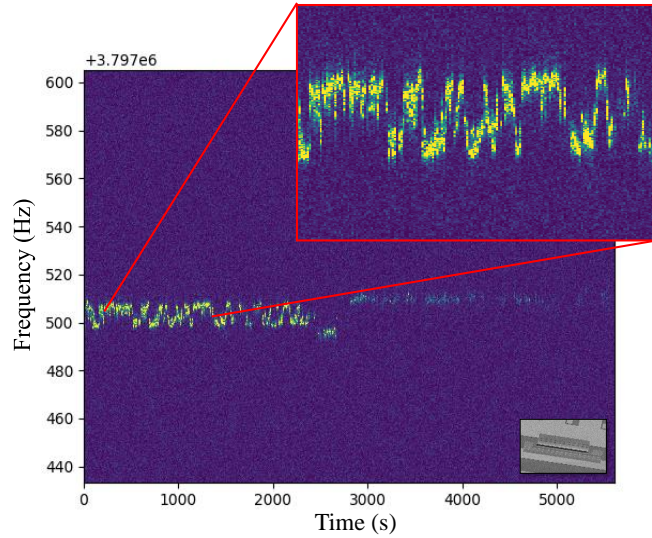


FIGURE 7.7 – Stokes resonance peak of the beam mode (amplitude in color scale, frequency from Ω_m on the left) as a function of time at about 1 mK (0.6 nW applied power, blue-detuned pumping scheme). Huge amplitude jumps are seen, together with frequency (and damping) fluctuations (see text).

With the aim of searching for the origin of this effect, we have characterized it in various situations. We first realized that cycling the system from the lowest temperatures to above 100 mK was producing a sort of "reset". But very quickly (a matter of hours), after cooling down again the large spikes happen to dominate the signal again. We then tried to apply a small magnetic field to the system; this was not very conclusive. However, applying a DC voltage had a drastic effect on these random features. This is illustrated in Fig. 7.9 using the beam device: with a few volts on the chip's coplanar transmission line all the large features are shifted at low amplitude. The averaged signal (deeply buried

into the noise) recovers a reasonable Lorentzian lineshape (see fits in Fig. 7.9), while the shape of the spikes is not resolved (Figs. 7.7 and 7.8).

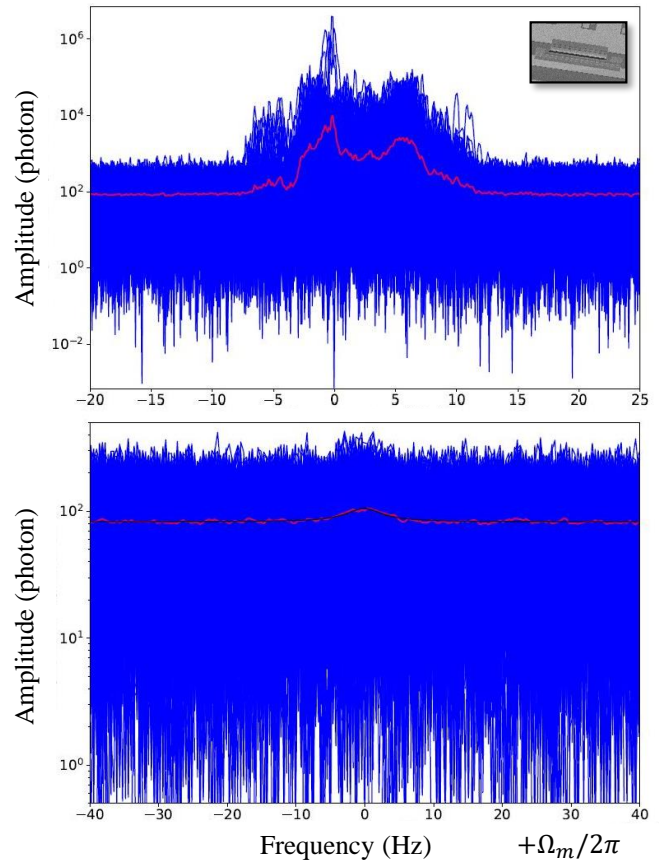
FIGURE 7.8 – Spectrogram of the Stokes resonance peak (amplitude in color scale) as a function of time measured with the beam at 5 mK (0.6 nW applied power, blue-detuned pumping scheme). Huge amplitude fluctuations are observed as well as a clear frequency telegraphic noise.



In discussing the source of this feature, a few comments have to be made. What is shown in Figs. 7.7 and 7.8 is primarily fluctuations of the output optical field. These are detected only on the Stokes and Anti-Stokes peaks, for any of the schemes presented in Chapter 2. Furthermore, the threshold to self-oscillation in the blue-detuned pumping scheme displays a large hysteresis (certainly due to nonlinearities in the system). We have noticed that when the microwave power applied (at frequency $\omega_{cav} + \Omega_m$) lies within this hysteresis, the spiky events seem to be able to trigger the self-oscillation. This would not be possible if the amplitude fluctuations measured were only in the detected signal, at the level of the HEMT. We thus have to conclude that we see genuine mechanical amplitude fluctuations. However, these cannot be due to damping fluctuations alone that could trigger self-oscillations, since we do see the same type of features when pumping red-detuned or in-cavity.

If these fluctuations were due to the input field itself, from Fig. 7.3 we would reasonably conclude that the NEMS beam would be heated to rather high temperatures, leading to broad and very shifted in frequency (see Fig. 7.2) Stokes/Anti-Stokes peaks. This is not compatible with the measurement of Figs. 7.7 and 7.8. The only reasonable conclusion seems thus to be that we do suffer from a genuine extra stochastic force acting on the mechanical element. This is consistent with a stronger sensitivity to the phenomenon when the effective damping of the mode Γ_{eff} is small (blue-detuned scheme). Since a DC voltage applied only to the cell can drastically modify the measured features, the source has to be on-chip. Leading to the same conclusions, we can point out that with an in-cavity pumping, it disappears when the NEMS temperature exceeds a certain temperature (typically 100 mK for the beam and about 30 mK for drums). This temperature depends on the device and we observe that the strength/occurrence of spikes is linked to the number of photon stored in the cavity n_{cav} . We conclude that it should even be within the mechanical element. But the mechanism remains mysterious: citing only documented effects in other areas of research, is it linked to vortex motion in the superconductor [52], trapped charges [27], adsorbed molecules [191], the propagation of mechanical cracks [18, 100] or to atomic-size Two-Level-Systems in dielectrics (beyond the standard friction model) [104] ? With the interesting idea that perhaps a sound track can reveal features

FIGURE 7.9 – Comparing beam measurements with and without applied DC voltage in similar conditions. Top: resonance lines (blue) obtained at 5 mK with 0.6 nW drive; 2 hours acquisition shown in 560 averaged traces, with no DC voltage bias. Bottom: resonance lines obtained at 7 mK with 0.8 nW drive; 18 hours in 770 averaged traces, with +3 V DC applied on the transmission line (see text). The scheme used for both data sets is blue-detuned pumping, and the thick black line is a fit of the average curve (in red). Note the 10^4 difference in the vertical axes.



that an image cannot, this strange phenomenon has been "sonified" by Miles Blencowe, see Ref. [196]

The low temperature properties of NEMS are described within the tunneling model of Two-Level-Systems (TLSs): for damping, frequency shifts, and phase fluctuations [221, 46, 123, 170]. It is thus natural to consider strongly coupled individual TLSs as the most probable source of our problems. Besides, while the actual nature of these microscopic defects remains elusive in most systems, they could be generated in many ways beyond the standard atomic configuration argument [5]; an electron tunneling between nearby traps would be a TLS strongly coupled to its electromagnetic environment, among other possibilities [191]. For Al-based NEMS, these would create (only a few) defects present in (or on) the Al layer; they should carry a dipole moment, which couples them to the microwave drive as well as to the electric field generated by the applied DC voltage. This field distorts their potentials, such that they could get locked in one state and "freeze". Furthermore, our results seem to be very similar to those of Ref. [75] obtained with a macroscopic mechanical glass sample, where "spiky" events were demonstrated to be originating in the interaction with low-level radioactivity (gamma rays). These results suggest a parametric coupling to TLS at Giga-Hertz frequencies mediated by the microwave drive, but were the energy corresponding to the large peaks would be provided by the external radiation.

The reason why the mechanism should be dependent on the low phononic dimensionality or size of the device (typical width of beams about 100 nm, much smaller than the phonon wavelength at 10 mK) is nontrivial. One simple argument could be that the spring constant of the modes under consideration are very different: about 1 N/m for megahertz beams and 100 N/m for drumheads. This could justify why beam-based structures are

more reactive to external force fluctuations; an immediate consequence of this argument is then that membrane-based AI devices are not truly immune to force fluctuations, but are just less sensitive: this is true, cooling them to low enough temperatures revive the same features as for beam-based NEMS. Indeed, on Fig. 7.10 we present a comparison of experimental measured statistics between the beam device and the badly-coupled drum NEMS. We observe a rather equivalent impact of lowering temperature and applying a DC voltage bias, the "spike" statistics of both structure being very similar.

For the strongly coupled drum device, spike-type behavior has been seen only when using the green pumping scheme, where the number of photons in the cavity is large. In contrast, we could measure with red and blue schemes down to about 100 photons without any visible "spike" problem.

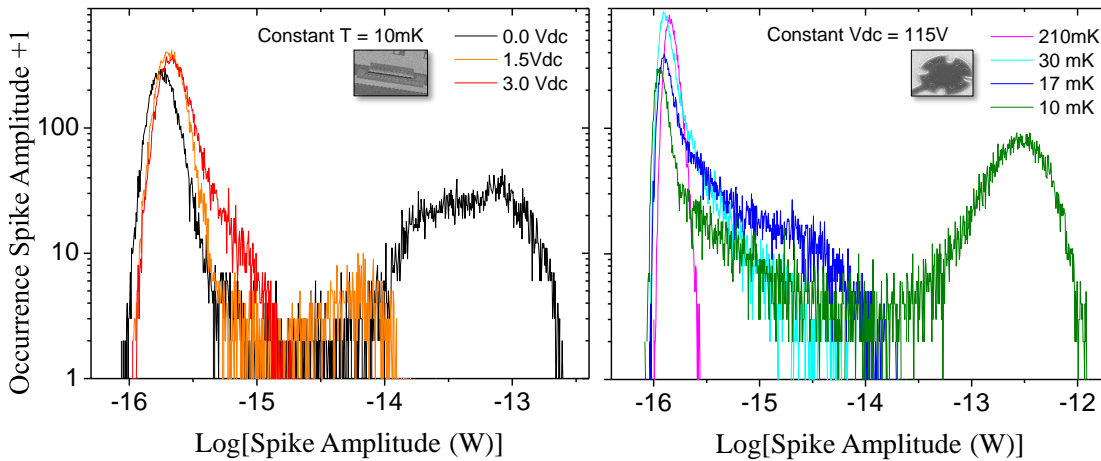


FIGURE 7.10 – Left: Statistics of the "spike" amplitude of the beam device at constant cryostat temperature T_{cryo} but at 3 different applied DC voltage. Right: Statistics of the "spike" amplitude of the badly-coupled drum NEMS at constant applied DC voltage but at 4 different T_{cryo} . Both were measured with a blue-detuned pumping. We clearly see that the drumhead and the beam devices have very similar spiky behavior and we can postulate that there is a sort of equivalence between temperature and DC voltage bias. Temperature and DC voltage bias have the same effect on the statistics, they shift high-amplitude "spikes" down to low-amplitudes but unfortunately the integral of the statistics remains essentially identical. Note the huge difference in applied voltage between the beam and the drum; indeed in the design of the drumhead chip the transmission line is much further from the mechanical element than in the design of the beam chip.

To conclude, let us concentrate on the measurements performed at ultra-low temperatures with a DC voltage bias applied to the beam device (i.e. of the type of Fig. 7.9, bottom). Even with the help of the in-built parametric amplification, the signal is very small and requires decent averaging, typically here about 30 minutes for reasonable error bars. Even if the resonance peak is Lorentzian, below typically 20 mK the measured area \mathcal{A} does not correspond to the actual cryostat's temperature T_{cryo} : it is always bigger, but the actual value presents large fluctuations in magnitude. This is demonstrated in Fig. 7.11, with identical measurements performed at 23 mK and 7 mK. What is shown is how the measured area of the Stokes peak evolves over time, performing a sliding average over the whole set of acquired data. In the former case, we see that the fluctuations of the measured area are not more than about +60%; they are much smaller for higher temperatures, leading to proper estimates of T_{mode} . However, for the latter these are greater than 300%. Besides, fluctuations happen to have an extremely slow dynamics: while spikes switch on/off faster than our acquisition time, their overall occurrence fluctuates over a day (Fig. 7.11). By no means could this behavior be explained by a thermal

decoupling of the device from the cryostat. As a consequence, even the calm zones in Figs. 7.7 and 7.8 are corrupted by the phenomenon shown in Fig. 7.11. This is essentially why no reliable data could be acquired below 10 mK for this beam NEMS; but from the DC biasing and the continuous monitoring of the Stokes peak, thermal equilibrium has been demonstrated at about ten times lower temperature than previously reported in microwave doubly-clamped beam NEMS experiments [88, 111, 200].

Besides, the drumhead bulk temperature has been demonstrated to cool down to at least 3 mK. The visible saturation can be interpreted as thermal decoupling (which would mean that some heat load is present on the device, and would deserve to be understood). It could also be that the saturation is a property of the materials, say the coupling to TLSs or even the presence of the "spikes".

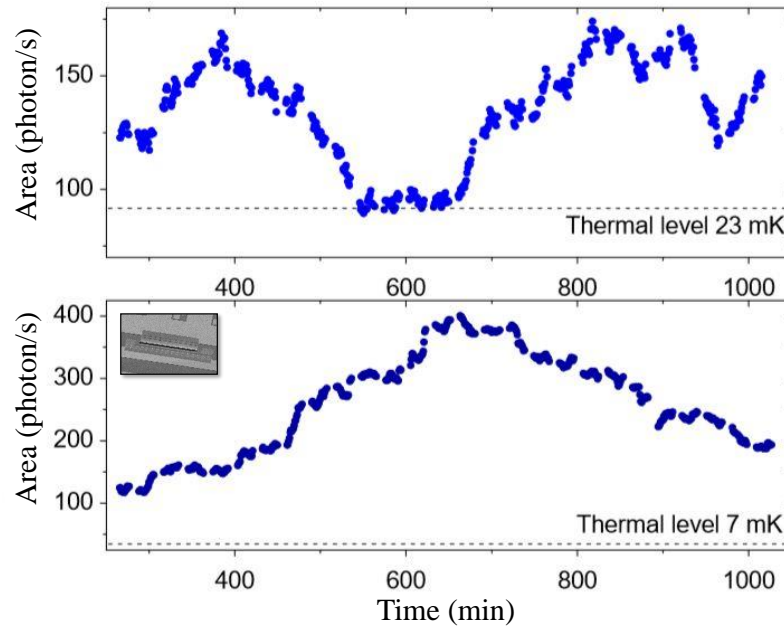


FIGURE 7.11 – Beam measurements. Top: area of peak extracted from a sliding average performed with a window of 26 minutes at 23 mK, with applied power 0.8 nW (blue-detuned pumping). Bottom: same measurement performed at 7 mK. The horizontal dashed lines are the thermal population expected values, matched at 23 mK in the stable zone (middle of graph). At the lowest temperatures, we observe very large amplitude fluctuations which cannot be of thermal origin; the measured area remains always larger than the expected value (see text).

7.4 GROUND STATE COOLING

In this section, we present state-of-the-art quantum measurements performed with the highly-coupled drumhead device down to about $500 \mu\text{K}$ [218]. In particular, we demonstrate for the first time in-equilibrium observation of motional sideband asymmetry, which allows us to perform sideband asymmetry thermometry at ultra-low temperatures. Besides, reaching the quantum ground state of motion of this macroscopic device, in-equilibrium with its direct environment, enables the measurement of genuine thermodynamical quantum properties (see next section).

7.4.1 Sideband asymmetry thermometry

Sideband asymmetry has already been used to demonstrate ground state cooling of mechanical modes, mainly using optomechanical crystals [133, 33]. In particular, it has been demonstrated with trapped ultra-cold atoms that sideband asymmetry is relevant for mode thermometry [159, 239]. In this Section, we report on sideband asymmetry ther-

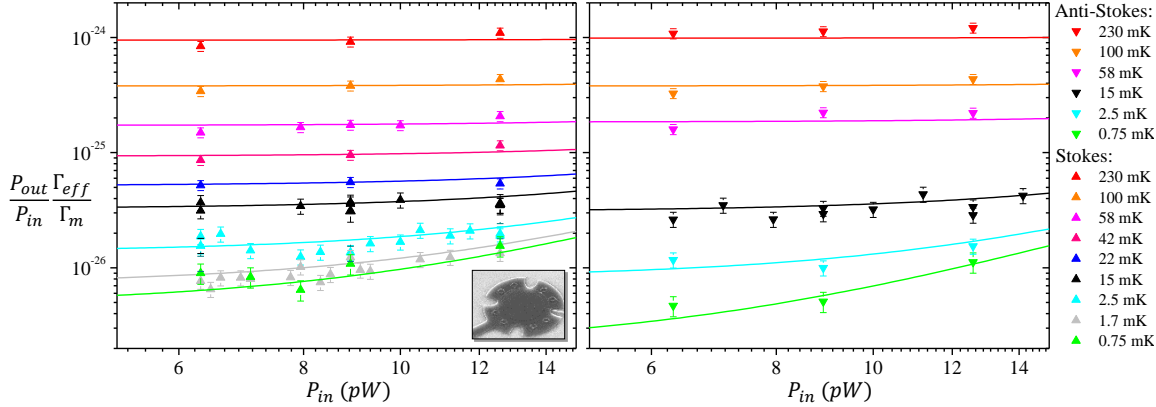


FIGURE 7.12 – Measured sideband peak area normalized to the dynamical term at different cryostat temperatures as a function of the input microwave power for the blue detuned pumping scheme (left panel with $\Gamma_{eff} = \Gamma_m - \Gamma_{opt}$) and for the red detuned pumping scheme (right panel with $\Gamma_{eff} = \Gamma_m + \Gamma_{opt}$). The same temperature-independent out-of-equilibrium photon contribution is observed for both pumping schemes. Note the appearance of the motional sideband asymmetry effect below typically 15 mK.

metry measurements performed on the highly-coupled drumhead device. Careful characterization of the contribution due to in-cavity out-of-equilibrium photons coming from the phase noise of the input pump signal has been done. On Fig. 7.12, we present experimental measurements of both sideband peak areas, which have been normalized by the optomechanical dynamical part. For both pumping schemes (red and blue) and all temperatures, an identical empirical fit $\propto P_{in}^{2.5}$ has been fit on the data in order to extract an effective temperature T_{eff} for both sidebands. At high temperatures, for both sidebands $T_{eff} \approx T_{mode}$ (see also preceding Section) and the out-of-equilibrium contribution is essentially negligible. But at very low temperatures, when sideband asymmetry becomes visible (typically below 10 mK for this device), we clearly observe deviations coming from the cavity backaction term. Note that the used input power range (about 6 – 14 pW) for the measurements has been carefully chosen: not too high powers to avoid a too strong out-of-equilibrium photons contribution, and not too small powers to be able to average a signal over a reasonable amount of time. Similarly to Fig. 7.6 bottom right, we summarized the measured effective temperatures T_{eff} for both sidebands in Fig. 7.13 bottom. We defined as previously (see Chapter 2 and previous Section) for the area of the Stokes sideband measured within the blue detuned pumping scheme (blue theoretical curve):

$$T_{eff} = \frac{\hbar\Omega_m}{k_B}(n+1), \quad (7.4.1)$$

and for the anti-Stokes sideband measured within the red detuned pumping scheme (red theoretical curve):

$$T_{eff} = \frac{\hbar\Omega_m}{k_B}n, \quad (7.4.2)$$

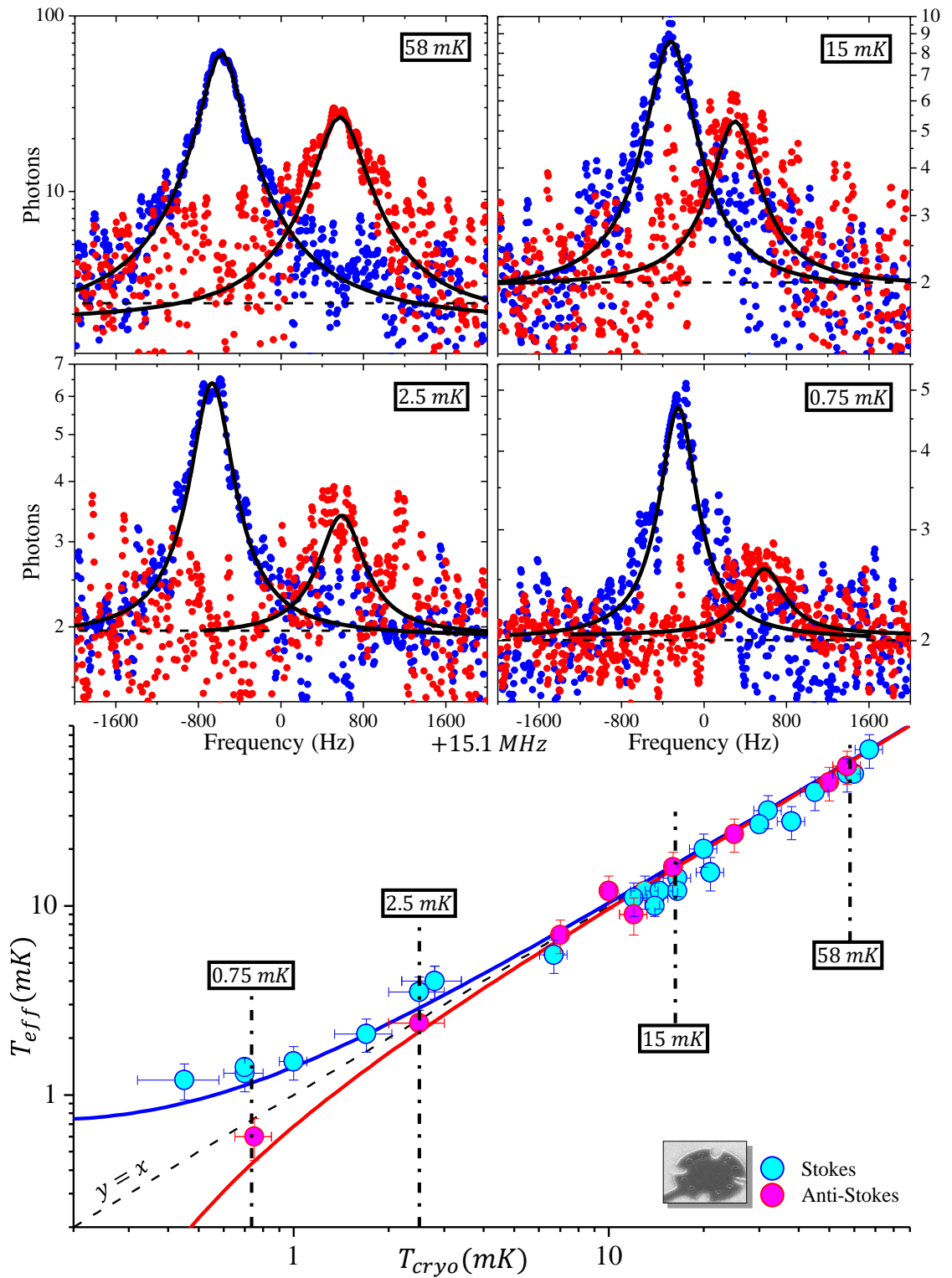


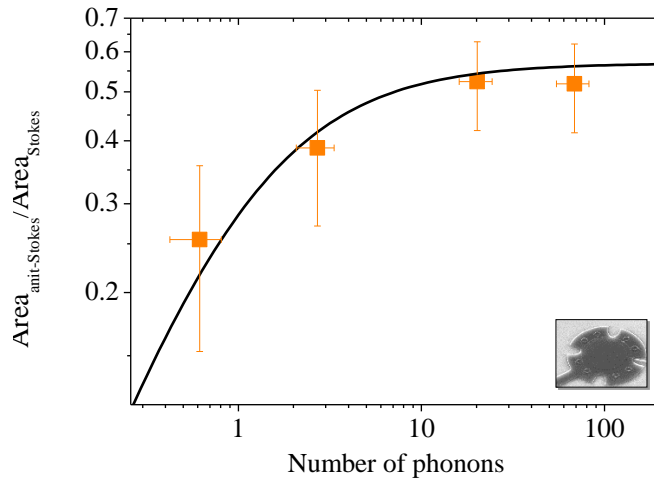
FIGURE 7.13 – Observation and characterization of motional sideband asymmetry: Fitted T_{eff} (obtained from Fig. 7.12) as a function of the cryostat temperature for both Stokes (blue dots in bottom panel) and anti-Stokes sideband (magenta dots in bottom panel) within the blue/red detuned pumping schemes. In the bottom panel blue ($n + 1$) and red (n) curves correspond to theoretical expressions (see text). For four different temperatures (58 mK, 15 mK, 2.5 mK and 0.75 mK) we present in the four top panels the corresponding measured sideband peaks at an input power of 6.3 pW; the backgrounds have been shifted to 2 photons for display purposes (dashed lines). The slight difference in peak positions comes from a remnant small optical spring effect (see following Section). Black curves are lorentzian fits (see text for details).

with as usual the Bose expression:

$$n = \frac{1}{e^{\frac{\hbar\Omega_m}{k_B T_{\text{cryo}}} - 1}}. \quad (7.4.3)$$

On Fig. 7.13 top we present four measurements at different temperatures which clearly illustrate motional sideband asymmetry. From 58 mK down to about 0.75 mK we display both measured sidebands obtained at 6.3 pW input power. A tiny contribution from out-of-equilibrium photon noise has been corrected for (using Fig. 7.12's fits); but it is marginal for *all* displayed lines, except for the coldest anti-Stokes peak (but it remains noticeably smaller than the effect discussed in this Section). At this power, the dynamical part of the optomechanical backaction being non-zero, both sidebands do not have exactly the same amplitude: on one hand, the Stokes sideband is slightly amplified while the anti-Stokes peak is slightly damped. This effect is here independent of temperature as Γ_m saturates at about 400 Hz below 100 mK (see Fig. 7.2 right panel), which explains the small asymmetry observed at high temperature (see 58 mK and 15 mK measurements on Fig. 7.13 top). Note that at ultra-low temperatures (0.75 mK), the anti-Stokes sideband was so small that in order to obtain a consequent signal-to-noise ratio we integrated over more than 4 days.

FIGURE 7.14 – Sideband asymmetry thermometry: Ratio of the area of both sidebands measured with blue and red detuned schemes as a function of the phonon number in the mechanical mode. Orange squares are experimental measurements obtained from about 70 phonons down to about 0.3 phonons. The black curve is the theoretical calculation (see text). Note that at large phonon numbers the curve saturates to a ratio of 0.57 instead of 1 because of the (relatively small) dynamical contribution ($\pm\Gamma_{\text{opt}}$) observed in the data of sideband asymmetry measured for a used power of 6.3 pW (see Fig. 7.13).



Thermometry at nuclear demagnetization temperatures using Stokes/anti-Stokes sideband asymmetry is for the first time demonstrated in-equilibrium for this kind of device on Fig. 7.14. Orange squares correspond to the ratio of the area of both sidebands at iso input power (displayed peaks in Fig. 7.13). The black theoretical curve (see Chapter 2) is taking into account the asymmetry due to the dynamical pumping term $(\Gamma_m - \Gamma_{\text{opt}})/(\Gamma_m + \Gamma_{\text{opt}})$, here about 57%:

$$\frac{Area_{\text{anti-Stokes}}}{Area_{\text{Stokes}}} = 0.57 \frac{n}{n + 1}, \quad (7.4.4)$$

where n is as usual the phonon number.

7.4.2 Thermodynamic equilibrium below 1 mK

In this thesis we demonstrated for the first time thermalization of a $10\ \mu\text{m}$ drumhead NEMS down to $500\ \mu\text{K}$ by measuring the occupation number of its first mode as well as its mechanical frequency shift. Furthermore, we were able to prove motional ground state cooling of this device using sideband asymmetry thermometry (see previous section) [218]. We now present in this Section statistical thermodynamical properties measured in extreme conditions of very and ultra-low temperatures, down to almost zero phonon occupation.

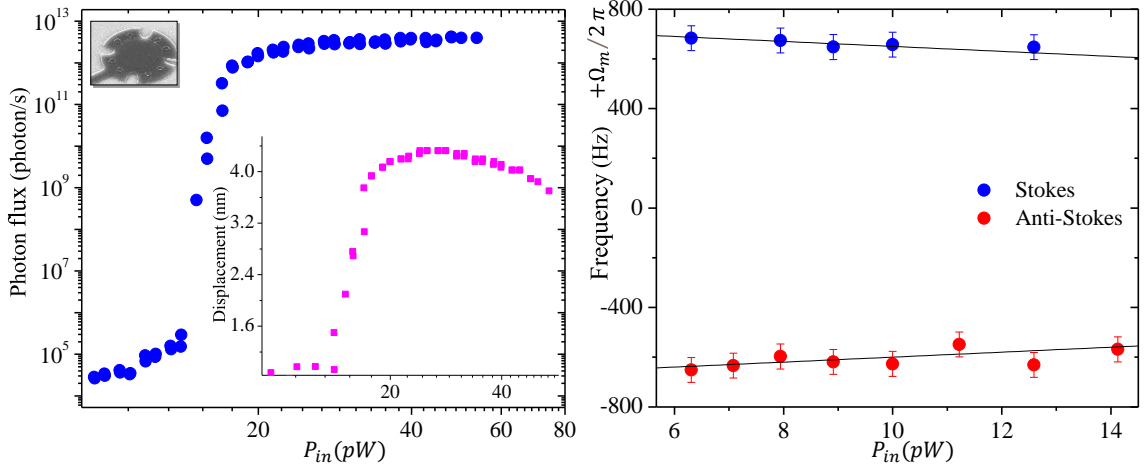


FIGURE 7.15 – Left: Output photon flux measurements performed up to the self-sustained oscillation regime with the highly-coupled drum structure sweeping the input power P_{in} up and down (driving the Stokes sideband at 18 mK). Inset: Corresponding Amplitude of motion calculated from the measured mechanical frequency shift of the self-oscillating (Stokes) peak with a $\beta_m \approx 2 \times 10^{19} \text{Hz/m}^2$. Right: Optical spring measured on both sidebands at about 15 mK. Black lines are linear fits, the tendency remains the same over the full range of temperatures. The frequency difference between both sidebands comes from the fact that the data have been taken at different demagnetization runs.

$R(\text{nm})$	$d(\text{nm})$	$e(\text{nm})$	$E(\text{GPa})$	$\rho(\text{kg/m}^3)$	ν
est.	est.	est.	bulk val.	bulk val.	bulk val.
7300	50	100	70	2700	0.35

TABLE 7.1 – Typical highly-coupled drumhead NEMS parameters; the in-built stress is estimated to be ≈ 240 MPa. Corresponding mode effective mass $m_{eff} = 10^{-14}$ kg and spring constant $k_{eff} = 90$ N/m.

Some characterizations shall be performed before describing the genuine properties of the device. On Fig. 7.15, we present measurements of a power-dependent remnant optical spring effect (right panel) at fixed temperature. We find out that this effect, coming from a small detuning error of the pumping tone, remains the same over the full range of temperature. It is the cause of the slight difference in peak position in Fig. 7.13. We use the frequency shift produced by this effect to give an upper bound to the NEMS microwave heating effect, in a similar manner to what is done for the other drumhead device (see Chapter 8). We calculated a negligible heating $\frac{dT}{dP_{in}} P_{in,max}$ of about 15%, meaning that for the maximum used input power $P_{in,max} \approx 15$ pW, at $500\ \mu\text{K}$ the drum heating would be at maximum of about $80\ \mu\text{K}$. This is very small and clearly within our error bars, and can be safely neglected. On Fig. 7.15 left panel, we present data measured at zero detuning in the self-induced oscillation regime and in particular we converted the observed mechanical frequency shift into displacement using the method presented in

the next chapter. Estimating the dimensional parameters of this highly coupled drum-head device (see Tab. 7.1), we could evaluate a Duffing parameter around $2 \times 10^{19} \text{ Hz/m}^2$ (see Chapter 8 for details) and conclude that self-oscillations achieve amplitudes of motion of about 1 nm, which is a rather macroscopic number when compared to atomic size. Besides, sweeping the power up and down through the threshold, we find no evidence of hysteresis, in accordance with the other drum device (Chapter 8), but in clear contrast with the beam device (Chapter 8).

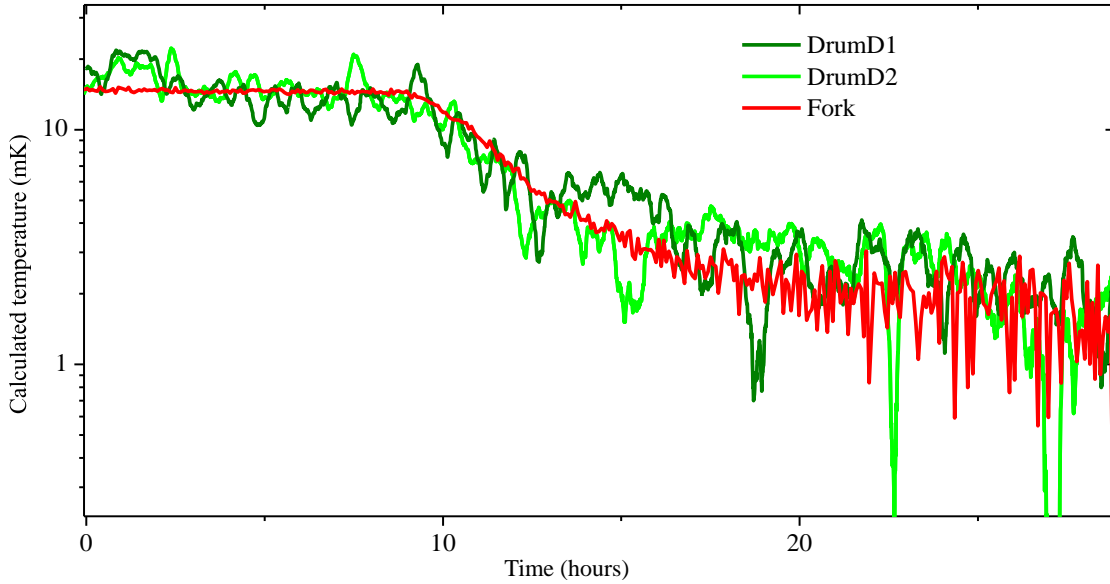


FIGURE 7.16 – Drum mode temperature (recalculated from mode occupation) measured with the blue scheme (and $P_{in} \approx 12.5 \text{ pW}$), and fork temperature (recalculated from damping) monitored as a function of time during two adiabatic nuclear demagnetizations (down to the T_C of ^3He). Note the large (and very slow) fluctuations on the mode temperature.

In order to quantify how well our drumhead device thermalizes to the nuclear stage, we monitored both the drum mode and the ^3He thermometer temperatures. On Fig. 7.16 we display them both, as monitored during two typical adiabatic nuclear demagnetization cycles (*D1* and *D2*). The drum mode temperature is recalculated from the average mode occupation obtained with the blue scheme, subtracting the temperature independent out-of-equilibrium photon contribution fitted on Fig. 7.12 (the power used is $P_{in} \approx 12.5 \text{ pW}$, which leads to an amplification Γ_{eff}/Γ_m of about $\times 3$). Data is acquired continuously (one spectrum file every 30 seconds), and the curve is obtained by means of a sliding average with a window of 20 minutes (technique similar to the one used to study "spikes" in Section 7.3). The fork temperature is recalculated from its damping measurement (see Chapter 6). For all demagnetizations, we observed that the drum mode temperature follows reasonably well the fork temperature down to the T_C of ^3He . Below 1 mK, both the mode and the tuning fork take much more time to cool down (typically a few days for cooling down to $500 \mu\text{K}$), which explains why we display only the first 24 hours on Fig. 7.16.

As shown on Fig. 7.17, we performed an accurate statistical analysis of phonon fluctuations in the first mode of this highly-coupled drumhead device as a function of temperature. We present typical time domain traces of the average phonon number measured at different temperatures (from 230 mK down to $700 \mu\text{K}$, central graphs Fig. 7.17), recalculated from the fits of the areas performed in Fig. 7.12 (same conditions as for the cooling trace of Fig. 7.16), and demonstrate ground state cooling by measuring the frac-

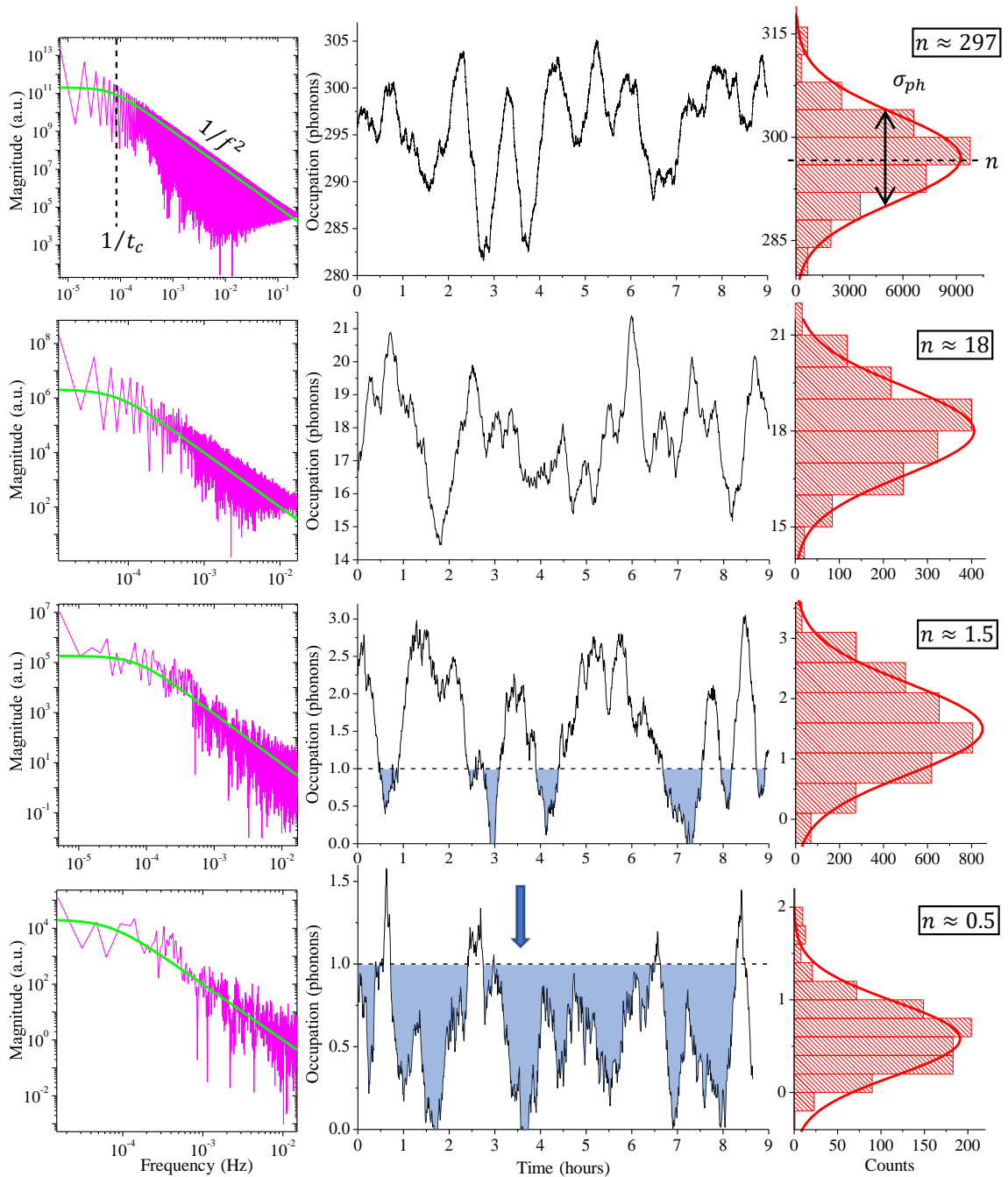
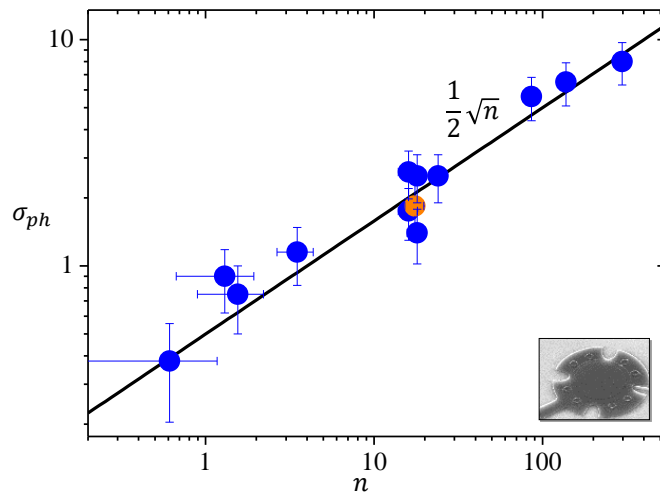


FIGURE 7.17 – Temperature dependence of the phonon fluctuations: Central column: Time domain traces of the average mode occupation over about 9 hours (same microwave settings as for Fig. 7.16). The blue shaded area represents the part of the time that the average occupation number spends below 1 phonon. Left column: Phonon spectrum (defined from the FFT of the amplitude correlator). Green line is a $1/f^2$ fit, with a low-frequency cutoff $1/t_c$ at about a few hours (see text). Right column: Corresponding phonon statistical distribution (red curve is a Gaussian fit). From top to bottom: $T_{\text{cryo}} \approx 230$ mK (averaging window of 20 minutes, acquisition rate of 2 seconds, total trace time of about 20 hours), $T_{\text{cryo}} \approx 14$ mK (averaging window of 20 minutes, acquisition rate of 30 seconds, trace time of about 12 hours), $T_{\text{cryo}} \approx 1.4$ mK (averaging window of 20 minutes, acquisition rate of 30 seconds, trace time of about 26 hours), $T_{\text{cryo}} \approx 0.7$ mK (averaging window of 20 minutes, acquisition rate of 30 seconds, trace time of about 10 hours). The arrow on the lowest central graph indicates a time slot where the mode remained *completely empty* for more than 5 minutes (see text).

tion of the time the device spends below 1 phonon on average (blue shaded area). In particular, on the trace measured at $700 \mu\text{K}$, we demonstrate for the first time, that the

mechanical object is essentially *completely empty* during more than 5 minutes continuously (blue arrow). Indeed, as the first mode is empty, higher-order modes shall with a very high probability be empty too. The calculated phonon spectra (on the left, Fig. 7.17), are all essentially low-pass filters with a $1/f^2$ noise tendency, and display a seemingly temperature-independent low frequency cutoff around $t_c = 5 \pm 1$ hours. On the other hand, we expect a high-frequency cutoff (out of reach for our measurement) fixed by the $\tau_m = 2/\Gamma_m$ time constant of the mode. Such a $1/f^2$ is expected for a white spectrum of *phonon flux* in/out of the drum (since phonon occupation is basically the primitive of it). Such a white flux spectrum would be rather similar to electronic transport in e.g. an SET, where each jump is uncorrelated with the others [216]. On the other hand, the long time t_c could be interpreted as a *loss of memory* for the correlations among phonons localized onto the drum. This parameter could be of geometrical origin, since it does not seem to depend on any measurement parameters (especially T). The corresponding calculated phonon statistical distribution remains Gaussian for all temperatures, to the best of what we can say (see right graphs Fig. 7.17). Of course since the measurement scheme (blue pumping at finite power) amplifies by a $\times 3$, all statistics shall essentially look Gaussian after recalculation; there is no chance that, with our resolution, we can discriminate say Poissonian from Gaussian. The temperature dependence of the phonon standard deviation σ_{ph} is shown on Fig. 7.18. A clear $\sigma_{ph} = 0.5\sqrt{n}$ tendency is observed. We carefully test all possible statistical biases and an accurate error bar analysis has been performed (see Fig. 7.19 and discussion below). The error bars in the following graphs correspond to the reproducibility of the data, and not to measurement/fit accuracy. We also confirm that there is no bias in the analysis arising from the finite power used (and finite amplification): one set was measured at lower powers, with an amplification of only 50%. The resulting parameters are equivalent to those measured at higher powers (see orange dots in Figs. 7.18 and 7.20). A $\propto \sqrt{n}$ tendency is expected for any process, which guarantees a well-defined statistical limit at large n . But the prefactor 0.5 is clearly a genuine signature of the process at stake, directly linked to the cutoff time ($\sigma_{ph}^2 \propto t_c$); one would have naively expected a 1, matching a Poissonian distribution. This is not what we obtain, and is asking for further theoretical input.

FIGURE 7.18 – Phonon fluctuations σ_{ph} (standard deviation) measured with the blue detuned pumping scheme as a function of the average phonon occupation n over the full range of temperatures. All blue points have been measured at an input power $P_{in} \approx 12.5$ pW whereas the orange dot has been taken at $P_{in} \approx 6.3$ pW. Data follow a clear tendency $\sigma_{ph} \propto \sqrt{n}$ (black curve, see text).



down. Such tendencies have been observed also for other NEMS at low temperatures, and were attributed to two-level systems (TLS) [221]. Both types of fluctuations display a $1/f^2$ -type spectrum without low-frequency cutoff (see insets Fig. 7.20), similarly to the fluctuations observed in the self-oscillating state (Chapter 8). Indeed we show that, within our (approximative) $\pm 40\%$ error bars, the frequency noise measured in the self-oscillating state is consistent with the one measured within Brownian motion (see black dot in Fig. 7.20, recalculated from Fig. 7.15 taking into account the small averaging time correction). Therefore frequency noise seems to be independent of the measurement regime. From all these aspects, we can conclude that frequency and damping noises are caused by a process different from the one at the origin of phonon fluctuations. At ultra-low temperatures (typically below 10 mK) damping fluctuations are much higher than frequency ones and indeed, even large damping jumps are observed (see inset Fig. 7.20, similarly to frequency jumps [139]). This large damping noise is certainly the main source of irreproducibility in the data. Most of the time frequency noise and damping noise seem uncorrelated (see the inset Fig. 7.20: damping jump with no accident on the frequency). Furthermore, a very strange dynamics has been observed on the resonance frequency below 10 mK: the frequency shift becomes strongly hysteretic with the direction of the temperature sweep (cooling/heating).

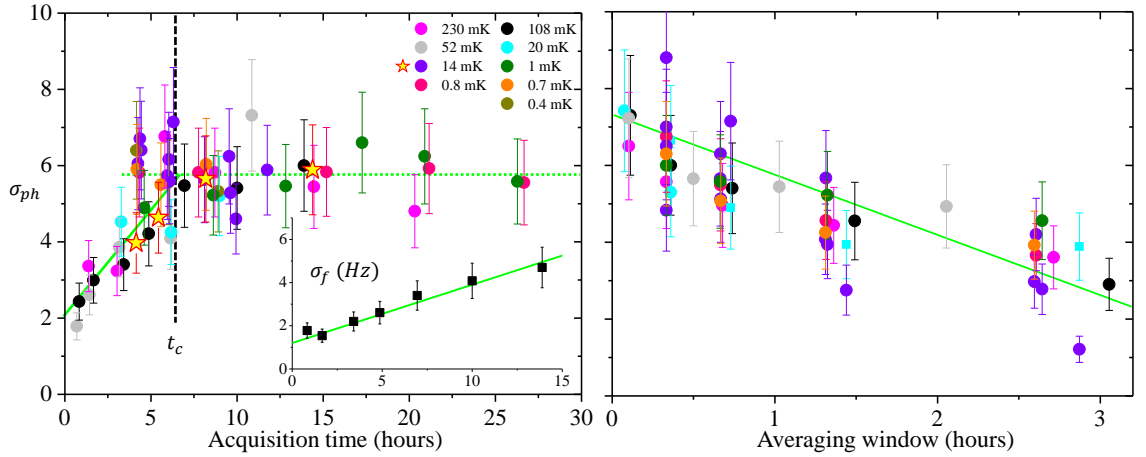


FIGURE 7.19 – Main left: Phonon standard deviation σ_{ph} normalized to the 108 mK value as a function of the acquisition time at different cryostat temperatures T_{cryo} (all data with averaging window of about 20 minutes). All dots have been measured at fixed power $P_{in} \approx 12.5$ pW whereas 14 mK yellow stars correspond to an input power of $P_{in} \approx 6.3$ pW. The full green line is a linear fit, and the dashed line corresponds to the long time asymptote. The intersection between the dashed and the full line defines the cutoff time t_c of about a few hours (see text). Left inset: Frequency standard deviation σ_f as a function of the acquisition time measured at 108 mK and $P_{in} \approx 12.5$ pW (green line is linear fit). Right: Phonon standard deviation σ_{ph} normalized to the 108 mK value as a function of the averaging window at different temperatures (and fixed $P_{in} \approx 12.5$ pW, for 10 or more hours of acquisition). The green line is a linear fit.

To conclude the Section, we shall discuss the statistical tests made to avoid biases in the analysis. On Fig. 7.19, we compare the influence of the averaging window and of the total length of the acquisition on the standard deviations. All σ_{ph} data have been scaled on the 108 mK result, and within typically 20% error bars, the statistical behavior of phonon fluctuations remains temperature independent. Looking at the dependence of phonon fluctuations on the acquisition time (left panel), we recover the genuine temperature-independent cutoff time $t_c \approx 5$ hours and a plateau is observed at long time values. Below this cutoff time, the signal drops essentially linearly, as expected for a $1/f^2$ spectrum.

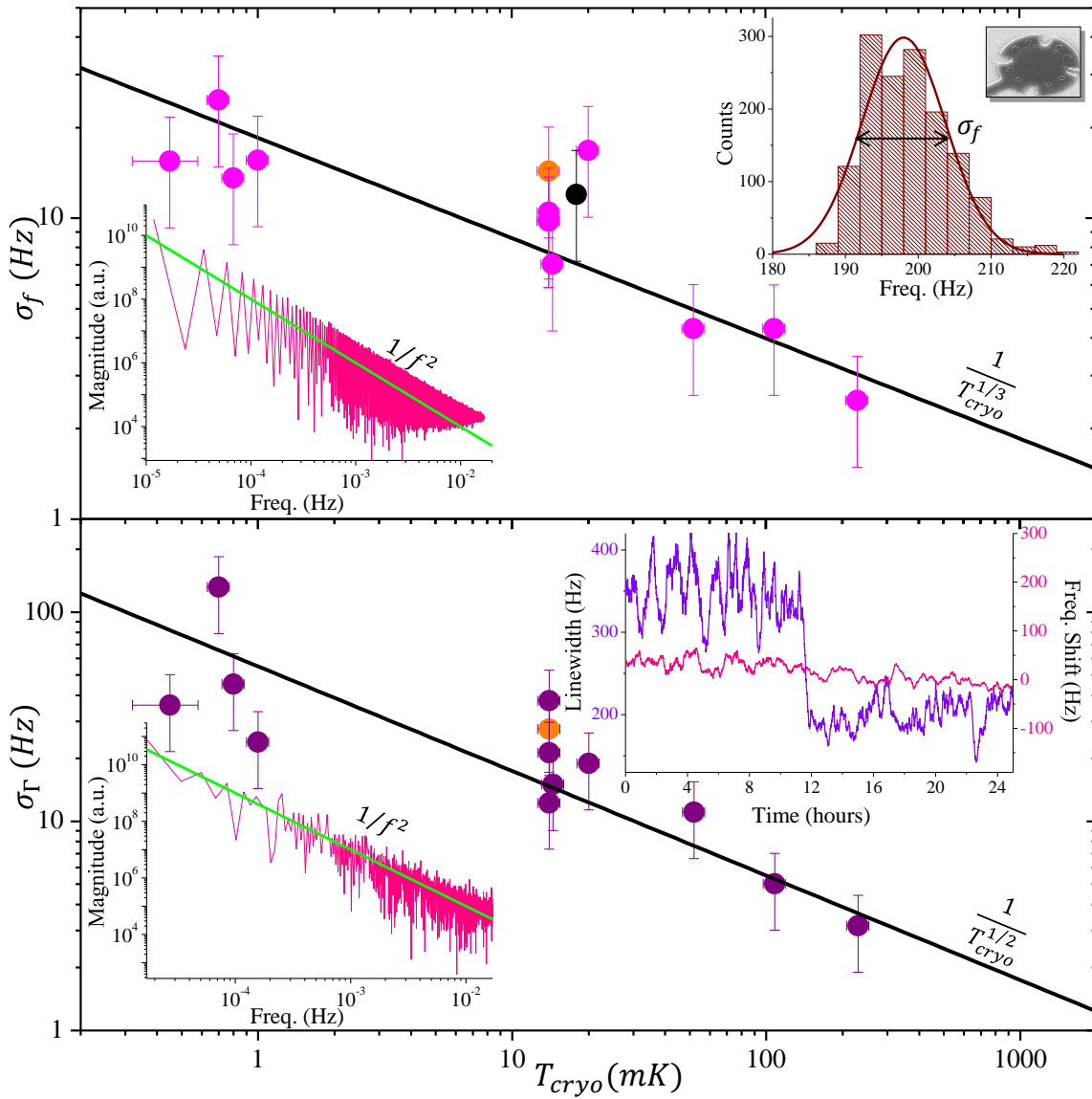


FIGURE 7.20 – Main top: Frequency fluctuations σ_f (standard deviation) measured over 10 hours with the blue detuned pumping scheme as a function of the cryostat temperature T_{cryo} . All pink points have been measured at an input power $P_{in} \approx 12.5$ pW whereas the orange dot has been taken at $P_{in} \approx 6.3$ pW. The black dot has been recalculated from the self-sustained oscillation data shown in Fig. 7.15 (see text). Data follow a $\sigma_f \propto T^{-1/3}$ curve (black line). Top left inset: Typical frequency spectrum (defined as the FFT of the resonance position correlator) measured at 1 mK and $P_{in} \approx 12.5$ pW (green line is a $1/f^2$ fit, with no low frequency cutoff). Top right inset: Corresponding calculated frequency distribution measured at 1 mK and $P_{in} \approx 12.5$ pW over about 1400 measurements (wine curve is a typical Gaussian fit). Main bottom: Damping fluctuations σ_Γ (standard deviation) measured over 10 hours with the blue detuned pumping scheme as a function of the cryostat temperature T_{cryo} . All purple points have been measured at an input power $P_{in} \approx 12.5$ pW whereas the orange dot has been taken at $P_{in} \approx 6.3$ pW. Data follow a $\sigma_\Gamma \propto T^{-1/2}$ curve (black line). Bottom left inset: Typical damping spectrum (defined as the FFT of the resonance linewidth correlator) measured at 0.6 mK and $P_{in} \approx 12.5$ pW (green line is again a $1/f^2$ fit). Bottom right inset: Example of time domain trace displaying a damping jump (violet) and corresponding frequency shift (pink, with no jump; see text).

The dependence of phonon fluctuations on the averaging window is shown on the right panel, Fig. 7.18, for acquisition times longer than 10 hours (corresponding therefore to the plateau of the left panel). As expected, with more averagings the estimated fluctuations drop, roughly linearly. Therefore Fig. 7.18 displays the σ_{ph} corresponding to the plateau region (acquisition times long enough to exceed a few times t_c), corrected for the averag-

ing window (correction always smaller than 20%). Therefore Fig. 7.18 corresponds to all the phonon noise that is extracted from our data, including all possible sources. Clearly contributions from the electronics (which would be temperature-independent) and from the damping noise (which would grow at lower T) are not dominant. Besides, it is also remarkable that we obtain *less* than \sqrt{n} . Furthermore, in agreement with the spectra of Fig. 7.20, no cutoff is observed for frequency fluctuations (see left inset Fig. 7.19, the linear fit with no plateau). As a result, frequency (and the same is true for damping noise) is a true non-stationary noise, and as such the quoted standard deviations in Fig. 7.20 are reported for a fixed acquisition time (here, 10 hours).

7.5 CONCLUSION

As a conclusion, we presented measurements of microwave optomechanical systems performed on a nuclear adiabatic demagnetization cryostat, able to reach temperatures well below the 10 mK limit of conventional dilution machines. Relying on a fairly standard microwave wiring and the in-built parametric amplification provided by a blue-detuned pumping, we devised a method providing accurate thermometry of both the mechanical mode and its on-chip environment (the Two-Level Systems to which it couples). The experiment was conducted on 3 different mechanical devices, all three embedded in their on-chip microwave cavity. The efficiency of the method has been demonstrated with a very low opto-mechanical coupling and has been applied to other systems, namely drumhead devices demonstrating much larger couplings. Thermalization is demonstrated from 10 mK to 1 K with no sign of thermal decoupling, for all baths: the bulk of the device T_{NEMS} and the mode temperature T_{mode} . For one of the drumhead devices, we demonstrate thermalization of the material down to about 3 mK, while for the other we could follow both mode population and frequency shift down to the lowest achievable temperatures, about 500 μ K here.

At very low temperatures we report strong fluctuations in the signal amplitude for two devices: the beam and the badly coupled drum. These features appear around 100 mK for beams and about 30 mK for drums, and have been observed in different laboratories, but had never been studied in details so far. We demonstrated with the highly-coupled drum device that using a small number of driving photons allows us to avoid this so-called "spikes" dynamics. We present the basic characteristics of these fluctuations, and argue that they are due to an extra stochastic driving force of unknown origin. Microwave irradiation seems to trigger the phenomenon. Applying a DC voltage of a few Volts on-chip cancels the large spiky events, but a small component of this extra random drive persists, with variations over a typical timescale of about a day.

It is unclear if all the fluctuations characteristics present in these devices (amplitude, frequency, damping) are linked to the same underlying mechanism. One could even imagine that temperature-dependent non-linear effects could impact the phonon-photon coupling, beyond the lowest (geometrical) order g_0 . However, it appears that these effects are present in all experimental systems at different levels of expressions, since all NEMS/MEMS share the same overall characteristics (especially damping, frequency shifts and phase noise typical of Two-Level Systems physics). It is thus tempting to relate this stochastic force to a mechanism mediated by some kind of microscopic TLSs, driven by microwaves but blocked under DC voltage biasing. This stochastic driving force can mimic to some extent a thermal decoupling, and could explain why some drumhead devices in the literature refuse to cool down below typically 20 – 30 mK. While being a

limitation for experimentalists, this phenomenon definitely deserves theoretical investigations.

The main objective of this thesis has thus been achieved, a mesoscopic mechanical structure has been cooled down to microkelvin temperatures and reached its quantum ground state (about 0.3 phonons on average is its fundamental mode of vibration).

7.6 RÉSUMÉ EN FRANÇAIS

En conclusion, nous avons présenté des mesures d'optomécanique micro-onde effectuées sur un cryostat à désaimantation adiabatique nucléaire capable d'atteindre des températures bien plus basses que le 10 mK accessible aux réfrigérateurs à dilution conventionnels. En s'appuyant sur un système micro-onde standard et l'amplification paramétrique intrinsèque procurée par l'application d'une pompe détunée vers le bleu, nous avons élaboré une méthode permettant un accès précis à la température du mode mécanique ainsi qu'à celle de son environnement (systèmes à deux niveaux auxquels celui-ci se couple). L'expérience a été conduite sur 3 différents objets mécaniques, chacun étant couplé à sa propre cavité micro-onde. L'efficacité de la méthode a été démontrée grâce à un couplage optomécanique extrêmement faible et celle-ci a ainsi été appliquée à d'autres systèmes, en particulier de type tambour ayant un couplage bien supérieur. Nous avons ainsi démontré une thermalisation des objets mécaniques étudiés depuis 1 K jusqu'à 10 mK sans aucun signe de découplage thermique, concernant chacun des bains: T_{NEMS} étant la température du système et T_{mode} celle du mode mécanique. Pour un de nos systèmes de type tambour, nous avons démontré une thermalisation du matériaux jusqu'à 3 mK et pour l'autre, nous avons pu suivre la population de son mode fondamental ainsi que son décalage en fréquence correspondant jusqu'à la température la plus basse atteignable, environ 500 μ K ici.

A très basses températures nous avons observé de très fortes fluctuations de l'amplitude du signal pour deux de nos systèmes mécaniques: la poutre et le tambour peu couplé. Ces fluctuations apparaissent aux alentours de 100 mK pour les structures de type poutre et autour de 30 mK pour les tambours. Elles ont été observées dans différents laboratoires, mais n'ont jamais été étudiées en détails. Nous avons démontré, avec le système basé sur un tambour fortement couplé, qu'en utilisant un nombre faible de photons d'excitations, nous pouvions éviter l'apparition de cette dynamique instable. Nous présentons donc ici certaines des caractéristiques basiques de ces fluctuations, et supposons qu'elles seraient dues à une force stochastique extérieure d'origine inconnue. L'irradiation micro-onde semble déclencher ce phénomène. Appliquer une tension DC de quelques volts sur la ligne de transmission semble supprimer les événements les plus importants, néanmoins une petite partie de ces excitations stochastiques persistent, accompagnées de variation ayant pour échelle de temps la journée.

On ne peut actuellement pas établir si toutes les caractéristiques de ces fluctuations présentes dans ce type de système (amplitude, fréquence, dissipation) sont liées au même mécanisme sous-jacent. On peut éventuellement imaginer que la dépendance en température des effets nonlinéaires pourrait impacter le couplage photon-phonon au-delà de l'ordre géométrique le plus bas g_0 . Cependant, il apparait que ces effets sont présents dans tous les systèmes expérimentaux à différents niveaux de sensibilité, ces technologies NEMS/MEMS partageant les mêmes caractéristiques générales (dissipation, décalage en fréquence et bruit en phase typiques de la physique des systèmes à deux niveaux). Il est donc tentant de mettre en relation cette force stochastique avec un certain mécan-

isme commandé par un genre de système à deux niveaux microscopique, déclenché par les micro-ondes et bloqué sous tension DC. Cette force d'excitation stochastique peut reproduire dans une certaine mesure un découplage thermique, et pourrait expliquer pourquoi certains tambours, dans la communauté scientifique, n'ont pas pu être refroidis en dessous de 20 – 30 mK. Etant la principale limitation expérimentale, ce phénomène a donc maintenant besoin d'investigations théoriques.

L'objectif principal de cette thèse a donc été atteint. Un objet mécanique mésoscopique a été refroidi en dessous du millikelvin et a ainsi été opéré dans son état quantique fondamental (environ 0.3 phonons en moyenne dans son mode de vibration fondamental).

8

STOKES SIDEBAND: SELF-OSCILLATION BEYOND LINEAR OPTOMECHANICS

In this chapter we explore the nonlinear dynamics of a standard microwave optomechanical system consisting of a NEMS capacitively coupled to a microwave cavity. Experiments are performed under a strong microwave Stokes pumping which triggers mechanical self-sustained oscillations. We analyze the results in the framework of an extended nonlinear optomechanical theory presented in Chapter 2, and demonstrate that quadratic and cubic coupling terms in the opto-mechanical Hamiltonian have to be considered concerning drumhead type geometries. In this case, quantitative agreement with the measurements is obtained considering only genuine geometrical nonlinearities: no thermo-optical instabilities are observed, in contrast with laser-driven systems. Based on these results, we describe a method to quantify nonlinear properties of microwave optomechanical systems. This method is clearly a new technique available in the quantum electro-mechanics toolbox, where higher-order coupling terms are proposed as a new resource for specific quantum schemes like quantum non-demolition (QND) measurements. We also find that the motion imprints a wide comb of extremely narrow peaks in the microwave output field, which could also be exploited in specific microwave-based measurements, potentially limited only by the quantum noise of the optical and the mechanical fields for a ground-state cooled NEMS device. These results are published in Ref. [219]. We finally explore briefly the attractor diagram of a beam type mechanical device and demonstrate a very different nonlinear behaviour compared to drumhead devices.

CONTENTS

8.1	Experimental measurement of attractor diagrams	163
8.1.1	Comb structure generation	164
8.1.2	Heating and material dependent effects	164
	Microwave heating	164
	TLS power-dependencies	165
	Cavity Kerr effect	165
8.1.3	Microwave measurement technique	167
8.2	Quantifying geometric nonlinearities	167
8.2.1	Optical and mechanical induced frequency shifts	167
8.2.2	3D Fitting procedure	168
8.2.3	Basic estimate of nonlinear coupling strengths	171
8.3	Comparing Beams and Drums behaviour	174
8.3.1	Beams and Drums attractor diagrams	174
8.3.2	Frequency and amplitude fluctuations	176
8.4	Conclusion	178
8.5	Résumé en français	178

8.1 EXPERIMENTAL MEASUREMENT OF ATTRACTOR DIAGRAMS

In order to perform such a measurement we employ a standard microwave optomechanical system already described in previous chapters [54, 112] consisting of a microfabricated lumped microwave cavity resonator coupled to an aluminum drumhead NEMS

[57]. The chip is installed into a commercial dilution cryostat with base temperature 10 mK, equipped with a high electron mobility transistor (HEMT) detection circuitry (see Chapter 6). The cryogenics, thermometry and measurement techniques have been described in Chapters 6 and 7. The chip is designed for reflection measurements and its parameters for both the cavity and the mechanics are given in Tab. 6.1; we refer to this device as the "badly-coupled drumhead" one. We remind here that for this chip the aluminum microwave cavity resonates at $\omega_{cav}/2\pi \approx 6.8$ GHz. The cavity displays a one-directional external coupling rate of $\kappa_{ex}/2\pi \approx 2$ MHz and a total damping rate of $\kappa/2\pi \approx 4$ MHz. We performed the experiment using the fundamental mode of the drum NEMS device which resonates around $\Omega_m/2\pi \approx 6.7$ MHz and exhibits a typical damping rate of about $\Gamma_m/2\pi \approx 150$ Hz at 50 mK.

8.1.1 Comb structure generation

Within the Brownian motion regime, this mechanical mode imprints sidebands in the optical spectrum that we measure. The motion amplitude being very small, no extra non-linearity has to be considered and the optical damping (when cooling) and anti-damping (when amplifying) observed are linear in applied power P_{in} [136]. This is used to calibrate the linear optomechanical interaction of our setup [223]. In this case we obtain a single photon-phonon coupling strength $g_0/2\pi \approx 10$ Hz. Blue-detuned pumping at $\omega_{cav} + \Delta$ (with $\Delta > 0$) gives rise to downward scattering of photons, leading to the creation of phonons in the mechanical mode, hence enhancing the Stokes sideband. This is accompanied by a narrowing of the mechanical peak due to the antidamping backaction. At very strong powers, the total mechanical damping can thus be totally canceled: this is called the parametric instability. Above this threshold, the system enters into self-sustained oscillations, the amplitude of the mechanical motion being defined self-consistently [136]. In this regime the mechanical amplitude of motion is so large (reaching several nanometers) that the mechanical sidebands are not limited to a couple of peaks: a full comb appears and can be measured (see Fig. 2.8). The peaks detected are not Lorentzian anymore, and their shape is defined by the phase noise in the system [28]. They are extremely narrow (only a few Hz wide at GHz frequencies), essentially equally-spaced (by Ω_m) and of extremely high amplitude: they can even be detected without any HEMT pre-amplification. As well, all nonlinearities in the device will impact this complex optomechanical dynamics.

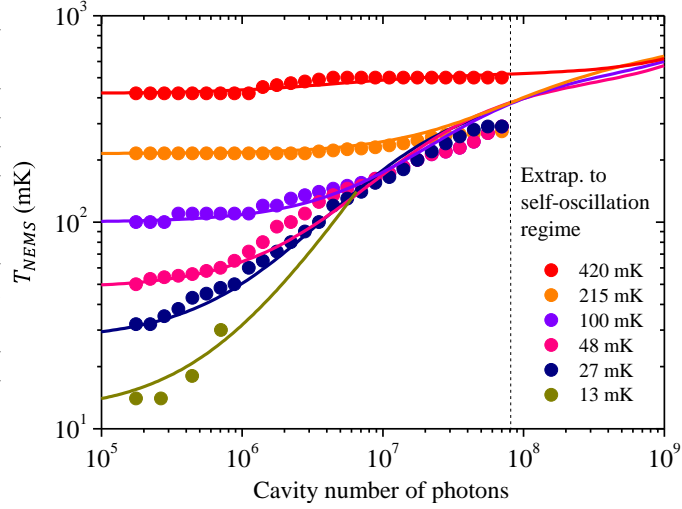
8.1.2 Heating and material dependent effects

At milliKelvin temperatures, microwave photon heating arising from the absorption in dielectrics does not produce any thermal expansion: there are thus no thermo-optical nonlinearities in our system, in strong contrast with devices actuated by laser beams where they dominate [50, 197, 198, 32]. However, the strong pump signal required to reach the threshold of the parametric instability does give rise to some material dependent effects. These are carefully characterized and taken into account experimentally in order to be quantitative in the fitting.

MICROWAVE HEATING The first of these is microwave heating of dielectrics due to absorption of the radiation. In order to characterize it independently of the self-oscillating regime, we use red-detuned sideband pumping. As we increase the injected power P_{in} ,

we measure the area of the anti-Stokes peak. Knowing the theoretical dependence of this parameter on both P_{in} and NEMS temperature T_{NEMS} , we can recalculate T_{NEMS} for each setting (see Fig.8.1). This effect being local, the absorbed power has to be proportional to the intracavity field, i.e. the photon population n_{cav} . We can therefore extrapolate what should be the heating effects in the self-oscillating regime using the actual intracavity photon number $\sum_n |\alpha_n|^2$. Empirical fits are shown in Fig.8.1 (see lines). The curves merge

FIGURE 8.1 – Mechanical device temperature versus applied microwave power (expressed in terms of intracavity photons n_{cav}). Dots are experimental data measured by red detuned pumping, integrating the anti-Stokes power spectrum peak. The curves are empirical expressions used for the extrapolation in the self-oscillating range (above 10^8 photons). At high enough powers, all the curves collapse, as they should. The discrepancies in the numerics in the extrapolated range is smaller than $\pm 20\%$.



when the heating effect dominates over the starting temperature; we therefore estimate that our extrapolation in the region of interest is accurate within $\pm 20\%$. Of the parameters appearing in the theory of Chapter 2, the only temperature dependent ones are ω_{cav} , Ω_m and Γ_m . The mechanical damping is fit to measurements performed in the Brownian regime by the expression $\Gamma_m/2\pi = 70.5 + 1300T_{NEMS}$, while the mechanical resonance frequency is fit by $\Omega_m/2\pi = 6.747 \times 10^6 + 430 \ln(T_{NEMS})$, with T_{NEMS} in Kelvin. While for this sample, the mechanical element is very sensitive to heating, the microwave cavity seems to be rather insensitive. We attribute this to the fact that the cavity is much larger than the drum, and directly coupled to the substrate instead of being suspended.

TLS POWER-DEPENDENCIES However, we do measure a power dependence of the microwave resonance frequency which shifts upwards logarithmically with increasing powers. At the same time, we do not measure any change in the cavity Q factor within our resolution. These power-dependencies of superconducting microwave resonators are commonly attributed to microscopic Two Level Systems present in the devices [102]. Pragmatically, we take into account this effect by adding this logarithmic frequency shift to the calculation of ω_{cav} when fitting the experimental data: $\delta\omega_{cav} = 1.8 \times 10^5 \ln(P_{in})$, with P_{in} in Watts.

CAVITY KERR EFFECT Similarly to the Duffing effect of the mechanics, there is an equivalent nonlinearity in the microwave resonance called Kerr nonlinearity. This leads to an additional frequency shift $\propto n_{cav}$. This effect comes from the nonlinear behavior of the

mode effective inductance L_0 when the current density J flowing in the superconductors becomes too large [167, 162]:

$$L_0(J) = L_0(0) \left[1 + \alpha_l \frac{J^2}{J_*^2} \right], \quad (8.1.1)$$

with $J_* = (2/3)^{3/2} J_C$ and J_C the critical current density, and $\alpha_l = L_{kin}/L_0$ the fraction of the total inductance of kinetic origin. For our Al film of about 100 nm, α_l should be smaller than 0.1 typically. The cavity resonance frequency thus shifts as:

$$\omega_{cav}(n_{cav}) = \omega_{cav}(0) + 3\beta_{cav}n_{cav}, \quad (8.1.2)$$

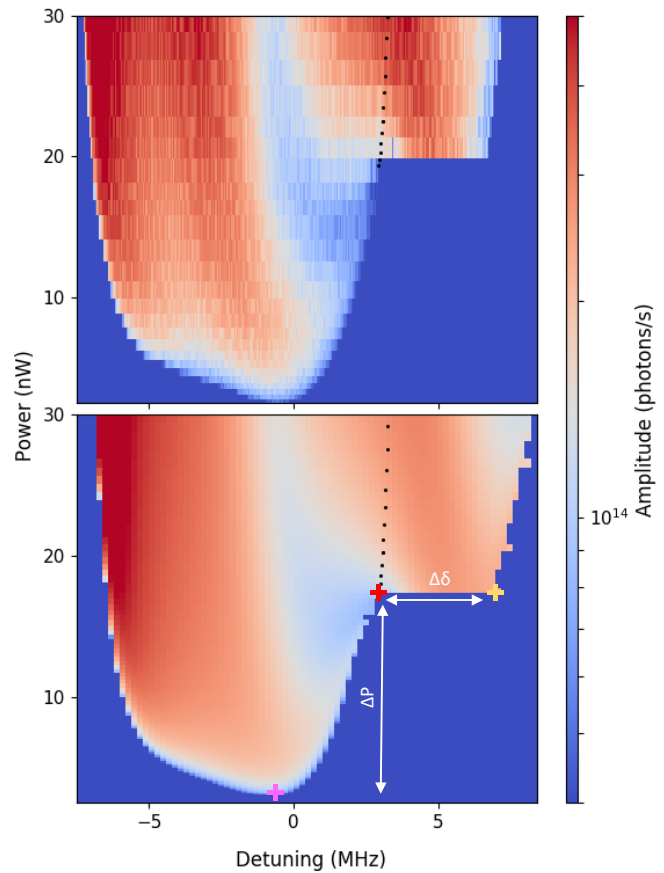
with:

$$\beta_{cav} = -\frac{\alpha_l \hbar \omega_{cav}}{3L_0 A^2 (2/3)^3 J_C^2}, \quad (8.1.3)$$

and A the cross-section of the microwave cavity strip. A crude estimate taking the bulk value for the critical current density leads to $3\beta_{cav} \approx -10^{-4}$ Rad/s, which is completely negligible.

As such, the nonlinearities that prevail in microwave based systems are of geometrical origin: the mechanical Duffing effect, and more importantly in the optomechanical coupling itself.

FIGURE 8.2 – Top: Measured output photon flux (Stokes peak) as a function of input power P_{in} and detuning δ at 214 mK. Bottom: Corresponding calculated colormap from the basic theory of self-sustained oscillations developed in Chap. 2 for $N = 0$ (no nonlinearities) [84, 28]. The region on the right of the dashed line (high powers, positive detuning) is bistable and exists only when entering from the self-oscillating state (up-sweeping frequencies). The pink cross marks the minimum power necessary for self-oscillations, while the red cross corresponds to the position of the beginning of the hysteresis. The yellow cross marks the end of this bistable region (at same power). ΔP and $\Delta\delta$ are discussed in the text.



8.1.3 Microwave measurement technique

The experiment is performed in the mechanical self-induced oscillation regime, by measuring the output microwave signal corresponding to the Stokes peak (at frequency $\omega_{cav} + \delta$), varying the detuning δ and the power P_{in} of the input blue-detuned pump (at frequency $\omega_{cav} + \Omega_m + \delta$). The measured photon flux is shown in Fig. 8.2 top. As a comparison, the calculation based on the theoretical model of self-sustained oscillations developed in Chap. 2 for $N = 0$ (no nonlinearities) [84, 28] is displayed in the bottom panel. The two plots are very similar, and display strikingly a bistable region at high powers and large positive detunings. However, calculation and theory do not match perfectly, which is expected: this has to be the signature of nonlinear effects which were neglected so far.

The region of the stability diagram which seems to be the most impacted by nonlinearities is precisely the hysteretic one (Fig. 8.2 beyond the dashed line). Therefore, in addition to the overall topography of the measured signal in the (P_{in}, δ) space, we shall measure the importance of nonlinear features by reporting the position of the bistability in powers with respect to the beginning of the self-sustained region ΔP and its width in detuning $\Delta\delta$ (see Fig. 8.2 bottom).

8.2 QUANTIFYING GEOMETRIC NONLINEARITIES

The question that arises is thus: which nonlinearities need to be included in a quantitative model? One would immediately think about the Duffing effect in mechanical devices [242], and correspondingly to the Kerr effect [162] for the microwave cavity. Both are not the dominant nonlinear features essentially because small frequency shifts have only a marginal impact on the optomechanical scheme itself. We have thus to consider nonlinearities in the coupling itself, that is higher-order derivatives in the Taylor expansion of the coupling capacitance $C(x)$. For this purpose we use the theory presented in Chap. 2 truncating at order $N = 2$, i.e taking into account only the linear g_0 , quadratic g_1 and cubic g_2 coupling strengths.

8.2.1 Optical and mechanical induced frequency shifts

The aim is thus now to go beyond Fig. 8.2, and obtain quantitative agreement between theory and experiment. The theory of self-sustained oscillations developed in Chap. 2 allows us to calculate the amplitude of the mechanical motion including geometrical nonlinearities in the couplings. However, to obtain estimates of the mechanical frequency we need to also include important contributions from other effects (see previous Section).

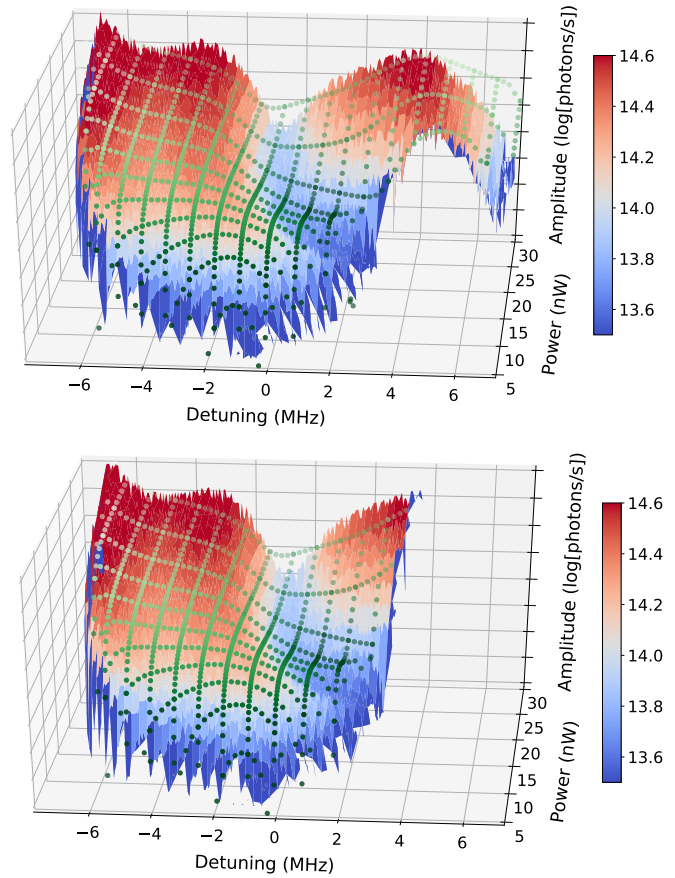
As soon as the system self-oscillates, the actual cavity frequency is slightly renormalized in $\omega'_{cav} = \omega_{cav} - g_1 B^2$. Besides, there is also a material-dependent shift with a logarithmic power-dependence that is attributed to Two-Level-Systems present in the dielectrics which is taken into account (see previous Section). On the other hand, the cavity Kerr nonlinearity β_{cav} is expected to be extremely small for our device; we give an upper bound in Tab. 8.1. The mechanical resonance is also renormalized by the optomechanical coupling, with a tiny frequency shift $\delta\Omega_m$. However, the dominant source of mechanical frequency shift is due to the Duffing effect (i.e. the mechanical nonlinearity arising from the stretching of the drum [217]), leading to $\Omega'_m = \Omega_m + \delta\Omega_m + 3\beta_m B^2$, with a normalized Duffing parameter β_m in Hz per phonon. For simplicity, we will omit the prime

on ω_{cav} and Ω_m , remembering in the following that the measured mechanical frequency shift includes all terms.

8.2.2 3D Fitting procedure

The measured output photon flux is plotted in Fig. 8.3 as a function of detuning δ and power P_{in} (same data as Fig. 8.2 top panel, 214 mK). The amplitude of the signal is extremely large, but the most striking feature is the bistable region at high powers and positive detunings. The measured mechanical frequency shift is shown in Fig. 8.4; strikingly, we find that it is largest in the bistable regime.

FIGURE 8.3 – Top: Output photon flux of the self-oscillating (Stokes) peak at frequency $\omega_c + \delta$, as a function of both the power P_{in} and the detuning δ of the input pump signal (pump frequency $\omega_c + \omega_m + \delta$, with $-7 \text{ MHz} < \delta < +7 \text{ MHz}$) at 214 mK. The colormap is experimental data measured up-sweeping the pump detuning (from $\delta = -7 \text{ MHz}$ to $\delta = +7 \text{ MHz}$) and the pump power, and green points are theoretical fits computed by solving self-consistently Eq. (2.7.25), $\Gamma_m + \Gamma_{opt} = 0$, see text. (b) Experimental colormap measured down-sweeping the pump detuning (from $\delta = +7 \text{ MHz}$ to $\delta = -7 \text{ MHz}$) with pump power swept upwards. Green points are also theoretical computations; the hysteresis of the large power and large detuning region is clearly visible.



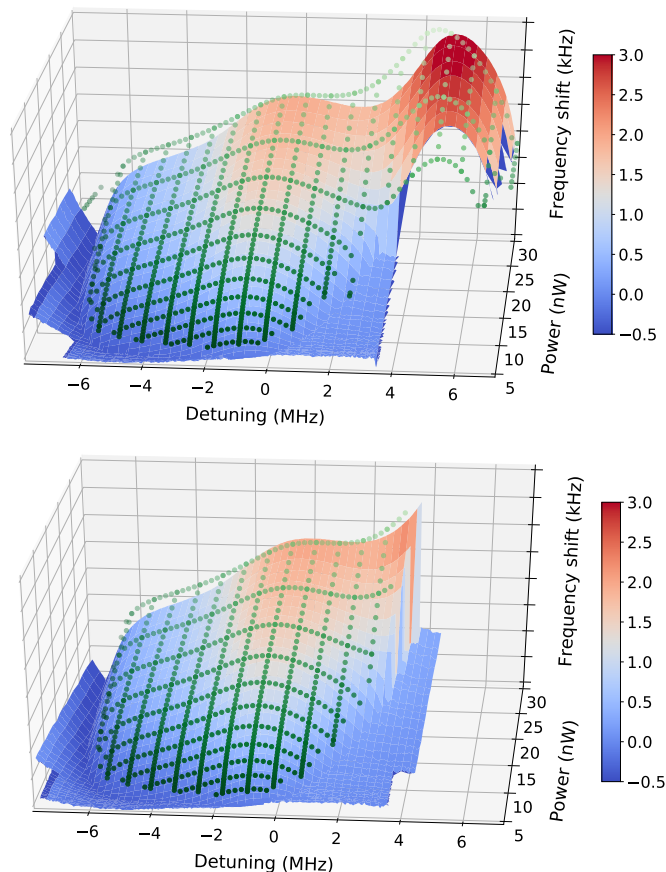
This mechanical shift cannot be captured by the optomechanical contribution $\delta\Omega_m$ alone. One has to take into account the Duffing effect to quantitatively fit it (see below). However, the mechanical frequency shifts remain very small (a few kHz at most, see Fig. 8.4); we thus verified that they have only a marginal impact on the limit cycle dynamics (i.e. the amplitudes, B), see Chap. 2.

In the hysteretic region the amplitude B becomes very large, hence the optomechanical response becomes sensitive to the nonlinear coupling coefficients, g_1 and g_2 . For symmetry reasons (see next section), the sign of the g_0 parameter is irrelevant and we take it to be positive for simplicity. However then, the sign of the other coefficients is uniquely defined.

To calculate the amplitudes of the limit cycles (and hence the photon flux) using the approach in Chap. 2, the only free parameters are the quadratic and cubic nonlinear cou-

pling terms g_1 and g_2 , respectively. These two coefficients have a different impact on the calculated flux: around our best fit parameters, g_1 narrows/broadens the self-oscillating region with respect to detuning (altering the $\Delta\delta$ parameter), while g_2 mostly shifts the bistable feature to higher/lower powers (ΔP parameter). More precisely, by increasing g_1 the self-oscillating region is getting more narrow in the δ direction, while increasing $|g_2|$ up-shifts in power the starting line of the bistable region. This is represented in Fig. 8.6 and demonstrated in Fig. 8.5 varying both parameters in a dichotomic process (multiplying or dividing the optimal values by 2). The optimal values match the experimental findings: $\Delta P \approx 16$ nW ($\pm 10\%$), $\Delta\delta \approx 3.5$ MHz (± 200 kHz). We can therefore choose the red cross position in Fig. 8.5 (central graph, optimal g_1 and g_2) as a good marker for fitting these g_1 and g_2 parameters. Indeed at the same time the overall shape of the theoretical maps displayed in Fig. 8.3 (flux) and Fig. 8.4 (mechanical frequency) are very sensitive to the nonlinear parameters. We can therefore reasonably well determine the values of these two terms, typically within a factor of 2 (see Tab. 8.1 for error bars estimated for the coupling nonlinear parameters). The theoretical fits are displayed as green dots in Figs. 8.3 and 8.4; as a comparison the colormap of Fig. 8.2 bottom panel is computed for $g_1 = g_2 = 0$.

FIGURE 8.4 – Top: Mechanical frequency shift of the self-oscillating (Stokes) peak as a function of both the power P_{in} and the detuning δ of the input pump signal (same conditions as Fig. 8.3, sweeping δ towards positive values). Note that in the hysteretic region, the calculated points lie slightly below the experimental ones, but obviously match the threshold position of Fig. 8.3. Bottom: Experimental colormap measured down sweeping the pump detuning. Green points are theoretical computations.



We performed this procedure at various cryostat temperatures. However, because of microwave absorption in the materials, the drum temperature is not homogeneous over the complete measured range of $(\delta; P_{in})$. This effect is taken into account, see previous section.

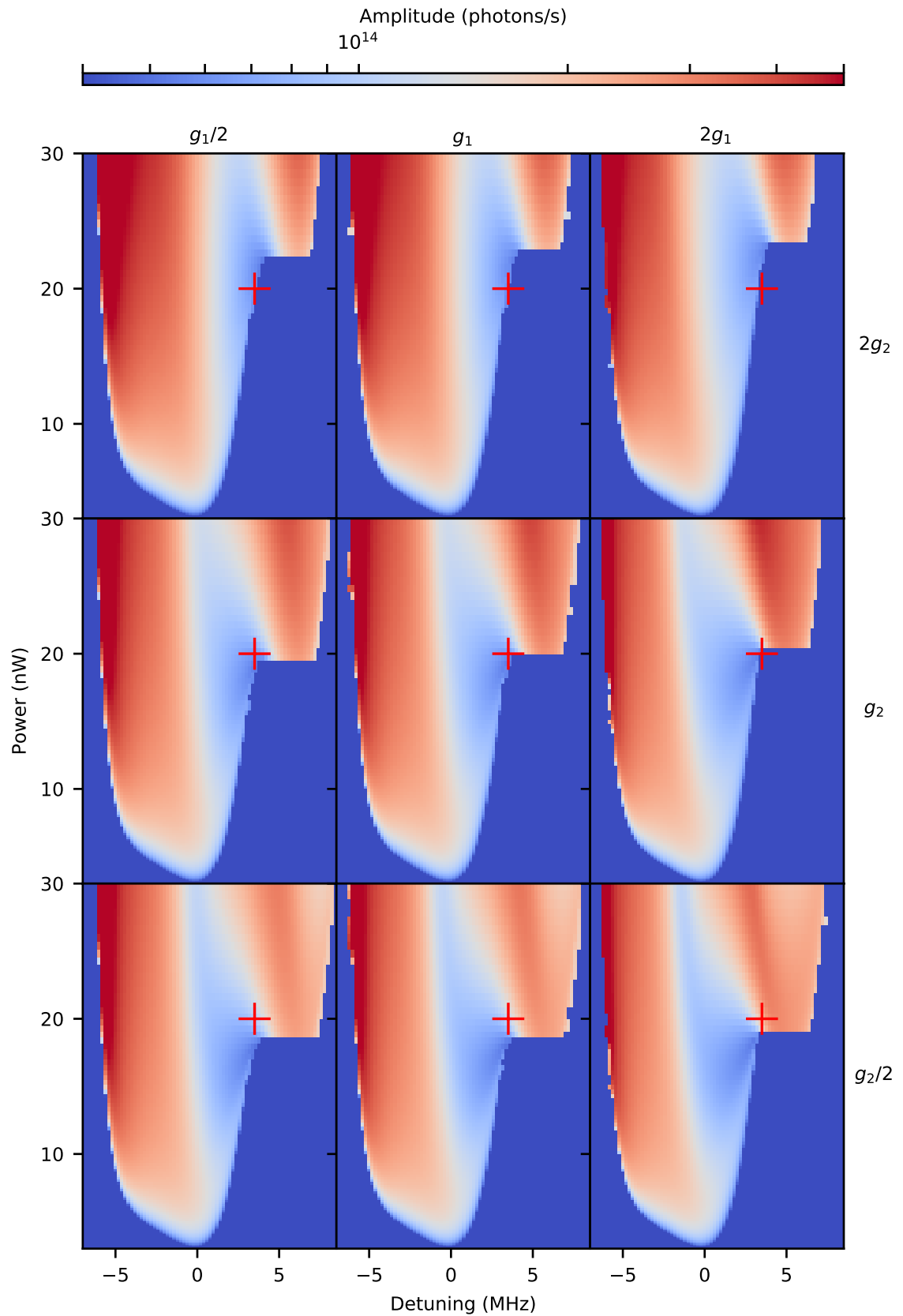


FIGURE 8.5 – Impact of the variation of g_1 and g_2 on the theoretical map giving the output photon flux as a function of both the detuning δ and the input pump power P_{in} . The colormaps are calculated taking into account all mechanical and optical shifts, with $g_0 > 0$. The central one is the same as in the 3D plot of Fig. 8.3. From these graphs, one can extract the ΔP , $\Delta\delta$ parameters shown in Fig. 8.6. The red cross marks the position of the beginning of the hysteresis for the central graph (optimal g_1 and g_2 fit parameters).

The most constrained point for the definition of the couple $(g_1;g_2)$ is the junction between the main stable region and the bistable part, defined by the red cross mark in Fig. 8.2 and 8.5. We shall thus define an effective temperature T_{eff} characteristic of the fit at this precise point. From the measured mechanical frequency shift (Fig. 8.4), we can finally fit the Duffing term β_m . The summary of our results is given in Tab. 8.1.

Within our error bars, we can infer a unique set of parameters that fits all temperatures. This is a strong evidence that the nonlinear features $(g_1;g_2)$ and β_m are of geometrical origin. We give in the following theoretical estimates obtained from basic arguments: a circular plate stretching nonlinearity for β_m [217] and a corresponding plate-capacitor nonlinear expansion for $(g_1;g_2)$. The magnitudes match our findings within typically a factor of 2, apart from g_2 which prediction is the worst because of the crudeness of the plate capacitor analytic expansion.

$T(\text{mK})$	$T_{eff}(\text{mK})$	g_1/g_0	g_2/g_0	$3\beta_m(\text{Hz})$	$3\beta_{cav}(\text{Hz})$
cryo.	$\pm 20\%$	within $\times 2$	within $\times 2$	$\pm 10\%$	est.
417	520	$+1 \cdot 10^{-7}$	$-10 \cdot 10^{-14}$	$+2.1 \cdot 10^{-9}$	-10^{-4}
215	320	idem	idem	idem	idem
50	290	idem	idem	idem	idem

TABLE 8.1 – Fitted parameters at different temperatures. "cryo" is the cryostat measured temperature, while T_{eff} is the characteristic fit temperature; nonlinear couplings are given in units of g_0 , with $g_0 > 0$. The Kerr parameter of the cavity is estimated.

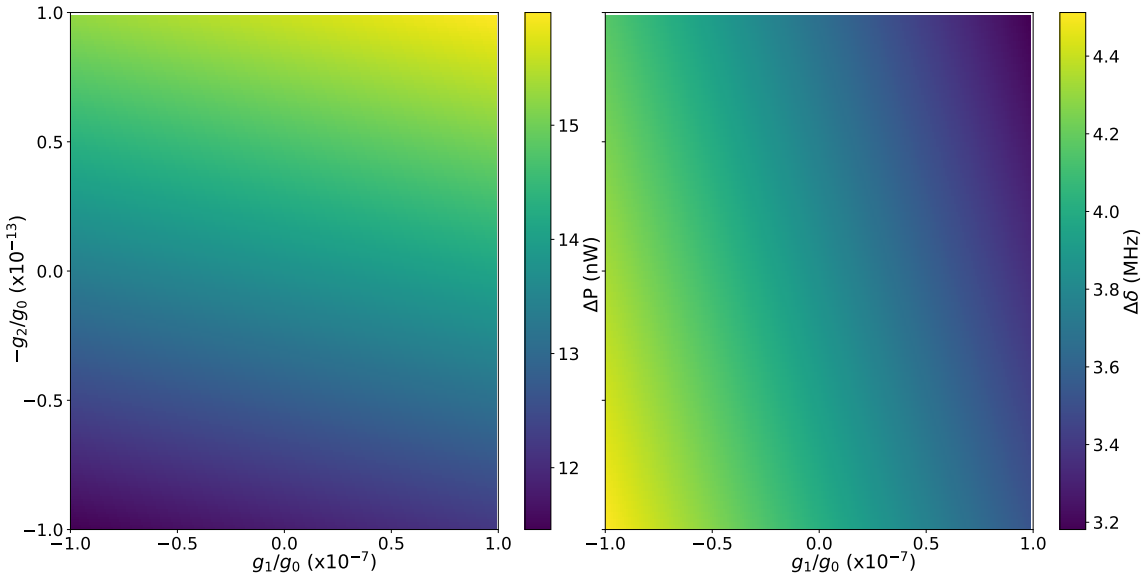


FIGURE 8.6 – Left: Calculated ΔP parameter as a function of $(g_1;g_2)$ coefficients. Right: Calculated $\Delta\delta$ parameter as a function of $(g_1;g_2)$. Both are essentially described by plane equations, with each nonlinear coefficient being the leading one for one of the parameters (g_1 for $\Delta\delta$ and g_2 for ΔP). Full colormaps are also presented in a matrix form in Fig. 8.5.

8.2.3 Basic estimate of nonlinear coupling strengths

The mechanical device used in this work is a typical aluminum drumhead. As can be seen on the SEM picture in Fig. 6.3, the actual structure is rather complex; we will simply approximate it as two discs of radius R (one being fixed and the other movable)

separated by a gap d . The thickness of the drum is e . These geometrical characteristics are summarized in Tab. 8.2 together with typical material parameters. These numbers

$R(\text{nm})$	$d(\text{nm})$	$e(\text{nm})$	$E(\text{GPa})$	$\rho(\text{kg}/\text{m}^3)$	ν
est.	est.	est.	bulk val.	bulk val.	bulk val.
8500	150	170	70	2700	0.35

TABLE 8.2 – Typical drumhead NEMS parameters; the in-built stress is estimated to be < 60 MPa. Corresponding mode effective mass $m_{\text{eff}} = 2.3 \times 10^{-14}$ kg and spring constant $k_{\text{eff}} = 41$ N/m.

are estimated from the Kirchhoff-Love theory of plates, producing the right mechanical resonance frequency of 6.7 MHz: assuming either high-stress limit (in-built stress of 60 MHz and neglecting the Young's modulus) or low-stress (0 in-built stress). Besides, from Ref. [217] we can produce a theoretical estimate for the Duffing parameter β_m in Hz/m^2 . We obtain about $3\beta_m \approx 2 \times 10^{19} \text{Hz}/\text{m}^2$ for a device in the high-stress limit (a drum), and about $3\beta_m \approx 1 \times 10^{19} \text{Hz}/\text{m}^2$ in the low-stress case (a membrane). From the fit value quoted in Tab. 8.1 in units of Hz/phonons, we get a number in between these two numerical estimates: this validates the quantitative evaluation within $\pm 50\%$.

The linear coupling strength g_0 is defined as usual:

$$g_0 = -Gx_{zpf}, \quad (8.2.1)$$

$$G = \frac{d\omega_{\text{cav}}}{dx} = \frac{d\omega_{\text{cav}}}{dC} \frac{dC}{dx}, \quad (8.2.2)$$

with x_{zpf} the zero-point-fluctuation.

For simplicity we will neglect the mode-shape here and consider two planar electrodes; as such, we will take as reference for the mode mass and spring constant calculation the center of the drum (i.e. maximum of mode shape equal to 1). Numbers are given in the caption of Tab. 8.2.

In the previous Equation Eq. (8.2.2), we have $d\omega_{\text{cav}}/dC = -\omega_{\text{cav}}/(2C_0)$ with C_0 the mode effective capacitance. From standard electromagnetism we write $dC/dx = +\epsilon_0\pi R^2/d^2$, neglecting fringing effects which are small in the limit $d/R \ll 1$ (ϵ_0 being the vacuum permittivity) [204]. By definition, we take the direction of the X-axis pointing towards the fixed electrode. Reversing the direction of the X-axis changes the sign of g_0 but also of g_2 , producing an overall $(-1)^n$ in Eq. 2.7.14. This has no impact on physical quantities (such as Γ_{opt} , $\delta\Omega_m$ and $|\alpha_n|^2$): the problem at stake is invariant under a mirror symmetry. We then obtain from Eq. 8.2.1 a value of about 20 Hz for g_0 (choosing $g_0 > 0$) taking for the cavity mode $C_0 \approx 100$ fF which is consistent with the microwave design. This over-estimates g_0 (by about a factor of two) since in reality not all the drum electrode moves, the borders being clamped.

Expanding the plate capacitor expression in a Taylor series of x/d , we obtain for the cavity resonance frequency:

$$\omega_{\text{cav}}(x) = \omega_{\text{cav}}(0) - \left[g_0 \left(\frac{x}{x_{zpf}} \right) + \frac{g_1}{2} \left(\frac{x}{x_{zpf}} \right)^2 + \frac{g_2}{2} \left(\frac{x}{x_{zpf}} \right)^3 + \dots \right], \quad (8.2.3)$$

at third order, where we identify:

$$g_1 = g_0 \left[+2 \frac{x_{zpf}}{d} - 3 \frac{g_0}{\omega_{cav}(0)} \right] \quad (8.2.4)$$

$$g_2 = g_0 \left[+2 \left(\frac{x_{zpf}}{d} \right)^2 - 6 \frac{x_{zpf}}{d} \frac{g_0}{\omega_{cav}(0)} + 5 \left(\frac{g_0}{\omega_{cav}(0)} \right)^2 \right] \quad (8.2.5)$$

In our case, only the first terms in the above are relevant: the magnitude with respect to g_0 of these g_n coefficients is thus fixed by $(x_{zpf}/d)^n$. Computing numerical estimates, we see that with the chosen value of d we under-estimate g_1 by only about 20%, but under-estimate $|g_2|$ by a factor of 7 approximately. The sign of g_2 is also not captured, which shows that this crude modeling fails for high-order derivatives.

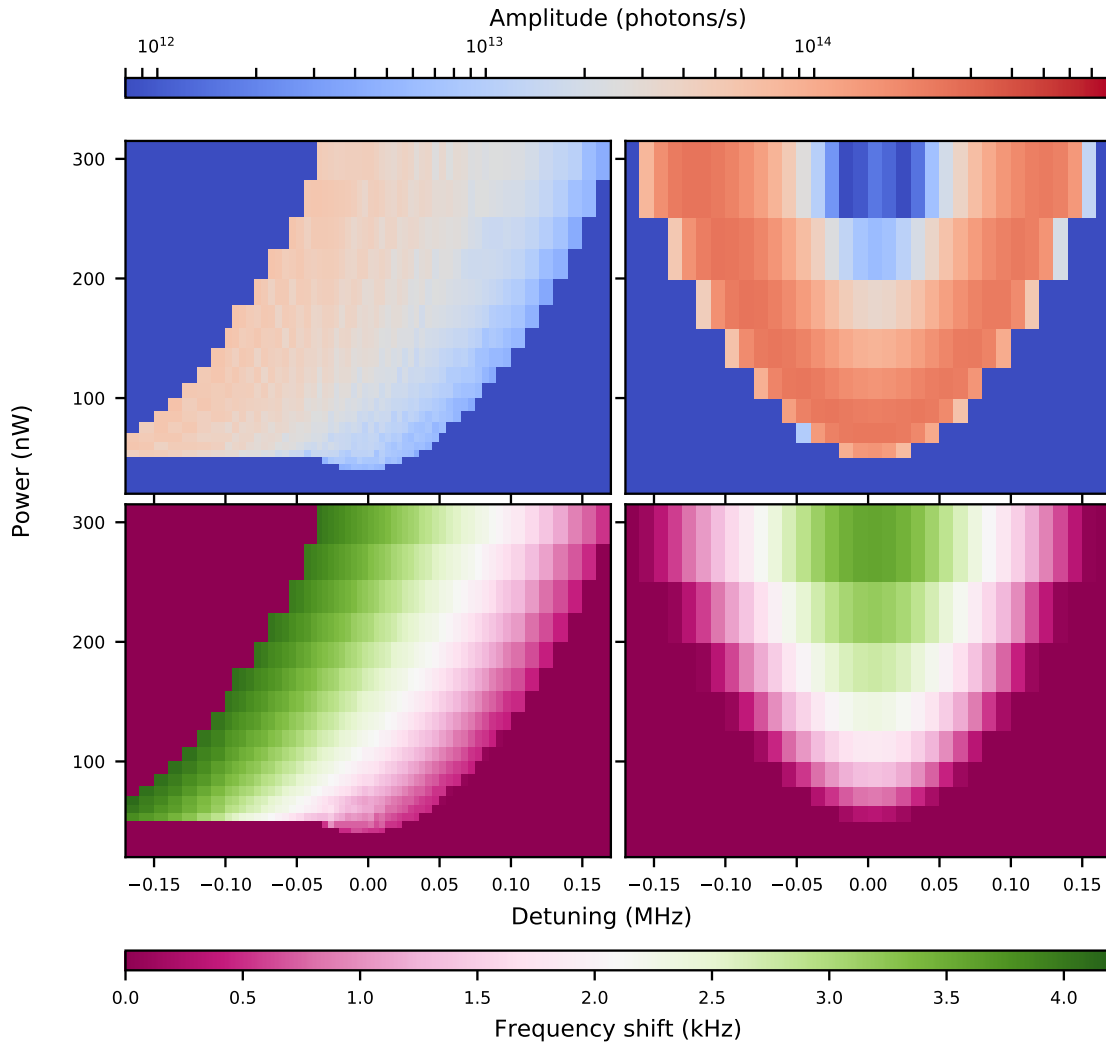


FIGURE 8.7 – Top: Experimental colormap giving the output photon flux (left) measured at 450 mK with the standard beam device presented in Chapter 6 compared to the theoretical map expected (right) calculated with zero g_1 and g_2 parameters. Bottom: Experimental colormap giving the total frequency shift of the mechanical resonance (left) compared to the calculated map (right) with zero g_1 and g_2 parameters.

8.3 COMPARING BEAMS AND DRUMS BEHAVIOUR

8.3.1 Beams and Drums attractor diagrams

Experimental measurements with the beam device chip presented in Chapter 7 revealed a completely different self-sustained oscillation behavior. Indeed, the measured attractor diagram presented in Fig. 8.7 giving the output amplitude and the frequency shift of the mechanics as a function of the input power P_{in} and the detuning δ are completely different compared to the measurement of the drumhead type device.

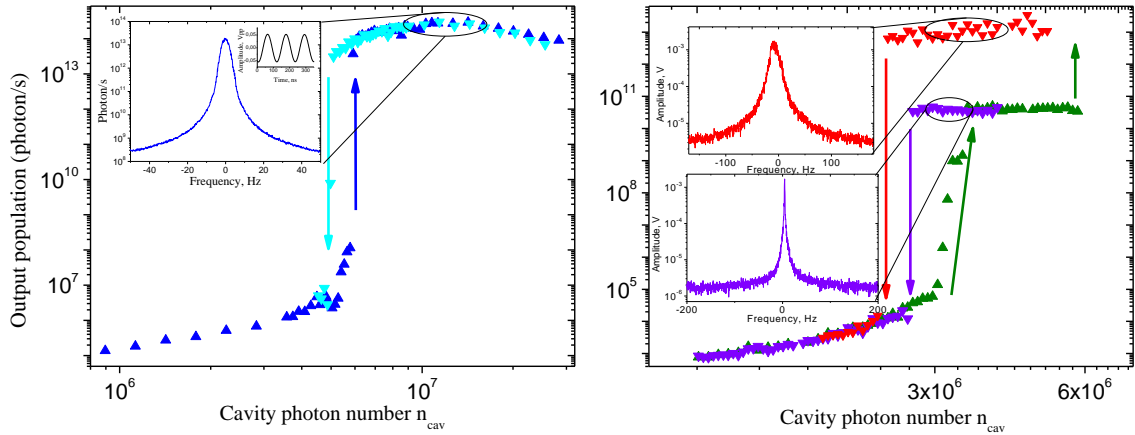
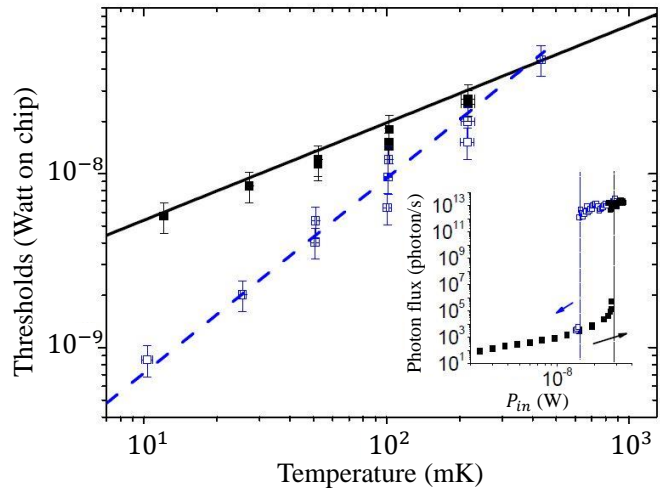


FIGURE 8.8 – Left: Drumhead device measurement of the output photon flux, up (dark blue triangles) and down (light blue triangles) sweeping the input pump power at fixed detuning $\delta = 0$ MHz and 214 mK. The inset represents a measured PSD in the self-induced oscillation regime. Right: Same measurement performed with the beam device. In this case two stable states appear, with a broad one of large amplitude (red PSD) similar to the drum self-oscillating state, and a very narrow state of much smaller amplitude (purple PSD).

FIGURE 8.9 – Main: Power threshold P_{thr} to self-oscillation regime (blue-detuned pump scheme) measured with the beam device [223]. A large hysteresis is seen, certainly due to nonlinearities in the system. The black line is the calculated value $\propto \Gamma_m$ from Eq. (7.1.4), and the dashed line is a guide to the eyes $\propto \Gamma_m^2$. Inset: peak height measured sweeping the power up (full black), and down (empty blue symbols) at 210 mK. The dashed verticals are the threshold positions.



The main tongue-shaped structure is present but an hysteresis is visible (in both P_{in} and δ) on the cavity side for the beam device, and not on the other side. This feature could be due to the cavity nonlinearity, knowing that the cavity is made of niobium

instead of aluminum in the case of the drumhead device. Indeed, niobium is found to be more nonlinear than aluminum; the Kerr nonlinearity of the cavity could be responsible for this qualitative difference between the measured chips.

Below typically 300 mK both geometries (beams and drums) display a really different limit cycle dynamics. Indeed the beam device displays a multistable behavior at very low temperature although we observe only one oscillation state concerning the drum device. This multistability appears clearly on Fig. 8.8: one state is broad and very similar to the one measured with the drumhead device, and the other, which is even not captured by the theory, is very narrow and very stable. Both devices display a hysteresis in power (see Fig. 8.8 representing typically an horizontal cut in previous displayed attractor diagrams) which appears to be temperature-dependent. While for the drum device this hysteresis seems to be almost temperature independent, for the beam device it grows as we cool down, see Fig. 8.9. This feature is not captured by the theory and other types of nonlinearities should probably be included in the hamiltonian formulation to explain this.

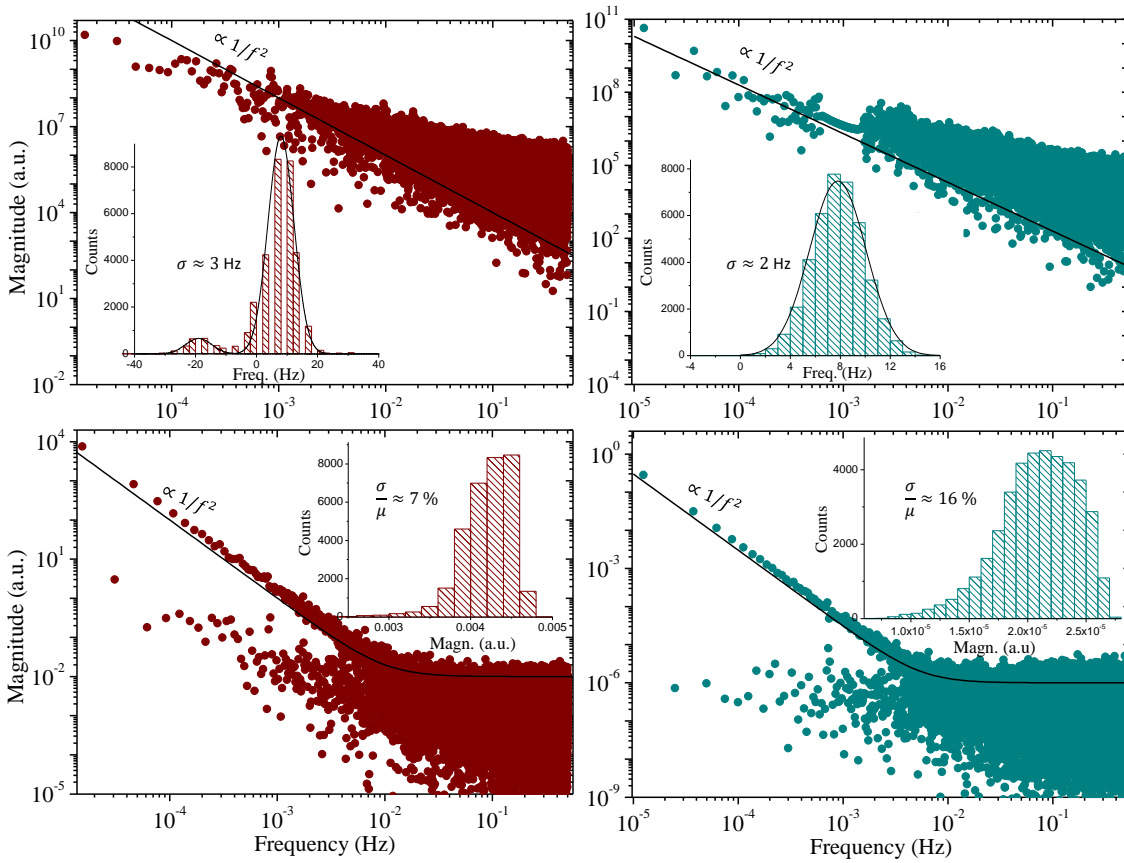
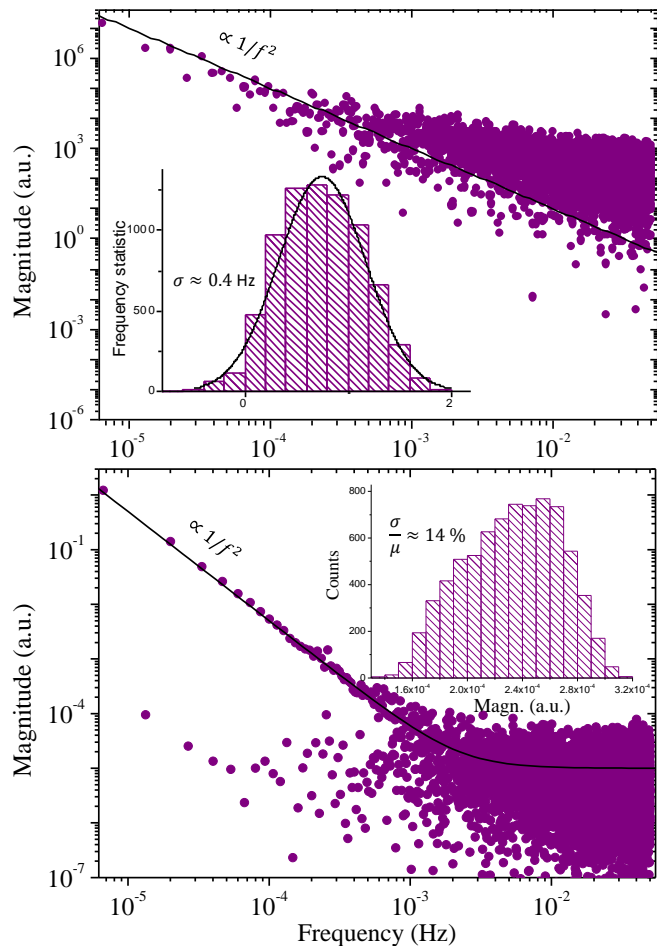


FIGURE 8.10 – Top left: Frequency spectrum (defined as the fast fourier transform of the resonance position correlator) measured on the broad state of the beam device at 25 mK. Bottom left: Amplitude spectrum measured on the broad state of the beam device at 25 mK. Top right: Frequency spectrum measured on the broad state of the badly-coupled drum device at 210 mK. Bottom right: Amplitude spectrum measured on the broad state of the badly-coupled drum device at 210 mK. Black lines are fits $\propto 1/f^2$. Beam statistics are calculated on 32000 measurements whereas drum statistics are calculated on 40000 (both measured with a 1 second sampling rate for an overall measurement time around 10 hours similarly to Chapter 7). Beam measurements have been performed with an input power of $P_{in} \approx 15$ nW whereas drum measurements have been obtained for $P_{in} \approx 4.8$ nW (both at zero detuning). Note the white noise tail on both amplitude spectra, which could be reminiscent of electronic noise. Insets: All insets correspond to the calculated statistics [on the frequency position (top) and of the amplitude of the peak (bottom)]. Black lines are Gaussian fits.

8.3.2 Frequency and amplitude fluctuations

We also report on frequency and amplitude fluctuations observed within the self-oscillating mechanical states. Indeed, concerning the so-called "broad" state generated with both the badly-coupled drum (blue curve in Fig. 8.8) and the beam device (red curve in Fig. 8.8), we observed very similar fluctuations (see Fig. 8.10). Omitting the fact that the beam device displays two clearly different frequency positions at low temperature (see Fig. 8.10 top-left inset), a feature usually characteristic of telegraph-like frequency noise [139], the measured frequency noises of both mechanical devices follow a $1/f^2$ law and their statistics are Gaussian with a standard deviation of order 3 Hz (see Fig. 8.10 top). Note that the actual value of this standard deviation depends on the pump settings (detuning from ideal "blue" pumping, power). These fluctuations could be reminiscent of what is measured in ground-state cooled experiments (on the other drum device, Section 7.4), and could be an *intrinsic* property of the materials, independent of the self-oscillating scheme.

FIGURE 8.11 – Top: Frequency spectrum (defined as the fast fourier transform of the correlator) measured on the narrow state of the beam device at 25 mK. Bottom: Corresponding Amplitude spectrum (note the saturation presumably due to the electronic white noise). Black lines are fits $\propto 1/f^2$. Measurements have been performed for $P_{in} \approx 7.5$ nW (at zero detuning). Insets: Both insets correspond to the calculated statistics [on the frequency position (top) and of the amplitude of the peak (bottom)] computed over about 7500 measurements (sampled at 1 second). The black line is a Gaussian fit.



Regarding amplitude fluctuations of both measured broad states, we observed the same noise tendency following a $1/f^2$ spectrum. Also for both devices, fluctuations are of rather large magnitude, of the order of 10% to 20%, their statistics being clearly non-Gaussian. Such large amplitude fluctuations can actually be explained by *intrinsic damping* fluctuations (which have the proper $1/f^2$ spectrum). Assuming a Gaussian damping noise (matching the results of Chapter 7), we can compute the corresponding amplitude

fluctuations at any point of the attractor diagram. To do so, we first recalculate how the output photon flux is altered by a change in linewidth, at fixed pump settings (and cryostat temperature). For large enough damping fluctuations (typically, of the order or larger than 10%), the photon flux amplitude is altered by more than 10% here, and most importantly the numerical result $Amplitude=function(Damping)$ can be well approximated by a second order polynom with a *nonzero quadratic term*. This is what explains how an initially Gaussian fluctuation in Γ_m can be transduced in a non-Gaussian amplitude fluctuation. To be a bit more quantitative, we tried to simulate the situation measured in Fig. 8.10. Using Mathematica to generate a list of 50000 Gaussian-distributed random numbers, we recalculated the expected amplitude distribution. This is shown in Fig. 8.12 left panel. We can obtain a very good match, fitting the damping standard deviation and considering a slight quantitative error in the theoretical calculation of the quadratic term in the damping dependence (typically between a factor 2 to 10). This error is not so much of a surprise, given the complexity of the modeling and the number of adjustable parameters. As such, it is already remarkable to predict the proper sign asymmetry in the amplitude distribution. But since the asymmetry does not impact much the standard deviation that we fit (and correspondingly the $1/f^2$ fluctuation spectrum), we can extract it from the calculation performed for the set of measurements we have from about 100 mK to 500 mK. This is shown in Fig. 8.12 together with the measured frequency noise, with about 10 hours integration time for both. Note that they show the same tendency in temperature. Frequency noise has been discussed in the literature, especially in the self-oscillating state [122]. However damping fluctuations are not much discussed in the literature, especially in this range of temperatures. This is however certainly the limiting factor to many experiments, especially the ones proposing to squeeze amplitude noise in the self-oscillating state [28]. We shall not speculate here on the possible origins, but simply note that because fluctuations do depend on temperature, they should be genuine. The range explored here is much higher in T_{cryo} than the one of Chapter 7, which certainly explains the difference in the tendencies.

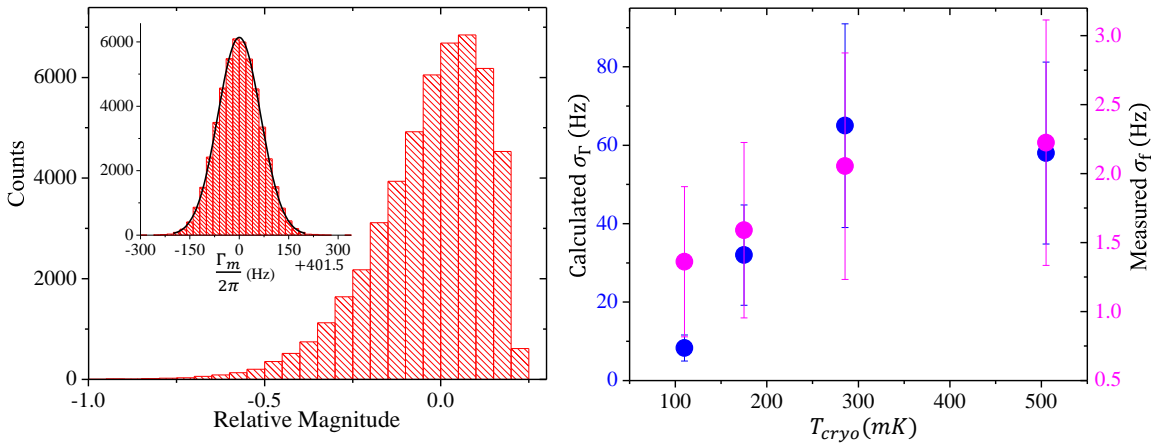


FIGURE 8.12 – Main left: Self-oscillating amplitude statistics simulated for the badly-coupled drum assuming only a mechanical damping noise (shown in inset, 50000 counts), for the settings displayed in Fig. 8.10 (210 mK, 4.8 nW and no detuning). Right: Temperature dependencies of the measured frequency and calculated damping standard deviations in the self-sustained oscillation regime of the badly-coupled drum (for 10 hours integration time, see text for discussion).

Finally, the mysterious so-called "narrow" state appearing with the beam device (purple curve in Fig. 8.8) displays the same amplitude fluctuations characteristics even if its absolute magnitude is rather different (see Fig. 8.11). However, frequency fluctuations in

this state are about 10 times smaller than in the broad one (see Fig. 8.11 top inset). The origin of this frequency stability remains unknown.

8.4 CONCLUSION

As a conclusion we report on microwave optomechanical experiments performed in the self-sustained oscillation regime. The output spectrum of a microwave cavity coupled to a mechanical device is measured as a function of input power P_{in} , pump frequency detuning δ and temperature. A high amplitude and narrow-peak comb structure is measured in the output spectrum, and quantitative understanding is obtained for drumhead devices. We demonstrate that the limit cycle dynamics is sensitive to nonlinearities in the optomechanical coupling. We therefore validate the theory presented in Chap. 2 that goes beyond the standard linear optomechanical Hamiltonian, introducing quadratic and cubic terms g_1 and g_2 . Data is fit quantitatively (for $N = 2$), and we show that these g_1 and g_2 must be of geometrical origin, as opposed to the thermo-optical nonlinear features present in laser driven systems. The work described here can thus be proposed as a new method to characterize nonlinearities in microwave nanomechanical platforms.

With the development of new quantum-limited optomechanical schemes building on higher-order couplings, it represents a very useful new resource. The method is also particularly straightforward since it simply relies on the strong pumping of the mechanics via the microwave field. Besides, the generated comb itself could be used in schemes requiring microwave multiplexing. One could imagine specific designs with multiple cavities and NEMS producing much wider combs. Further work is needed to understand the extent to which the geometrical nonlinearities affect the fluctuations of the system in the limit-cycle regime and to determine whether they can give rise to squeezing of the mechanical state.

Finally we gave a brief experimental outline on how a beam-type device behaves in the self-sustained oscillation regime by measuring attractor diagrams significantly different of drumhead type geometries. In this case other types of nonlinearities should probably be taken into account, as e.g. higher order optical (Kerr) terms. Finally the observed multistable behaviour of the beam is not yet well understood.

8.5 RÉSUMÉ EN FRANÇAIS

Dans ce dernier chapitre nous nous sommes tournés vers l'étude expérimentale d'un système optomécanique micro-onde dans lequel le mode mécanique évolue dans le régime particulier d'auto-oscillation. Le spectre optique en sortie d'une cavité micro-onde couplée à un objet mécanique est mesuré en fonction de la puissance de pompe injectée P_{in} , du désaccord fréquentiel de la pompe δ et de la température. Le spectre mesuré présente une structure en peigne composée de pics, chacun étant extrêmement fin et de très haute amplitude. Une comparaison quantitative avec la théorie est obtenue pour les structures mécaniques de type tambour. Nous avons démontré que la dynamique du régime d'auto-oscillation est très sensible aux non-linéarités de couplage optomécanique. Nous avons donc validé la théorie présentée au Chap. 2 allant au-delà de l'optomécanique linéaire standard, en introduisant des termes de couplage d'ordres supérieurs, et en particulier quadratique et cubique (g_1 et g_2 pour $N = 2$). Un accord quantitatif avec les données expérimentales est obtenu pour $N = 2$ et nous démontrons ainsi que ces termes ont une

origine purement géométrique, en opposition aux systèmes optomécaniques laser qui restent dominés par les nonlinéarités thermo-optiques. Le travail effectué ici peut ainsi être proposé comme une nouvelle méthode de caractérisation des nonlinéarités présentes dans les systèmes nanomécaniques micro-ondes.

Avec l'essor de l'optomécanique à la limite quantique basée sur l'exploitation des nonlinéarités d'ordre supérieur, ce travail représente une nouvelle ressource très utile. Cette méthode est également facile à mettre en oeuvre attendu qu'elle requiert seulement un pompage particulièrement fort du mode mécanique par le signal micro-onde. Outre cela, le peigne micro-onde généré pourrait très bien être utilisé pour des systèmes nécessitant un multiplexage micro-onde. Nous pourrions très bien imaginer une architecture multiplexée comportant de multiples cavités intégrant plusieurs NEMS dans le but de produire des peignes bien plus larges. Un approfondissement de l'étude effectuée est nécessaire pour comprendre l'impact des nonlinéarités géométriques sur les fluctuations du système évoluant en régime d'auto-oscillation ainsi que pour savoir si celles-ci pourraient être à l'origine de squeezing d'états mécaniques.

Les mesures expérimentales effectuées sur un NEMS de type poutre ont finalement montré un comportement en régime d'auto-oscillation significativement différent des NEMS de type tambour. D'autres types de nonlinéarités sont probablement à prendre en compte, nous pourrions par exemple citer les nonlinéarités de cavité (Kerr) d'ordre supérieur. Finalement, les états multistables observés lors des mesures sur le NEMS de type poutre ne sont pas encore compris.

CONCLUSION: MICROWAVE OPTOMECHANICS NEAR ZERO TEMPERATURE

In this final section, we conclude on the achieved work and discuss future developments that could follow our findings. In particular, we summarize the relevance of the results obtained in this thesis and provide future outlooks concerning the next steps towards experimental testing of the grounds of quantum mechanics.

MICROWAVE/MICROKELVIN PLATFORM

We have thus built an experimental platform for microwave optomechanics on a nuclear demagnetization cryostat able to reach sub-milliKelvin temperatures. This well calibrated homemade machine is now ready and running, and we were able to demonstrate its ability to perform brute force-cooling of mesoscopic mechanical objects embedded in on-chip microwave cavities. We have thus presented a method based on a Stokes side-band pumping scheme providing precise thermometry of both the mechanical phononic temperature and its on-chip environment. In order to provide the most reliable measurements, we performed calibrations on two other commercial dilution cryostats. All machines being independently calibrated, we reached an absolute error on microwave losses and gains as small as ± 2 dBm. We took extreme care in characterizing all possible sources of errors and misinterpretations, such as on-chip heating due to microwave absorption and out-of-equilibrium photon population due to the imperfection of microwave generators (phase noise). Also, careful modeling of both microwave circuits and mechanical elements (including the optomechanical coupling) has been performed.

To obtain a quantitative understanding of our results, we needed to present both classical and quantum theories of microwave optomechanics. We re-derived the complete one-tone optomechanical quantum theory based on the input-output formalism, and derived its classical electric analogue. We discussed the quantum-to-classical boundary of microwave optomechanics and exposed the link between both formalisms, demonstrating which features rely on quantumness and which do not. Deriving quantum and classical limits of microwave optomechanics is essential, since we show that quantum signatures rely essentially on a *quantitative* analysis of the measurements.

We presented a new method based on the self-sustained oscillation regime which allows a complete characterization of all types of relevant optomechanical nonlinearities. Indeed, in this specific regime the mechanical amplitude of motion becomes very large and reveals the geometrical nonlinearities of the system. In particular, for a typical drumhead device, we demonstrated a quantitative understanding of the optomechanical coupling nonlinearities up to the second order, as well as of the mechanical Duffing nonlinearity. Perfect knowledge of the Hamiltonian at stake is essential for the accurate comparison of measurements to new theories, especially those based on collapse models and quantum gravity.

On the experimental side, we are the first ones to demonstrate thermalization of a mesoscopic mechanical object down to about $500 \mu\text{K}$. Such measurements have been performed using a highly-coupled drumhead device resonating around 15 MHz brought to its quantum ground state (about 0.3 phonons on average in the fundamental mode). All

higher mechanical modes are thus empty, and the *whole macroscopic structure* hosts no thermal excitations for about half of the time. This state-of-the-art result opens now the field of in-equilibrium quantum experiments, which is of fundamental interest for the comprehension of quantum mechanical decoherence due to bath interactions. As such, we report on the thermodynamic fluctuations of phonon number, damping and resonance frequency measured at these extreme temperatures. These are not yet understood, and clearly deserve theoretical input.

For the first time in the literature, we report on an unknown stochastic driving force observed in these microwave optomechanical devices. We demonstrated that this feature is generic to all types of NEMS devices embedded in microwave cavity detectors, and that it is the main limitation to brute-force cooling experiments. The observed random "spikes" in the spectrum are obviously linked to the bath dynamics to which the mode is coupled, and their occurrence depends on both the on-chip temperature and the intra-cavity drive photon occupation. It seems that the bigger the optomechanical coupling strength is, the least "spikes" are observed because the cavity occupancy can be kept very low. Therefore, for devices with not too high frequencies, and not too large coupling, the only solution to reach the quantum ground state of motion is to cool down in a dilution cryostat to not too low temperatures to prevent the "spikes" appearance, and then to actively cool the mode with red-sideband pumping. This is actually the solution in use in the literature so far. We thus conclude that brute-force cooling does require not only demagnetization cryogenics and 15 MHz (or higher) mechanical devices, but also reasonably large coupling strengths in order to avoid the "spiking", and concomitantly drive-dependent thermal decoupling.

NEXT STEPS TOWARD QUANTUM DECOHERENCE

In this thesis, we demonstrated that bringing a mesoscopic object such as a NEMS device in the quantum motional ground state is effectively experimentally possible using brute-force cooling instead of active optical cooling. This obtained state-of-the-art result now paves the way towards quantum decoherence measurements.

Here, in order to set-up the technology we performed single-tone measurements, the simplest optomechanical pumping schemes. However, recent works demonstrated that performing multi-tone optomechanical pumping schemes provides useful new capabilities. Indeed, a back-action evading (BAE) measurement can be realized by pumping both anti-Stokes and Stokes sidebands simultaneously with perfectly balanced powers [25]. This particular scheme provides a means to measure a weak motion at (in principle) arbitrarily large pump powers without suffering from back-action noise from the cavity, thus beating the standard quantum limit (SQL) of single-tone schemes. BAE measurements should now be experimentally investigated profoundly as measurements involving several tones display much more complexity in microwave circuits than single-tone ones. Besides, the specific instability that occurs in two-tone driving (analogous to the blue pumping instability) and that limits the capabilities of the measurements has not yet been studied in details [99].

In order to proceed towards quantum decoherence mechanical studies, such NEMS optomechanical devices should now be dispersively coupled to a superconducting quantum bit. This would allow to perform e.g. the "Echo scheme" proposed by A.D. Armour and M.P. Blencowe [155], or to create non-classical states (Fock states) [113, 134] and study their dynamics. Another exciting possibility is to entangle two mechanical objects

through the microwave field in order to study the decoherence of the entanglement [57]. Building such on-chip systems is challenging but effectively feasible [113, 134]. With such designs, it should be possible to prepare the mesoscopic mechanical motion in an entangled state in order to probe the decoherence due to the bath interaction. It becomes then possible to study the mechanical decoherence of mesoscopic moving objects as a function of drive/environment parameters, with motion far larger than the atomic size. The experimental results obtained should then be compared to theoretical models, building on the careful control of the NEMS' bath, such as continuous stochastic collapse theories, thus testing the grounds of quantum mechanics. The quantum nature of the gravity field is one of the exciting subject that could be addressed, with implications far outside of the scope of mesoscopic physics.

BIBLIOGRAPHY

ARTICLES

1. A. Ashkin & J.M. Dziedzic. "Feedback stabilization of optically levitated particles". *Applied Physics Letters*, 30, 202 (1977). (Cit. on p. 4)
2. A. Auffèves & P. Grangier. "A Generic Model for Quantum Measurements". *Entropy*, 21, 904 (2019). (Cit. on p. 15)
3. A. Bassi & G. Ghirardi. "A General Argument Against the Universal Validity of the Superposition Principle". *Physics Letters A*, 275, 5–6 (2000). (Cit. on p. 13)
4. A. Bassi, K. Lochan, S. Satin, T.P. Singh & H. Ulbricht. "Models of wave-function collapse, underlying theories, and experimental tests". *Reviews of Modern Physics*, 85, 471 (2013). (Cit. on pp. 12, 13, 15 and 18)
5. A. Bilmes *et al.* "Electronic Decoherence of Two-Level Systems in a Josephson Junction". *Physical Review B*, 96, 064504 (2017). (Cit. on p. 148)
6. A. Dorsel, J.D. McCullen, P. Meystre, E. Vignes & H. Walther. "Optical Bistability and Mirror Confinement Induced by Radiation Pressure". *Physical Review Letters*, 51, 1550 (1983). (Cit. on p. 4)
7. A. Einstein. "On the developpement of our views concerning the nature and constitution of radiation". *Phys. Z.*, 10, 817–826 (1909). (Cit. on p. 4)
8. A. Einstein. "On the present status of the radiation problem". *Phys. Z.*, 10, 185–193 (1909). (Cit. on p. 4)
9. A. Einstein, B. Podolsky & N. Rosen. "Can Quantum-Mechanical Description of Physical Reality Be Considered Complete ?" *Physical Review Journals Archive*, 47, 777 (2035). (Cit. on pp. 11 and 14)
10. A. Heidmann *et al.* "Observation of Quantum Noise Reduction on Twin Laser Beams". *Physical Review Letters*, 59, 2555 (1987). (Cit. on p. 11)
11. A. Metelmann & A.A. Clerk. "Nonreciprocal Photon Transmission and Amplification via Reservoir Engineering". *Physical Review X*, 5, 021025 (2015). (Cit. on p. 10)
12. A. Palacios-Laloy. "Bits quantiques supraconducteurs et resonateur: Test de l'inégalité de Leggett-Garg et lecture en un coup". Thesis (2010). (Cit. on p. 112)
13. A. Pontin, N.P. Bullier, M. Toros & P.F. Barker. "Ultranarrow-linewidth levitated nanoscillator for testing dissipative wave-function collapse". *Physical Review Research*, 2, 023349 (2020). (Cit. on p. 18)
14. A. Rueda *et al.* "Efficient microwave to optical photon conversion: an electro-optical realization". *Optica*, 3, 6 (2016). (Cit. on p. 10)
15. A. Schliesser, O. Arcizet, R. Rivière, G. Anetsberger & T.J. Kippenberg. "Resolved-sideband cooling and position measurement of a micromechanical oscillator close to the Heisenberg uncertainty limit". *Nature Physics*, 5, 509–514 (2009). (Cit. on p. 88)
16. A. Schliesser, P. Del'Haye, N. Nooshi, K.J. Vahala & T.J. Kippenberg. "Radiation Pressure Cooling of a Micromechanical Oscillator Using Dynamical Backaction". *Physical Review Letters*, 97, 243905 (2006). (Cit. on pp. 6 and 7)
17. A. Shibahara *et al.* "Primary current-sensing noise thermometry in the millikelvin regime". *Trans. R. Soc. A*, 374, 20150054 (2016). (Cit. on p. 124)

18. A. Tantot *et al.* "Sound and Light from Fractures in Scintillators". *Physical Review Letters*, 111, 154301 (2013). (Cit. on p. 147)
19. A. Venkatesan *et al.* "Dissipation due to tunneling two-level systems in gold nanomechanical resonators". *Physical Review B*, 81, 073410 (2010). (Cit. on p. 141)
20. A. Vinante, R. Mezzena, P. Falferi, M. Carlesso & A. Bassi. "Improved Noninterferometric Test of Collapse Models Using Ultracold Cantilevers". *Physical Review Letters*, 119, 110401 (2017). (Cit. on p. 17)
21. A. Vinante *et al.* "Upper Bounds on Spontaneous Wave-Function Collapse Models Using Millikelvin-Cooled Nanocantilevers". *Physical Review Letters*, 116, 090402 (2016). (Cit. on pp. 12, 16 and 18)
22. A. Vinante *et al.* "Testing collapse models with levitated nanoparticles: Detection challenge". *Physical Review A*, 100, 012119 (2019). (Cit. on pp. 12 and 18)
23. A. Wallraff *et al.* "Strong coupling of a single photon to a superconducting qubit using circuit quantum electrodynamics". *Nature*, 431, 162–167 (2004). (Cit. on p. 9)
24. A.A. Clerk. "Quantum-limited position detection and amplification: A linear response perspective". *Physical Review B*, 70, 245306 (2004). (Cit. on p. 8)
25. A.A. Clerk, F. Marquardt & K. Jacobs. "Back-action evasion and squeezing of a mechanical resonator using a cavity detector". *New Journal of Physics*, 10, 095010 (2008). (Cit. on pp. 8, 71, 72 and 182)
26. A.A. Clerk, M.H. Devoret, S.M. Girvin, F. Marquardt & R.J. Schoelkopf. "Introduction to quantum noise, measurement, and amplification". *Reviews of modern physics*, 82, 1155 (2010). (Cit. on pp. 7, 26, 35, 37, 39, 48, 76, 77, 82, 87, 88 and 92)
27. A.B. Zorin *et al.* "Background charge noise in metallic single-electron tunneling devices". *Physical Review B*, 53, 13682 (1996). (Cit. on p. 147)
28. A.D. Armour & D.A. Rodrigues. "Quantum dynamics of a mechanical resonator driven by a cavity". *C.R. Physique*, 13, 440–453 (2012). (Cit. on pp. 8, 64, 164, 166, 167 and 177)
29. A.D. Armour & M.P. Blencowe. "Probing the quantum coherence of a nanomechanical resonator using a superconducting qubit: I. Echo scheme". *New Journal of Physics*, 10 (2008). (Cit. on pp. 12 and 20)
30. A.D. O'Connell *et al.* "Quantum ground state and single phonon control of a mechanical resonator". *Nature*, 464, 697–703 (2010). (Cit. on pp. 9, 10, 12, 18, 19 and 143)
31. A.E.H Love. "The Small Free Vibrations and Deformation of Thin Elastic Shell". *Philosophical Transactions of the Royal Society of London, A*, Volume 179, pp. 491–546 (1888). (Cit. on p. 104)
32. A.G. Krause *et al.* "Nonlinear Radiation Pressure Dynamics in an Optomechanical Crystal". *Physical Review Letters*, 115, 233601 (2015). (Cit. on pp. 8 and 164)
33. A.H. Safavi-Naeini *et al.* "Observation of Quantum Motion of a Nanomechanical Resonator". *Physical Review Letters*, 108, 033602 (2012). (Cit. on p. 151)
34. A.J. Leggett. "Macroscopic Quantum Systems and the Quantum Theory of Measurement". *Progress of Theoretical Physics Supplement*, 69, 80–100 (1980). (Cit. on p. 13)
35. A.J. Leggett. "Testing the limits of quantum mechanics: motivation, state of play, prospects". *Journal of Physics: Condensed Matter*, 14, 15 (2002). (Cit. on p. 11)
36. A.J. Leggett & A. Garg. "Quantum mechanics versus macroscopic realism: Is the flux there when nobody looks?" *Physical Review Letters*, 54, 857 (1985). (Cit. on p. 14)
37. A.J. Weinstein *et al.* "Observation and Interpretation of Motional Sideband Asymmetry in a Quantum Electromechanical Device". *Physical Review X*, 4, 041003 (2014). (Cit. on pp. 10, 48, 55, 60, 62, 85, 89 and 91)
38. A.L. Schawlow & C.H. Townes. "Infrared and optical masers". *Physical Review*, 112 (1940). (Cit. on p. 4)

39. A.M. Guénault, V. Keith, C.J. Kennedy, S.G. Mussett & G.R. Pickett. "The mechanical behavior of a vibrating wire in superfluid $^3\text{He} - B$ in the ballistic limit". *Journal of Low Temperature Physics*, 62, 511 (1986). (Cit. on p. 131)
40. A.M. Jayich *et al.* "Dispersive optomechanics: a membrane inside a cavity". *New Journal of Physics*, 10 (2008). (Cit. on p. 8)
41. A.N. Cleland & M. L. Roukes. "Fabrication of high frequency nanometer scale mechanical resonators from bulk Si crystals". *Applied Physics Letters*, 69, 2653 (1996). (Cit. on p. 7)
42. A.O. Barvinsky, D. Carney & P.C.E. Stamp. "Structure of correlated worldline theories of quantum gravity". *Physical Review D*, 98, 084052 (2018). (Cit. on p. 17)
43. A.P. Higginbotham *et al.* "Harnessing electro-optic correlations in an efficient mechanical converter". *Nature Physics*, 14, 1038–1042 (2018). (Cit. on p. 10)
44. B. Yurke, D.S. Greywall, A.N. Pargellis & P.A. Bush. "Theory of amplifier-noise evasion in an oscillator employing a nonlinear resonator". *Physical Review A*, 51, 4211 (1995). (Cit. on p. 102)
45. B.D. Hauer, A. Metelmann & J.P. Davis. "Phonon quantum nondemolition measurements in nonlinearly coupled optomechanical cavities". *Physical Review A*, 98, 043804 (2018). (Cit. on p. 8)
46. B.D. Hauer, P.H. Kim, C. Doolin, F. Souris & J.P. Davis. "Two-level system damping in a quasi-one-dimensional optomechanical resonator". *Physical Review B*, 98, 214303 (2018). (Cit. on pp. 141, 144 and 148)
47. C. Bäuerle, Y. Bunkov, S.N. Fisher, C. Gianese & H. Godfrin. "The new Grenoble 100 microKelvin refrigerator". *Czechoslovak J. of Phys.*, 46, suppl S5, 2791–2792 (1996). (Cit. on pp. 129 and 130)
48. C. Genes, D. Vitali, P. Tombesi, S. Gigan & M. Aspelmeyer. "Ground-state cooling of a micromechanical oscillator: Comparing cold damping and cavity-assisted cooling schemes". *Physical Review A*, 77, 033804 (2008). (Cit. on p. 57)
49. C. Laflamme & A.A. Clerk. "Weak Qubit Measurement with a Nonlinear Cavity: Beyond Perturbation Theory". *Physical Review Letters*, 109, 123602 (Sept. 19, 2012). (Cit. on pp. 70 and 71)
50. C. Metzger *et al.* "Self-Induced Oscillations in an Optomechanical System Driven by Bolometric Backaction". *Physical Review Letters*, 101, 133903 (2008). (Cit. on pp. 8 and 164)
51. C. Monroe *et al.* "Resolved-Sideband Raman Cooling of a Bound Atom to the 3D Zero-Point Energy". *Physical Review Letters*, 75, 4011 (1995). (Cit. on p. 7)
52. C. Song *et al.* "Microwave response of vortices in superconducting thin films of Re and Al". *Physical Review B*, 79, 174512 (2009). (Cit. on p. 147)
53. C. U. Lei *et al.* "Quantum Nondemolition Measurement of a Quantum Squeezed State Beyond the 3 dB Limit". *Physical Review Letters*, 117, 100801 (2016). (Cit. on p. 74)
54. C.A. Regal, J.D. Teufel & K.W. Lehnert. "Measuring nanomechanical motion with a microwave cavity interferometer". *Nature Physics*, 4, 555 (2008). (Cit. on pp. 9, 10, 74, 132, 138, 143 and 163)
55. C.B. Winkelmann, E. Collin, Y.M. Bunkov, H. Godfrin & G.R. Pickett. "Vibrating wire thermometry in superfluid ^3He ". *Journal of Low Temperature Physics*, 135, 3 (2004). (Cit. on p. 131)
56. C.F. Ockeloen-Korppi *et al.* "Quantum Backaction Evading Measurement of Collective Mechanical Modes". *Physical Review Letters*, 117, 140401 (2016). (Cit. on p. 10)
57. C.F. Ockeloen-Korppi *et al.* "Stabilized entanglement of massive mechanical oscillators". *Nature*, 556, 478 (2018). (Cit. on pp. 11, 12, 19, 114, 121, 143, 164 and 183)
58. C.M. Caves. "Quantum-Mechanical Radiation-Pressure Fluctuations in an Interferometer". *Physical Review Letters*, 45, 75 (1980). (Cit. on p. 4)
59. C.M. Caves. "Quantum-Mechanical noise in an interferometer". *Physical Review D*, 23, 1693 (1981). (Cit. on p. 6)

60. D. Bohm. "A Suggested Interpretation of the Quantum Theory in Terms of "Hidden" Variables. I". *Physical Review Journals Archive*, 85, 166 (1952). (Cit. on p. 14)
61. D. Bohm. "A Suggested Interpretation of the Quantum Theory in Terms of "Hidden" Variables. II". *Physical Review Journals Archive*, 85, 180 (1952). (Cit. on p. 14)
62. D. Kleckner *et al.* "Creating and verifying a quantum superposition in a micro-optomechanical system". *New Journal of Physics*, 10 (2008). (Cit. on pp. 12, 17, 18 and 19)
63. D. Malz & A. Nunnenkamp. "Floquet approach to bichromatically driven cavity-optomechanical systems". *Physical Review A*, 103901 (Aug. 1, 2016). (Cit. on pp. 71 and 72)
64. D. Zheng *et al.* "Room temperature test of the continuous spontaneous localization model using a levitated micro-oscillator". *Physical Review Research*, 2, 013057 (2020). (Cit. on pp. 17 and 18)
65. D.A. Rodrigues & A.D. Armour. "Amplitude Noise Suppression in Cavity-Driven Oscillations of a Mechanical Resonator". *Physical Review Letters*, 104, 053601 (2010). (Cit. on p. 8)
66. D.C. Carless, H.E. Hall & J.R. Hook. "Vibrating wire measurements in liquid ^3He . I. The normal state". *Journal of Low Temperature Physics*, 50, 583 (1983). (Cit. on p. 131)
67. D.C. Carless, H.E. Hall & J.R. Hook. "Vibrating wire measurements in liquid ^3He . II. The superfluid B phase". *Journal of Low Temperature Physics*, 50, 605 (1983). (Cit. on p. 131)
68. D.C. Mattis & J. Bardeen. "Theory of the anomalous skin effect in normal and superconducting metals". *Physical Review*, 111, 412 (1958). (Cit. on p. 116)
69. D.I. Bradley *et al.* "The damping of a quartz tuning fork in superfluid $^3\text{He} - B$ at low temperatures". *Journal of Low Temperature Physics*, 157, 476 (2009). (Cit. on pp. 131 and 132)
70. D.I. Bradley *et al.* "Thermometry in Normal Liquid ^3He Using a Quartz Tuning Fork Viscometer". *Journal of Low Temperature Physics*, 171, 750 (2013). (Cit. on pp. 131 and 132)
71. D.K. Armani, T.J. Kippenberg, S.M. Spillane & K.J. Vahala. "Ultra-high-Q toroid microcavity on a chip". *Nature*, 421, 925–928 (2003). (Cit. on p. 7)
72. D.P. Kleckner. "Micro-Optomechanical Systems for Quantum Optics". *PhD Thesis of University of California, Santa Barbara* (2010). (Cit. on p. 19)
73. E. Collin, Y.M. Bunkov & H. Godfrin. "Addressing geometric nonlinearities with cantilever microelectromechanical systems: Beyond the Duffing model". *Physical Review B*, 82, 235416 (2010). (Cit. on p. 103)
74. E. Collin *et al.* "Metallic coatings of microelectromechanical structures at low temperatures: Stress, elasticity, and nonlinear dissipation". *Journal of Applied Physics*, 107(11), 114905 (2010). (Cit. on p. 102)
75. E. Nazaretski *et al.* "Effect of Low-Level Radiation on the Low Temperature Acoustic Behavior of a-SiO₂". *Physical Review Letter*, 92, 245502–1 (2014). (Cit. on p. 148)
76. E.A. Sete & H. Eleuch. "High-efficiency quantum state transfer and quantum memory using a mechanical oscillator". *Physical Review A*, 91, 032309 (2015). (Cit. on p. 10)
77. E.E. Wollman *et al.* "Quantum squeezing of motion in a mechanical resonator". *Science*, 349, 952 (2015). (Cit. on pp. 10 and 143)
78. E.F. Nichols & G.F. Hull. "A Preliminary Communication on the Pressure of Heat and Light Radiation". *Physical Review*, 13, 307 (1901). (Cit. on p. 4)
79. F. Acernese *et al.* & (LIGO Scientific Collaboration and Virgo Collaboration). "Increasing the astrophysical reach of the advance Virgo detector via the application of squeezed vacuum states of light". *Physical Review Letters*, 123, 231108 (2019). (Cit. on pp. 5 and 6)
80. F. Diedrich, J.C. Bergquist, W.M. Itano & D.J. Wineland. "Laser Cooling to the Zero-Point Energy of Motion". *Physical Review Letters*, 62, 403 (1989). (Cit. on p. 4)
81. F. Fogliano *et al.* "Cavity nano-optomechanics in the ultrastrong coupling regime with ultrasensitive force sensors". *arXiv:1904.01140* (2015). (Cit. on p. 7)

82. F. Hoehne *et al.* “Damping in high-frequency metallic nanomechanical resonators”. *Physical Review B*, 81, 184112 (2010). (Cit. on p. 144)
83. F. Karolyhazy. “Gravitation and quantum mechanics of macroscopic objects”. *Il Nuovo Cimento A*, 42, 390–402 (1966). (Cit. on p. 16)
84. F. Marquardt, J.G.E. Harris & S.M. Girvin. “Dynamical Multistability Induced by Radiation Pressure in High-Finesse Micromechanical Optical Cavities”. *Physical Review Letters*, 96, 103901 (2006). (Cit. on pp. 166 and 167)
85. F. Marquardt, J.G.E. Harris & S.M. Girvin. “Dynamical multistability induced by radiation pressure in high-finesse micromechanical optical cavities”. *Physical Review Letter*, 96, 103901 (2006). (Cit. on pp. 8, 64 and 83)
86. F. Marquardt, J.P. Chen, A.A. Clerk & S.M. Girvin. “Quantum Theory of Cavity-Assisted Sideband Cooling of Mechanical Motion”. *Physical Review Letters*, 99, 093902 (Aug. 28, 2007). (Cit. on pp. 37, 41, 42 and 57)
87. F. Massel *et al.* “Microwave amplification with nanomechanical resonators”. *Nature*, 480, 351 (2011). (Cit. on p. 75)
88. F. Massel *et al.* “Multimode circuit optomechanics near the quantum limit”. *Nature Communication*, 3, 987 (2012). (Cit. on pp. 11, 144 and 150)
89. G. Anetsberger *et al.* “Near-field cavity optomechanics with nanomechanical oscillators”. *Nature physics*, 5, 909–914 (2009). (Cit. on p. 7)
90. G.A. Peterson *et al.* “Demonstration of Efficient Nonreciprocity in a Microwave Optomechanical Circuit”. *Physical Review X*, 7, 031001 (2017). (Cit. on p. 10)
91. G.C. Ghirardi, A. Rimini & T. Weber. “Unified dynamics for microscopic and macroscopic systems”. *Physical Review D*, 34, 470 (1986). (Cit. on pp. 15 and 17)
92. G.C. Ghirardi, P. Pearle & A. Rimini. “Markov processes in Hilbert space and continuous spontaneous localization of systems of identical particles”. *Physical Review A*, 42, 78 (1990). (Cit. on p. 15)
93. G.F. Hull. “Concerning the action of the Crookes Radiometer”. *American Journal of Physics*, 16, 185–186 (1948). (Cit. on p. 4)
94. G.S. MacCabe *et al.* “Phononic bandgap nano-acoustic cavity with ultralong phonon lifetime”. *arXiv:1901.04129v1* (2019). (Cit. on pp. 18 and 143)
95. H. Everett. ““Relative State” formulation of Quantum Mechanics”. *Reviews of Modern Physics*, 29, 454 (1957). (Cit. on p. 15)
96. H.-D. Doebner & G.A. Goldin. “On a general nonlinear Schrodinger equation admitting diffusion currents”. *Physics Letters A*, 162, 5 (1992). (Cit. on p. 15)
97. I. Pikovski, M.R. Vanner, M. Aspelmeyer, M.S. Kim & C. Brukner. “Probing Planck-scale physics with quantum optics”. *Nature Physics*, 8, 393–397 (2012). (Cit. on p. 17)
98. I. Shomroni, L. Qiu, D. Malz, A. Nunnenkamp & T.J. Kippenberg. “Optical backaction-evading measurement of a mechanical oscillator”. *Nature Communications* (2019). (Cit. on pp. 8, 71 and 72)
99. I. Shomroni *et al.* “Two-Tone Optomechanical Instability and Its Fundamental Implications for Backaction-Evading Measurements”. *Physical Review X*, 9, 041022 (2019). (Cit. on pp. 10, 71, 72 and 182)
100. J. Aström *et al.* “Fracture processes observed with a cryogenic detector”. *Physics Letters A*, 356, 4–5 (2006). (Cit. on p. 147)
101. J. Bochmann, A. Vainsencher, D.D. Awschalom & A.N. Cleland. “Nanomechanical coupling between microwave and optical photons”. *Nature Physics*, 9, 712–716 (2013). (Cit. on p. 10)
102. J. Burnett, A. Bengtsson, D. Niepce & J. Bylander. “Noise and loss of superconducting aluminium resonators at single photon energies”. *Journal of Physics: Conf. Series*, 969, 012131 (2018). (Cit. on p. 165)

103. J. Chan *et al.* "Laser cooling of a nanomechanical oscillator into its quantum ground state". *Nature*, 478, 89–92 (2011). (Cit. on pp. 6, 7 and 18)
104. J. Gao *et al.* "A semiempirical model for two-level system noise in superconducting microresonators". *Applied Physic Letter*, 92, 212504 (2008). (Cit. on p. 147)
105. J. Li *et al.* "Proposal for optomechanical quantum teleportation". *Physical Review A*, 102, 032402 (2020). (Cit. on p. 11)
106. J. Mertz, O. Marti & J. Mlynek. "Regulation of a microcantilever response by force feedback". *Applied Physics Letters*, 62, 2344 (1993). (Cit. on p. 6)
107. J. Suh *et al.* "Mechanically detecting and avoiding the quantum fluctuations of a microwave field". *Science*, 344, 6189 (2014). (Cit. on pp. 8, 10 and 143)
108. J. von Neumann. "Mathematical Foundations of Quantum Mechanics". *Princeton University Press* (1955). (Cit. on p. 12)
109. J.B. Hertzberg *et al.* "Back-action-evading measurements of nanomechanical motion". *Nature Physics*, 6, 213 (2010). (Cit. on pp. 10 and 74)
110. J.D. Teufel, J.W. Harlow, C.A. Regal & K.W. Lehnert. "Dynamical Backaction of Microwave Fields on a Nanomechanical Oscillator". *Physical Review Letters*, 101, 197203 (2008). (Cit. on p. 10)
111. J.D. Teufel, T. Donner, M.A. Castellanos-Beltran, J.W. Harlow & K.W. Lehnert. "Nanomechanical motion measured with an imprecision below that at the standard quantum limit". *Nature Nanotechnology*, 4, 820 (2009). (Cit. on pp. 74, 75, 92, 144 and 150)
112. J.D. Teufel *et al.* "Sideband cooling of micromechanical motion to the quantum ground state". *Nature*, 475, 359363 (2011). (Cit. on pp. 9, 10, 18, 74, 143 and 163)
113. J.M. Pirkkalainen *et al.* "Hybrid circuit cavity quantum electrodynamics with a micromechanical resonator". *Nature*, 494, 211 (2013). (Cit. on pp. 10, 143, 182 and 183)
114. J.T. Hill, A.H. Safavi-Naeini, J. Chan & O. Painter. "Coherent optical wavelength conversion via cavity optomechanics". *Nature Communications*, 3, 1196 (2013). (Cit. on p. 10)
115. K. Hornberger, S. Gerlich, P. Haslinger, S. Nimmrichter & M. Arndt. "Colloquium: Quantum interference of clusters and molecules". *Review of Modern Physics*, 84, 157 (2012). (Cit. on pp. 16, 18 and 19)
116. K. Jacobs, P. Tombesi, M.J. Collett & D.F. Walls. "Quantum-nondemolition measurement of photon number using radiation pressure". *Physical Review A*, 49, 1961 (1994). (Cit. on p. 8)
117. K. Piscicchia *et al.* "CSL Collapse Model Mapped with the Spontaneous Radiation". *Entropy*, 19–7 (2017). (Cit. on p. 17)
118. K.J. Lulla, M. Defoort, C. Blanc, O. Bourgeois & E. Collin. "Evidence for the Role of Normal-State Electrons in Nanoelectromechanical Damping Mechanisms at Very Low Temperatures". *Physical Review Letters*, 110, 177206 (2013). (Cit. on pp. 103 and 141)
119. K.J. Lulla *et al.* "Nonlinear modal coupling in a high-stress doubly-clamped nanomechanical resonator". *New Journal of Physics*, 14, 113040 (1995). (Cit. on p. 102)
120. K.J. Lulla *et al.* "Nonlinear modal coupling in a high-stress doubly-clamped nanomechanical resonator". *New Journal of Physics*, 14, 113040 (2012). (Cit. on p. 19)
121. K.S. Thorne, R.W.P. Drever, C.M. Caves, M. Zimmermann & V.D. Sandberg. "Quantum Nondemolition Measurements of Harmonic Oscillators". *Physical Review Letters*, 40, 667 (1978). (Cit. on p. 8)
122. K.Y. Fong, M. Poot, X Han & H.X. Tang. "Phase noise of self-sustained optomechanical oscillators". *Physical Review A*, 90, 023825 (2014). (Cit. on pp. 8 and 177)
123. K.Y. Fong, W.H.P. Pernice & H.X. Tang. "Frequency and phase noise of ultrahigh Q silicon nitride nanomechanical resonators". *Physical Review B*, 85, 161410 (2012). (Cit. on p. 148)
124. L. Casparis *et al.* "Metallic Coulomb blockade thermometry down to 10 mK and below". *Review of Scientific Instruments*, 83, 083903 (2012). (Cit. on p. 128)

125. L. Childress *et al.* "Cavity optomechanics in a levitated helium drop". *Physical Review A*, 96, 063842 (2017). (Cit. on p. 8)
126. L. Dellantonio, O. Kyriienko, F. Marquardt & A.S. Sorensen. "Quantum nondemolition measurement of mechanical motion quanta". *Nature Communications*, 9, 3621 (2018). (Cit. on pp. 8 and 20)
127. L. DiCarlo *et al.* "Preparation and measurement of three-qubit entanglement in a superconducting circuit". *Nature*, 467, 574–578 (2006). (Cit. on p. 11)
128. L. Diosi. "A universal master equation for the gravitational violation of quantum mechanics". *Physical Letters A*, 120, 377 (1987). (Cit. on p. 16)
129. L. Diosi. "Continuous quantum measurement and itô formalism". *Physical Letters A*, 129, 8–9 (1988). (Cit. on p. 15)
130. L. Diosi. "Quantum Stochastic processes as models for state vector reduction". *Journal of Physics A: Mathematical and General*, 21, 13 (1988). (Cit. on p. 15)
131. L. Diosi. "Testing Spontaneous Wave-Function Collapse Models on Classical Mechanical Oscillators". *Physical Review Letters*, 114, 050403 (2015). (Cit. on p. 18)
132. L. Mercier de Lépinay *et al.* "Nano-optomechanical measurement in the photon counting regime". *arXiv:1503.03200* (2015). (Cit. on p. 7)
133. L. Qiu *et al.* "Floquet dynamics in the quantum measurement of mechanical motion". *Physical Review A*, 100, 053852 (2019). (Cit. on p. 151)
134. L.R. Sletten, B.A. Moores, J.J. Viennot & K.W. Lehnert. "Resolving Phonon Fock States in a Multimode Cavity with a Double-Slit Qubit". *Physical Review X*, 9, 021056 (2019). (Cit. on pp. 10, 12, 19, 182 and 183)
135. M. Aspelmeyer, S. Gröblacher, K. Hammerer & N. Kiesel. "Quantum optomechanics". *Journal of the Optical Society of America B*, Vol. 27, Issue 6 (2010). (Cit. on p. 83)
136. M. Aspelmeyer, T.J. Kippenberg & F. Marquardt. "Cavity optomechanics". *Reviews of Modern Physics*, 86, 1391 (2014). (Cit. on pp. 4, 8, 9, 38, 39, 43, 45, 81, 82, 83, 85, 87, 88, 89, 91, 92, 117, 138 and 164)
137. M. Bilardello, S. Donadi, A. Vinante & A. Bassi. "Bounds on collapse models from cold-atom experiments". *Physica A: Statistical Mechanics and its Applications*, 462, 764–782 (2016). (Cit. on p. 17)
138. M. Carlesso, A. Bassi, P. Falferi & A. Vinante. "Experimental bounds on collapse models from gravitational wave detectors". *Physical Review D*, 94, 124036 (2016). (Cit. on p. 17)
139. M. Defoort. "Non-linear dynamics in nano-electromechanical systems at low temperatures". *Thesis* (2014). (Cit. on pp. 158 and 176)
140. M. Defoort *et al.* "Stressed Silicon Nitride Nanomechanical Resonators at Helium Temperatures". *Journal of Low Temperature Physics*, 171, 731 (2013). (Cit. on p. 121)
141. M. Eichenfield, M. Chan, R.M. Camacho, K. J. Vahala & O. Painter. "Optomechanical crystals". *Nature*, 462, 78–82 (2009). (Cit. on p. 7)
142. M. Göppl *et al.* "Coplanar waveguide resonators for circuit quantum electrodynamics". *Journal of Applied Physics*, 104, 113904 (2008). (Cit. on p. 74)
143. M. Hamoumi *et al.* "Microscopic Nanomechanical Dissipation in Gallium Arsenide Resonators". *Physical Review Letter*, 120, 223601 (2018). (Cit. on p. 141)
144. M. Pinard, C. Fabre & A. Heidmann. "Quantum-nondemolition measurement of light by a piezoelectric crystal". *Physical Review A*, 51, 2443 (1995). (Cit. on p. 8)
145. M. Sansa *et al.* "Frequency fluctuations in silicon nanoresonators". *Nature Nanotechnology*, 11, 552–558 (2016). (Cit. on p. 145)
146. M. Steffen *et al.* "Measurement of the Entanglement of Two Superconducting Qubits via State Tomography". *Science*, 313, 5792 (2006). (Cit. on p. 11)

147. M. Toros, G. Gasbarri & A. Bassi. "Colored and dissipative continuous spontaneous localization model and bounds from matter-wave interferometry". *Physics Letters A*, 381, 47 (2017). (Cit. on p. 17)
148. M. Tse *et al.* & (LIGO Scientific Collaboration and Virgo Collaboration). "Quantum-enhanced advanced LIGO detectors in the era of gravitational-wave astronomy". *Physical Review Letters*, 123, 231107 (2019). (Cit. on pp. 5 and 6)
149. M. Vogel, C. Mooser & K. Karrai. "Optically tunable mechanics of microlevers". *Applied Physics Letters*, 83, 1337 (2003). (Cit. on p. 6)
150. M. Yuan, V. Singh, Y.M. Blanter & G.A. Steele. "Large cooperativity and microkelvin cooling with a three-dimensional optomechanical cavity". *Nature Communications*, 6, 8491 (2015). (Cit. on p. 10)
151. M.C. Cross & R. Lifshitz. "Elastic wave transmission at an abrupt junction in a thin plate with application to heat transport and vibrations in mesoscopic systems". *Physical Review B*, 64, 085324 (2001). (Cit. on p. 141)
152. M.H. Matheny, L.G. Villanueva, R.B. Karabalin, J.E. Sader & M.L. Roukes. "Nonlinear Mode-Coupling in Nanomechanical Systems". *Nano Letters*, 13, 1622 (2013). (Cit. on p. 102)
153. M.I. Dykman. "Heating and cooling of local and quasilocal vibrations by a nonresonance field". *Sov.Phys.Sol.St.*, 20, 1306 (1978). (Cit. on p. 8)
154. M.J. Weaver *et al.* "Coherent optomechanical state transfer between disparate mechanical resonators". *Nature Communications*, 8, 824 (2017). (Cit. on p. 10)
155. M.P. Blencowe & A.D. Armour. "Probing the quantum coherence of a nanomechanical resonator using a superconducting qubit: II. Implementation". *New Journal of Physics*, 10 (2008). (Cit. on pp. 12, 20 and 182)
156. M.S. Khalil, M.J.A. Stoutimore, F.C. Wellstood & K.D. Osborn. "An analysis method for asymmetric resonator transmission applied to superconducting devices". *Journal of applied physics*, 111, 054510 (2012). (Cit. on p. 111)
157. N. Bohr. "The Quantum Postulate and the Recent Development of Atomic Theory". *Physics Letters A*, 121, 580–590 (1928). (Cit. on p. 12)
158. N. Bohr. "Discussions with Einstein on Epistemological Problems in Atomic Physics". *publ. Cambridge University Press* (1949). (Cit. on p. 14)
159. N. Brahms, T. Botter, S. Schreppler, D.W.C. Brooks & D.M. Stamper-Kurn. "Optical Detection of the Quantization of Collective Atomic Motion". *Physical Review Letters*, 108, 133601 (2012). (Cit. on p. 151)
160. N. Gisin. "A simple nonlinear dissipative quantum evolution equation". *Journal of Physics A: Mathematical and General*, 14, 9 (1981). (Cit. on p. 15)
161. N. Gisin. "Quantum Measurements and Stochastic Processes". *Physical Review Letters*, 52, 1657 (1984). (Cit. on p. 15)
162. N. Maleeva *et al.* "Circuit quantum electrodynamics of granular aluminum resonators". *Nature Communications*, 9, 3889 (2018). (Cit. on pp. 29, 112, 116, 166 and 167)
163. N.R. Bernier *et al.* "Nonreciprocal reconfigurable microwave optomechanical circuit". *Nature Communication*, 8, 604 (2017). (Cit. on p. 143)
164. N.R. Bernier *et al.* "Nonreciprocal reconfigurable microwave optomechanical circuit". *Nature Communications*, 8, 604 (2017). (Cit. on p. 10)
165. N.S. Lawson. "A simple heat switch for use at millikelvin temperatures". *Cryogenics*, 22, 667 (1982). (Cit. on p. 129)
166. O. Arcizet, P.-F. Cohadon, T. Briant, M. Pinard & A. Heidmann. "Radiation-pressure cooling and optomechanical instability of a micro-mirror". *Nature*, 444, 71–74 (2006). (Cit. on p. 7)
167. O. Dupré *et al.* "Tunable sub-gap radiation detection with superconducting resonators". *Superconductor Science and Technology*, 30, 045007 (2017). (Cit. on pp. 112, 116 and 166)

168. O. Maillet, F. Vavrek, A.D. Fefferman, O. Bourgeois & E. Collin. "Classical decoherence in a nanomechanical resonator". *New Journal of Physics*, 18, 073022 (2016). (Cit. on pp. 19 and 145)
169. O. Maillet *et al.* "Non-linear Frequency Transduction of Nano-mechanical Brownian Motion". *Physical Review B*, 96, 165434 (2017). (Cit. on pp. 19 and 102)
170. O. Maillet *et al.* "Measuring frequency fluctuations in nonlinear nanomechanical resonators". *ACS Nano*, 12, 5753 (2018). (Cit. on pp. 144, 145, 146 and 148)
171. P. Delsing *et al.* "The 2019 surface acoustic waves roadmap". *Journal of Physics D: Applied Physics*, 52, 35 (2019). (Cit. on p. 18)
172. P. Langevin. "Sur la théorie du mouvement brownien". *C. R. Acad. Sci. (Paris)*, 146, 530–533 (1908). (Cit. on p. 26)
173. P. Lebedew. "Experimental examination of light pressure". *Annalen der Physik*, 311, 433 (1901). (Cit. on p. 4)
174. P. Mohanty *et al.* "Intrinsic dissipation in high-frequency micromechanical resonators". *Physical Review B*, 66, 085416 (2002). (Cit. on p. 141)
175. P. Pearl & E. Squires. "Bound state excitation, nucleon decay experiments and models of wave function collapse". *Physical Review Letters*, 73, 1 (1994). (Cit. on p. 15)
176. P. Pearle. "Reduction of the state vector by a nonlinear Schrodinger equation". *Physical Review D*, 13, 857 (1976). (Cit. on p. 15)
177. P.B. Abbott *et al.* & (LIGO Scientific Collaboration and Virgo Collaboration). "GW150914: First results from the search for binary black hole coalescence with Advanced LIGO". *Physical Review D*, 93, 122003 (2016). (Cit. on p. 5)
178. P.B. Abbott *et al.* & (LIGO Scientific Collaboration and Virgo Collaboration). "GW150914: The Advanced LIGO Detectors in the Era of First Discoveries". *Physical Review Letters*, 116, 131103 (2016). (Cit. on p. 5)
179. P.B. Abbott *et al.* & (LIGO Scientific Collaboration and Virgo Collaboration). "Observation of Gravitational Waves from a Binary Black Hole Merger". *Physical Review Letters*, 116, 061102 (2016). (Cit. on p. 5)
180. P.F. Cohadon, A. Heidmann & M. Pinard. "Cooling of a mirror by radiation pressure". *Physical review letters*, 83, 3174 (1999). (Cit. on p. 6)
181. R. Blaauwgeers *et al.* "Quartz Tuning Fork: Thermometer, Pressure and Viscometer for Helium Liquids". *Journal of Low Temperature Physics*, 146, 537 (2007). (Cit. on p. 131)
182. R. Penrose. "On Gravity's role in quantum state reduction". *General Relativity and Gravitation*, 28, 581–600 (1996). (Cit. on p. 16)
183. R. Riedinger *et al.* "Remote quantum entanglement between two micromechanical oscillators". *Nature*, 556, 473–477 (2018). (Cit. on p. 12)
184. R.W. Andrews *et al.* "Bidirectional and efficient conversion between microwave and optical light". *Nature Physics*, 10, 321–326 (2014). (Cit. on p. 10)
185. S. Barzanjeh *et al.* "Mechanical on-chip microwave circulator". *Nature Communication*, 8, 953 (2017). (Cit. on pp. 10, 143 and 144)
186. S. Belli *et al.* "Entangling macroscopic diamonds at room temperature: Bounds on the continuous-spontaneous-localization parameters". *Physical Review A*, 94, 012108 (2016). (Cit. on pp. 16 and 18)
187. S. Gröblacher *et al.* "Demonstration of an ultracold micro-optomechanical oscillator in a cryogenic cavity". *Nature physics*, 5, 485–488 (2009). (Cit. on pp. 6 and 7)
188. S. Mancini, D. Vitali & P. Tombesi. "Optomechanical cooling of a macroscopic oscillator by homodyne feedback". *Physical Review Letters*, 80, 688 (1998). (Cit. on pp. 6 and 19)
189. S. Stenholm. "The semiclassical theory of laser cooling". *Reviews of moder physics*, 58, 699 (1986). (Cit. on p. 4)

190. S.A. McGee, C.A. Regal, K.W. Lehnert & M.J. Holland. "Mechanical resonators for storage and transfer of electrical and optical quantum states". *Physical Review A*, 87, 053818 (2013). (Cit. on p. 10)
191. S.E. de Graaf *et al.* "Suppression of low-frequency charge noise in superconducting resonators by surface spin desorption". *Nature Communication*, 9, 1143 (2018). (Cit. on pp. 147 and 148)
192. S.L. Adler. "Lower and upper bounds on CSL parameters from latent image formation and IGM heating". *Journal of Physics A: Mathematical and Theoretical*, 4013501 (2007). (Cit. on p. 17)
193. S.L. Adler & A. Vinante. "Bulk heating effects as tests for collapse models". *Physical Review A*, 97, 052119 (2018). (Cit. on p. 17)
194. S.M. Spillane, T.J. Kippenberg, O.J. Painter & K.J. Vahala. "Ideality in a Fiber-Taper-Coupled Microresonator System for Application to Cavity Quantum Electrodynamics". *Physical Review Letters*, 91, 043902 (2003). (Cit. on p. 7)
195. S.P. Kumar & M.B. Plenio. "Quantum-optical tests of Planck-scale physics". *Physical Review A*, 97, 063855 (2018). (Cit. on pp. 17 and 19)
196. "Sonification of spikes". <https://youtu.be/bB7jkVqAsFs> (2020). (Cit. on p. 148)
197. T. Carmon, H. Rokhsari, L. Yang, T.J. Kippenberg & K.J. Vahala. "Temporal behaviour of radiation pressure induced vibrations of an optical microcavity phonon mode". *Physical Review Letters*, 94, 223902 (2005). (Cit. on pp. 8, 83 and 164)
198. T. Carmon, M.C. Cross & K.J. Vahala. "Chaotic Quivering of Micron-Scaled On-Chip Resonators Excited by Centrifugal Optical Pressure". *Physical Review Letters*, 98, 167203 (2007). (Cit. on pp. 8 and 164)
199. T. Kovachy *et al.* "Quantum superposition at the half-metre scale". *Nature*, 528, 530–533 (2015). (Cit. on pp. 16 and 18)
200. T. Rocheleau *et al.* "Preparation and Detection of a Mechanical Resonator near the Ground State of Motion". *Nature (London)*, 463, 72 (2010). (Cit. on pp. 10, 60, 62, 144 and 150)
201. T.A. Palomaki, J.D. Teufel, R.W. Simmonds & K.W. Lehnert. "Entangling Mechanical Motion with Microwave Fields". *Science*, 342, 6159 (2013). (Cit. on pp. 11 and 12)
202. T.A. Palomaki, J.W. Harlow, J.D. Teufel, R.W. Simmonds & K.W. Lehnert. "Coherent state transfer between itinerant microwave fields and a mechanical oscillator". *Nature*, 495, 210 (2013). (Cit. on pp. 10, 11, 75 and 143)
203. T.J. Kippenberg, H. Rokhsari, T. Carmon, A. Scherer & K.J. Vahala. "Analysis of Radiation-Pressure Induced Mechanical Oscillation of an Optical Microcavity". *Physical Review Letters*, 95, 033901 (2005). (Cit. on p. 7)
204. "The Feynman lectures on physics vol II, electromagnetism and matter". Addison-Wesley Publishing Company, inc. Reading, Massachusetts (1963). (Cit. on p. 172)
205. U. Delic *et al.* "Cooling of a levitated nanoparticle to the motional quantum ground state". *Science*, 367, 6480 (2020). (Cit. on p. 7)
206. V. Singh *et al.* "Optomechanical coupling between a multilayer graphene mechanical resonator and a superconducting microwave cavity". *Nature Nanotechnology*, 9, 820 (2014). (Cit. on pp. 139 and 143)
207. V.B. Braginsky, A.B. Manukin & M.Y. Tikhonov. "Investigation of dissipative ponderomotive effects of electromagnetic radiation". *Journal of Experimental and Theoretical Physics*, 58, 1549–1552 (1970). (Cit. on p. 4)
208. V.B. Braginsky & F.Y. Khalili. "Quantum nondemolition measurements: the route from toys to tools". *Review of modern physics*, 68, 1 (1996). (Cit. on p. 8)
209. V.B. Braginsky, Y.I. Vorontsov & K.S. Thorne. "Quantum Nondemolition Measurements". *Science*, 209, 4456 (1980). (Cit. on pp. 7 and 8)
210. W. Marshall, C. Simon, R. Penrose & D. Bouwmeester. "Towards Quantum Superpositions of a Mirror". *Physical Review Letters*, 91, 130401 (2003). (Cit. on p. 18)

211. W.A. Phillips. "Two-level states in glasses". *Reports on Progress in Physics*, 50, 1657 (1987).
(Cit. on pp. 140 and 141)
212. W.H. Zurek. "Decoherence and the Transition from Quantum to Classical". *Physics Today*, 44, 10 (1991).
(Cit. on pp. 13 and 19)
213. W.P. Bowen, N. Treps, R. Schnabel & P.K. Lam. "Experimental Demonstration of Continuous Variable Polarization Entanglement". *Physical Review Letters*, 89, 253601 (2002). (Cit. on p. 11)
214. Y. Yanay, J.C. Sankey & A.A. Clerk. "Quantum backaction and noise interference in asymmetric two-cavity optomechanical systems". *Physical Review A*, 93, 063809 (2016). (Cit. on p. 8)
215. Y. Zhao *et al.* "Frequency-Dependent Squeezed Vacuum Source for Broadband Quantum Noise Reduction in Advanced Gravitational-Wave Detectors". *Physical Review Letters*, 124, 171101 (2020).
(Cit. on p. 6)
216. Y.M Blanter & M. Büttiker. "Shot noise in mesoscopic conductors". *Physics Reports*, 336, 1 (2000).
(Cit. on p. 157)

MY ARTICLES

217. D. Cattiaux, S. Kumar, X. Zhou, A. Fefferman & E. Collin. "Geometrical nonlinearity of circular plates and membranes: An alternative method". *Journal of Applied Physics*, 128, 104501 (2020).
(Cit. on pp. 99, 105, 106, 107, 108, 109, 167, 171 and 172)
218. D. Cattiaux *et al.* "A macroscopic object in its quantum ground state of motion". *In preparation* (2021).
(Cit. on pp. 137, 150 and 154)
219. D. Cattiaux, X. Zhou, S. Kumar, I. Golokolenov, R. R. Gazizulin, A. Luck, L. Mercier de Lépinay, M. Sillanpää, A. D. Armour, A. Fefferman & E. Collin. "Beyond linear coupling in microwave optomechanics". *Physical Review Research*, 2, 033480 (2020). (Cit. on pp. 115 and 163)
220. I. Golokolenov, D. Cattiaux, S. Kumar, M. Sillanpää, L. Mercier de Lépinay, A. Fefferman & E. Collin. "Microwave optomechanics in the classical regime". *arXiv:2011.13814* (2020).
(Cit. on pp. 89 and 90)
221. O. Maillet, D. Cattiaux, X. Zhou, R.R. Gazizulin, O. Bourgeois, A.D. Fefferman & E. Collin. "Nanomechanical damping via electron-assisted relaxation of two-level systems". *arXiv:2009.03804* (2020).
(Cit. on pp. 103, 141, 148 and 158)
222. X. Zhou, D. Cattiaux, D. Theron & E. Collin. "Electric circuit model of microwave optomechanics". *arXiv:2007.14438*; in print *J. of Appl. Phys.* (2021).
(Cit. on pp. 73 and 76)
223. X. Zhou, D. Cattiaux, R.R. Gazizulin, A. Luck, O. Maillet, T. Crozes, J.-F. Motte, O. Bourgeois, A. Fefferman & E. Collin. "On-chip Thermometry for Microwave Optomechanics Implemented in a Nuclear Demagnetization Cryostat". *Physical Review Applied*, 12, 044066 (2019).
(Cit. on pp. 74, 75, 94, 111, 137, 164 and 174)

BOOKS

224. A. Einstein. *Die Grundlage der Allgemeinen Relativitätstheorie* (Annalen der Physics, 1916).
(Cit. on p. 5)
225. A.H. Nayfeh & D.T. Mook. *Nonlinear Oscillations* (Wiley VCH, New York, 2nd revised edition, 1995).
(Cit. on p. 103)
226. A.N Cleland. *Foundations of Nanomechanics* (Springer, Berlin, 2003 edition, 2002).
(Cit. on pp. 99, 101 and 103)
227. C. Cohen-Tannoudji, B. Diu & F. Laloë. *Quantum Mechanics: Volume 1 and 2* (Wiley, 2015).
(Cit. on p. 30)

228. C. Kittel & P. McEuen. *Introduction to Solid State Physics* (John Wiley and Sons, 2019, 2019). (Cit. on pp. 125 and 126)
229. C.W. Gardiner & P. Zoller. *Quantum Noise: A Handbook of Markovian and Non-Markovian Quantum Stochastic Methods with Applications to Quantum Optics* (Springer, 2004). (Cit. on pp. 26, 27 and 30)
230. D. Vollhardt & P. Wolfle. *The Superfluid Phases of Helium 3* (Dover Books on Physics, NY, 2013). (Cit. on p. 131)
231. D.F. Walls & G.J. Milburn. *Quantum Optics* (Springer, 2008). (Cit. on pp. 30 and 32)
232. D.M. Pozar. *Microwave Engineering* (John Wiley and Sons, Inc. 4th Ed., 2012). (Cit. on pp. 76 and 111)
233. E. Joos *et al.* *Decoherence and the Appearance of a Classical World in Quantum Theory* (Springer, 2003). (Cit. on pp. 12, 13 and 14)
234. F. Pobell. *Matter and methods at low temperature* (Springer, Third Edition, 2007). (Cit. on pp. 122, 124, 126 and 128)
235. J. Kepler. *De Cometis Libelli Tres. I. Astronomicus, II. Physicus, III. Astrologicus* (1619). (Cit. on p. 4)
236. J.C. Maxwell. *A treatise on electricity and magnetism, Part IV. Electromagnetism* (Nature, 1873). (Cit. on p. 4)
237. L.D. Landau & E.M. Lifshitz. *Mechanics, Third Edition: Volume 1* (Butterworth-Heinemann, Amsterdam u.a, 3 edition edition, 1976). (Cit. on p. 103)
238. L.D. Landau & E.M. Lifshitz. *Theory of elasticity* (Butterworth-Heinemann, Oxford 3rd Ed., 1986). (Cit. on p. 99)
239. M. Aspelmeyer, T.J. Kippenberg & M. Marquardt. *Cavity optomechanics: Nano- and Micromechanical resonators interacting with light* (Springer, 2013). (Cit. on pp. 7, 9, 111 and 151)
240. M. Tinkham. *Introduction to Superconductivity* (Courier Corporation, 2004). (Cit. on p. 115)
241. O.V. Lounasmaa. *Experimental principles and methods below 1K* (Academic Press, 1974). (Cit. on p. 122)
242. R. Lifshitz & M.C. Cross. *Reviews of Nonlinear Dynamics and Complexity Vol. 1* (Wiley-VCH, Weinheim edited by H.G. Schuster, p. 152, 2008). (Cit. on pp. 102, 103, 108, 109 and 167)
243. S. Chu, J.E. Bjorkholm, A. Ashkin, L. Hollberg & A. Cable. *Cooling and trapping of atoms with laser light* (Springer, Methods of Laser Spectroscopy, 1986). (Cit. on p. 4)
244. S. Schmid, L.G. Villanueva & M.L. Roukes. *Fundamentals of Nanomechanical Resonators* (Springer, 2016). (Cit. on p. 104)
245. S. Timoshenko. *Strength of materials, Part I and Part II* (Krieger Publishing U.S.A, third edition, 1983). (Cit. on p. 99)
246. S. Timoshenko, D.H. Young & W.H. Weaver Jr. *Vibrations problems in engineering* (John Wiley and Sons, fourth edition, 1974). (Cit. on p. 100)
247. S. Timoshenko & S. Woinowsky-Krieger. *Theory of plates and shells* (McGraw-Hill New York, 1959). (Cit. on p. 104)
248. V.B. Braginsky & A.B. Manukin. *Measurement of weak forces in physics experiments* (University of Chicago press, 1977). (Cit. on p. 4)
249. V.B. Braginsky & F.Y. Khalili. *Quantum Measurement* (Cambridge University Press, 1995). (Cit. on p. 4)
250. W. Heisenberg. *Physics and philisophy: the revolution in modern science* (Harper Perennial Modern Classics, 1958). (Cit. on p. 1)

Abstract:

Recent advances in observing and exploiting macroscopic mechanical motion at the quantum limit brought opto-mechanical experiments down to always lower temperatures and smaller sizes, boosting a new research area where (more compatible) low energy photons are employed: microwave opto-mechanics.

Superconducting microwave circuits are in use and bridge opto-mechanics with quantum electronics, which positions the former as a new resource for quantum information processing. But microwave opto-mechanical platforms provide also unique capabilities for testing quantum mechanics at the most basic level: if one thinks about these devices in terms of quantum-limited detectors, the focus is on the *thermodynamic baths* that continuously interact with the mechanical degree of freedom. The fundamental questions that are addressed are then quantum thermodynamics, the boundary between classical and quantum mechanics defined by wavefunction collapse, and ultra-low temperature materials properties.

In order to perform such experiments at the frontier of modern physics, we created a unique micro-wave/micro-Kelvin opto-mechanical platform. We demonstrate for the first time the passive cooling of a 15 MHz aluminium drumhead mechanical device down to 500 micro-K, reaching a population for the fundamental mode of 0.3 quanta on average; all higher modes being empty to a very high probability. Using microwave opto-mechanics as a non-invasive detector, we report on the *in-equilibrium* thermal properties of this lowest frequency mode, challenging theory in an unprecedented experimental area.

